

5-1994

The Effects of Channel Curvature and Protusion Height on Nucleate Boiling and the Critical Heat Flux of a Simulated Electronic Chip

John E. Leland

University of Dayton, john.leland@udri.udayton.edu

Follow this and additional works at: http://ecommons.udayton.edu/ofr_pub

 Part of the [Electrical and Electronics Commons](#), [Power and Energy Commons](#), and the [Propulsion and Power Commons](#)

eCommons Citation

Leland, John E., "The Effects of Channel Curvature and Protusion Height on Nucleate Boiling and the Critical Heat Flux of a Simulated Electronic Chip" (1994). *Office for Research Publications and Presentations*. 42.
http://ecommons.udayton.edu/ofr_pub/42

This Article is brought to you for free and open access by the Office for Research at eCommons. It has been accepted for inclusion in Office for Research Publications and Presentations by an authorized administrator of eCommons. For more information, please contact frice1@udayton.edu, mschlangen1@udayton.edu.

WL-TR-94-2051

THE EFFECTS OF CHANNEL CURVATURE
AND PROTRUSION HEIGHT ON NUCLEATE BOILING AND
THE CRITICAL HEAT FLUX OF A SIMULATED ELECTRONIC CHIP

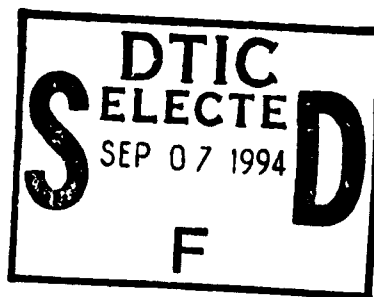


1

AD-A284 090



JOHN ERNEST LELAND



MAY 1994

FINAL REPORT FOR 08/01/89-05/01/94

APPROVED FOR PUBLIC RELEASE; DISTRIBUTION IS UNLIMITED.

This material may be only by or for US Govt pursuant to the copyright
license under the clause at DFARS 252.227-7013 dtd Oct 88.

AEROPROPULSION AND POWER DIRECTORATE
WRIGHT LABORATORY
AIR FORCE MATERIEL COMMAND
WRIGHT PATTERSON AFB OH 45433-7251

DTIC QUALITY INSPECTED 3

94-28991



2768

94 9 06 047

NOTICE

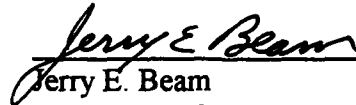
When Government drawings, specifications, or other data are used for any purpose other than in connection with a definitely Government-Related procurement, the United States Government incurs no responsibility or any obligation whatsoever. The fact that the government may have formulated or in any way supplied the said drawings, specifications, or other data, is not to be regarded by implication, or otherwise in any manner construed, as licensing the holder, or any other person or corporation, or as conveying any rights or permission to manufacture, use, or sell any patented invention that may in any way be related thereto.

This report is releasable to the National Technical Information Service (NTIS). At NTIS, it will be available to the general public, including foreign nations.

This technical report has been reviewed and is approved for publication.



John E. Leland
Project Engineer
Thermal Technology Section



Jerry E. Beam
Section Chief
Thermal Technology Section



Michael D. Braydich, Lt Col, USAF
Deputy Chief
Aerospace Power Division

If your address has changed, if you wish to be removed from our mailing list, or if the addressee is no longer employed by your organization, please notify WL/POOS-3, WPAFB, OH 45433-7251 to help us maintain a current mailing list.

Copies of this report should not be returned unless return is required by security considerations, contractual obligations, or notice on a specific document.

REPORT DOCUMENTATION PAGE

Form Approved
OMB No. 0704-0188

Public reporting burden for this collection of information is estimated to average 1 hour per response, including the time for reviewing instructions, searching existing data sources, gathering and maintaining the data needed, and completing and reviewing the collection of information. Send comments regarding this burden estimate or any other aspect of this collection of information, including suggestions for reducing this burden, to Washington Headquarters Services, Directorate for Information Operations and Reports, 1215 Jefferson Davis Highway, Suite 1204, Arlington, VA 22202-4302, and to the Office of Management and Budget, Paperwork Reduction Project (0704-0188), Washington, DC 20503.

1. AGENCY USE ONLY (Leave blank)		2. REPORT DATE May 1994	3. REPORT TYPE AND DATES COVERED FINAL 08/01/89 - 05/01/94	
4. TITLE AND SUBTITLE THE EFFECTS OF CHANNEL CURVATURE AND PROTRUSION HEIGHT ON NUCLEATE BOILING AND THE CRITICAL HEAT FLUX OF A SIMULATED ELECTRONIC CHIP			5. FUNDING NUMBERS PE 62 PR 3145 TA 20 WU 49	
6. AUTHOR(S) John Ernest Leland				
7. PERFORMING ORGANIZATION NAME(S) AND ADDRESS(ES) Aero Propulsion and Power Directorate Wright Laboratory Air Force Materiel Command Wright Patterson AFB OH 45433-7251			8. PERFORMING ORGANIZATION REPORT NUMBER	
9. SPONSORING / MONITORING AGENCY NAME(S) AND ADDRESS(ES) Aero Propulsion and Power Directorate Wright Laboratory Air Force Materiel Command Wright Patterson AFB OH 45433-7251			10. SPONSORING / MONITORING AGENCY REPORT NUMBER WL-TR-94-2051	
11. SUPPLEMENTARY NOTES				
12a. DISTRIBUTION / AVAILABILITY STATEMENT Approved for Public Release; Distribution is Unlimited.			12b. DISTRIBUTION CODE	
13. ABSTRACT (Maximum 200 words) The quest for higher power yet smaller electronics has given rise to the need for very effective cooling of these electronics. Because one of the foremost problems in electronics cooling is achieving high heat flux cooling within small packages while expending minimal pumping power, one focus of this study was to investigate the effects of channel curvature on the CHF. Experimental data were obtained for flow rates of 1-7 m/s, subcoolings of 5-35°C, and radii of curvature of 25.4 and 50.8 mm. A correlation was obtained for these data which provided an excellent fit. One condition that has been ignored in the literature is the effect of the simulated heat source not being flush with the flow channel wall. In manufacturing an electronics cooling device, it will be very difficult to maintain the flush chip condition because of the dissimilar materials involved and the numerous thermal cyclings that the device will go through. Experiments showed a significant effect on CHF of the simulated heat source not being flush. A series of data was obtained for flow velocities of 1-4 m/s and subcoolings of 20-35°C. CHF data were obtained for a surface recessed 0.127 mm, a flush surface, and surfaces protruded 0.229, 0.457, and 0.635 mm into the flow stream. <div style="text-align: right;">DTIC QUALITY INSPECTED 3</div>				
14. SUBJECT TERMS Electronics Cooling, Curved Channel Boiling, Protruding Heat Sources, Direct Immersion Cooling, Dielectric Coolant, Flow Boiling			15. NUMBER OF PAGES 276	
			16. PRICE CODE	
17. SECURITY CLASSIFICATION OF REPORT UNCLASSIFIED	18. SECURITY CLASSIFICATION OF THIS PAGE UNCLASSIFIED	19. SECURITY CLASSIFICATION OF ABSTRACT UNCLASSIFIED	20. LIMITATION OF ABSTRACT UL	

ACKNOWLEDGMENTS

There are many people I would like to thank for encouraging me to undertake this course of study and for supporting me over the years it took to complete it. First, I would like to thank Dr. E. Thomas Mahefkey and my advisor, Dr. Louis C. Chow, for their encouragement. I would never have undertaken this effort without the confidence I obtained from them. I would like to thank my parents for instilling in me, the values and work ethic that are necessary for completing a work of this magnitude. I would also like to thank my friends and family for supporting me during the time it took to complete this work. I would especially like to thank them for being there during the rough times and for being patient and understanding during my long absences from them. I am also grateful to Dr. Martin Pais for his friendship, practical advice, and hospitality when I needed a place to stay in Lexington.

I would also like to acknowledge the efforts of Mr. Donald Brigner who patiently and diligently helped me obtain data during the last year. I would also like to thank him for his friendship, and the keen interest and enthusiasm with which he approaches his work. Mr. John Tennant is also to be thanked for his meticulous assembly of some of the more complicated test sections. I would also like to thank Mr. Joe Kern, Mr. Elijah B. Yates and Mr. Austin Pyle, of the University of Kentucky and members of the US Air Force machine shop for making the numerous parts that made up the test sections. I also thank Mr. Sylvan Ferrel for his humor and his help in scrounging the important bits and pieces that make up an experimental apparatus. Mr. Donald L. Reinmuller is to be thanked for coordinating some of the machine shop activities between the US Air Force and University of Kentucky. I would also like to thank Mr. John Grant of Universal Energy Systems, Inc., who helped me obtain the surface composition analyses by using an x-ray photoelectron spectrometer.

My appreciation goes to the US Air Force which financially supported me during my stay at UK. I also want to acknowledge UK for funding the experimental apparatus through internal funding. The 3M company is also thanked for their donation of FC-72.

TABLE OF CONTENTS

ACKNOWLEDGEMENTS	iii
RULES FOR USE OF DISSERTATION	iv
LIST OF FIGURES	viii
LIST OF TABLES	xii
NOMENCLATURE	xiii
Chapter	
1 INTRODUCTION	1
1.1 Motivation	2
1.2 Background	3
2 EFFECTS OF SURFACE CHARACTERISTICS AND ABSORBED AIR	7
2.1 Experimental Apparatus	7
2.2 Experimental Procedure	12
2.3 Uncertainty Analysis	13
2.4 Effects of Surface Roughness	17
2.4.1 Effect of Surface Roughness on Nucleate Boiling	17
2.4.2 Effect of Surface Roughness on CHF	20
2.5 Effect of Surface Contamination	21
2.6 Effect of Surface Aging	28
2.7 Effect of Absorbed Air	28
2.8 Conclusions	33
3 EFFECT OF CHANNEL HEIGHT ON CHF	35
3.1 An Introduction to the Mechanisms and Modeling of Pool Boiling CHF	35
3.2 An Introduction to the Mechanisms and Modeling of Flow Boiling CHF	45
3.3 Effect of Channel Height - Previous Results	55
3.4 Effect of Channel Height - Experimental Results	56
3.5 Dependence of CHF on Velocity for $We < 100$ and $We > 10^4$	65
3.6 An Improved Correlation	66

3.7	Boiling Incipience	75
3.8	Conclusions	76
4	EFFECT OF CHANNEL CURVATURE ON CHF	78
4.1	Experimental Apparatus - Curved Channel Details	85
4.2	Experimental Results	87
4.3	An Improved Correlation for Curved Channels	105
4.4	Conclusions	108
5	BOILING FROM A NONFLUSH SIMULATED ELECTRONIC CHIP	111
5.1	Experimental Apparatus - Nonflush Chip Details	112
5.2	Uncertainty Analysis - Nonflush Chip Details	116
5.3	Experimental Results	118
5.3.1	Flush Surface	119
5.3.2	Recessed Surface	121
5.3.3	Protruded Surface	122
5.4	Correlation of Protruded Surface CHF Results	140
5.5	Conclusions	142
5.5.1	Flush	142
5.5.2	Recessed Surface	142
5.5.3	Protruded Surface	144
6	OTHER EFFECTS OF PROTRUDING CHIP GEOMETRY ON BOILING AND CHF	146
6.1	Experimental Apparatus - Thin Foil Heater	146
6.2	Uncertainty Analysis - Thin Foil Heater	150
6.3	Experimental Results	153
6.3.1	Foil Heater Test Section	153
6.3.2	Copper Block Test Section	160
6.4	Conclusions	167
7	CONCLUSIONS AND RECOMMENDATIONS	170
	REFERENCES	181

Appendix

A	DETAILS OF CURVED CHANNEL TEST SECTION GEOMETRY	203
B	DEFINITION OF ROUGHNESS PARAMETERS	212
C	UNCERTAINTY ANALYSIS FOR EXPERIMENTAL APPARATUS OF CHAPTERS 2-5	214
	C.1 Heat Flux	214
	C.2 Wall Temperature	221
	C.3 Electrical Power	222
	C.4 Flow Velocity	223
D	DERIVATION OF MODEL FOR SURFACE TEMPERATURE VARIATION	225
E	UNCERTAINTY ANALYSIS FOR AVERAGE WALL TEMPERATURE OF THIN FOIL HEATER	232
F	DATA	237
	BIBLIOGRAPHY	250
	VITA	257

Accession For	
NTIS CRA&I	<input checked="" type="checkbox"/>
DTIC TAB	<input type="checkbox"/>
Unannounced Justification	<input type="checkbox"/>
By	
Distribution /	
Availability Codes	
Dist	Avail and/or Special
A-1	

LIST OF FIGURES

Figure		Page
2.1	Flow loop schematic.	8
2.2	Flow channel design.	9
2.3	Curved section test heater and enclosure.	11
2.4	Effect of surface roughness on nucleate boiling.	18
2.5	Composition of silicone contaminated surface.	23
2.6	Composition of clean surface.	24
2.7	Effect of contamination on nucleate boiling and CHF.	26
2.8	Effect of contamination on nucleate boiling curve.	27
2.9	Effect of surface aging on straight section heater.	29
2.10	Effect of surface aging on curved section heater.	30
2.11	Effect of absorbed air on nucleate boiling curve.	32
3.1	Regions of boiling mechanisms for water boiling on 4/0 polished surface. ⁴⁹	38
3.2	Schematic of pool boiling regimes. ⁴⁹	39
3.3	Schematic of pool boiling CHF mechanisms. ⁹⁴	43
3.4	Schematic representation of flow boiling CHF mechanism. ¹⁹ (a) Low velocity mechanism. (b) High velocity mechanism.	46
3.5	Heat flux versus wall superheat for 5° C subcooling.	58
3.6	Heat flux versus wall superheat for 20° C subcooling.	59
3.7	Heat flux versus wall superheat for 35° C subcooling.	60
3.8	Effect of channel height on CHF.	61
3.9	Comparison of data with Eq. (3.23).	62
3.10	Comparison of data with Eq. (3.23).	63
3.11	Comparison of data with Eqs. (3.23) and (3.27).	67
3.12	Comparison of data with Eq. (3.23) and <i>Re</i> modified Eq. (3.23).	71
3.13	Comparison of data with Eqs. (3.23) and (3.31).	74

4.1	Secondary flow pattern in a curved pipe.	81
4.2	Secondary flow pattern and azimuthal velocity contours in a square duct. ¹⁴⁷ (a) $R/h = 125$, (b) $R/h = 15.63$. Center of curvature is to the left.	82
4.3	Heat flux versus wall superheat for curved channel and 5°C subcooling.	88
4.4	Heat flux versus wall superheat for curved channel and 20°C subcooling.	89
4.5	Heat flux versus wall superheat for curved channel and 35°C subcooling.	90
4.6	Comparison of straight and curved channel boiling curves for $\Delta T_{sub} = 5^\circ\text{C}$.	91
4.7	Comparison of straight and curved channel boiling curves for $\Delta T_{sub} = 20^\circ\text{C}$.	92
4.8	Comparison of straight and curved channel boiling curves for $\Delta T_{sub} = 35^\circ\text{C}$.	93
4.9	Comparison of CHF for straight and curved test sections.	95
4.10	Comparison of straight and curved section data with Eq. (3.23).	96
4.11	Comparison of data to Eqs. (4.9), (4.10) and Re modified Eq. (4.10).	102
4.12	Relative difference of $q_{M, str}$ and $q_{M, cur}$.	104
4.13	Comparison of data with Eqs. (3.31), (4.16), and (4.17).	109
5.1	Flow loop schematic.	113
5.2	Flow channel cross section with test heater.	114
5.3	Simulated electronic chip and heater enclosure.	115
5.4	Comparison of new straight channel data with various correlations.	120
5.5	Comparison of recessed and flush cases for $\Delta T_{sub} = 20^\circ\text{C}$ and $U = 1$ and 4 m/s.	123
5.6	Comparison of recessed and flush cases for $\Delta T_{sub} = 20^\circ\text{C}$ and $U = 2$ and 3 m/s.	124
5.7	Comparison of recessed and flush cases for $\Delta T_{sub} = 35^\circ\text{C}$ and $U = 1$ and 4 m/s.	125
5.8	Comparison of recessed and flush cases for $\Delta T_{sub} = 35^\circ\text{C}$ and $U = 2$ and 3 m/s.	126
5.9	Comparison of protruded and flush cases for $\Delta T_{sub} = 35^\circ\text{C}$ and $U = 1$ and 4 m/s.	128

5.10	Comparison of protruded and flush cases for $\Delta T_{sub} = 20^\circ\text{C}$ and $U = 2$ and 3 m/s.	129
5.11	Comparison of protruded and flush cases for $\Delta T_{sub} = 35^\circ\text{C}$ and $U = 1$ and 4 m/s.	130
5.12	Comparison of protruded and flush cases for $\Delta T_{sub} = 35^\circ\text{C}$ and $U = 2$ and 3 m/s.	131
5.13	Variation of CHF with heater height and velocity for 20°C subcooling.	132
5.14	Variation of CHF with heater height and velocity for 35°C subcooling.	133
5.15	Progression of boiling and instability for $U = 2$ m/s, $h_p = 0.635$ mm, and $\Delta T_{sub} = 20^\circ\text{C}$.	134
5.16	Behavior of boiling curve with heater height.	136
5.17	Variation of maximum power dissipation with h_p and U for $\Delta T_{sub} = 20^\circ\text{C}$.	138
5.18	Variation of maximum power dissipation with h_p and U for $\Delta T_{sub} = 35^\circ\text{C}$.	139
5.19	Comparison of protruded surface data with Eqs. (5.1) and (5.2).	141
5.20	Comparison of protruded surface data with Eqs. (5.1), (5.2), and (5.6).	143
6.1	Thin foil heater assembly.	147
6.2	Foil heater thermocouple locations.	149
6.3	Front face insulator details.	151
6.4	Variation of surface temperatures relative to T_1 with heat flux.	155
6.5	Comparison of CHF with heater height and velocity for thin and thick heaters.	161
6.6	Schematic of boiling from thin and thick heater test sections.	162
6.7	Behavior of boiling curve with and without insulators.	164
6.8	Insulated and non-insulated protruding heater CHF compared with flush heater CHF.	165
6.9	Power dissipation versus velocity for heaters with and without insulators.	168
A.1	Front lamina of channel test section.	204
A.2	Center lamina of channel test section.	205
A.3	Back lamina of channel test section.	206

A.4	Details of curved section heater insertion hole.	207
A.5	Details of straight section heater insertion hole.	208
A.6	Curved section heater enclosure.	209
A.7	Copper block heater/simulated electronic chip.	210
A.8	Backside cover for heater enclosure.	211
B.1	Roughness profile with basic parameters for measuring surface roughness.	212
B.2	Definition of R_p .	213
B.3	Definition of S.	213
C.1	Schematic of curved test section heater.	214
C.2	Schematical representation of thermocouple bead in hole.	218
C.3	Heat flux uncertainty versus heat flux.	220
C.4	Electrical schematic of heater power circuit.	222
D.1	Mechanisms of heat flux variation beneath a bubble.	225
D.2	Schematic of model to describe surface temperature variation. ³²	226
E.1	Electrical circuit used for obtaining heater temperature and power.	233

LIST OF TABLES

Table		Page
2.1	Flow channel parameters and geometry factor.	10
3.1	Flow channel parameters and geometry factor.	57
3.2	Laminar sublayer and buffer layer thicknesses for geometry of Mudawar and Maddox. ¹⁹	68
3.3	Correlation constants and accuracy parameters.	70
4.1	Velocity layer thicknesses for channel #2.	98
4.2	Change of velocity profile, buoyancy, and secondary flow with velocity.	101
4.3	Correlation constants and accuracy parameters.	105
6.1	Predicted temperature variation.	152
6.2	Predicted values of asymptotic thickness and q_M/q_{asy} for current experiments.	157

NOMENCLATURE

a	acceleration, U^2/R
A_v	vapor column area of a unit boiling cell
A_w	area of a unit boiling cell
CHF	Critical Heat Flux
C_f	skin friction coefficient
c	specific heat of a solid
c_p	specific heat at constant pressure
d_d	bubble departure diameter
D_h	hydraulic diameter based on wetted perimeter
f	pressure drop friction factor
h	channel height
h_{fg}	latent heat of vaporization
h_p	heater protrusion height
g	gravitational constant, 9.81 m/s^2
It	dimensionless quantity found by Ito ³⁰ , $Re (D_h/2R)^2$
Ja	Jakob number, $c_p \Delta T_{sub} / h_{fg}$
Ja*	modified Jakob number, $\rho_f c_p \Delta T_{sub} / \rho_g h_{fg}$
k	thermal conductivity
K	Dean number, $Re \sqrt{D_h/2R}$
L	surface heated length
NBR	Nucleate Boiling Regime
q	heat flux
q_{asy}	asymptotic value of CHF obtained when further increasing the product of heater thickness and effusivity has no effect
q_M	critical heat flux (CHF)
$q_{M,c-c}$	critical heat flux of protruded chips based on cross-sectional area alone
q_M^{**}	dimensionless critical heat flux
Q_M	maximum power dissipation

r^*	radius of largest unflooded cavity
R	radius of curvature
R_a	International Organization for Standardization standard (ISO R468) for surface roughness
Re	Reynolds number, UD_h / ν
Ri	Richardson number, $a(\rho_f - \rho_g)L / U^2 \rho_f$, where $a = g$ for some analyses
S	mean peak-to-peak spacing of surface roughness elements
t	heater thickness
T_n	Surface temperature at location n
T_b	fluid inlet bulk temperature
T_{sat}	saturation temperature based on measured static pressure
T_w	heated surface wall temperature
ΔT_{sub}	subcooling, $T_{sat} - T_b$
ΔT_w	wall superheat, $T_w - T_{sat}$
u	local temporal mean velocity in streamwise direction
u_τ	friction velocity
u^+	dimensionless velocity, u/u_τ
U	bulk mean velocity based on channel cross section
w	channel width
We	Weber number, $\rho U^2 L / \sigma$
y	distance outward normal from heater
y^+	dimensionless wall coordinate, yu_τ / ν
α_0	temperature coefficient of electrical resistance
λ_c	Taylor instability critical wavelength
λ_d	Taylor instability most dangerous wavelength
λ_H	Helmholtz instability critical wavelength
μ	dynamic viscosity
ν	kinematic viscosity
ρ	density
ρ	electrical resistivity

σ surface tension
 v specific volume

Subscripts

b bubble
 cur curved section
 f liquid
Flush flush heater surface
 g vapor
 str straight section

Chapter 1

INTRODUCTION

The main focus of this dissertation is the quantification of various geometry and fluid effects on boiling from a discrete heat source in a rectangular flow channel. This topic is relevant to the direct immersion cooling of electronics by a dielectric fluid. The effects of flow channel geometry, (including channel curvature and height), surface roughness, surface composition, air absorbed in the fluid were studied. The effect of the heated surface being protruded or recessed from the flow channel wall was also studied. In all cases, the fluid conditions were varied in flow rate and temperature, and the above effects were ascertained in relation to these fluid parameters. Boiling heat transfer is generally very effective as compared to more conventional means of cooling. This effectiveness is characterized by the ability to attain large heat fluxes for a small temperature difference or in other words, a high heat transfer coefficient. Temperature difference is the potential that drives all heat transfer.

Because the boiling heat transfer in this study occurs with a flowing liquid, it is characterized as flow boiling as opposed to pool boiling. Pool boiling is the most thoroughly studied area and is analogous to the situation of water boiling in a pot. Flow boiling can be further divided into boiling in continuously heated tubes or channels, (an area pertinent to nuclear reactor cooling), and boiling from small discrete heat sources in a channel. In the former case, the net vapor generation becomes an important factor in the boiling heat transfer as pipe length increases. This encompasses the well-studied area of two-phase flow, which is still not completely understood and nonetheless difficult to model. In boiling from discrete surfaces of a size on the order of electronic chips, the volume of vapor leaving the surface is generally small relative to the bulk liquid flow over the surface. Therefore, the effects of net vapor generation are much less important. This is a relatively new area of study however, because the need to cool small surfaces at high heat fluxes has not existed until recently.

Another characteristic of boiling heat transfer is the existence of various boiling regimes. As a fluid is heated, boiling from discrete sites occurs. As the heat transferred

to the fluid increases, the number of sites increases and discrete bubbles emanating from these sites turn into vapor columns. This regime is termed nucleate boiling and is the regime of interest because it is the most effective. As the heat supplied to the surface is increased, a point is reached where the nucleate boiling mechanism breaks down and a transition to a much less effective film boiling mechanism ensues. This transition is also marked by a large and sudden excursion in surface temperature and thus the CHF is also called the burnout heat flux in the literature. As the name implies, film boiling is identified by a thin vapor film that separates the heated surface from the liquid. A much larger temperature difference is required to transport the same amount of heat through this layer and consequently, film boiling is generally not desirable. Obviously it is very important to know the point at which CHF occurs in the application of boiling heat transfer. The variation of the CHF with the geometry and fluid conditions described above was studied in depth.

It must be noted that CHF is usually measured by making small incremental changes of the heat flux until CHF occurs. The last measured steady-state value of the heat flux is then taken as the CHF. Some researchers have studied the CHF occurring under transient conditions created by large step inputs of heat flux. All results discussed in this work, whether obtained experimentally or cited, will have been acquired by the former method.

1.1 Motivation

The initial motivation of this work was to investigate high heat flux cooling methods for electronics cooling applications. Heat fluxes of 100 W/cm^2 and maximum chip operating temperatures of 85°C are often predicted^{1,2} for logic devices to be introduced in the near future. This heat flux is well beyond the capability of conventional single-phase electronics cooling methods. Already Cray Research Inc., has introduced direct immersion two-phase cooling with the Cray-2 supercomputer. Besides the high heat fluxes envisioned for logic devices, the Air Force envisions the development of power electronics, specifically metal oxide semiconductor controlled thyristors (MCT), that will dissipate over 500 W/cm^2 and possibly up to 1 kW/cm^2 . Power electronics by

the nature of their use will dissipate more heat than logic devices. Power electronics devices have important applications in the control of advanced motors and generators for aircraft, electric car, and high speed rail applications. Other devices that will require high heat flux cooling are laser diode arrays (LDA) and microwave power transistors. The effective cooling of tomorrow's high heat flux logic and power electronics devices, and LDAs is essential. To provide a method for cooling these high heat flux electronic devices, flow boiling in a curved channel was studied. Results of a few incomplete studies^{3,4} suggest that very high heat fluxes, ($>17,000 \text{ W/cm}^2$), may be obtained with flow boiling in concave geometries. While this avenue was being pursued, other issues arose and were investigated because they were considered important to the field of electronics cooling.

1.2 Background

A vast amount of experimental work has been performed trying to develop a means of cooling the high-speed, large-scale integrated circuits envisioned to be in service in the future. An excellent review of this work was performed by Incropera¹. Bar-Cohen², Chu⁵ and Nakayama and Bergles⁶ have also given state-of-the-art assessments of electronics cooling technologies. As electronics cooling requirements have become more demanding, complex air cooled designs are slowly yielding to equally complex yet much more effective liquid cooled designs. And of the proposed liquid cooled designs, those designs incorporating boiling are by far the most predominant where very high heat fluxes are envisioned. Boiling, or two-phase heat transfer has two distinct advantages over single-phase heat transfer, 1) higher achievable heat fluxes for a given operating temperature, and 2) a high heat transfer coefficient. The latter means that heat flux can vary substantially with only a small change in temperature. Therefore, the control of electronics temperatures is much easier to implement with boiling heat transfer designs. Temperature control is extremely important because electronics failure rates approximately double for every 10°C rise in the operating temperature⁷. Single-phase methods, such as microchannel cooling, require a much larger temperature difference for

similar change in heat flux and are not as desirable from a thermal stress and reliability point of view.

The idea of direct immersion cooling dates back to an effort to cool airborne electronics at Wright-Patterson AFB in 1948⁸. The devices, (tubes, transformers, relays and capacitors), were mammoth in size compared to today's integrated circuit (IC) chips. These airborne electronic devices were direct immersion cooled mainly for size and weight benefits and because better means did not exist. After the advent of the IC in 1958 and the subsequent development of large scale integrated (LSI) chip technology in 1970, a new interest in direct immersion cooling emerged to satisfy the high heat flux demands, (10 W/cm² then), of these type of electronics. Researchers such as Baker⁹ performed extensive studies of pool boiling from small heat sources using R-113 which has a CHF of 20 W/cm² for zero subcooling.* Cray Research, Inc. and other computer manufacturers have since employed this technique. And, the day when personal computers use direct immersion cooling is near. Pentium processor (Intel Corp.), based notebook computers using indirect liquid cooling will be released in 1994¹⁰. There are also Air Force applications of this method¹¹.

As the number of chip level components and gates increase as result of the development of very large scale integrated (VLSI) and ultra large scale integrated (ULSI) chip technologies, the dissipated heat and consequently the heat flux of ICs have also increased. In parallel, the Air Force is developing high current, high voltage, power electronics devices no bigger than their IC complements. These power electronics devices are envisioned to pass 100s of amperes and dissipate heat at over 500 W/cm²! With no end in sight to the increasing heat flux problem of electronics, an explosion of high heat flux direct immersion cooling began during the 1980s and continues today. While early studies^{12,13} considered FC-75 (3M Industrial Chemical Products Division) and R-113 (a Freon produced by Dupont), current studies have concentrated on boiling heat transfer using an inert fluorocarbon, FC-72. FC-72 is used because of its dielectric

* The term, "subcooling," denotes how far the fluid temperature is below the fluid saturation temperature.

properties and because its boiling characteristics correspond to the generally desired chip operating temperature of 85°C. The heat transport properties of FC-72 are poor however, compared to water and the soon to be banned R-113, a comparable chlorofluorocarbon. Thus, boiling heat flux enhancement schemes such as surface treatment¹⁴⁻¹⁶, plain forced convective boiling¹⁷⁻¹⁹, jet impingement boiling^{20,21} and spray cooling²² are being pursued. The focus of the present work is boiling enhancement by channel curvature.

The high CHF, (17 kW/cm² using water), capabilities of flow boiling over a concave surface have been known since the work of Gambill and Greene³. Gambill and Greene³ attributed the effectiveness of their strategy to the increased inward radial transport of bubbles caused by increased buoyant forces due to the centrifugal acceleration of the fluid. They achieved more than a three-fold increase over a comparable straight geometry for an induced acceleration of 8,390 g. Recently, Leslie et al.⁴ reported heat fluxes of 25 kW/cm² for water in another concave geometry. Miropol'skiy and Pikus²³ obtained CHF data for water flowing in a heated 360° tube coil. They found that with increasing heat input, CHF first occurred on the inner radius and then (at a much higher heat input), on the outer radius of the bend. For subcooled and low quality flow, CHF (averaged over the tube circumference), was less than that for a straight tube of equal diameter. At higher qualities, the reverse was true. Higher heat transfer rates on the outer portion of the tube circumference for high-quality flow was attributed to secondary flows. A significant factor of heat transfer in curved ducts is secondary flow. As a tube flow with a typical laminar or turbulent velocity profile enters a bend, the higher velocity fluid in the core attains a larger radial momentum. The core fluid moves to the radially outward wall and then migrates along the pipe wall to the radially inward area of the wall. Secondary flows are typically less vigorous for turbulent flow because of the flatter velocity profile.

Gu et al.²⁴ were the first to obtain results for a simulated electronic chip in a curved rectangular channel. The simulated chip was placed on the radially outward wall where the largest enhancement would be obtained. CHF was found to increase 8 and 44% over results for a straight channel at velocities of 1 and 4 m/s respectively. This geometry is similar to that of the present study. To ensure that the effects of channel

curvature are not obscured by other influences, the effects of channel height, absorbed air in the fluid, and heated surface finish were also explored.

During their investigation, Gu et al.²⁴ discovered that CHF decreases markedly if the heated surface is not maintained flush with the flow channel wall. This degradation occurred for surface recess and protrusion heights of about 0.1 mm. As mentioned, much work has been done in the area of flow boiling heat transfer using fluorocarbons. Most studies^{9,17,19,25,26} have been concerned with heat transfer from simulated electronic chip heat sources that are flush with the flow channel wall. Mudawar and Maddox²⁷ have studied enhanced surfaces with various fin types that protrude into the flow path, however. During the present investigation, McGillis et al.²⁸ reported on the effect of heated surface protrusion height (0.8 to 2.4 mm), for velocities of 9.6 to 103.9 cm/s and subcoolings of 20 to 40°C. Heated surface refers to the top surface of the protruding block. They found a reduction in CHF for all combinations of velocity, subcooling and surface height.

Because it is difficult to maintain flushness after repeated thermal cycling, even under closely controlled laboratory conditions, it is felt that the same problem will exist under application to electronic chip cooling. Thus, the present effort also strives to quantify and explain the effect of nonflush heated surfaces on heat transfer and CHF.

Chapter 2

EFFECTS OF SURFACE CHARACTERISTICS AND ABSORBED AIR

Preliminary experiments were conducted to determine the impact of secondary effects, such as surface roughness and fluid absorbed air content, on boiling CHF. The effect of surface roughness on nucleate boiling and CHF is not clear by the available literature. Thus it was necessary to determine the sensitivity of the results to surface roughness. During the course of the experiments, it was discovered that microscale contamination also had an effect on nucleate boiling and CHF. This contamination was imperceptible to a scanning electron microscope (SEM), and was estimated to be only few molecular layers deep by use of another method, x-ray photoelectron spectroscopy. Finally, the effect of surface aging is noted. These data were available by virtue of the longevity of this study and were not planned initially. The work described in this chapter was not the main focus of this thesis. Consequently, only sufficient data to determine the existence of an effect were taken and the results are primarily qualitative in form. The data in this chapter provided information which was extremely valuable for developing an experimental procedure which would provide reliable data on the effects which are pertinent to this study.

2.1 Experimental Apparatus

The experimental apparatus has three primary components, the flow loop, flow channel, and heater test section. This is the same basic apparatus used to obtain the results of the following chapters. The flow loop consists of a magnetically coupled centrifugal pump, preheater, flow meters, condenser, and pressure control tank. Figure 2.1 shows the flow loop system. The preheater is an immersion heater within the flow path and is used to obtain the desired test section inlet fluid temperature. Tap water flowing through the condenser/reservoir is used to obtain high liquid subcooling and to avoid exceeding the maximum inlet fluid temperature for the pump. Cavitation in the pump was difficult to control if the fluid entering the pump was not subcooled at least 10°C. Thus, very little data were obtained for a subcooling of less than 10°C.

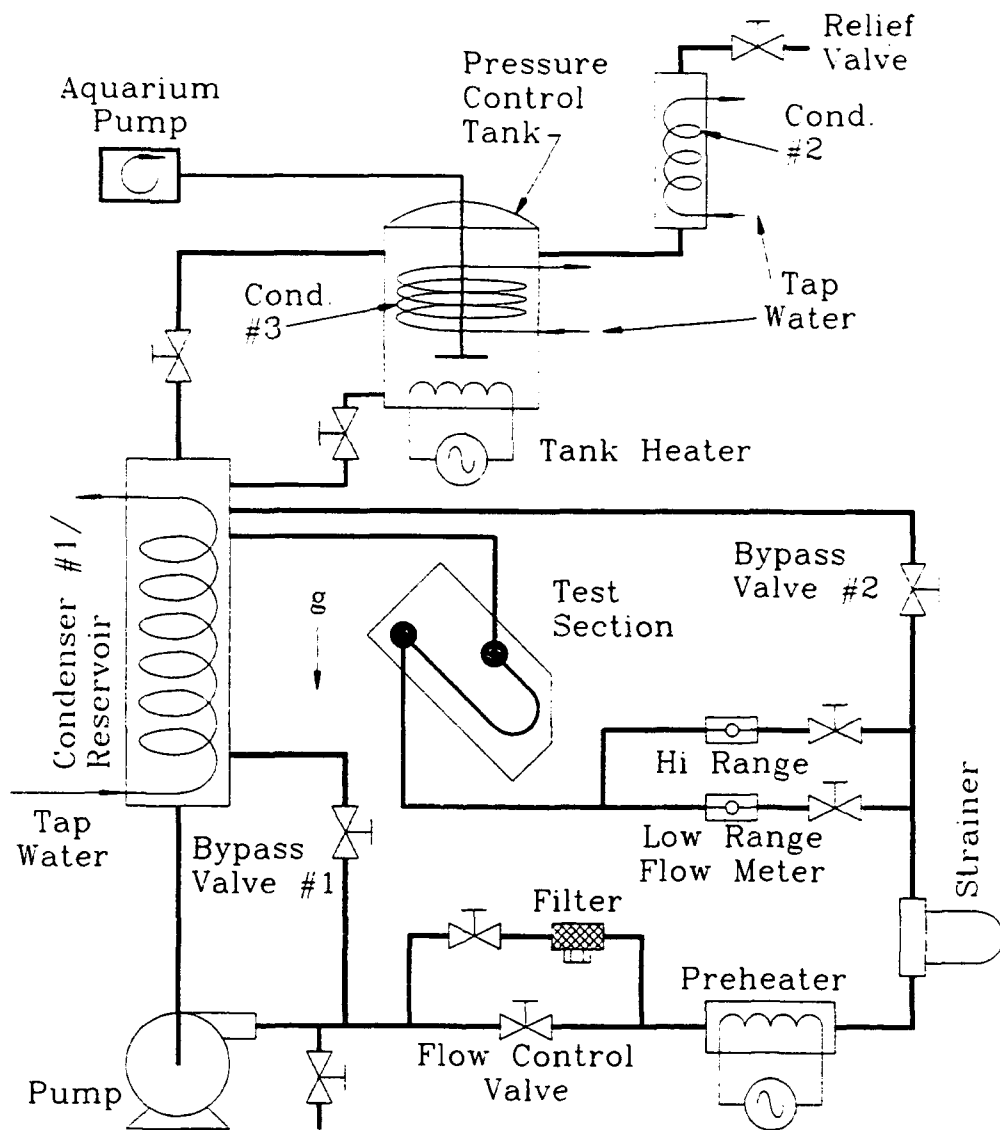


Figure 2.1 Flow loop schematic.

A pressure control tank allowed independent control of system pressure and was also used for aeration or deaeration of the test fluid. The tank was in communication with the flow path through a vapor line. Another line allowed gravity filling of the system after aerating or deaerating the liquid. By regulating the power to a Kapton heater, (Minco Corp.), in the bottom of the tank and the flow rate of condenser #3, the pressure at the test section could be controlled. An aquarium aeration pump was also connected to the pressure control tank. Two diffusers were installed in the bottom of the tank to break up the air stream from the aquarium pump into small bubbles.

Figure 2.2 shows the general design of the three test sections or flow channels. Table 2.1 gives the dimensions associated with these channels. Appendix A also contains detailed design information for channel #3 which is quite similar to channels #1 and #2. The channels were made of Zelux-W optical grade plastic for the purpose of flow visualization. Zelux-W can withstand higher temperatures and is more shatter resistant than plexiglas. The entrance length is greater than 20 hydraulic diameters in all cases to insure fully developed flow at the heater section. The curved section heater was placed 135° from the bend entrance where the secondary flow is believed to be fully developed. A flexible coupling at the intake of the channel allowed the channel to be rotated. This was done so that the heater surfaces could be maintained in a vertical orientation with the flow direction being upward. Orientation to gravity was found to

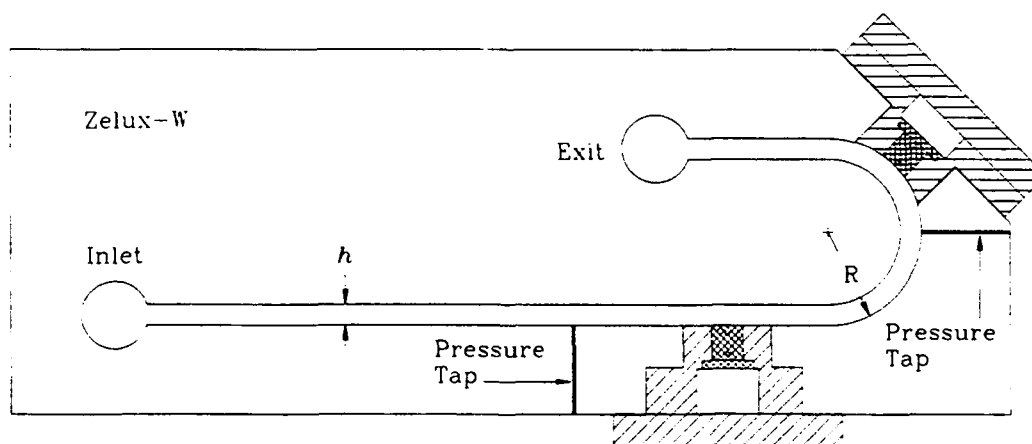


Figure 2.2 Flow channel design.

Table 2.1 Flow channel parameters and geometry factor.

Channel →	#1	#2	#3
R	56.4 mm	28.6 mm	28.6 mm
w	27.0 mm	27.0 mm	27.0 mm
h	5.56 mm	3.18 mm	6.35 mm
L	9.52 mm	9.52 mm	9.52 mm
D_h	8.91 mm	5.68 mm	10.3 mm

have little effect on the results for the straight section heater and velocities greater than 2 m/s, though. This has since been confirmed by Gersey and Mudawar²⁹ who did an exhaustive study on the effects of chip orientation to gravity. They showed that in addition to the above result, orientation has little effect on CHF for large subcooling (36°C). The effect of orientation on the curved section heater results is presumed to be similar.

Static pressure measurements are made at the channel wall at a distance of 35 mm upstream of each straight section heater leading edge. This distance was 33 mm and 23 mm for the 56.4 mm and 28.6 mm radius curved sections, respectively. The saturation temperature at the heater surface is based on the static pressure measurement, thus a small error in saturation temperature is incurred because of the pressure drop from the point of measurement to the heater surface. This error is slightly greater for the curved section due to the developing secondary flow and induced acceleration. The bulk temperature is measured at a point 40 to 50 mm upstream of the straight section heater. Temperature drop from the point of measurement to the test heater is negligible as confirmed by measurements taken at the test section exit with both heaters off. High and low range turbine flow meters were used for the determination of the bulk velocity.

An oxygen free copper block was used to simulate an electronic device and is shown in Fig. 2.3. The copper block was enclosed in low thermal conductivity ($k = 0.3$ W/m-K) Glatherm HT (General Electric Corp.) and heated from the back side. Two actual heater designs were employed. For the straight section and the curved section of

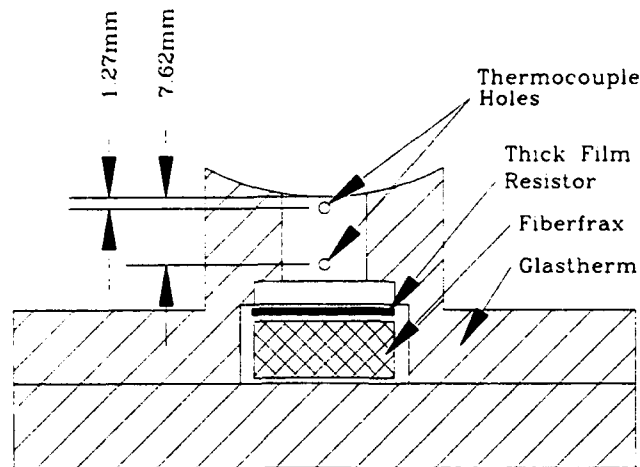


Figure 2.3 Curved section test heater and enclosure.

channel #1, the copper block was heated by a nichrome wire sandwiched between two plates of boron nitrate ($k = 65 \text{ W/m-K}$). For the curved section heater of channels #2 and #3, a thick film resistor (Emtron Corp.) was used to heat the copper block. This modification was made so that higher heat fluxes could be obtained. The thick film resistor could be soldered directly to the copper block, thus reducing the contact resistance and operating temperature of the heater enclosure. Because of the temperature limitations of the Glatherm HT, CHF values could not be obtained with channel #1 for higher velocities. Note that the same heater enclosure was used for the straight segment of all flow channels and the same test heater and enclosure was used for the curved segments of channels #2 and #3. The thermocouple locations for the curved section heaters of channels #2 and #3 are as shown in Fig. 2.3. The straight section heater and the curved section heater of channel #1 had similar thermocouple locations with the addition of one thermocouple at an intermediate location. Because initial tests showed the temperature profile of the three thermocouple versions to be nearly linear, the intermediate thermocouple was not used and consequently omitted in the later designs.

Care was taken to ensure that the sides of the copper block sealed well against the Glatherm enclosure. High temperature silicone sealant, (Ultra Copper, Permatex Corp.), was used for this purpose. Nucleation would initiate prematurely in the crevice at the leading or trailing edge of the heated surface if good sealing was not maintained. Great

care was also taken to ensure that the copper surface was flush with the wall of the flow channel. Gu et al.²⁴ reported a significant reduction of CHF for surfaces that were slightly (≈ 0.1 mm) below or above the flow channel wall. A jig was used to keep the copper block flush with the heater enclosure until the sealant dried. Type K, 0.51-mm-diameter thermocouples were imbedded in the block through 0.57-mm-diameter holes and a one-dimensional approximation of heat conduction was made to calculate heat flux. Heat loss, which occurred predominantly through the back of the enclosure was about 10% near CHF for a flow velocity of 1 m/s and decreased slightly as heat flux increased. The heater enclosure with the thick film resistor showed a loss of about 2% less at the same condition owing to the lower operating temperature.

2.2 Experimental Procedure

Before installation into the enclosure, the exposed face of the copper block was sanded in alternate directions with Wetordry (3M Corp.) wet sanding paper. Grits of 250, 600, and 1000 were used as well as 1500 followed by polishing to obtain various surface roughness qualities. After the roughness measurements were made, the surface was cleaned with potassium hydroxide to remove silicone residue, followed by methanol to remove finger oil and other residue. The copper block and enclosure were installed into the flow channel and the same high temperature sealant was used to ensure a leak proof test section. The heater enclosure retaining screws were tightened against an o-ring seal and the high temperature sealant to varying degrees until the enclosure aligned with the channel wall. The sealant was allowed to dry overnight before the system was filled with FC-72.

Before each day of testing, the fluid was passed through a 0.5-micron filter for at least 30 minutes. The filter was then bypassed and the desired flow rate was attained. The saturation temperature near the test heater was determined from the static pressure measurement. Power to the preheater and coolant flow rate of the condenser were then adjusted to obtain the desired subcooling. Once test conditions were reached, power to the test heater was increased in small increments from single phase convection through the nucleate boiling regime to CHF. Once CHF occurred, the power was quickly shut off

and the surface temperature of the copper block typically did not exceed 140°C.

For experiments where control of absorbed air was desired, the fluid was first loaded into the pressure control reservoir. To reduce the amount of absorbed air, the fluid was boiled. Condenser #2 (Fig. 2.1) was used to keep the FC-72 from escaping while noncondensable gas exited through the relief valve. To increase the amount of absorbed air, air was bubbled through the FC-72 by using the aquarium air pump. Condenser #2 was again used to trap the expensive FC-72 while allowing excess air to escape. Fluid samples were periodically extracted and absorbed air content was measured using a Seaton-Wilson Aereometer which was connected directly to the flow system. Either process was terminated when the desired air content was achieved. The relief valve was then closed and the fluid was passed to the flow system which was placed under a vacuum prior to filling.

After filling the system, the fluid was passed through a 7-micron filter for at least 30 minutes. The filter was then bypassed and the desired flow rate and fluid temperature were obtained as described above. The heater and condenser #1 in the pressure control tank were used to obtain the desired system pressure. Once test conditions were acquired, power to the test heater was increased and the test proceeded as described above. Fluid samples were taken and absorbed air content was measured before, during, and after a test run.

Deaeration is time consuming and subsequently requires control of the system pressure (since the system must remain closed to the atmosphere). For tests where the control absorbed air content was not necessary, aeration or deaeration was foregone and the system was operated with the relief valve open. For this case, the absorbed air content was about 32 and 45% for the 20 and 35°C subcooling cases respectively.

2.3 Uncertainty Analysis

For all tests, CHF was calculated from the one-dimensional heat conduction equation. Because the Seebeck coefficient is nearly constant over the temperature range (20 - 150°C) of the experiments, the temperature difference of two type K thermocouples was measured directly, to obtain a higher accuracy. Furthermore, the measured gradient

was always less than 20°C, making the constant Seebeck coefficient assumption a good one. For all test heaters, the thermocouple pairs were compared to a precision thermistor (0.1°C accuracy) over the temperature range of the experiments. The thermocouples of each pair agreed to within 0.3°C over the entire temperature range. All the thermocouples agreed with the precision thermistor to within 0.5°C. Thus, the thermocouple accuracies are considered to be well within 1°C for these experiments. A Helios I (John Fluke Mfg.) data acquisition system was used for these measurements. This device has a resolution of 0.02°C and a rated accuracy of 0.45°C for K type thermocouples.

The uncertainty of the pressure measurement was 5 Pa. The error induced by the pressure taps being upstream of the heater was estimated using the Blasius relationship,

$$f_{str} = 0.316 Re^{-1/4} \quad (2.1)$$

and that of Ito³⁰,

$$\frac{f_{cur}}{f_{str}} = \left[Re \left(\frac{D_h}{2R} \right)^2 \right]^{1/20} \quad (2.2)$$

for the friction factors of the straight and curved sections, respectively. The calculated pressure drop error ranges from 70 Pa at $U = 1$ m/s to 2.36 kPa at $U = 5$ m/s. This range was nearly the same for both the straight and curved sections of each channels because the pressure drop distance in the curved sections was shorter to compensate for the larger friction factor. For the channels where $h \geq 5.56$ mm, the error at $U = 5$ m/s was 1.21 kPa. Using the Clausius-Clapeyron equation,

$$\left(\frac{\partial P}{\partial T} \right)_{sat} = \frac{h_{fg}}{(v_g - v_f)T} \quad (2.3)$$

the resulting error in saturation temperature reaches an average maximum of less than 0.5°C for both the straight and curved sections. Because the error is small and the

correction factor would vary for each geometry, flow rate, and subcooling, and considering the uncertainty of applying Ito's³⁰ equation, no correction of T_{sat} for pressure drop was made.

The standard Kline and McClintock³¹ approach to the calculation of random uncertainty was taken, as is shown in detail in Appendix C. The uncertainty of the bulk mean velocity calculation was dominated by the uncertainty of the turbine flow meter which was 0.5% of the reading. Although the flow meters were calibrated for water, the manufacturer (EG&G Flow Technology) and two other manufacturers of turbine flow meters indicated that the error induced by lower viscosity fluids, such as FC-72, is negligible.

The uncertainty equation for heat flux contains many variables which remain constant during experimentation and one that varies, the temperature difference. Because temperature difference is the only true variable during testing, the uncertainty in CHF decreases monotonically with temperature difference or heat flux. The uncertainty in CHF was calculated for best and worst case temperature difference uncertainties of 0.5 and 1°C. For a temperature difference uncertainty of 0.5°C, the uncertainties in CHF are 13.4, 7.8 and 6.9% for heat fluxes of 34, 85 and 132 W/cm² respectively. For a 1°C uncertainty, the uncertainties in CHF are 24.5, 11.3 and 8.7% for the same heat fluxes.

Previous results¹⁹ give a maximum upstream to downstream temperature difference of only 2.2°C for a flush mounted copper heater under similar heat flux, subcooling and flow conditions. Because of this, additional thermocouples to obtain the surface temperature distribution were considered an unnecessary complexity, and were not used. Because of the high thermal diffusivity of copper and the distances of the thermocouples from the boiling surface, the measured temperatures, and thus the calculated heat flux and wall temperature, fluctuated very little under all conditions. The maximum unsteadiness (less than 0.1°C) occurred near CHF and translates into a heat flux variance of less than 1 W/cm².

Nevertheless, Kenning³² has shown that large errors may occur in the surface temperature measurement of boiling surfaces. These errors are caused by the large variation in heat flux below a single bubble at a nucleation site. The average heat flux at

a given nucleation site also varies greatly from that between nucleation sites. Kenning⁹ measured a spatial temperature variation of 26°C for water boiling at 10 W/cm² on a stainless steel foil 0.13 mm thick. He developed a conduction model, (see Appendix D), of the spatial temperature variation which required the fitting of two constants, a and b , to his data. Characteristic values of $b^2 = 0.66$, $a^2 = 0$ and $b^2 = 0.36$, $a^2 = 0.30$ were given for the aforementioned water/stainless steel heater combination. Results obtained by applying Kenning's⁹ model to the present experiment show that at a depth equal to that of the thermocouple closest to the surface (0.127 mm), site-to-site thermal gradients are completely damped. This was true for worst case conditions and all practical values of a and b . High bubble density, small maximum bubble diameters and the high thermal conductivity of copper are the reasons for a negligible temperature variation. Under the conditions of the present experiments, it was found that thermal gradients disappeared at a distance of about one bubble diameter (i.e., < 0.1 mm), below the surface. Thus, the small unsteadiness of the thermocouple closest to the boiling surface is expected.

A precision shunt with a resistance uncertainty of 0.05% was used to calculate heat flux based on electrical power input. For the worst case, the random uncertainty of this value was less than 0.3%. The heat loss from the heater test section was estimated by the solution of a numerical model of an axisymmetric approximation of the test section. This model was constructed and solved using a commercial finite element based solver, ANSYS, (Swanson Analysis Systems, Inc.). This model predicted that heat loss would be less than 10% for a range of cases. Because the heat flux based on thermocouple measurement was always 7 to 10% less than that based on electrical input, it is believed that the actual uncertainty of the thermocouple measurements is less than calculated. The use of the same heater and enclosure for all straight sections and two of the three curved sections also increases the accuracy of the comparative results.

The repeatability of CHF values was generally within 5% for heat fluxes greater than 50 W/cm². Finally, the bias error was not estimated; however, the percentage of heat loss measured compares with that previously reported by Mudawar and Maddox¹⁹ for a similar design.

2.4 Effects of Surface Roughness*

The effect of surface roughness has been studied to determine the sensitivity of the data on this parameter. The effect of surface roughness on CHF was the primary concern although qualitative results are also given for its effect on nucleate boiling heat transfer. Data were taken for surfaces prepared with various grits of wet-sanding paper including, 250, 600, and 1000 grit. One polished surface was also tested.

2.4.1 Effect of Surface Roughness on Nucleate Boiling

The effect of surface roughness on nucleate boiling and CHF has been studied by many investigators for all imaginable geometries, surface and fluid combinations, and boiling configurations. Unfortunately, a generally applicable correlation of nucleate boiling to roughness is still lacking. Jakob and Fritz³³ are commonly credited with being the first to ascertain the effect of surface roughness on nucleate boiling heat transfer. Corty and Faust³⁴ provided the first attempt to quantify the effect of surface roughness on nucleate boiling. They showed that for a surface prepared with different grits of emery paper, that the wall superheat, ΔT_w , for a given heat flux decreased as roughness increased. This common phenomenon is shown in Fig. 2.4 for the present data. More recently, Nishikawa et al.³⁵ performed a similar investigation using R-21, R-113, and R-114 pool boiling on copper. They found that the effect of roughness vanishes as the fluid pressure approaches the critical pressure. They also propose a general equation for the nucleate boiling heat transfer coefficient which includes pressure and roughness as variables. Nishikawa et al.³⁵ characterized roughness by the measured value of R_p , (see Appendix B for definition of R_p). In the boiling literature, R_a , (also see Appendix B), is most commonly used to characterize surface roughness. In either case, these parameters were developed to gauge the finish of machined parts for bearings, and other running part

* In this study roughness refers to micro-roughness with physical characteristics less than $10 \mu\text{m}$. Micro-roughness is typically the result of sanding, sandblasting, or polishing. Others may refer to macro-roughness which is the result of deliberate machining of fins or studs, or the scoring, knurling or drilling of the surface.

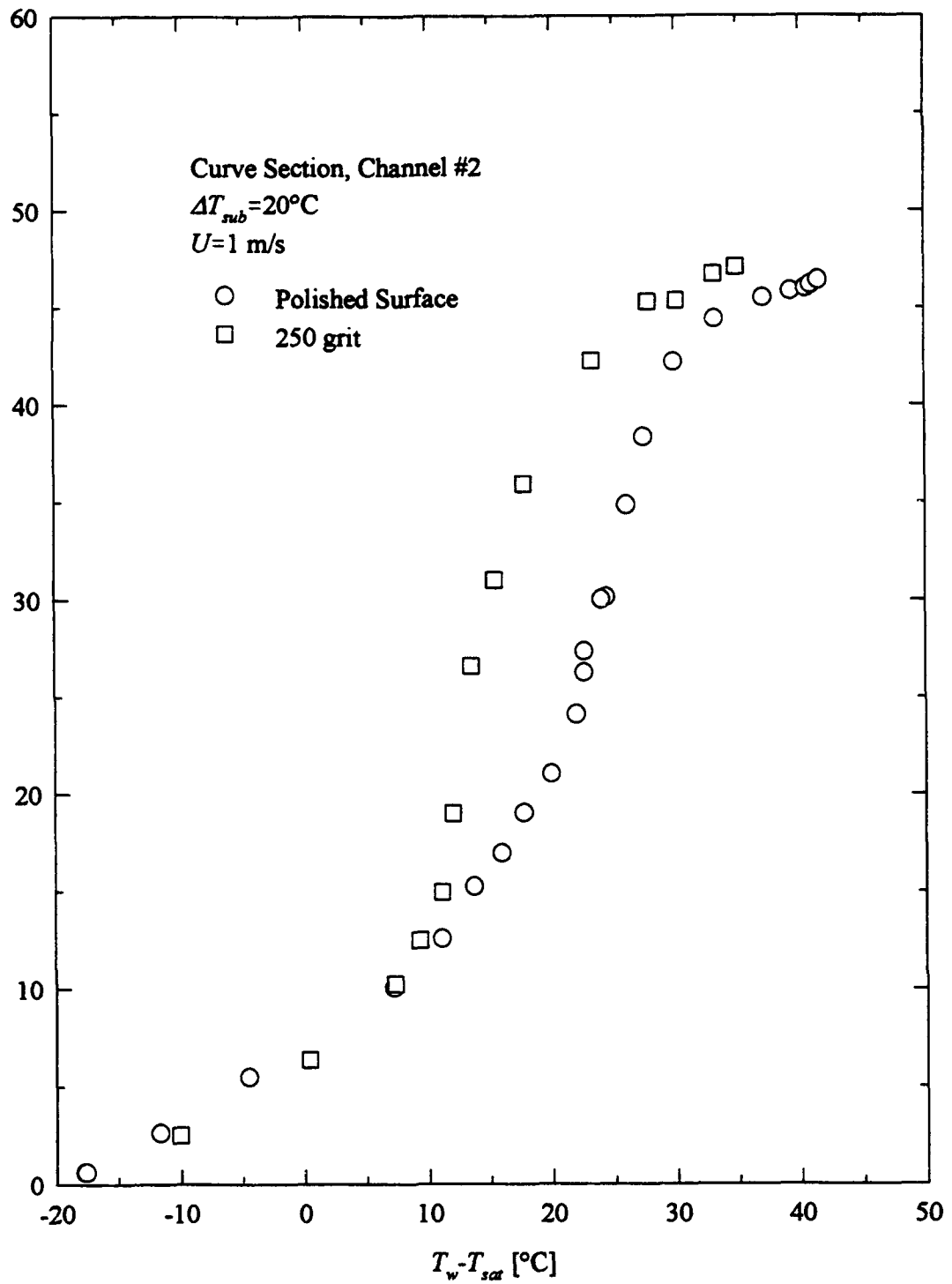


Figure 2.4 Effect of surface roughness on nucleate boiling.

applications and are not directly applicable to estimating boiling heat transfer coefficients. The reason that these parameters show any success at all is that rough surfaces usually have a larger number of nucleation sites and a much broader size distribution of nucleation sites. Nucleation theory^{36,37} predicts the existence of a critical cavity or nucleation site radius, r_c . The critical cavity radius is the size of cavity that will nucleate first when a minimum ΔT_w is attained. As ΔT_w is increased, the range of cavity sizes about r_c increases. If a surface does not have cavities of radius r_c , (i.e., a smooth surface), then a larger wall superheat is required for nucleation to occur. Thus, the heat transfer coefficient is generally smaller for smooth surfaces.

Unfortunately, there is no way to directly measure the size and distribution of cavities on a surface. Since roughness implies size distribution, various ways of measuring surface roughness are employed. The flaw in this method is well illustrated by the analogy of Hsu and Graham³⁸; "if one knows the mean height and distribution of hills in a certain region (equals surface finish, or rms roughness) it does not mean one knows the population distribution of lakes and ponds (equals cavity distribution)." Nonetheless, roughness measurements are the best tool that researchers have at this time.

For some later tests with the surface prepared with 1000 grit paper, measurements with a surface profilometer confirmed that surface roughness was uniform over the entire face. A Surtronic P3 profilometer, (Rank-Taylor-Hobson), was used to measure the surface roughness of the various test heaters. Eight measurements at various surface locations were taken to obtain an average roughness for each heater surface. R_a , an ISO standard parameter for surface roughness, was obtained as the average of five 50 μm sampling lengths. Although larger sampling lengths had no discernable effect on R_a , this small sampling length was used because the expected nucleation cavity size was expected to be much smaller than 50 μm . The previously described sanding technique provided very uniform surfaces because R_a was found to range from only 3 to 6 nm for all the surfaces with a single surface R_a variance of ± 1 nm.

As alluded to above, the same R_a can be produced by drastically different machining processes which would yield different cavity size distributions. Thus, a more appropriate roughness parameter, obtainable by profilometry, might be the range of peak-

to-peak distances of the roughness elements, S_n . Although not perfectly applicable, S_n does give an indication of physical characteristics that are more indicative of cavity size. To borrow from Hsu and Graham's³⁸ analogy; If one knows the width distribution of valleys (equals the distribution of S_n), one has some indication of the possible size distribution of lakes (equals size distribution of cavities). After all, a lake cannot be bigger than the valley that contains it. Unfortunately, only the mean spacing, S (see Appendix B for definition), was obtainable using the aforementioned profilometer. S was found to range from 8 to 21 nm for the same set of heater surfaces.

Further confusing the matter is the fact that highly wetting fluids such as FC-72 have the ability to flood larger cavities, thus making them inactive and requiring larger superheats for nucleation of the remaining smaller cavities. Therefore, correlations for lesser wetting fluids such as R-113, R-11, and water underpredict the incipient superheat. Hahne et al.³⁹ modified the flow boiling incipient superheat equation for flow boiling originally proposed by Davis and Anderson⁴⁰ to predict the superheat of highly wetting fluids such as FC-72, to obtain,

$$T_w - T_{sat} = \frac{2 \sigma T_{sat} (v_g - v_f)}{r^* h_{fg}} \quad (2.4)$$

This equation is similar to the well known bubble superheat equation for pool boiling where T_b and r_b have been replaced by T_w and r^* , respectively. Using Eq. (2.4), r^* was estimated to be about 60 nm, thus satisfying the conditions for Eq. 2.4, (i.e., $r^* < 400$ nm). It can be seen that S and r^* are of the same order. Thus, it is possible that S may be more appropriate than the widely used R_n as a roughness parameter for boiling surfaces. A much more thorough study must be performed to verify this assumption.

2.4.2 Effect of Surface Roughness on CHF

There is some controversy in the literature over whether or not roughness has an effect on CHF. Aladyev, et al.⁴¹, Bernath⁴², Bier, et al.⁴³, and Leung, et al.⁴⁴, report that

there is no effect of surface roughness on CHF. Their data were acquired under various conditions, geometries, fluids and wall materials, not to mention both pool and forced flow boiling. On the other hand, Berenson⁴⁵, Roy Chowdhury and Winterton⁴⁷, Ramilison and Lienhard⁴⁶, and Weatherhead⁴⁸, reported that as a surface becomes smooth, CHF decreases. The reduction of CHF occurred for highly polished surfaces and was typically 10-20%. Weatherhead⁴⁸ was the only one to give data on forced flow boiling. The data of this study tend to support the latter opinion that CHF is decreased for highly polished surfaces. For the surface highly polished with Buehler 0.5 μm paste, a reduction of 11% occurred for a flow velocity of 2 m/s and subcooling of 20°C. Data at 1 m/s and the same subcooling show no reduction in CHF, however. Insufficient data were taken to make this a conclusive study. To avoid problems associated with surface roughness, all surfaces were prepared with 1000 grit wet-sanding paper for the remainder of this study. This grit paper appeared to give the most uniform surface as was evidenced by later profilometer measurements.

2.5 Effect of Surface Contamination **

During the course of experimentation, it was noted that nucleation became more difficult, thus causing a reduction of the heat transfer coefficient. Although the surface appeared clean, a recleaning returned the nucleation pattern to its original state. The cleaning procedure consisted of scrubbing the surface with methanol and cotton swabs. Cleaning of the surface was only marginally effective because the inhibited nucleation condition quickly reappeared. Cleaning, followed by sanding and recleaning was much more effective and prevented the reoccurrence of the above phenomenon for a longer period of time. The period of time that elapsed during the change in nucleation pattern was too short to be attributed to oxidation. Thus, it was concluded that some type of contamination of the surface occurred. Visual inspection of the surface indicated that

** Contamination refers to micro-contamination which is imperceptible to visual methods, including scanning electron microscopy. Some boiling literature refers to macro-contamination, typically scale or mineral deposits, which is clearly visible to the naked eye.

while the color of the copper had changed slightly, no other indication of contamination existed. In fact, scanning electron microscope (SEM) photos at 1000X did not show any particulate or other type of contamination.

X-Ray photoelectron spectroscopy (XPS) measurements on the surface were subsequently made. This instrument measures the energy of electrons rebounding off the surface much in the same way that a mass spectrometer works. The first three molecular layers of the surface give rise to the results. Thus, the XPS truly analyzes the surface as opposed to other methods such as Auger spectroscopy which penetrate relatively far below the surface. Large numbers of electrons rebounding with a certain characteristic energy indicate the existence of a particular element. This test was performed on the heater surface after it was cleaned and the nonnucleating condition reoccurred. The same surface could not be used since contamination by vacuum oil vapors from the SEM would compromise the results. Figure 2.5 shows the results of this test. The first of the four large peaks corresponds to oxygen, the second to carbon, and the last two to silicone. Remarkably, the copper was completely obscured by these elements. The XPS has analyzation capabilities that provide the relative quantities of the detected elements. Carbon composed about 50% of the surface material while oxygen and silicone composed 24% and 26%, respectively.

The surface energy of clean metal is very high and it is nearly impossible to keep such a surface clean. The presence of oxygen is obviously expected and it was learned that carbon is also commonly present in our atmosphere and is also to be expected. Silicone is unexpected however in most clean environments. Through subsequent XPS tests, it was found that the source of the silicone contamination was the silicone sealant around the sides of the copper block heater leaching out during the experiments. Some contamination occurred upon assembly also. It was also found that cleaning with methanol had no effect on removing the silicone. Even cleaning with methanol followed by sanding and recleaning with methanol did not completely remove the silicone. A new cleaning procedure was adopted, the methanol, potassium hydroxide, methanol procedure described in section 2.2. Figure 2.6 shows the XPS results for the surface cleaned under this procedure. Silicone was completely absent and the composition was 12% copper,

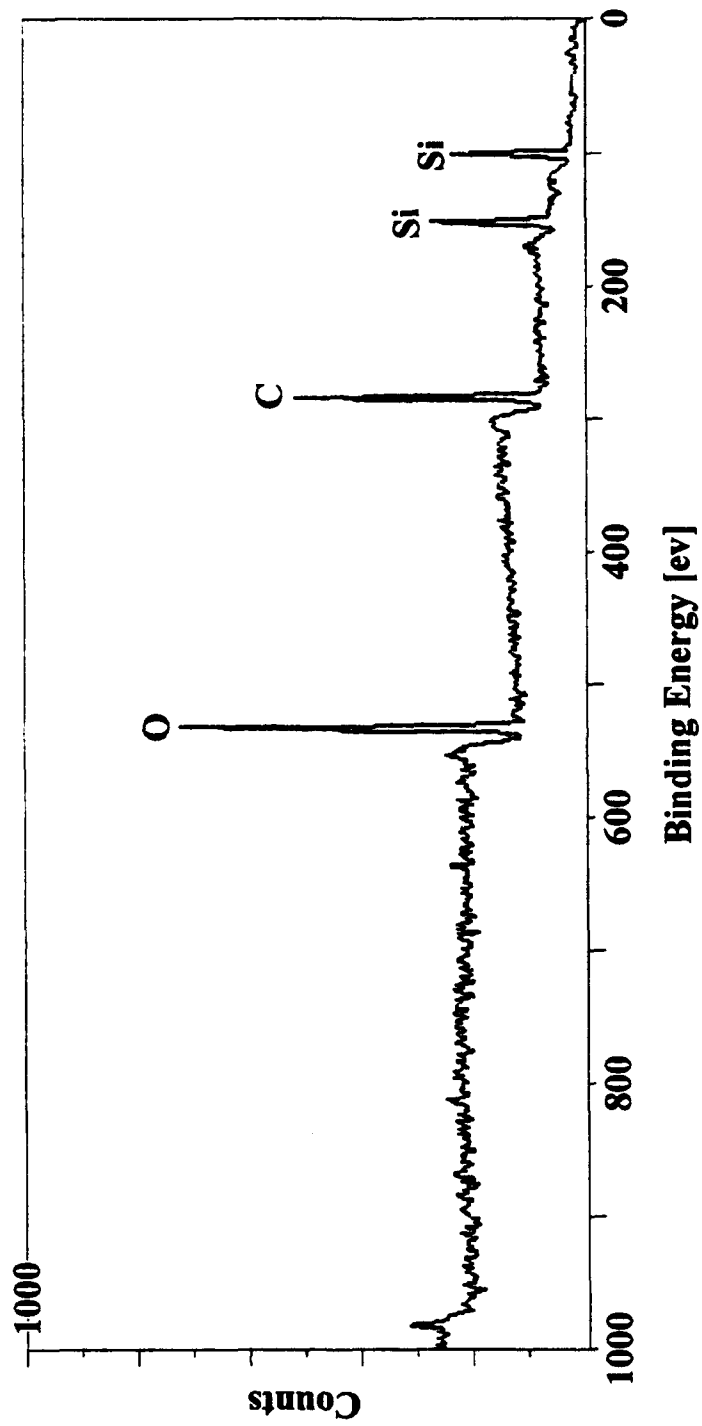


Figure 2.5 Composition of silicone contaminated surface.

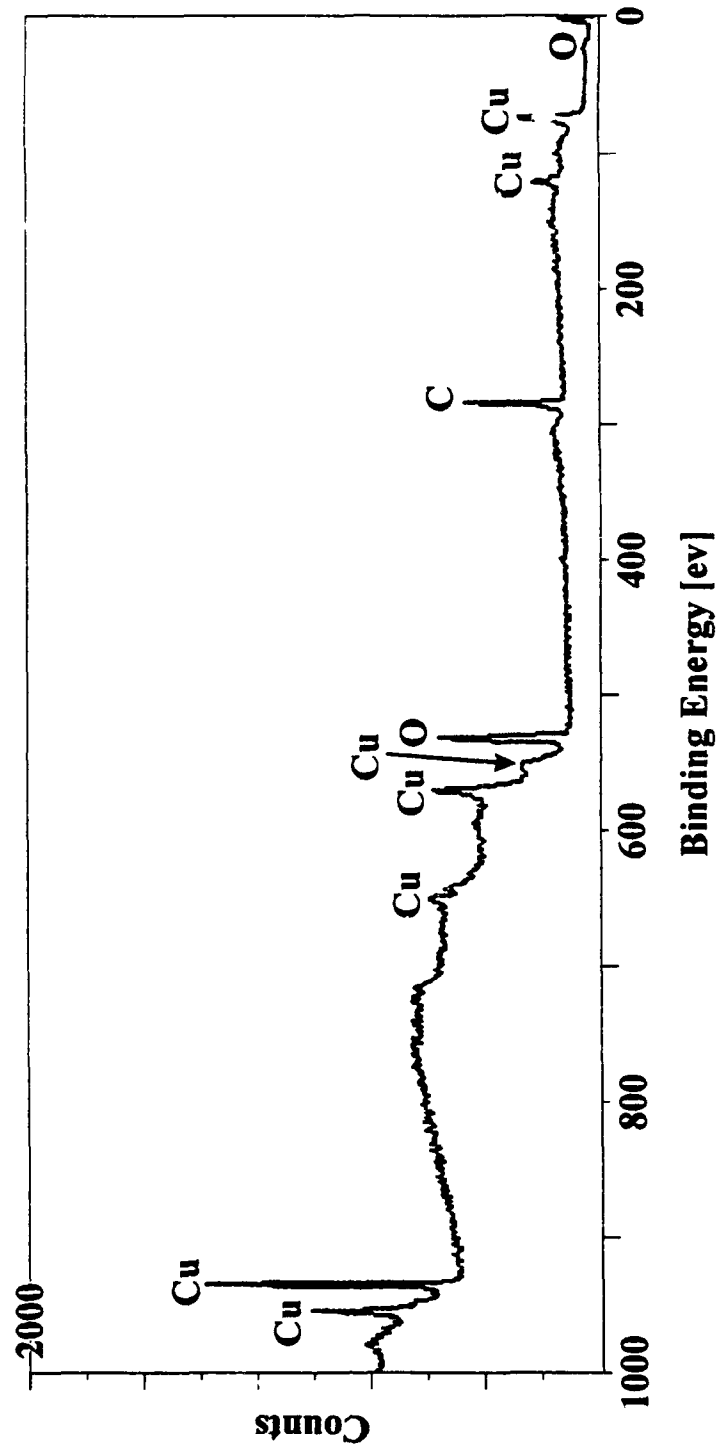


Figure 2.6 Composition of *clean* surface.

34% oxygen and 54% carbon. As noted above, cleaning the surface with methanol alone did not remove the silicone, although nucleation did improve. The XPS averages the surface characteristics over a 0.4 mm by 1 mm patch. This is many orders of magnitude greater than the typical nucleation site diameter, (60 nm as estimated above). Therefore, it is possible that upon vigorous cleaning with methanol, changes to the cavities were made that were not revealed by the XPS. Regardless, the effect of contamination by silicone was controlled by improved assembly procedures and the above cleaning procedure. The term *clean surface* is certainly a misnomer, though. The problem of surface contamination must be common for this type of heater design because the necessity for frequent cleaning is often noted in the current literature. This study is the first to determine the source of contamination, however.

Only one mention of the effect of silicone contamination on nucleate boiling was found in the literature. Gaertner⁴⁹ found that for pool boiling of water on a surface with a thin coating of silicone, nucleation was inhibited to such a degree that film boiling occurred at the incipient heat flux. In general surface contamination causes a reduction in CHF^{45,50,51}. For silicone contaminated surfaces, wetting of the surface by the liquid is dramatically reduced because the cohesive forces of the liquid out weight the adhesive forces of the liquid to the surface. Gaertner⁴⁹ notes that upon nucleation, bubbles grew on the surface to the point that they coalesced with neighboring bubbles, thus creating a vapor film over the surface. Costello and Heath⁵⁰, showed that the reason for this was that the bubble buoyancy forces are greatly reduced when the liquid contact angle is large, (i.e., nonwetting surface). It is generally noted that nonwetting surfaces require a much larger superheat to initiate boiling and cannot sustain as high a superheat at CHF. One can see that in the extreme, the transition to film boiling will occur immediately after incipience. Figures 2.7 and 2.8 show the effect of silicone contamination on the boiling curve. Note the increased superheat for a given heat flux and the reduced CHF as compared to a *clean* surface, (Fig. 2.7). Figure 2.8 shows another interesting manifestation of contamination, the existence of an apparent second boiling incipience. The sudden nucleation of a large number of additional sites was witnessed during testing. Both of these figures show that contamination impedes nucleation.

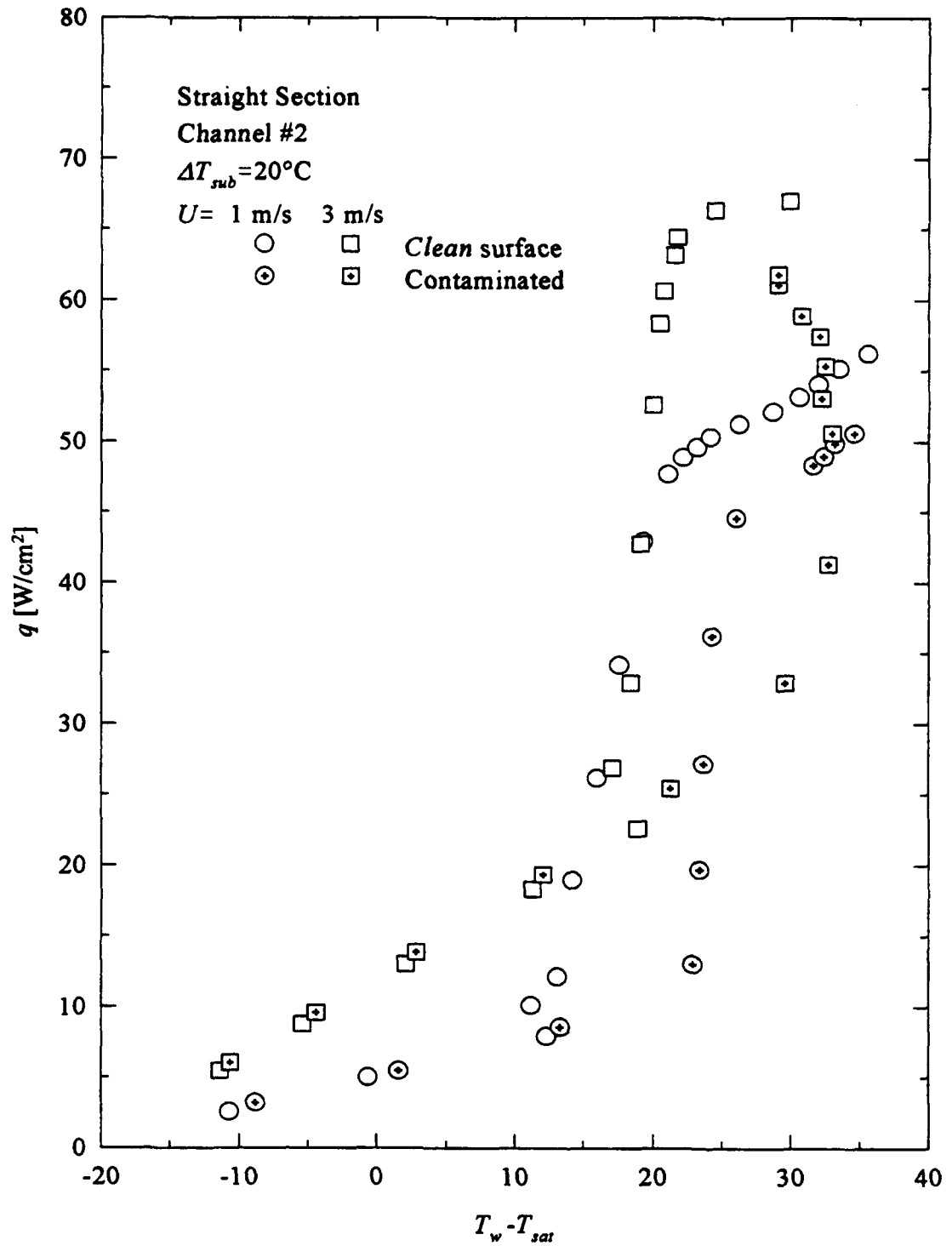


Figure 2.7 Effect of contamination on nucleate boiling and CHF.

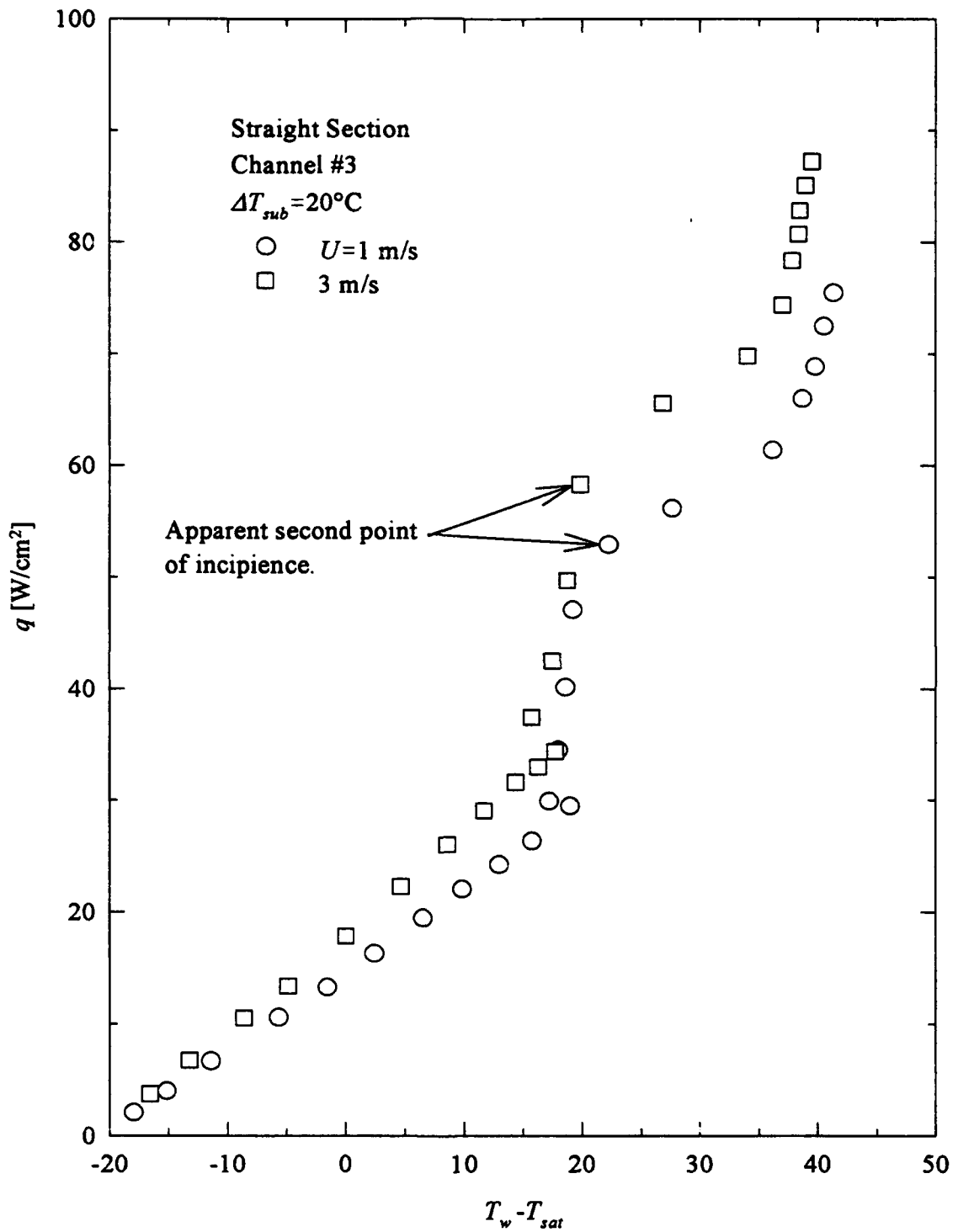


Figure 2.8 Effect of contamination on nucleate boiling curve.

2.6 Effect of Surface Aging

Figures 2.9 and 2.10 illustrate an interesting phenomenon discovered during the course of this study. Notice that the aged surface curves in Figs. 2.9 and 2.10 exhibit a protracted region near the normal point of CHF. CHF for the aged surfaces is marked by an increase of q_M and a very high wall superheat. The increase of q_M is about 20% for the above cases. Because the occurrence of this phenomenon was eliminated for both surfaces by sanding and cleaning the surfaces, it is presumed to be surface related. The large rise in wall superheat and a $q/(T_w - T_{sat})$ comparable to the single phase region suggests that as heat flux increases beyond the normal point of CHF, few additional sites are activated. Therefore, the additional heat transfer may be single-phase convection. In fact, for some cases the slope of the protracted region of the curve was nearly identical to that of the single-phase regime. This is conjecture, however, and there are probably other phenomena occurring.

There are many possible changes that may occur to a surface; as noted above, roughness, wettability, oxidation, and contamination are the most common. The effects of surface roughness and contamination as described above are manifested differently from the phenomenon shown in Figs. 2.9 and 2.10. Note that the wall superheat is effected little for the nucleate boiling regime. The only conceivable change, and therefore the most likely cause of the increased and protracted CHF phenomenon is oxidation. Both surfaces were exposed to air for a period of 6 to 14 months while not in use, and each attained a tarnished appearance. Each surface was then vigorously cleaned with potassium hydroxide and methanol before testing, thus eliminating the aforementioned possibility of contamination. Oxidation generally effects surface wettability and the distribution of cavity sizes. Oxidation generally has an effect on the surface which is opposite to that of contamination; it improves wetting. Thus, liquid attraction to the surface is more tenacious and higher superheats are sustained near CHF.

2.7 Effect of Absorbed Air

FC-72 is capable of absorbing large amounts of air relative to other common fluids. A typical value at room temperature is 40% by volume. Behar, et al.⁵², McAdams

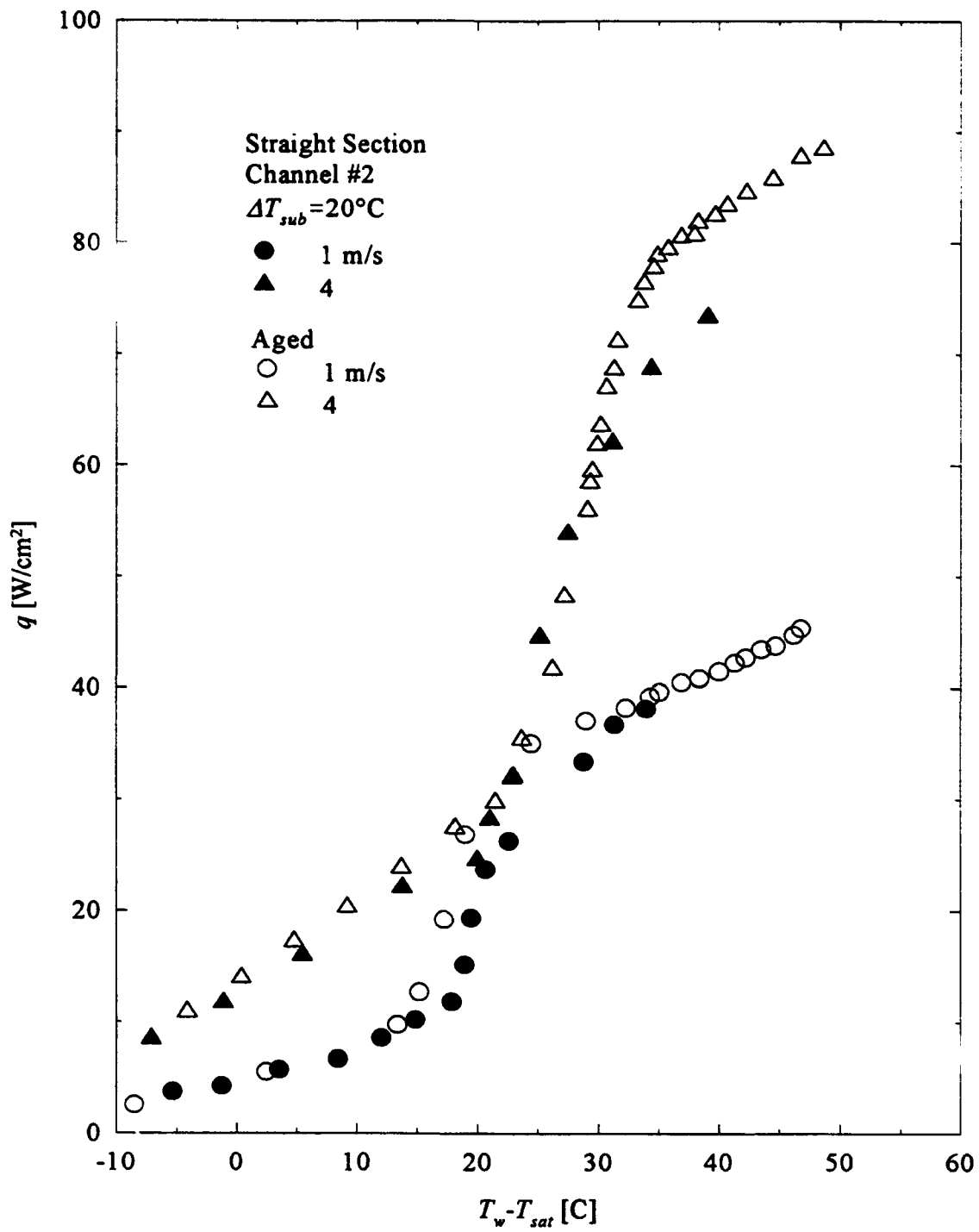


Figure 2.9 Effect of surface aging on straight section heater.

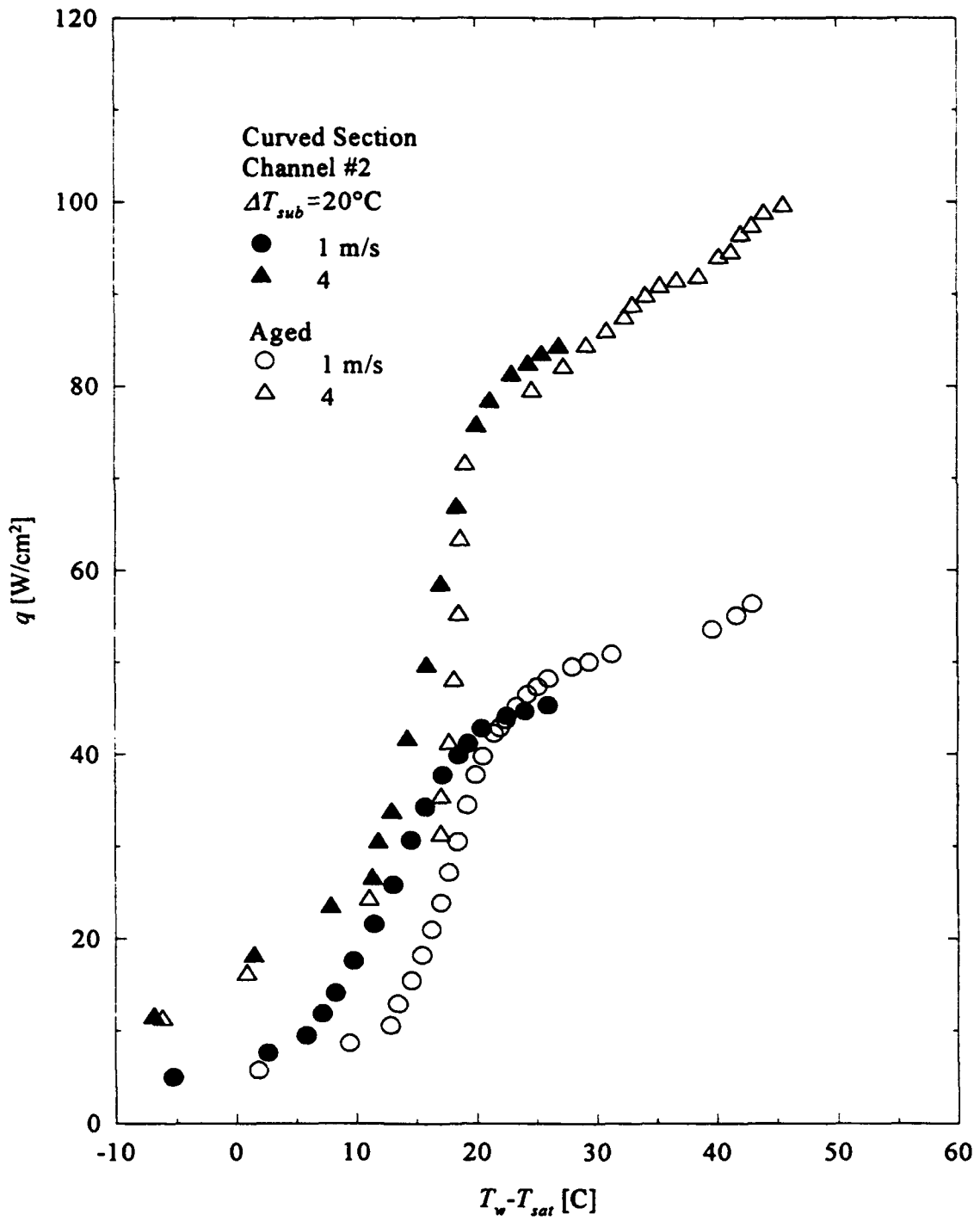


Figure 2.10 Effect of surface aging on curved section heater.

et al.⁵³, Murphy and Bergles⁵⁴, and Pike et al.⁵⁵ indicate that absorbed air has no discernable effect on boiling at high heat fluxes and CHF. Behar, et al.⁵², studied the effect of absorbed air in various fluids and pool boiling. They identified an onset of degassing region which preceded the actual onset of boiling. They also identified an onset of vaporization region which was defined as degassed boiling and covered the remainder of the NBR up to CHF. This region occurred at higher heat fluxes where all the gas was driven out of the thin layer of liquid near the surface where nucleation occurs. The results of McAdams et al.⁵³ were for absorbed air on flow boiling of water in a stainless steel annulus. They found that absorbed air tended to reduce wall superheat at low heat fluxes, but had no effect at high heat fluxes. Murphy and Bergles⁵⁴ obtained results for the flow boiling of R-113 in tubes and Pike et al.⁵⁵ studied the same problem but for pool boiling. All the above studies obtained the same qualitative features of absorbed air at low heat fluxes and a diminished effect of absorbed air at high heat flux. You et al.⁵⁶ have shown that increased air content reduces wall superheat by up to 10 °C for pool boiling of FC-72 under decreasing heat flux conditions. As with the other investigations,⁵²⁻⁵⁵ You et al.⁵⁶ attribute this reduction in wall superheat to decreased subcooling caused by a reduction of the partial pressure and increased convection caused by gas bubbles leaving the wall.

Another mechanism used to explain this phenomenon is thermocapillarity⁵². A gas bubble on the heated surface will reside in a temperature gradient. Evaporation at the heated surface and condensation at the top of the bubble may also occur. The resulting difference in surface tension will cause the interface to move toward the top of the bubble. The flow of this interface induces flow of the surrounding liquid and thus lowers the wall superheat for a given heat flux. This effect is probably negligible under most circumstances.

Once the nucleation sites were stabilized by repeated boiling, the results for a given day indicate that absorbed gas has little or no effect on forced flow boiling. Figure 2.11 shows the effect of absorbed air for the straight section heater. Similar results were obtained for the curved surface. Although Fig. 2.11 implies that absorbed air does have an effect on the CHF, it must be remembered that this small variance is well within the

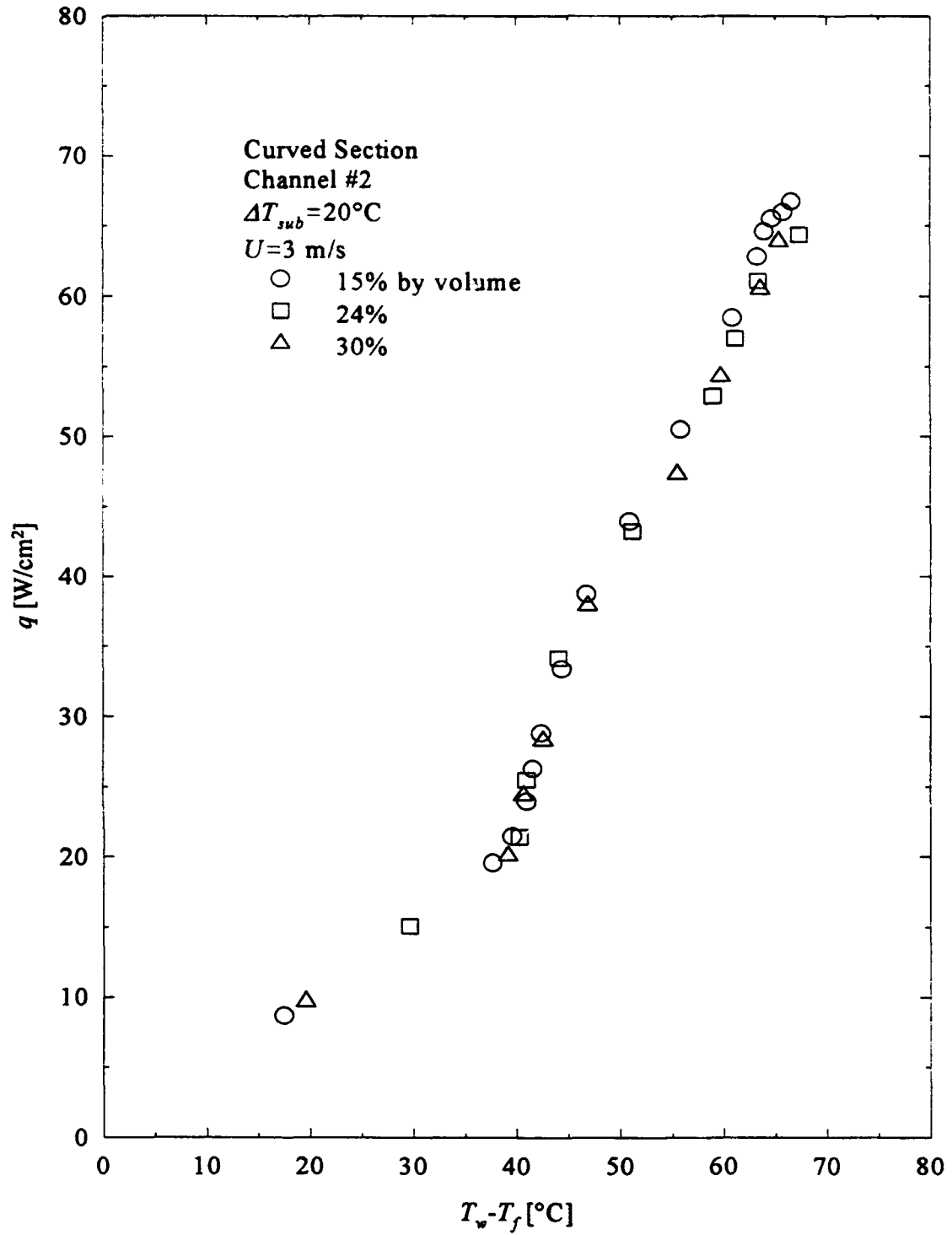


Figure 2.11 Effect of absorbed air on nucleate boiling curve.

limits of error. The combined results of other tests show that absorbed air has no discernable effect on CHF.

The flow boiling results of McAdams et al.⁵³ and Murphy and Bergles⁵⁴ were obtained for flow velocities of 0.3 and 1.3 m/s, respectively. Although a direct comparison to water and R-113 data and different geometries cannot be made, the lack of any effect on the present data may be attributed to the relatively high fluid velocity. The large convective contribution of the fluid certainly overshadows that of released gas bubbles and thermocapillary pumping. Furthermore, under the forced flow and moderate subcooling conditions of the current experiments, the fluid near the wall is sufficiently heated at the most downstream portion of the heater, (the point at which nucleation first occurs), that much of the gas has already been driven out before nucleation occurs. Thus, the reduced pressure effect, (i.e., increased subcooling effect), of the gas is eliminated.

2.8 Conclusions

1. It must be noted that the above results have been obtained for a copper surface and are only generally applicable to the silicon surfaces of electronics. On the other hand, power electronics typically have a nickel plated copper base for the purpose of heat transfer. The above results show that heat transfer from these devices may be improved by judicious preparation of the base material.
2. The effect of surface roughness on the nucleate boiling regime for the current configuration follows that of well established theory. As surface roughness increases, (i.e., size distribution of cavities increases), the superheat required for a given heat flux decreases.
3. The use of the width distribution of roughness (S_n) is possibly a better indicator of nucleation site or cavity size distribution than is the use of RMS roughness (R_a). Conclusive results must be obtained through more thorough testing, however.
4. Extremely smooth surfaces may cause a reduction of CHF. Smaller size of nucleation sites requires higher superheat for nucleation which leads to premature CHF.
5. Contamination by silicone is detrimental to nucleate boiling and CHF, but may be avoided through proper experimental procedures. The use of silicone sealants in an

electronic cooling application should be avoided because they gradually leach out silicone.

6. Oxidation caused by aging of the copper surface caused the CHF to increase. Part of this increase is at the expense of increased wall superheat. Wall superheat of the NBR does not appear to be appreciably changed by oxidation.

7. The effect of absorbed air is found to be negligible for boiling incipience, nucleate boiling and CHF. It is reasoned that the higher single-phase superheats required for nucleation cause much of the air to be driven out of the fluid prior to nucleation.

Chapter 3

EFFECT OF CHANNEL HEIGHT ON CHF

Before discussing the effects of channel height on CHF, it is necessary to discuss the various models of CHF and the theories upon which they are based. Critical heat flux models for pool and forced flow boiling CHF are still incomplete after over 40 years of development. Because current models for CHF rely heavily on information garnered from numerous pool boiling studies, it is necessary to first discuss the evolution of pool boiling CHF models. A chronological presentation is felt to best elucidate the underlying theories and assumptions that make up the foundation of the current forced flow CHF model.

3.1 An Introduction to the Mechanisms and Modeling of Pool Boiling CHF

During the period 1948 to 1951, Kutateladze⁵⁷⁻⁵⁹ analyzed the equations of motion and energy for two-phase flow and derived by dimensional analysis what has become the most well known equation in boiling heat transfer

$$q_M = K_c h_{fg} \rho_g \left[\frac{\sigma(\rho_g - \rho_f)}{\rho_g^2} \right]^{1/4} \quad (3.1)$$

where the constant K_c was empirically found to equal 0.16. Although Eq. (3.1) was derived by dimensional analysis, Kutateladze⁵⁷ postulated that CHF was purely a hydrodynamic phenomenon related to an instability of the two-phase flow. Chang⁶⁰ was the first to actually apply stability analysis to nucleate boiling heat transfer. However, his model was based on the now little accepted theory of Jakob⁶¹, Gunther⁶², and Rohsenow and Clark⁶³ and others who claimed that nucleate boiling heat transfer was primarily due to the enhanced convection created by bubble ebullition and not the exchange of latent heat.

Zuber⁶⁴ was the first to derive Eq. (3.1) from a hydrodynamic stability analysis of transition boiling. Actually, his equation is

$$q_M = \frac{\pi}{24} h_{fg} \rho_g \left[\frac{\sigma(\rho_g - \rho_f)}{\rho_g^2} \right]^{1/4} \left[\frac{\rho_f + \rho_g}{\rho_f} \right]^{1/2} \quad (3.2)$$

but the last factor on the RHS is unity for most fluids and pressures far removed from the critical pressure. The constant is a product of the theoretical analysis and compares well with Kutateladze's empirically obtained value. Although many assumptions were made in the derivation of Eq. (3.2), Zuber implied that the analysis and physical model of CHF must be correct since the correct answer, Eq. (3.1), was obtained and the constants were nearly the same. Zuber's⁶⁵ paper received much attention and errors in his analysis and physical model were pointed out. He consequently revised the physical model and the analysis several times⁶⁴⁻⁶⁷ to accommodate the current thoughts, but always arrived back at Eq. (3.2) by judiciously and sometimes dubiously making the necessary assumptions and approximations. Zuber's work was always accompanied by lengthy and often times vituperative debate which was in part due to Zuber's claims as to the absolute nature of the stability analysis. The foremost example is Ref. 67 where 27 pages of discussion follow a 6 page paper. Many others have arrived at Eq. (3.1) with models based on entirely different phenomena. Chang^{68,69} and Moissis and Berenson⁷⁰, who used hydrodynamic considerations, and Cole⁷¹ who describes his own model as well as others are but a few. Zuber⁷², himself presented additional ways of obtaining Eq. (3.1) which did not rely on the hydrodynamic instability theory.

In the final derivation of Eq. (3.2), Zuber⁶⁷ assumed a physical model of CHF which was composed of jets of vapor emanating from a thin blanket of vapor covering the heater surface. This assumption was based on the not so revealing still photographs of Westwater and Santangelo⁷³, (also Westwater⁷⁴), which show boiling from a wire. Boiling from a wire is essentially a two-dimensional system for the vapor effusion at a distance far from the surface, however. The jet spacing was assumed to be somewhere between the Taylor critical wave length, λ_c , and Taylor most dangerous wave length λ_d . Finally, CHF occurred when the vapor jets broke-down and merged because of a Helmholtz type instability of the vapor-liquid counterflow. Based on these criteria, a

balance for the CHF and vapor leaving the surface yielded Eq. (3.2). The major assumption is that CHF is purely the result of a Helmholtz instability which occurs away from the surface.

Gaertner^{49,75} and Westwater^{76,77} conducted a number of high-speed photographic studies of nucleate boiling from a horizontal surface during the period 1961 to 1965 and made a number of observations which reveal the true nature of nucleate boiling and CHF. Much of their work is still referenced today. Gaertner⁴⁹ identified the existence of four regimes of nucleate boiling. In the order of increasing heat flux they are 1) the discrete bubble region, 2) the first transition, 3) the vapor mushroom region, and 4) the second transition. These regimes are shown in Fig. 3.1 as a function of heat flux and schematically in Fig. 3.2. The first region is exactly as the name implies while the first transition region is composed of discrete bubbles, discrete vapor jets, and coalesced vapor jets. Gaertner called the coalesced jets vapor mushrooms because of their appearance, (see Fig. 3.2 (b)). These vapor jets are much smaller and different in nature from those shown in the first photographs of Westwater^{73,74}. The vapor jets of Westwater's first photographs were the result of vapor coalescing at the wire surface and breaking into large jets along the ensuing liquid-vapor interface. The nature of high heat flux boiling is such that surface phenomena are obscured by large amounts of vapor. Considering the primitive high-speed photographic techniques available at the time of Westwater's⁷³ study, it is no wonder that Zuber's interpretation of CHF was limited to the larger jets. In fact, many investigators wrongly assumed from these photographs that the surface was not wetted by liquid at heat fluxes approaching CHF. Gaertner⁴⁹ termed the higher heat flux portion of the nucleate boiling regime the vapor mushroom region. Here the individual vapor jets have all coalesced into a large vapor mass that periodically departs from the surface. The individual jets form stems that feed the large vapor mass. The thin layer of liquid (~0.1 mm) separating the large vapor mass from the surface was termed the macrolayer, (see Fig. 3.2 (c)). The macrolayer should not be confused with the microlayer which is an even thinner layer of fluid which covers the surface under a forming vapor bubble. The macrolayer is often called the sublayer or subfilm in flow boiling studies. Finally, Gaertner describes a second transition region where dry patches

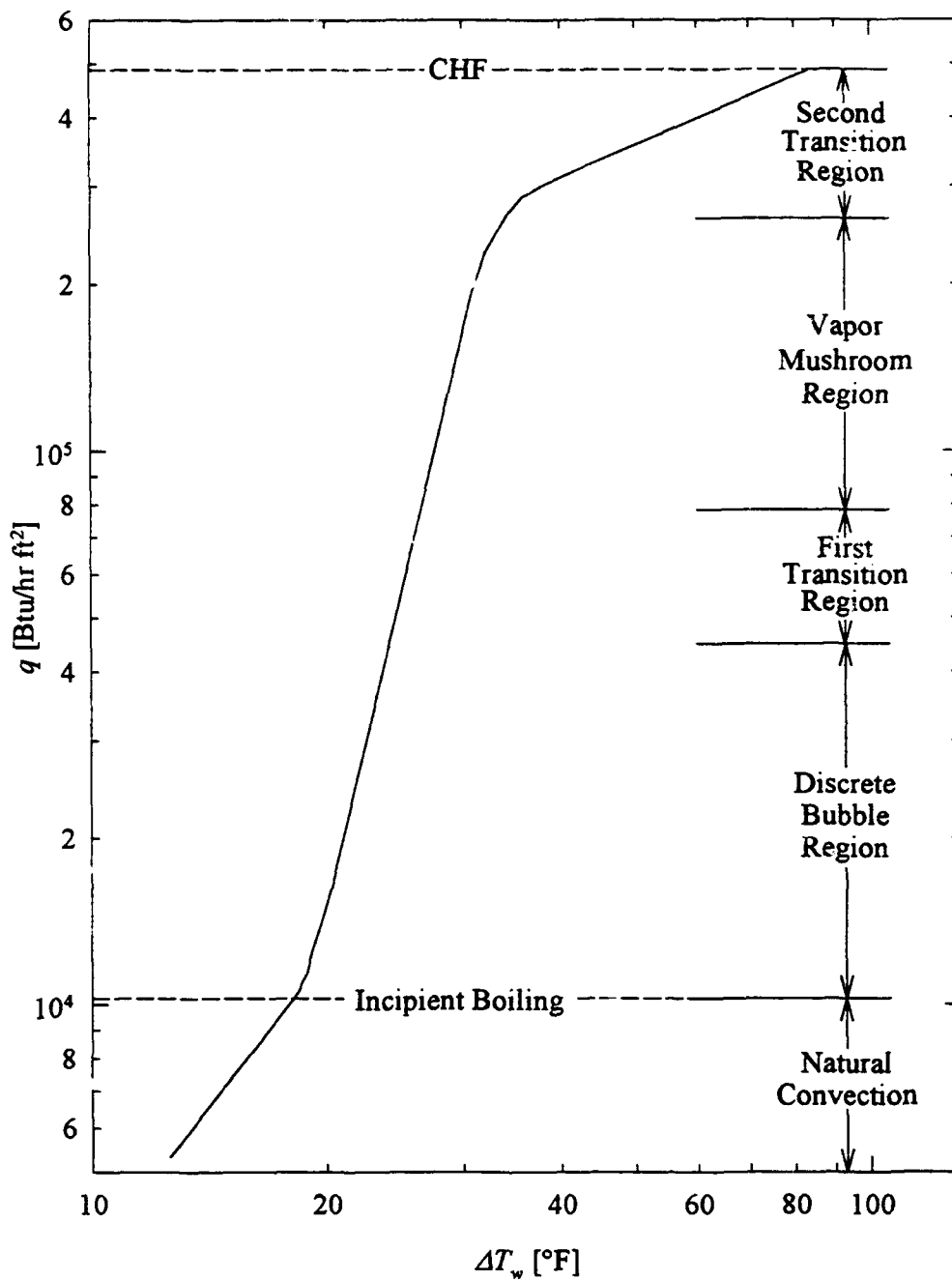


Figure 3.1 Regions of boiling mechanisms for water boiling on 4/0 polished surface.⁴⁹

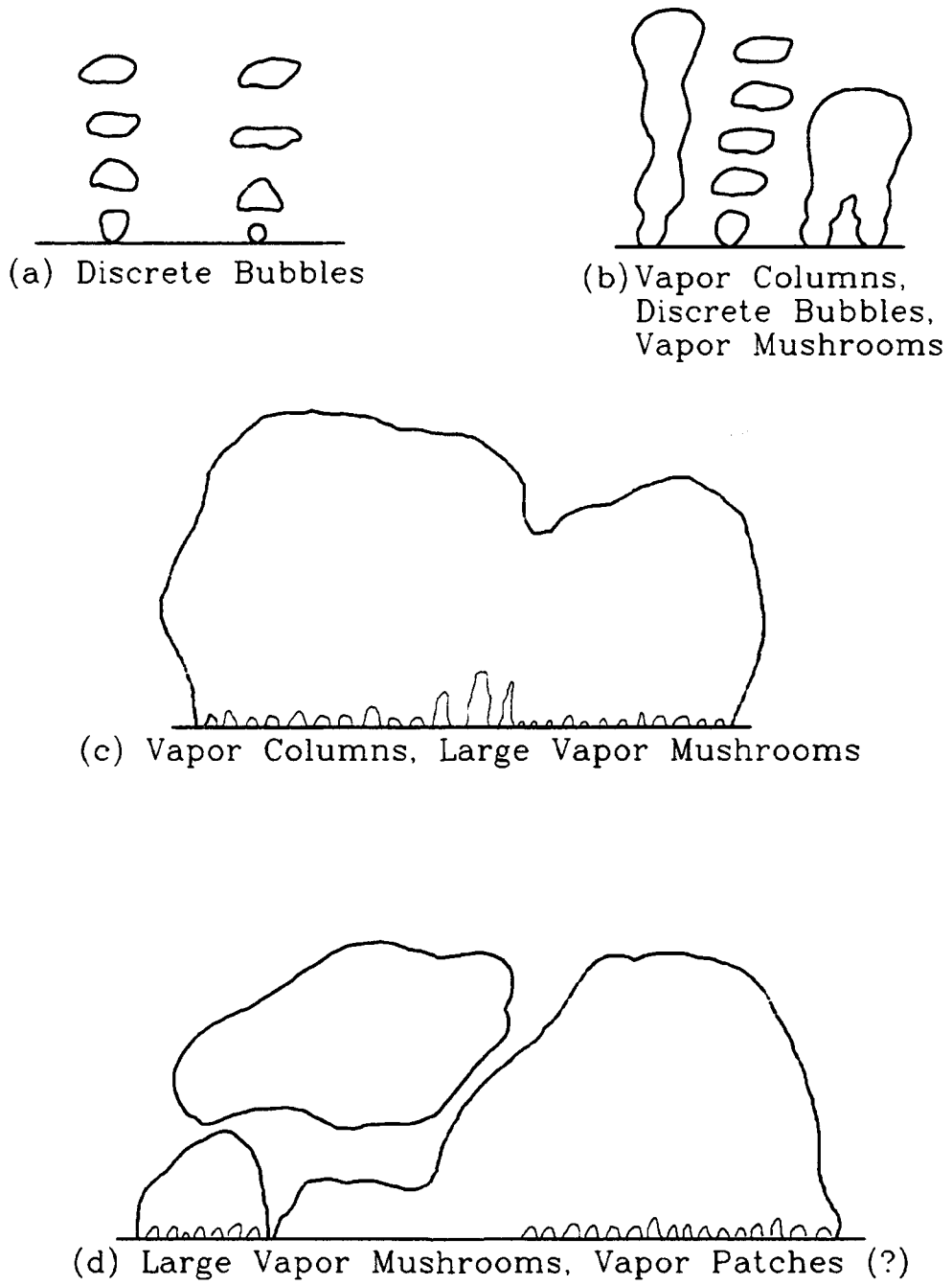


Figure 3.2 Schematic of pool boiling regimes.⁴⁹

intermittently occur on the surface below the individual large vapor masses, (see Fig. 3.2 (d)). Once a vapor mass departs, the surface is rewetted and the vapor mushrooms are almost instantaneously recreated. The liquid in the macrolayer may again be exhausted before the vapor mass departs and another dry patch may ensue. As heat flux is increased, the size and number of these dry spots increases. CHF occurs when a sufficiently large dry spot occurs and the surface cannot be rewetted. Heat previously removed by this dry spot location must consequently be removed by the surrounding area which is already near the point of dryout. Thus the surface dries out very quickly and a transition to film boiling occurs.

The final regime before CHF, the second transition region, and the existence of the macrolayer can explain many phenomena that Zuber's hydrodynamic instability theory is incapable of. Namely the effects of surface roughness, wettability, surface material, and heater thickness. Although roughness was found to have little or no effect on the CHF for the present experiments (see section 2.4.2), roughness has been shown to have an effect on CHF under some conditions, (cf. Berenson⁴⁵). Likewise, wettability has been shown to have an effect on CHF. The surface aging results of Section 2.6 are likely due to enhanced wettability for the oxidized surface. It is easy to see that roughness and wettability can have an effect on the process of macrolayer dryout and reformation. The heated surface material affects both the wettability and the transient spreading of heat which is a function of the material's thermal effusivity, $\sqrt{k\rho c}$. The heater thickness, t , also affects the transient spreading of heat as shown in detail by Kenning^{32,78,79} and others⁸⁰⁻⁸⁴. The product of material thermal effusivity and thickness, $t\sqrt{k\rho c}$, has been used to correlate thin heater CHF data. Bar-Cohen⁸⁴ has suggested that the term $t\sqrt{k\rho c}$ be called the heater thermal *capacitance*. Considering Gaertner's second transition region where dry spots momentarily occur, it can be seen that heaters with a high thermal capacitance can mitigate the dry spot effects better by more quickly and evenly redistributing the heat. This important fact will be discussed later in this chapter and in more detail in Chapter 6.

The above paragraph illustrates that Zuber's hydrodynamic model does not necessarily describe the CHF condition. This is not to say that hydrodynamic instability

does not play a role in CHF or that Eq. (3.1) is not valid, but that Zuber's contention that CHF is purely a hydrodynamic phenomenon and his particular physical description of CHF are incorrect. Nonetheless, Zuber's hydrodynamic instability theory of the pool boiling CHF phenomenon became widely accepted* over the years following his 1961 paper⁶⁷. As will be seen, his theories are easily extended to the mechanisms of pool boiling visualized by Gaertner⁴⁹ to yield the same answer, Eq. (3.1). The importance of his contribution of the hydrodynamic instability model should not be underestimated. Lienhard and others⁸⁵⁻⁸⁹ have used Zuber's hydrodynamic instability model extensively to explain the CHF from many geometries including wires, spheres, cylinders, and disks. Lienhard and Eichorn^{90,91} also developed the Mechanical Energy Stability Criterion for predicting CHF. Contrary to what the name may imply, this model does not rely on hydrodynamic instability analysis to explain the CHF phenomenon. Lienhard and Hasan⁹² used the Mechanical Energy Stability Criterion to show yet another way how Eq. (3.1) can be obtained, albeit with slight variation, using yet another physical model of CHF. The Mechanical Energy Stability Criterion has yet to receive wide spread use by the research community.

Katto and Yokoya⁹³ made a detailed photographic study of pool boiling from a small diameter horizontal heater in 1968. The small heater size limited the heater to one predominant vapor mass and dryout spot. Thus, they were able to study in detail the nature of dryout occurrence and rewetting as described for Gaertner's⁴⁹ second transition region. Based on a mechanistic model which balances the hovering time of the vapor mass and the time necessary to evaporate the macrolayer, they developed yet another predictive equation for pool boiling CHF. Not too surprisingly, their new equation was nearly identical to Eq. (3.1) with only slight variation. Nonetheless, this was the first instance that a CHF model was based on the phenomenon of dry spot occurrence, a phenomenon that was actually observed by experiment. Katto and Yokoya's model relied

* Equation (3.1) is most often called Zuber's equation in recognition of his strong advocacy of the hydrodynamic instability theory of CHF. Equation (3.1) is also called Kutateladze's equation and the Kutateladze-Zuber equation.

on empirical relations derived from the studies of Gaertner^{49,75} and Gaertner and Westwater⁷⁶ for the macrolayer thickness, mean vapor stem diameter, and vapor stem area to total area ratio.

Later, Haramura and Katto⁹⁴ revisited the description of CHF and used hydrodynamic instability theory to obtain another variation of Eq. (3.1). Their model is probably the most lucid description of the CHF phenomenon. Referring to Fig. 3.3, the large vapor mushrooms described by Gaertner are considered to be the result of jets of liquid coalescing due to a Helmholtz instability. Note that here, the instability is not the cause of CHF, but merely one of the precursors. The length of the vapor stems were postulated to be proportional to 1/4 the Helmholtz critical wavelength. Not much explanation was given for choosing the value 1/4. It is, however, possible for the macrolayer thickness to be greater than the predicted Helmholtz critical wavelength because the instability criterion does not consider the fact that the jets are stabilized at one end by the surface.

Based on Davidson's studies of gas bubbles forming at the wall of a pool of liquid^{96,97}, Haramura and Katto then derived a characteristic hovering time for the large vapor masses, or vapor mushrooms which was a function of the vapor mass growth rate. These vapor masses hover near the surface due to hydrodynamic considerations, rather than the surface tension forces of the vapor stems which are very weak⁹⁵⁻⁹⁷. The diameter of the hovering vapor masses was considered proportional to the Taylor most dangerous wavelength, λ_d , as shown in Fig. 3.3. These conditions, and the continuity of liquid entering and vapor exiting the macrolayer, defined the volume of the macrolayer and the total amount of heat entering it before a vapor mass departs. If the amount of heat entering the macrolayer exceeds the latent heat content of the macrolayer before the end of the hovering period, the macrolayer dries out and CHF ensues. The photographs of Gaertner and Westwater actually showed that dry spots are not a sufficient cause of CHF, but this condition occurs just before CHF. The heat flux necessary for dry patch formation is probably proportional to the CHF and consequently, Haramura and Katto's model of CHF is probably the most accurate.

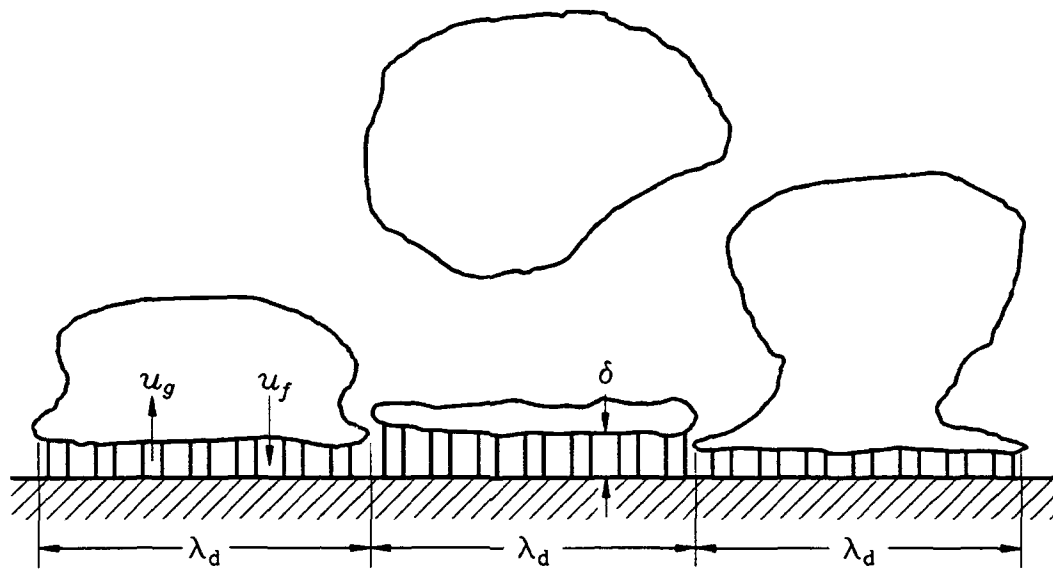


Figure 3.3 Schematic of pool boiling CHF mechanisms.⁹⁴

Unfortunately, their modified version of Eq. (3.1) contains complex functions of A_g/A_w ** and ρ_f/ρ_g . Rather than assuming A_g/A_w equal to some constant defined by a supposed vapor column packing configuration as has been done by Zuber⁴⁷ and Lienhard and Dhir⁸⁷, they equated their equation with Eq. (3.1) and obtained A_g/A_w as a function of ρ_g/ρ_f . This implicitly links their equation with Eq. (3.1), but the only information of A_g/A_w available to them was the 20-year-old data of Gaertner^{49,75}, Gaertner and Westwater⁷⁶ and Kirby and Westwater⁷⁷ which was obtained for a single surface by using a unique electroplating method. Pasamehmetoglu and Nelson⁹⁸ have analyzed the macrolayer thickness data of Yu and Mesler⁹⁹, Gaertner and Westwater^{49,76}, Bhat et al.¹⁰⁰⁻¹⁰², and others and suggest that A_g/A_w is proportional to $q^{1/4}$. Recently, Liaw and Dhir^{103,104} have obtained void fraction data near the wall for varying contact angle and heat flux which indicates that A_g/A_w is a strong function of both.

Haramura and Katto's contribution is important in spite of the fact that a reliable equation for A_g/A_w does not yet exist. Their model is the only one that is adaptable to the various secondary influences on CHF. Namely, the effects of surface roughness, wettability, surface material, and heater thickness. Pan and Lin¹⁰⁵⁻¹⁰⁷ have already made attempts to modify the macrolayer model to accommodate some of these effects. In summary, many years of investigation have identified to a good degree of certainty, that pool boiling CHF is the result of excessive vapor patch dryout due to the periodically restricted inflow of liquid caused by large hovering vapor mushrooms. A successful model of CHF has been derived which uses instability criteria to define macrolayer thickness and vapor mushroom diameter. Empirical correlations are used for other unknowns such as the hovering time and the ratio A_g/A_w . Considering all the proportionalities of the above analyses and the many different ways to reach the correct answer, it could be said that the above analyses are akin to dimensional analysis. These

** The ratio A_g/A_w is the vapor column area over the unit boiling cell area. It is often obtained by considering a square area containing a vapor column of equal diameter. Another variation is a hexagon containing a vapor column with a diameter equal to the major dimension. There is, however, no theoretical basis for either assumption.

analyses do serve the important function of defining the pertinent dimensionless quantities and also serve as the building blocks of more definitive models.

3.2 An Introduction to the Mechanisms and Modeling of Flow Boiling CHF

Now that the mechanism of pool boiling CHF is understood, the vast array of assumptions are known, and the difficulty of deriving an accurate model is appreciated, the even more nebulous area of flow boiling CHF will be discussed. Fortunately for the reader, this area is in its infancy, (at least for the case of discrete heat sources), and the steps leading up to the present model are much shorter.

Haramura and Katto⁹⁴ proposed a model of flow boiling CHF in the same article in which they described the development of the macrolayer model of pool boiling CHF. In fact, information from the pool boiling model is vital to the derivation of the flow boiling complement. From experiments¹⁰⁹ of a planar jet impinging either parallel to or at small angles to the leading edge of a small heater, Haramura and Katto postulated that CHF occurs when macrolayer is just depleted at the most downstream edge of the heater, see Fig. 3.4 (a). Figure 3.4 (a) shows a schematic of the boiling mechanisms for the case of a heat source in a channel. The supposed mechanisms are nearly identical to that assumed by Haramura and Katto except that they assume that the velocity profile is uniform. In addition, the thickness of the planar jet was thinner, being about two times the vapor blanket thickness. For the case of jet impingement, the liquid is continuously fed from the leading edge of the heater rather than from above by the intermittent departure of vapor mushrooms. Nevertheless, phenomena within the macrolayer are postulated to govern CHF. The detailed form of the macrolayer has not been observed by high speed photography, only the existence of a thin liquid film on the wall has been seen. However, based on what has been visualized for pool boiling, vapor jets feeding a large continuous vapor blanket or vapor mushroom are postulated. Compared to pool boiling, the macrolayer thickness at the upstream edge of the heater is assumed to be proportional to the Helmholtz unstable wavelength.

Katto and Ishii¹¹⁰ obtained photos that show that vapor leaving the surface separates the incoming liquid jet into a thin liquid film which stays on the wall and a

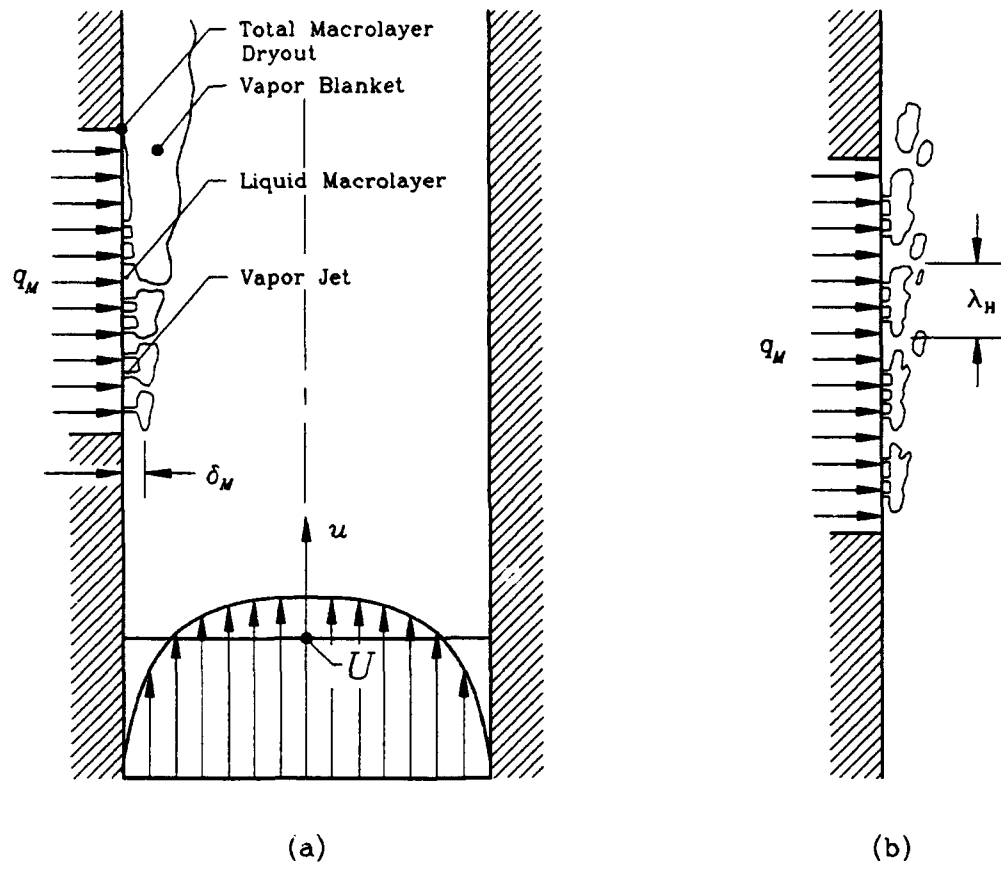


Figure 3.4 Schematic representation of flow boiling CHF mechanism.¹⁹
 (a) Low velocity mechanism. (b) High velocity mechanism.

stream of liquid which is ejected from the wall. As heat flux is increased, the point at which this separation occurs moves towards the upstream edge. Further increases of heat flux caused the separation point to reach the upstream edge and also caused the liquid macrolayer to begin drying out at the downstream edge of the heater. Note that these events did not necessarily occur simultaneously. CHF ensued once sufficient dryout of the macrolayer occurred.

Because the most current model of CHF follows from that of Haramura and Katto, a detailed description of their derivation and the pertinent assumptions are described. For the condition of macrolayer dryout in saturated flow, a heat balance gives

$$q_M L = \rho_f \delta U h_{fg} \quad (3.3)$$

Haramura and Katto assumed that the initial macrolayer thickness, δ , was equal to 1/4 the Helmholtz critical wavelength, λ_H . For two-dimensional planar counter flow of two inviscid fluids of differing densities, the wave velocity, c , of the interface is given by^{108,***}

$$c = \pm \left[\frac{2\pi\sigma}{(\rho_f + \rho_g)\lambda} - \frac{\rho_f \rho_g (u_f + u_g)^2}{(\rho_f + \rho_g)^2} \right]^{1/2} \quad (3.4)$$

*** The reason for assuming a planar rather than cylindrical interface is almost never mentioned in the literature. In fact, the author knows of only one instance.⁶⁶ For a circular jet of vapor flowing vertically in a concentric cylinder of liquid, the wave velocity is given by⁶⁶

$$c = \pm \left[\frac{\sigma(1-m^2)}{R_j m \left[\frac{\rho_g I_0(m)}{I_1(m)} + \frac{\rho_f K_0(m)}{K_1(m)} \right]} + \frac{\rho_f \rho_g (u_f + u_g)^2}{\left[\frac{\rho_g I_0(m)}{I_1(m)} + \frac{\rho_f K_0(m)}{K_1(m)} \right]^2} \frac{I_0(m)K_0(m)}{I_1(m)K_1(m)} \right]^{1/2}$$

where $m = 2\pi R_j / \lambda$ is the wave number, R_j is the vapor jet diameter, and $I_i(m)$ and $K_i(m)$ are the modified Bessel functions of the first and second kind, respectively. For $R_j \rightarrow \infty$, Eq. (3.7) is obtained. The complexity of the above equation provides adequate reason for making the planar assumption. Furthermore, a cumbersome variable, R_p , is ignored.

in the absence of gravity, (i.e., vertical sheets or jets). Instability occurs when c is imaginary. A heat balance for a unit boiling cell containing one vapor jet gives

$$q A_w = \rho_g u_g A_g h_{fg} \quad (3.5)$$

Similar to what is shown in Fig. 3.3, continuity of liquid and vapor flow to and from the surface gives

$$\rho_g u_g A_g = \rho_f u_f (A_w - A_g) \quad (3.6)$$

Assuming $\delta = 1/4 \lambda_H$, setting $c = 0$, and solving Eqs. (3.3)-(3.6) gives the following equation:

$$\delta = \frac{\lambda_H}{4} = C_A \frac{\pi \sigma}{2} \frac{\rho_f + \rho_g}{\rho_f \rho_g} \left(\frac{\rho_g h_{fg}}{q_M} \right)^2 \quad (3.7)$$

where

$$C_A = \left[\frac{\frac{A_g}{A_w}}{1 + \frac{\rho_g}{\rho_f} \frac{A_g}{A_w - A_g}} \right]^2 \quad (3.8)$$

The combination of Eqs. (3.5) to (3.7) is from Zuber's⁶⁷ final instability theory for pool boiling CHF. Note that δ is proportional to q_M^{-2} , this agrees well with pool boiling macrolayer measurements made by Yu and Mesler⁹⁹, Gaertner⁴⁹, Bhat et al.^{101,102}, and Liaw and Dhir¹⁰³ where δ was found to be roughly proportional to $q_M^{-1.5}$. The ratio $\rho_g / \rho_f = 0.0006, 0.005, \text{ and } 0.008$ for water, R-113 and FC-72, respectively and pressures near atmospheric. Thus, making the approximation, $C_A = (A_g / A_w)^2$ and by equating their

pool boiling CHF model with that of Zuber⁶⁵, (Eq. (3.1)), Katto and Haramura⁹⁴ obtained the following relation for A_g/A_w .

$$A_g/A_w = 0.0584 (\rho_g/\rho_f)^{0.2} \quad (3.9)$$

As mentioned earlier, the validity of Eq. (3.9) is suspect because it has been shown by various investigators that A_g/A_w is a function of heat flux, and surface roughness and surface wettability. Furthermore, A_g/A_w may be a different function of these parameters for flow boiling as opposed to pool boiling. Consequently, Eq. (3.9) cannot directly be applied to the flow boiling application. Notwithstanding, if Eqs. (3.3), (3.7), (3.9), and the small ρ_g/ρ_f approximation for Eq. (3.8), are combined, the following equation is obtained for the saturated flow boiling of a planar jet flowing parallel to a small heated surface.

$$\frac{q_M}{U\rho_f h_{fg}} = 0.175 \left(\frac{\rho_g}{\rho_f} \right)^{0.467} \left(1 + \frac{\rho_g}{\rho_f} \right)^{1/3} \left(\frac{\sigma}{\rho_f U^2 L} \right)^{1/3} \quad (3.10)$$

Dropping the second factor on the RHS because $\rho_g/\rho_f \ll 1$, it may be seen that Eq. (3.10) compares very well with the empirically derived equation of Katto and Kurata¹⁰⁹,

$$\frac{q_M}{U\rho_f h_{fg}} = 0.186 \left(\frac{\rho_g}{\rho_f} \right)^{0.559} \left(\frac{\sigma}{\rho_f U^2 L} \right)^{0.264} \quad (3.11)$$

for the same experimental data. Note that the second factor on the RHS of Eq. (3.11) is the inverse of the Weber number, We . Thus, Haramura and Katto were able to theoretically obtain the form of an equation derived by dimensional analysis much in the same way that Zuber and others have been able to theoretically obtain Kutateladze's equation, which was derived by dimensional analysis. Katto and others¹⁰⁹⁻¹²² have been able to empirically correlate the CHF data of impinging circular jets, thin flowing films,

falling films, cylinders in cross-flow and uniformly heated ducts using the general form of Eq. (3.11).

Mudawwar et al.²⁵ followed the same analysis to obtain a correlation for a falling film over a small rectangular heat source. Rather than assume $\delta=1/4\lambda_H$, they assigned an empirical constant, C_1 . They also assumed that the enigmatic ratio, A_g/A_w , was constant. They added a subcooling correction for the equation, (which was the same form as Eq. (3.11)), but had to empirically fit an exponent for the Weber number to obtain a good fit for the data. Mudawwar (sic) and Maddox¹⁹ most recently used the analysis of Haramura and Katto⁹⁴ and extended that of Mudawwar et al.²⁵ by adding the effect of a developed velocity profile at the wall. They developed a theoretical model of CHF for the boiling configuration of the present experiments, that is, flow boiling from a discrete heat source in a rectangular channel. Because the salient features of this model will be referred to often and will be modified in Chapter 4, the Mudawwar and Maddox model is presented as follows.

The boiling configuration for the model of Mudawwar and Maddox differs little from that postulated by Haramura and Katto and is shown schematically in Fig. 3.4 (a). Again, liquid is postulated to enter the macrolayer at the leading edge of the heater and to flow across the heater surface and feed the nucleation sites. As heat flux is increased, the macrolayer thickness decreases to the point that dryout occurs at the most downstream portion of the heated surface. Dryout of the liquid film at the most downstream section of the heater has been visualized by Monde and Katto¹¹³, Katto and Ishii¹¹⁰, Baines et al.¹²², Ueda et al.¹²¹, as well as Mudawwar et al.²⁵ for various jet impingement and falling film configurations. In some cases, partial dryout could be sustained for a small range of heat fluxes leading up to the CHF. However, following the lead of Haramura and Katto⁹⁴, CHF is postulated to occur when the heat flux is just sufficient to completely vaporize the liquid entering the macrolayer at the most upstream edge of the heater.

The above macrolayer dryout model was found to be valid for a limited range of velocities, (0.22 to about 2 m/s). Mudawwar and Maddox¹⁹ reported that a transition occurs, and for higher velocities the vapor blanket breaks into small vapor patches that allow liquid to enter from the bulk flow above. This is shown schematically in Fig. 3.4

(b). The photographic evidence supporting the existence of this transition is not conclusive, however. Furthermore, it must be remembered that the true nature of the macrolayer has been visualized only for the pool boiling situation. With this in mind, the macrolayer dryout model representing the configuration of the present study will be derived.

While Haramura and Katto⁹⁴ assumed a uniform velocity profile for the liquid entering the macrolayer, Mudawar and Maddox¹⁹ refined the macrolayer dryout model to include the effect of a fully developed turbulent velocity profile. Thus, considering the sensible heating of the subcooled liquid and a turbulent velocity profile, Eq. (3.3), the macrolayer dryout criterion is written as

$$q_M L = \rho_f (c_p \Delta T_{sub} + h_{fg}) \int_0^{\delta_M} u dy \quad (3.12)$$

where δ_M is the liquid sublayer thickness that is completely transformed to vapor. Maddox and Mudawar estimated the thickness of the laminar sublayer to be smaller than 0.015 mm for the velocity range of 0.22 to about 2 m/s. The thickness of the vapor blanket at the most upstream edge of the heater was observed to be 0.52 mm on the average. Thus, the power-law form of the *law of the wall* velocity profile, Eq. (3.13), was assumed to apply over the span of $0 \leq y \leq \delta_M$. Actually, an error was committed in estimating the thickness of the laminar sublayer. The macrolayer thickness for the geometry of Mudawar and Maddox was actually 0.100 and 0.015 mm for the velocities of 0.22 and 2 m/s, respectively. The ramifications of this error will be addressed later. Therewith, the assumed velocity profile is

$$u^* = 8.56 y^{+1/7} \quad (3.13)$$

where

$$u^+ = \frac{u}{u_\tau} = \sqrt{\frac{C_{f,sw}}{2}} \quad (3.14)$$

and

$$y^+ = \frac{yu_\tau}{\nu} \quad (3.15)$$

Using the Blasius solution,

$$f = 0.316 Re^{-1/4} \quad (3.16)$$

and assuming $C_f = f/4$, Eqs. (3.13)-(3.16) may be combined to obtain $u = \phi(y)$ and Eq. (3.9) may be integrated to obtain

$$\frac{q_M}{U\rho_g h_{fg}} = 1.183 \left(\frac{\rho_f}{\rho_g} \right) \left(1 + \frac{c_p \Delta T_{sub}}{h_{fg}} \right) \left(\frac{L}{D_h} \right)^{1/7} \left(\frac{\delta_M}{L} \right)^{8/7} \quad (3.17)$$

The only remaining unknown is δ_M which is obtained from a variation of Haramura and Katto's approximation that δ_M is proportional to the critical Helmholtz unstable wave length. By setting $c=0$ and setting δ_M proportional to λ_{Hb} , Eq. (3.4) becomes

$$\delta_M = C_\lambda \lambda_{Hb} = C_\lambda \frac{2\pi\sigma(\rho_f + \rho_g)}{\rho_f \rho_g} \frac{1}{(u_f + u_g)^2} \quad (3.18)$$

Next, considering that at CHF the bulk liquid flow in the channel is separated from the macrolayer by the vapor blanketing the surface, it can be assumed that direct sensible heating of the bulk liquid does not occur. Mudawwar et al.²⁵ considered the situation in the macrolayer where by a certain volume of liquid would replace an equal

volume of vapor departing from the surface. For equal volumes of liquid and vapor, the ratio of sensible heat to latent heat is given by the quantity $\rho_f c_p \Delta T / \rho_g h_{fg}$, which is called the modified Jakob number or Ja^* . Equation (3.5) is now rewritten to include the effect of subcooling

$$q A_w = \rho_g u_g A_g h_{fg} \left[1 + C_{sub} \frac{\rho_f c_p \Delta T}{\rho_g h_{fg}} \right] \quad (3.19)$$

where C_{sub} is an empirical constant which accounts for the volumetric ratio associated with the liquid-vapor exchange mechanism. The exact liquid-vapor exchange mechanism in the macrolayer is unknown, though. One could just as easily consider stable vapor columns continuously fed by liquid. For a mass of liquid replacing an equivalent mass of vapor, Eq. (3.19) would become

$$q A_w = \rho_g u_g A_g h_{fg} \left[1 + \frac{c_p \Delta T}{h_{fg}} \right] \quad (3.20)$$

Substituting Eqs. (3.6) and (3.19) into Eq. (3.18) gives

$$\frac{\delta_M}{L} = \psi \left(\frac{\rho_f}{\rho_g} \right) \frac{\frac{\sigma}{\rho_f U^2 L}}{\left(\frac{q_M}{U \rho_g h_{fg}} \right)^2} \left(1 + C_{sub} \frac{\rho_f c_p \Delta T_{sub}}{\rho_g h_{fg}} \right)^2 \quad (3.21)$$

where

$$\psi = 2 \pi C_\lambda C_A \quad (3.22)$$

and C_A is given by Eq. (3.8). Making the same assumption as before that C_A is constant, Eqs. (3.17) and (3.21) may be combined to give

$$q_M^{**} = 1.052 \psi^{8/23} We^{-8/23} \quad (3.23)$$

where

$$q_M^{**} = \frac{q_M}{U \rho_g h_{fg}} \left(\frac{\rho_f}{\rho_g} \right)^{\frac{15}{23}} \left(\frac{L}{D_h} \right)^{\frac{1}{23}} \left[1 + \frac{c_p \Delta T_{sub}}{h_{fg}} \right]^{\frac{7}{23}} \left[1 + C_{sub} \frac{\rho_f c_p \Delta T_{sub}}{\rho_g h_{fg}} \right]^{\frac{16}{23}} \quad (3.24)$$

The group $1.052 \psi^{8/23}$ and the constant C_{sub} were empirically found to equal 0.161 and 0.021, respectively. Comparing Eq. (3.24) to Eq. (3.17), one can see that the approximation for δ_M is responsible for an extra subcooling term, the Weber number, and the exponents of the original factors in Eq. (3.17). As mentioned earlier, the Weber number has been found to be an important quantity in the correlation of flow boiling CHF data.

In summary, the tortuous path that has led to Eqs. (3.23) and (3.24) is fraught with many assumptions and unknowns. Foremost is the assumption that the mechanism of CHF follows that shown in Fig. 3.4 (a). There is still insufficient experimental proof of this. It will be shown in later chapters that CHF is a function of heater thickness, and also of buoyancy for the curve channels. Neither case is readily handled by the mechanism described for Fig. 3.4 (a). If the mechanism of CHF is that shown in Fig. 3.4 (a), then other unknowns are to be answered. Is the macrolayer thickness really a function of the Helmholtz unstable wavelength? How does A_g/A_w vary with the flow conditions, subcooling, surface characteristics, and pressure? What is the true liquid-vapor exchange mechanism at the surface? These are but a few of the questions that must be answered before the nature of flow boiling CHF can be known well enough to have confidence in a mathematical model of CHF.

Most of these questions must be answered by employing the methods of high-speed photography. Through the high-speed photography of Gaertner, Westwater, and

Katto, a thorough understanding of the mechanism of pool boiling CHF has been attained. As the author knows by first hand experience, this is much easier said than done for flow boiling. The phenomena are generally an order of magnitude smaller in size and occur at rates that are one to three orders of magnitude faster. It is even Lienhard's¹²³ contention that high-speed photos of the flow boiling CHF phenomenon will never be obtained! Nonetheless, Galloway and Mudawar^{124,125} have recently attempted high-speed photography of the CHF phenomenon for the present configuration. Unfortunately, the two-dimensional features of the experimental setup have certainly compromised the results. The author believes that the means to obtain the necessary high-speed photos of flow boiling CHF already exist. By employing emerging high-speed video technology and stroboscopic laser sheet lighting, two-dimensional cross sections of the vapor blanket could be obtained. Unfortunately, the cost of this technology is well over \$200k and is currently beyond the financial means of all but the most wealthy of Government laboratories.

3.3 Effect of Channel Height - Previous Results

The literature is in disagreement over the effect of channel height on CHF. Tolubinskiy et al.^{126,127} found that for forced convective boiling of subcooled water in annuli of 0.5 and 4 mm, CHF was significantly lower for the smaller annulus. Hung and Yao¹²⁸ observed the same trend for R-113 flowing in annuli of 0.32, 0.80, and 2.58 mm. The reduction in CHF was most significant between the 0.32- and 0.80-mm annuli. On the other hand, Bergles¹²⁹ showed that CHF increases monotonically as tube diameter decreases from 7.6 to 0.5 mm. In his experiments of forced convective boiling of subcooled water, the tube L/D was held constant at 25, and CHF for the 0.5-mm tube was more than twice that for the 7.6-mm tube. Bergles' results indicate that CHF reaches some asymptotic constant for tube diameters greater than 6 mm. Glushchenko¹³⁰ and Ornatskii¹³¹ found that CHF increases for tube diameters less than 2 mm and is constant for diameters greater than 2 mm. Not only are the above results in disagreement, but they are for uniformly heated tubes or annuli and cannot be extrapolated to the present configuration.

Coincident with the present study¹³², McGillis et al.²⁸ studied various geometry effects on CHF. Their experiments used R-113 flowing at velocities of 0.15 to 1 m/s over a series of ten simulated electronic chips. No effect of channel height was noted for heights of 1.9, 3.2 and 6.4 mm. Later, Willingham and Mudawar¹³³ investigated the effect of channel height on a series of nine simulated electronic chips in a similar flow channel. For channel heights of 2, 5, and 10 mm, they found CHF to be significantly higher for the 5-mm channel, thus revealing that an optimum channel height exists. It must be noted that the results of McGillis et al.²⁸ were based only on the most downstream of the 10 heat sources while the conclusion of Willingham and Mudawar¹³³ was independent of the heat source location. Given the strong similarity of the test sections for these two investigations, the results appear to be in direct conflict with each other. The results of Willingham and Mudawar¹³³ for the most upstream of the nine heat sources is directly comparable to the present experiment, but only partially agree with the previously obtained results of Leland and Chow¹³².

3.4 Effect of Channel Height - Experimental Results

Data were obtained for the straight channel case to provide a good comparative base for the curved channel data and to determine the effect of flow channel height, (see Fig. 2.2), on CHF. It was desired to vary the channel height in order to change the magnitude of secondary flow for the curved channel tests. Thus, in order to separate the effects of secondary flow and channel height, the latter was studied for the straight section. Results were obtained for velocities of 1 to 7 m/s, and three subcoolings, 5, 20 and 35°C. Because of the cavitation problem mentioned earlier, (see Section 2.1), the effect of channel height results do not show data for 5°C subcooling. Three test sections (see Table 3.1, also see Fig. 2.2) offered channel heights of 3.18, 5.56 and 6.35 mm. Data for a height of 1.14 mm were obtained by insertion of a shim into the straight section flow path of channel #2. The flow was well within the turbulent regime for all cases.

Figures 3.5 - 3.7 show some characteristic boiling curves for channel #3. These are very similar to the other channels. Note the similarity to Gaertner's⁴⁹ pool boiling

Table 3.1. Flow channel parameters and geometry factor.

Channel	#1	#2	#3	#2 c/shim
R	56.4 mm	28.6 mm	28.6 mm	∞
w	27.0 mm	27.0 mm	27.0 mm	27.0 mm
h	5.56 mm	3.18 mm	6.35 mm	1.14 mm
L	9.52 mm	9.52 mm	9.52 mm	9.52 mm
D_h	8.91 mm	5.68 mm	10.3 mm	2.19 mm
$(LD_h)^{1/23}$	1.0029	1.0227	0.9967	1.0659

curve, Fig. 3.1. The similarity implies that the same basic mechanisms exist for the case of flow boiling. One notable difference is the decline in the magnitude of Gaertner's second transition region, (see Fig. 3.1), with increasing subcooling. Thus a transition in the CHF mechanism may occur with changing subcooling. However, Figs. 3.5 - 3.7 do not indicate a change in the CHF mechanism with velocity as show in Figs. 3.4(a) and 3.4(b). Figure 3.8 illustrates the effects of velocity, subcooling and channel height. It is readily seen that there is little difference for heights of 3.18 to 6.35 mm. However, as h is reduced to 1.14 mm, a significant change of q_M is observed. For this height, the CHF was increased for velocities less than 3 m/s and reduced for velocities greater than 3 m/s as compared to results for heights of 3.18 to 6.35 mm.

As noted previously, Mudawar and Maddox¹⁹ obtained data for a similar configuration and velocity and subcooling ranges of 0.22 to 4.1 m/s and 0 to 44°C, respectively. They developed the predictive correlation for CHF represented by Eqs. (3.23) and (3.24). These equations were found to fit the data for the range $We < 10^4$. McGillis et al.²⁸ later showed that Eqs. (3.23) and (3.24) are also bounded by a lower limit of $We > 100$. At near atmospheric pressure, $We \approx 10^4$ corresponds to a flow velocity of about 2 m/s while $We \approx 100$ corresponds to a velocity of 0.21 m/s. The present data are plotted against Eqs. (3.23) and (3.24) in Figs. 3.9 and 3.10 for subcoolings of 20 and 35°C, respectively. Noting that for $h \geq 3.18$ and $We < 10^4$, the data fall predominantly below the correlation for 20°C subcooling and above the correlation for 35°C subcooling,

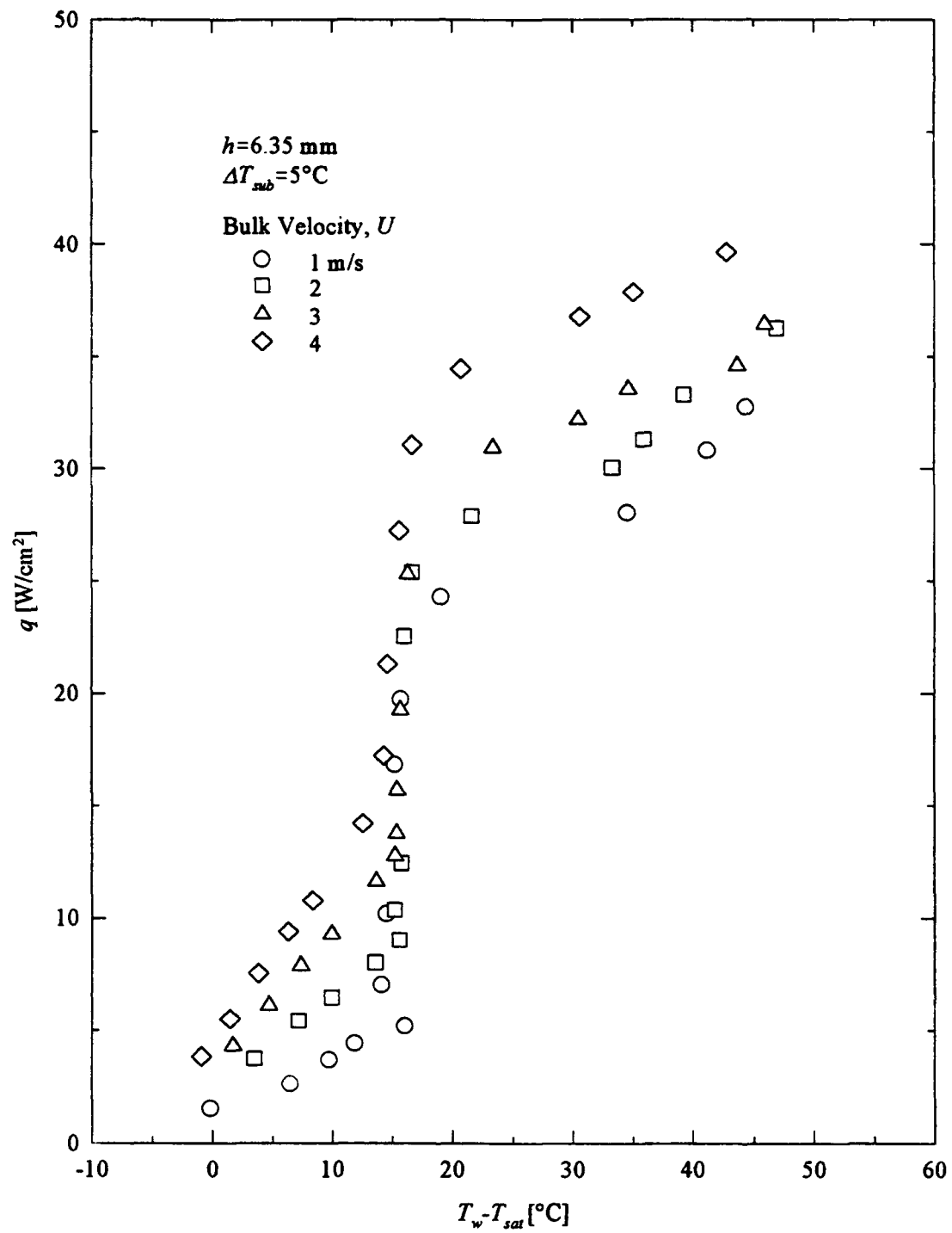


Figure 3.5 Heat flux versus wall superheat for 5°C subcooling.

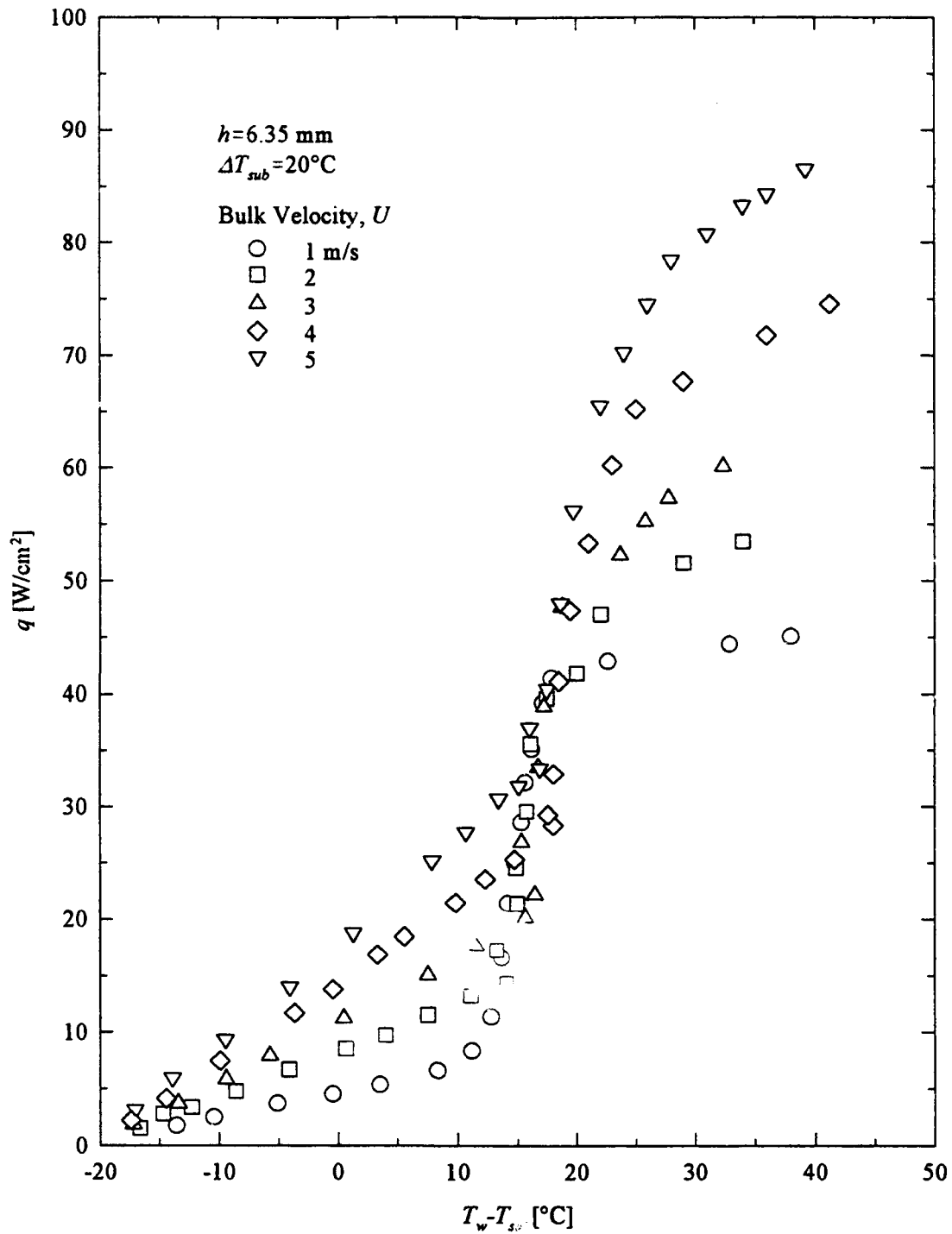


Figure 3.6 Heat flux versus wall superheat for 20°C subcooling.

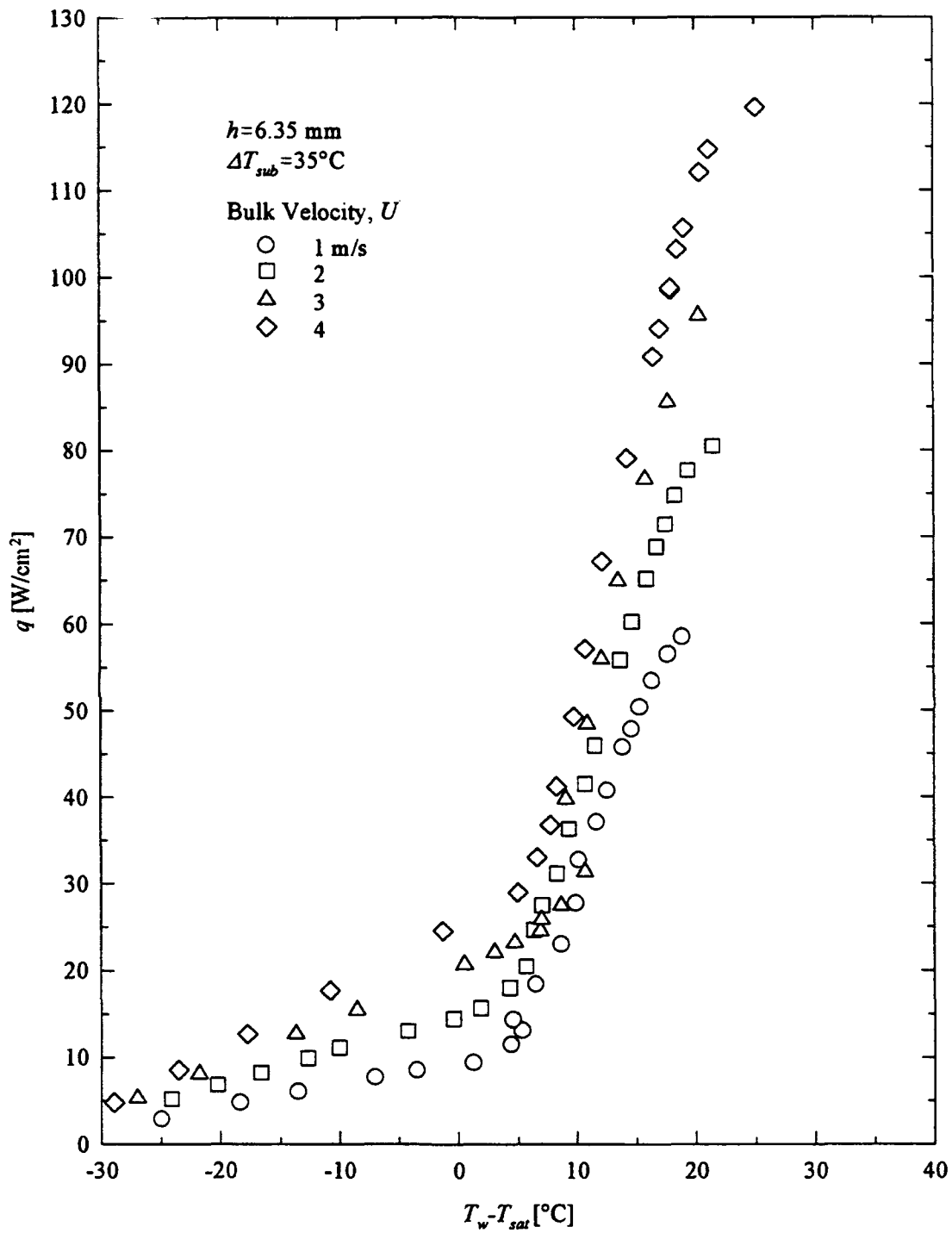


Figure 3.7 Heat flux versus wall superheat for 35°C subcooling.

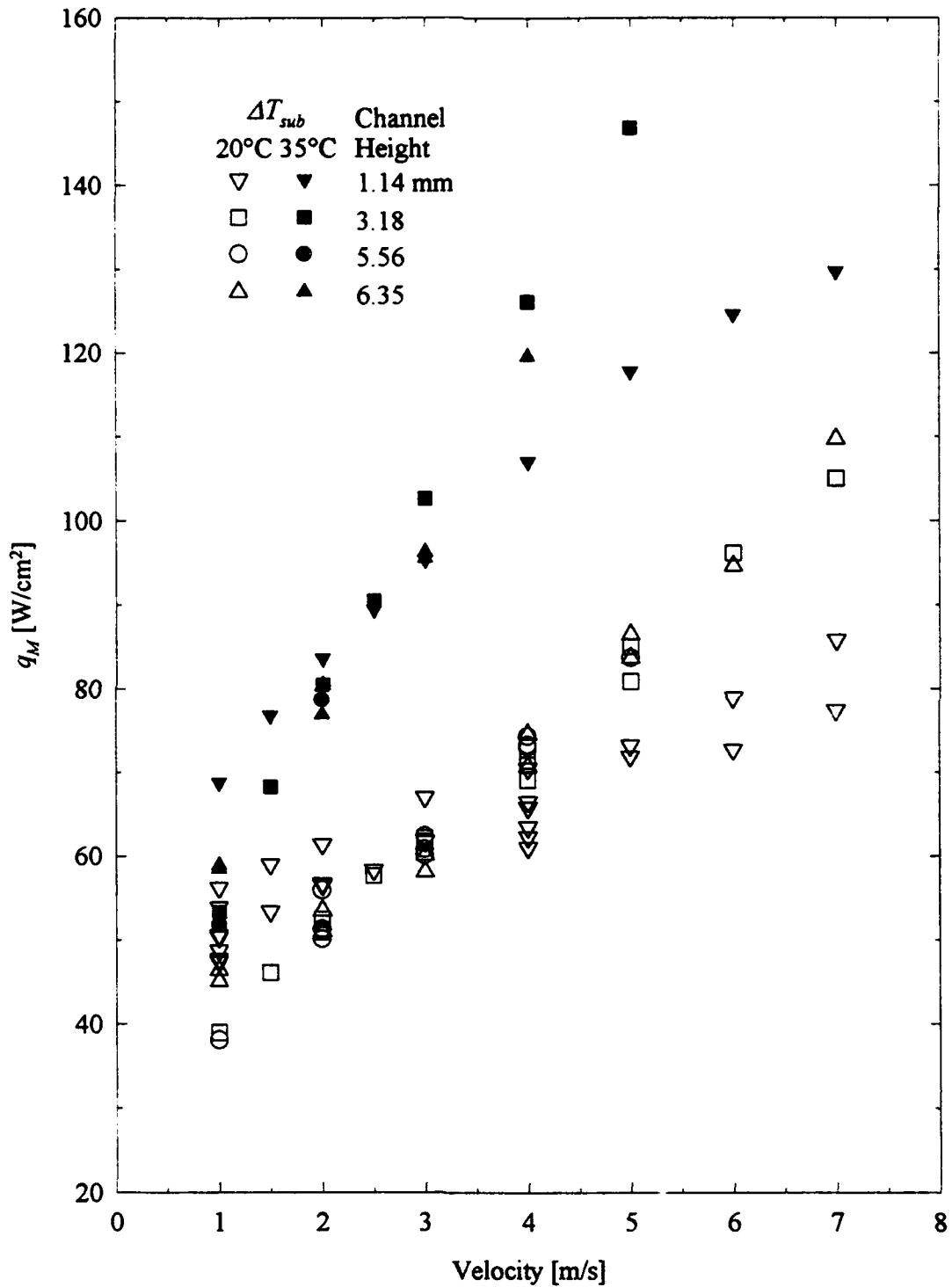


Figure 3.8 Effect of channel height on CHF.

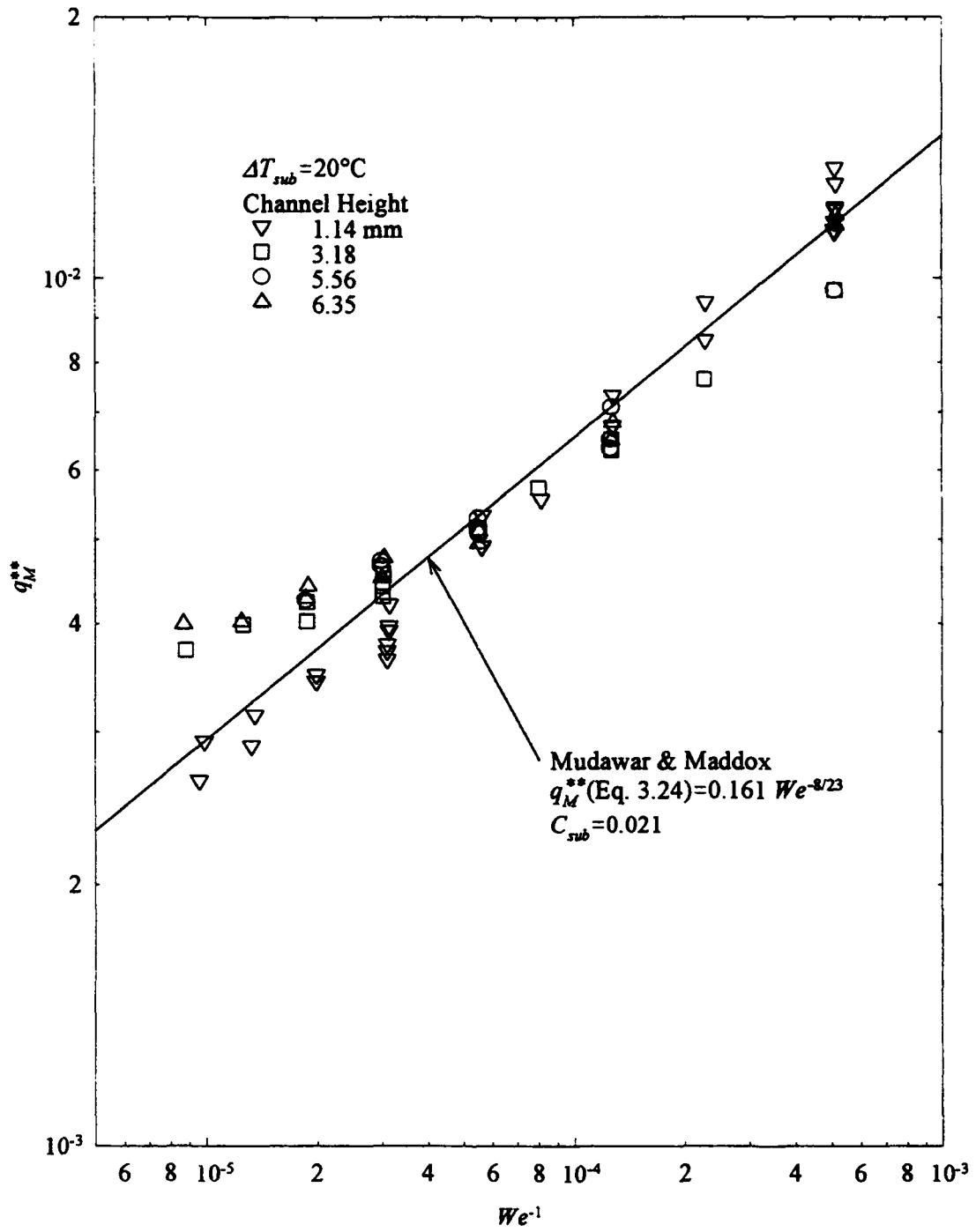


Figure 3.9 Comparison of data with Eq. (3.23).

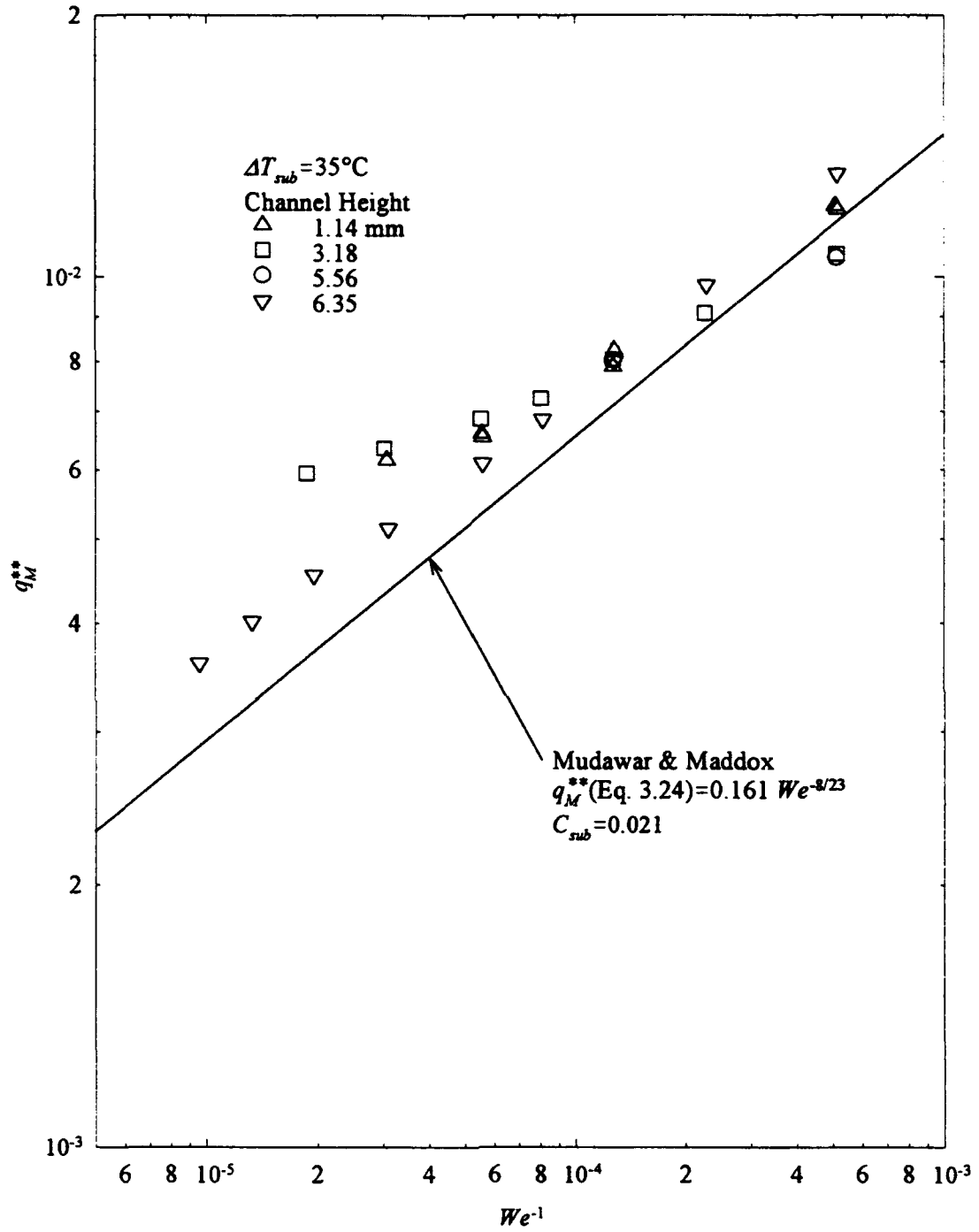


Figure 3.10 Comparison of data with Eq. (3.23).

Eq. (3.24) does not collapse the data with respect to subcooling as well as for the data of Mudawar and Maddox¹⁹. However, the dependence on velocity is in good agreement with that of Mudawar and Maddox¹⁹.

Equation (3.24) indicates a geometry dependence of $(L/D_h)^{1/23}$ on q_M . Thus q_M increases weakly as D_h decreases. Note that this trend is counter to what is generally found for single phase convection. The precise values of $(L/D_h)^{1/23}$ are given in Table 3.1. Table 3.1 indicates that q_M may be expected to increase 7% as the term, $(L/D_h)^{1/23}$, varies from 0.9967 (largest h) to 1.0659 (smallest h). Figure 3.8 clearly indicates that an even greater enhancement is realized over the range of validity of Eqs. (3.23) and (3.24). Much more interesting is the nature of CHF as nondimensionalized in Figs. 3.9 and 3.10. While the data for $h = 3.16, 5.56$ and 6.35 mm compare to previously reported results (Mudawar and Maddox¹⁹ and Leland and Chow¹⁸), the data for $h = 1.14$ mm compares well to Eqs. (3.23) and (3.24) throughout the entire range of We .

To understand why this is true, one must reconsider the CHF mechanism upon which Eqs. (3.23) and (3.24) are based. CHF occurs when the liquid sublayer below the bubble vapor blanket dries out. Eqs. (3.23) and (3.24) are based on a model which balances the mass flow of liquid into the liquid sublayer with the heat flux required to completely vaporize that amount of liquid, (i.e., a dryout model of CHF). Mudawar and Maddox¹⁹ reported that for bulk flow velocities up to 2 m/s, liquid was fed tangential to the surface from the leading edge of the heater. This liquid flowed along the surface through the macrolayer to supply liquid to the nucleation sites. Because the liquid macrolayer shrinks in thickness with the direction of flow, the liquid supply to the most downstream portion of the heater is the most impeded. Thus, dryout initially occurs at the most downstream portion of the heater. This mechanism is illustrated in Fig. 3.4 (a).

At higher velocities, the vapor blanket is much thinner and more uniform in thickness over the length of the heater. Mudawar and Maddox¹⁹ described the existence of vapor blankets prior to CHF that were much smaller in size than the heated surface area. The liquid sublayer beneath these blankets was fed by liquid from above and between the blankets instead of from the leading edge of the heater. This mechanism is

illustrated in Fig. 3.4 (b). Because the sublayer is more uniformly fed over the length of the heater, the transition to CHF is delayed and higher heat fluxes than are predicted by the model for Fig. 3.4 (a) are attained. This may be seen in Figs. 3.9 and 3.10 where for a given $We > 10^4$, the correlation under predicts the data for $h \geq 3.18$ mm.

For the case of $h = 1.14$ mm, the bubble layer thickness is of the same order as h . Thus, the liquid flow from above the vapor blanket is impeded and the first mechanism remains at higher velocities. Note that the two sets of data cross at $We^{-1} = 10^{-4}$, the same point at which the transition from the low to high velocity mechanism occurs. This does not explain the increase of q_M^{**} for $We^{-1} > 10^{-4}$. The vapor blanket is thickest at low velocities and approaches h near CHF for $U = 1$ m/s and $h = 1.14$ mm. A significant fraction of the flow area is thus blocked and the flow may be accelerated by as much as 50%. The data of Fig. 3.8 for $h = 1.14$ mm, $U = 1$ m/s and $h > 1.14$ mm, $U = 1.5$ m/s, indicate by comparison that this may be true. The uncharacteristic scatter in the data for $h = 1.14$ mm cannot be explained except to say that boiling throughout the nucleate boiling regime and near CHF was less stable, causing CHF to be less repeatable.

3.5 Dependence of CHF on velocity for $We < 100$ and $We > 10^4$

Equations (3.23) and (3.24) show that CHF is proportional to $U^{7/23}$. Figures 3.9 and 3.10 show that as We decreases (i.e., velocity increases), q_M^{**} exhibits a weaker dependence on We^{-1} . Thus, q_M is proportional to U at higher velocities. Furthermore, Eqs. (3.23) and (3.24) also imply a weaker dependence on surface tension and more importantly, the heated length, L . For the low velocity CHF mechanism described above, the liquid supply to the most down stream portion of the heater is the most impeded, because the vapor blanket grows in thickness with the direction of flow. Thus, dryout initially occurs at the most down stream portion of the heater. The onset of dryout was seen to occur almost uniformly over the entire width of the heater. For this mechanism, it is easy to see that CHF is inversely proportional to L .

For the high velocity CHF mechanism, there exists vapor blankets prior to CHF that are much smaller in size than the heated surface area. The liquid sublayer beneath these blankets is fed by liquid from between the blankets instead of from the leading

edge of the heater. Because the sublayer is more uniformly fed over the length of the heater, the dependence on L is not as strong as for the low velocity mechanism.

As mentioned above, McGillis et al.²⁸ conducted similar experiments over the velocity and subcooling ranges of 9.6 to 103.9 cm/s and 20 to 40°C respectively. A lower bound of $We > 100$ was suggested for Eqs. (3.23) and (3.24) as a result of their work. They also suggested the following modification to Eq. (3.23) for $We < 20$.

$$q_M^{**} = 0.321 We^{-1/2} \quad (3.25)$$

Figures 3.9 and 3.10 are combined and expanded in Fig. 3.11 to include the correlation of McGillis et al.²⁸. It is interesting to note the overall trend of q_M^{**} with We^{-1} .

3.6 An Improved Correlation

As well developed as Eqs. (3.23) and (3.24) are, they unfortunately do not fit the data as well as desired. The fit may be improved for $We < 10^4$ and the present data by determining new constants, ψ and C_{sub} , however, for $We < 10^4$ (high velocities), the fit is still poor. Part of the problem lies with the transition from a CHF mechanism described by the physical model to one that is not. As Fig. 3.8 shows, CHF correlates strongly with the flow velocity. Because the fit, as shown in Figs. 3.9 and 3.10, degenerates with increasing velocity and the assumed velocity profile gives rise to the exponents of the nondimensional quantities in Eqs. (3.23) and (3.24), shortcomings in the assumed form of the velocity profile were sought. A key assumption in the derivation of Eqs. (3.23) and (3.24) was that the macrolayer thickness at the upstream edge of the heater was much greater than the thickness of the laminar sublayer and thus, the laminar sublayer is a negligible portion of the flow feeding the liquid sublayer. Therefore, the velocity profile of the turbulent core was assumed over the thickness of the liquid sublayer, δ_M .

Specifically, the power-law form was assumed for the sake of simplicity.

However, as noted on page 51, an error was committed in estimating the thickness of the laminar sublayer. Mudawar and Maddox¹⁹ estimated that the sublayer thickness

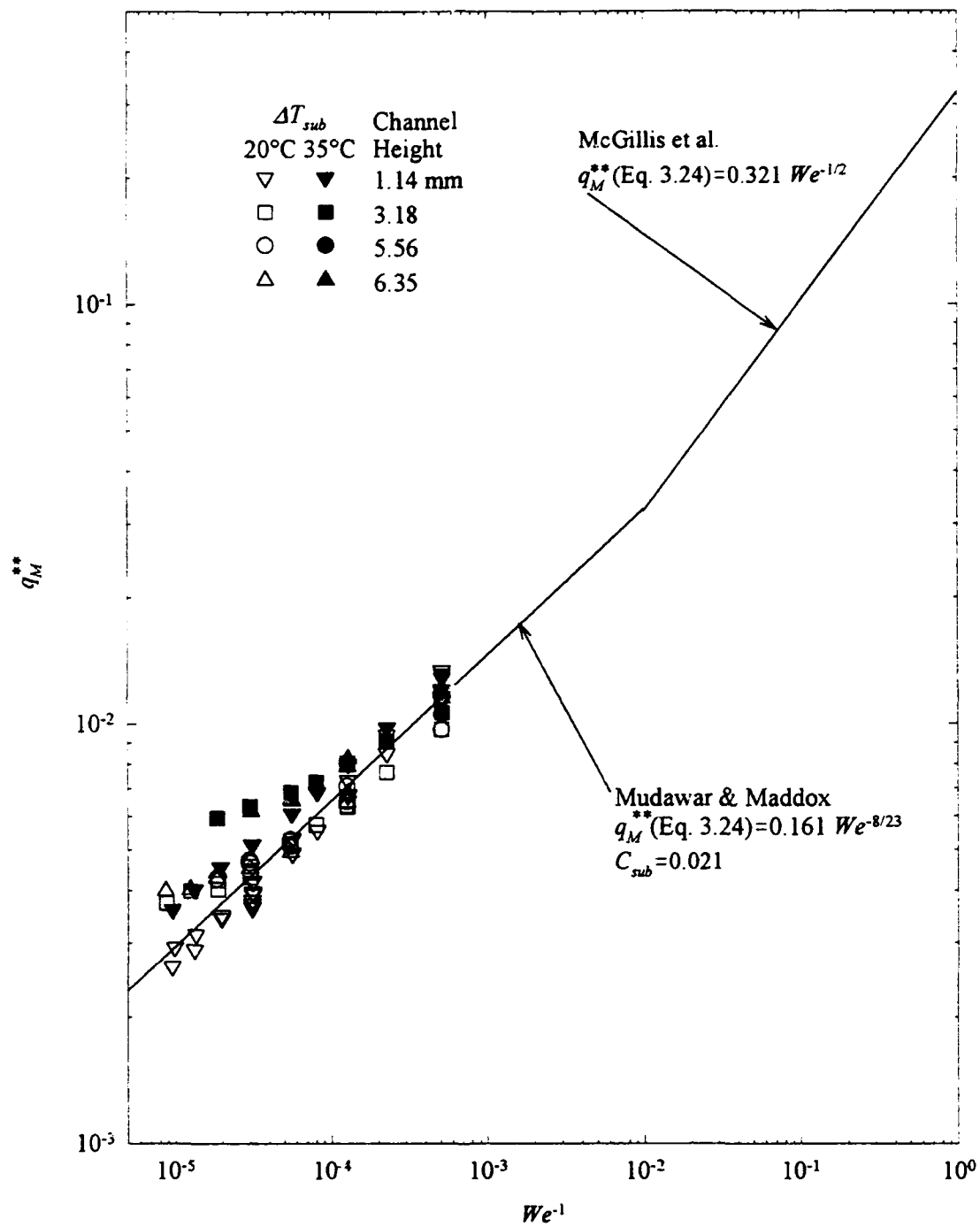


Figure 3.11 Comparison of data with Eqs. (3.23) and (3.27).

did not exceed 0.015 mm for the entire low velocity regime, (0.22 to 2 m/s). Table 3.2 lists the laminar sublayer and buffer layer thicknesses for some representative flow velocities. It can be seen that the laminar sublayer and buffer layer comprise a significant percent of the macrolayer thickness for Mudawar and Maddox's estimated macrolayer thickness of 0.52 mm. The macrolayer thickness estimate was assumed to be equal to the vapor blanket thickness at the upstream edge of the heater at near CHF conditions. The thickness of 0.52 mm is much greater than that visualized by the author, especially for any appreciable degree of subcooling. Admittedly, the author's estimate was obtained by direct visualization and is consequently prone to error. Finally, estimating the macrolayer thickness by Eq. (3.17) gives values that are an order of magnitude less than that estimated by Mudawar and Maddox. Equation (3.17) assumes the power law form of the velocity profile, however.

To use a composite of the appropriate *law of the wall* velocity profiles; (the laminar sublayer, buffer layer, and turbulent core), would yield a correlation so complex that it would be useless. Therewith, if Eqs. (3.23) and (3.24) are rederived by substituting the laminar sublayer velocity profile,

$$u^+ = y^+ \tag{3.26}$$

into Eq. (3.12), an extra term, $Re^{1/4}$, appears in the denominator of Eq. (3.24) and the exponents of the other nondimensional quantities are changed. If the buffer layer velocity profile

Table 3.2. Laminar sublayer and buffer layer thicknesses for geometry of Mudawar and Maddox¹⁹.

Velocity [m/s]	Laminar Sublayer [mm], ($y^+ = 5$)	Buffer Layer [mm], ($y^+ = 30$)
0.22	0.100	0.760
1	0.034	0.202
2	0.015	0.110

$$u^+ = 5 \ln(y^+) - 3.05 \quad (3.27)$$

is substituted into Eq. (3.12), Eq. (3.17) is modified by complex functions of $Re^{-1/4}$ and δ_M that replace the last two factors on the RHS of Eq. (3.17). Because of the shear complexity of the modified Eq. (3.17), further derivation is pointless. Although the correlations obtained by employing these velocity profiles alone are not applicable, the factor of $Re^{1/4}$ in both further implies that the velocity dependence of CHF is not fully described by Eqs. (3.23) and (3.24) and that their shortcomings are related to the assumed velocity profile.

Consequently, two modifications of the existing correlation with respect to velocity were explored: 1) adding the Reynolds number to the denominator of Eq. (3.24) and fitting an exponent to it, and 2) simply fitting a new exponent to the Weber number of Eq. (3.23). A weighted least squares scheme was used to fit the new constants along with new values for ψ and C_{sub} . To determine a baseline correlation for the curved channel, only the straight channel data of $h \geq 3.18$ mm were fit. The index of correlation****, i_{xy} , and the mean absolute percentage error were used to judge the efficacy of these modifications. The index of correlation, (a perfect fit is obtained as $i_{xy} \rightarrow 1$), is calculated only for q_M^* against We^{-1} . Table 3.3 shows that adding $Re^{0.146}$ to the denominator of Eq. (3.24) and finding new values for ψ and C_{sub} reduces the mean error

**** The index of correlation indicates how closely the data points cluster about the regression line. The index of correlation¹³⁴ is defined for the present data as

$$i_{xy} = \sqrt{1 - \frac{\sum_{i=1}^n (q_{M_i} - q_{M_i, \text{calculated}})^2}{\sum_{i=1}^n (q_{M_i} - \bar{q}_M)^2}}$$

The summation in the numerator is related to the standard error and the summation in the denominator is related to the standard deviation.

Table 3.3. Correlation constants and accuracy parameters.

Correlation	$1.052 \psi^{8/23}$	C_{sub}	i_{xy}	$\overline{\text{Error}} [\%]$
Eqs. (3.23) & (3.24)	0.161	0.021	0.85	13.1
Eqs. (3.23) & (3.24)	0.120	0.049	0.88	10.7
Eq. (3.23)/ $Re^{0.146}$	0.021	0.069	0.93	7.7
Eqs. (3.31) & (3.32)	N/A	N/A	0.96	5.7

by about 40% while simply determining new values for ψ and C_{sub} reduces the mean error by only 20%. Note that the exponent of Re is of the same order as the exponent provided by the derivation of Eq. (3.24) using the laminar sublayer velocity profile. The bottom of Fig. 3.12 also shows that this modification models the data well, although the same We^{-1} independence seems to hold at higher velocities.

As mentioned earlier, physical models serve to identify the pertinent dimensionless quantities and expected values of their exponents for correlating CHF data. Monde and Katto¹¹³ considered all the independent variables that play a role in flow boiling and by using the Buckingham Pi theorem, they obtained the following relation.

$$\frac{q_M}{\rho_g h_{fg} U} = C \left(\frac{\rho_f}{\rho_g} \right)^{\alpha_1} \left(\frac{\mu_g}{\mu_f} \right)^{\alpha_2} \left(\frac{\sigma}{\rho_f U^2 L} \right)^{\alpha_3} \left(\frac{\mu_f}{\rho_f UL} \right)^{\alpha_4} \left[\frac{g(\rho_f - \rho_g)L}{\rho_f U^2} \right]^{\alpha_5} \quad (3.28)$$

Viscosity was assumed to have a negligible effect on CHF. Borishanskiy¹³⁵ conducted experiments of pool boiling for an extensive number of fluids. He modified the Kutateladze-Zuber equation to include the effect of viscosity. However, he found the effect of viscosity on CHF to be very small. A similar study has not been done for flow boiling, however, most investigators use Borishanskiy's results to justify ignoring the viscosity terms when deriving a CHF correlation. In addition to viscosity, Monde and Katto also assumed buoyancy forces to be negligible. This is a rational assumption under the conditions of flow boiling where vapor departs from the surface because of shearing action rather than buoyancy forces. Moreover, Willingham and Mudawar⁴⁸ found

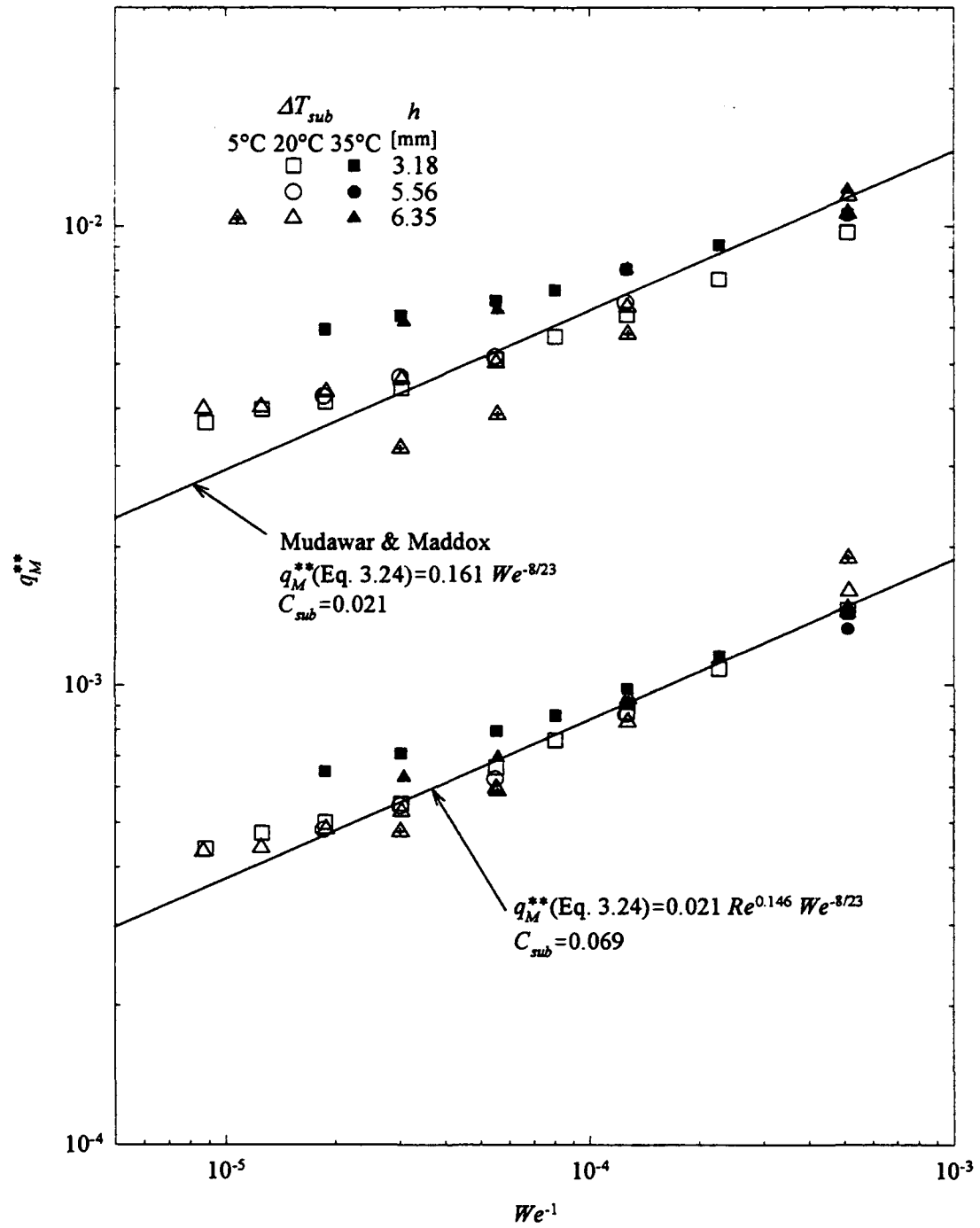


Figure 3.12 Comparison of data with Eq. (3.23) and Re modified Eq. (3.23).

orientation to gravity to be small or negligible for flow boiling over a wide range of conditions. This further indicates that buoyancy forces may be neglected for forced flow boiling. With only the first and third pi groups remaining on the RHS of the equation, Eq. (3.28) takes the form of the theoretically obtained Eq. (3.10). This form of Eq. (3.28) has been very useful for correlating jet impingement, falling film, cylinder in cross flow, and other forced flow boiling CHF data.

The correlation given by the reduced form of Eq. (3.28) was for a jet at saturation temperature. Monde and Katto also used the pi theorem to modify the simplified form of Eq. (3.28) to account for subcooling. The final form is

$$\frac{q_M}{\rho_g h_{fg} U} = C_1 \left(\frac{\rho_f}{\rho_g} \right)^{\alpha_1} \left(\frac{\sigma}{\rho_f U^2 L} \right)^{\alpha_2} \left[1 + C_2 \left(\frac{\rho_f}{\rho_g} \right)^{\alpha_3} \left[\frac{c_p (T_{sat} - T_f)}{h_{fg}} \right]^{\alpha_4} \right] \quad (3.29)$$

Note the similarity of the nondimensional factors of Eq. (3.29) to those of Eq. (3.24) and the absence of the factor in Eq. (3.24) containing D_h . Likewise, the same strategy was followed to develop a correlation for the present straight channel data. By including D_h in the group of independent variables and neglecting the buoyancy factor, $g(\rho_f - \rho_g)$, and only the vapor viscosity, (because Re was previously shown to be an important factor), the following relation was generated.

$$\frac{q_M}{\rho_g h_{fg} U} = C_1 \left(\frac{\rho_f}{\rho_g} \right)^{\alpha_1} \left(\frac{L}{D_h} \right)^{\alpha_2} \left(\frac{\rho_f U D_h}{\mu_f} \right)^{\alpha_3} \left(\frac{\sigma}{\rho_f U^2 L} \right)^{\alpha_4} \left[1 + C_2 \left(\frac{\rho_f}{\rho_g} \right)^{\alpha_5} \left[\frac{c_p \Delta T_{sub}}{h_{fg}} \right]^{\alpha_6} \right] \quad (3.30)$$

Fitting Eq. (3.30) to the data yielded the following correlation

$$q_M^{**} = 0.101 We^{-0.481} \quad (3.31)$$

where

$$q_M^{**} = \frac{q_M / \rho_g h_{fg} U}{\left(\frac{\rho_f}{\rho_g}\right)^{0.167} \left(\frac{L}{D_h}\right)^{0.310} \left(\frac{\rho_f U D_h}{\mu_f}\right)^{0.336} \left[1 + 4.561 \left(\frac{c_p \Delta T_{sub}}{h_{fg}}\right)^{1.392}\right]} \quad (3.32)$$

Figure 3.13 compares Eqs. (3.31) and (3.32) to the original correlation of Mudawar and Maddox, Eqs. (3.23) and (3.24). The data fit the new correlation very well but retain some scatter with reference to subcooling. This scatter is at least partly due to the lack of additional subcooling data at the higher Weber numbers. Thus, the fit is biased with respect to velocity and a subcooling of 20°C. Also of significance is that the scatter increases markedly for $We < 10^4$, the point at which the transition in CHF mechanisms, described in Figs. 3.4(a) and 3.4(b), occurs. Note that the new correlation spans this transition with much less loss of accuracy. This implies that the transition of CHF mechanisms is not abrupt. Table 3.3 also shows that Eqs. (3.31) and (3.32) compare very well against the other alternatives. This correlation is valid over the range $U = 1-7$ m/s, $\Delta T_{sub} = 5-35$ °C, and $\rho_f/\rho_g = 77.7-116.0$.

Finally, the absence of the density ratio in the correction for subcooling of Eq. (3.32) is a consequence of having to fit all of the exponents at once rather than taking the approach of Monde and Katto¹¹³ where the nonsubcooling exponents were first found for the zero subcooling data. In the above case, the two density ratio factors have a high dependency, (an increase in one causes a corresponding decrease in the other), and the curve fit routine will bias one or the other density ratios. The correlation coefficient for this equation was 0.96 and the mean absolute error was only 5.7%. By testing an alternate form of Eq. (3.32), Re was found to indeed be important for correlating the high velocity data. Through examination of Eq. (3.32), it is also apparent that D_h and consequently one nondimensional term, may be eliminated with little or no loss of accuracy. It is retained to maintain consistency with a correction for channel curvature to be developed in the next chapter, however.

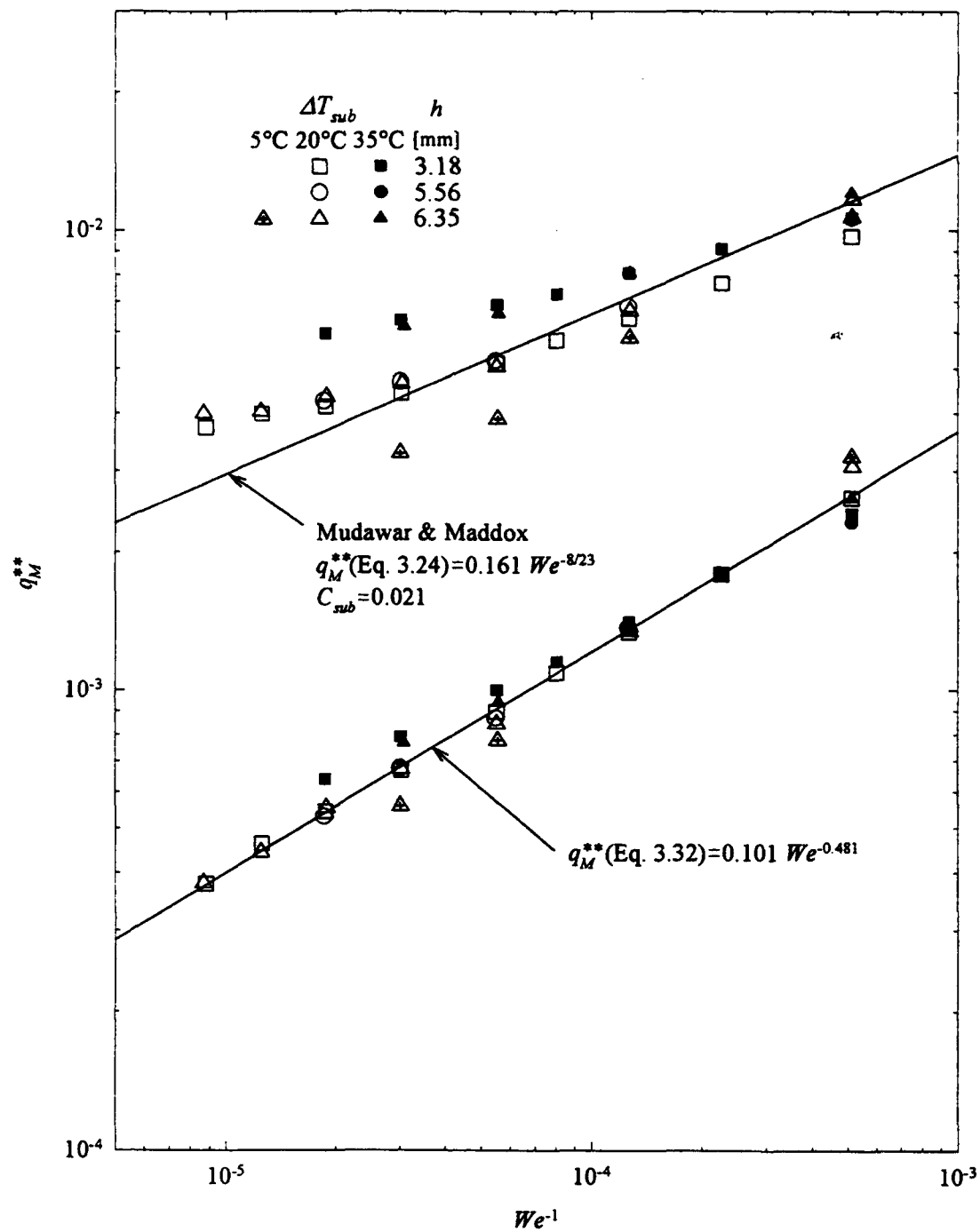


Figure 3.13 Comparison of data with Eqs. (3.23) and (3.31).

3.7 Boiling Incipience

Boiling incipience is generally marked by a sudden and sometimes large (20°C has been reported for some pool boiling tests¹³⁶ where FC-72 was used) temperature excursion. The thermal shock caused by this excursion is of obvious concern to those considering direct immersion cooling for electronics. Boiling incipience is stochastic by nature and unavoidable for a given surface and fluid combination. For the present experiments, the boiling incipience temperature overshoot did not exceed . This maximum occurred at a velocity of m/s and subcooling of 20°C. Temperature overshoot was negligible for the far majority of tests and was less than 1°C for almost all tests.

Incipience generally occurred at a downstream location that was greater than $2/3 L$, ($L = 9.5$ mm), as measured from the upstream edge of the heater. The breadth of the nucleation pattern grew rapidly with increasing heat flux while the front advanced upstream at a slower rate. The surface was fully nucleated at heat fluxes greater than 80% of CHF. As surface roughness was decreased, nucleation was suppressed and heat fluxes greater than 95% of CHF were required to fully populate the test surface. These results are similar to those previously reported^{45,34} and are reported here for later comparison with nonflush heater data. Departure bubble diameters were estimated to be 0.5 to almost 1 mm for $\Delta T_{sub} = 20^\circ\text{C}$ or less. At higher subcoolings the departure diameters were noticeably smaller.

The very low boiling incipience overshoot temperatures are attributed to the fact that the heater surface microstructure is very uniform for the present case and that the present experiments are for flow rather than pool boiling. As discussed in Section 2.4.1, highly wetting FC-72 floods the larger available nucleation sites. Thus the size distribution of nucleation sites is sharply reduced which also limits the range of superheats required to cause nucleation. Because the size distribution is narrow and the surface is very uniform, the probability of nucleation from a given heater location, (i.e., nucleation site), is very nearly the same as for any other location. Thus, for the case of pool boiling where the temperature gradient in the thermal layer is uniform, nucleation at one site is almost immediately followed by nucleation at other sites. The sudden increase

in heat flux causes the temperature of the heater surface to drop sharply upon this occurrence.

Two factors serve to mitigate the incipience overshoot temperature. First, forced convective single-phase heat transfer causes much higher heat fluxes to exist prior to nucleation. Consequently, the additional heat transfer rate due to sudden nucleation is not as large a percentage of the overall heat transfer rate and lower temperature excursions are experienced. Second, for the case of forced convective flow, a stream-wise temperature profile must exist across the heater. Given the uniformity of the surface and the small range of possible nucleating superheats, it is easy to see why nucleation occurs in the vicinity of the most downstream edge of the heater. Thus, a smaller number of sites nucleate simultaneously which yields a much smaller contribution of heat transfer. In summary, for flow boiling the sudden contribution of nucleate boiling heat transfer upon incipience is smaller in magnitude and is also a smaller percentage of the overall heat transfer.

Finally, it must be noted that the high thermal conductivity-capacitance of the copper heater also serves to lessen the incipient temperature overshoot. The limiting case of a very thin heater will be explored in Chapter 6 where it will be seen that the overshoot temperature is greater. This fact can be significant to the application of flow boiling to electronics. For the case of power electronics, heat transfer would occur from a copper pad with a thickness greater than 2 mm. Thus the results for the copper heater are applicable and boiling incipience temperature overshoot is not of concern. However, for the case of logic devices, heat transfer may occur from the silicon or plastic case in which event the low thermal conductivity-capacitance of the case could cause locally high temperature overshoots and subsequent thermal stresses.

3.8 Conclusions

1. Channel height has little effect on CHF until it reaches the same order as the bubble layer thickness. For small h , an increase of q_M at low velocities where the bubble layer is thickest may be due to an increase of velocity. A decrease of q_M for small h , at higher velocities is due to the inhibition of a more effective liquid supply mechanism.

2. The dependence of q_M^{**} on We^{-1} becomes weaker as We^{-1} decreases (i.e., velocity increases), especially for $We^{-1} < 10^{-5}$. Equations (3.23) and (3.24) thus imply that q_M is roughly proportional to U at higher velocities (> 2 m/s) as compared to $U^{7/23}$ for lower velocities (≤ 2 m/s).
3. Including the results of McGillis et al.²⁸, Fig. 3.11 suggests that q_M^{**} is a decaying function of decreasing We^{-1} for We^{-1} less than 1.
4. If Eqs. (3.23) and (3.24) correctly models CHF for $We^{-1} < 10^{-4}$, a weaker dependence of q_M on L is also suggested. This may be explained by a change in the mechanism of liquid supply to the sublayer.
5. The lesser fit of Eqs. (3.23) and (3.24) at high velocities is probably due to neglecting the contribution of the laminar sublayer and buffer layer to the shape of the velocity profile. The We^{-1} range of validity for Eqs. (3.23) and (3.24) may be improved by inclusion of the term, $Re^{0.146}$, to the denominator of Eq. (3.24).
6. Dimensional analysis proved successful in obtaining a correlation, Eqs. (3.31) and (3.32), which fit the data with a mean absolute error of only 5.7%. This correlation is valid over the range $U = 1-7$ m/s, $\Delta T_{sub} = 5-35$ °C, and $\rho_f/\rho_g = 77.7-116.0$.
7. The large temperature excursion associated with pool boiling incipience is nearly absent for the present flow boiling experiments. This is very important when applying boiling heat transfer to electronics cooling because large temperature excursions translate into thermal shock and increased thermal stresses.

Chapter 4

EFFECT OF CHANNEL CURVATURE ON CHF

The effect of stream-wise curvature of the flow path on CHF will be addressed in this chapter. Channel curvature was explored in an effort to increase the CHF for a given flow velocity and subcooling. The effects of channel curvature are manifested in at least three ways: 1) increased bubble buoyancy due to induced acceleration of the liquid, 2) increased fluid circulation due to secondary flow, and 3) increased wall shear stresses which yield higher velocity fluid near the wall. Channel curvature also increases the pressure at the radially outward wall. Increased pressure causes an effective increase of subcooling. The effect of increased pressure at the wall was small for the present experiments due to the limited range of accelerations, $a/g = 4$ to 100, and small fluid height, $h = 3.18$ to 6.35 mm. Furthermore, the effect of this small pressure rise was eliminated by adjusting the subcooling.

The effect of acceleration or increased gravity on boiling heat transfer was first reported in the late 1950s when Gambill and Greene³ sought to determine if the enhanced heat transfer reported for single-phase convection in swirl flow extended to boiling heat transfer. Their work was motivated by the high heat flux cooling requirements for nuclear reactors and rocket nozzles. In their experiments, swirl was induced on an annulus of liquid which flowed through a resistively heated tube. Extraordinarily high heat fluxes of over 17 kW/cm² were achieved with water as the coolant. Gambill and Greene³ attributed the effectiveness of their strategy to the increased inward radial transport of bubbles caused by increased buoyant forces due to the centrifugal force on the fluid. They achieved more than a three-fold increase over a comparable straight geometry for a maximum induced acceleration of 8,390 g. Other investigators^{137,138} including Gambill¹³⁹, obtained similar results for tubes with twisted tape inserts. Recently, Leslie et al.⁴ achieved heat fluxes of 25 kW/cm² for water flowing in the conical anode of an x-ray source. They estimated that the acceleration of the liquid reached a maximum of $a/g = 50,000$. Although, their reported CHF is probably overestimated due to neglecting the effect of heat spreading, it is nonetheless impressive.

Winovich and Carlson¹⁴⁰ demonstrated heat fluxes up to 14 kW/cm² for an interesting application of curved channel boiling to the cooling of a 60-MW arc-heater. The arc-heater was used to simulate space shuttle reentry conditions. The benefits of boiling heat transfer with stream-wise curvature has been well established qualitatively and quantitatively for specific systems.

The advent of the space program in the early 1960s and the desire to understand the role of acceleration in increasing CHF spawned a number of studies investigating the effect of gravity on pool boiling. In these early pool boiling studies, Merte and Clark¹⁴¹ found that for accelerations up to $a/g = 21$, heat transfer was enhanced for low heat flux boiling while there was no effect on high heat flux boiling. They reasoned that enhanced natural convection augmented the low heat flux boiling. At high heat fluxes, the augmentation was a much smaller percentage of the overall heat transfer and copious amounts of vapor at the surface impeded the increased single-phase convection. Costello and Adams¹⁴² found that CHF followed the acceleration trend ($q_M \propto a/g^{1/4}$) predicted by the Kutateladze-Zuber equation, Eq. (3.1), for $a/g > 10$. At lower accelerations they found that CHF was proportional to a/g to some power less than 1/4. Beckman and Merte¹⁴³ and Marto and Gray^{144,145} later conducted photographic studies of the pool boiling process under large accelerations. These studies found that as acceleration increased, bubble departure diameters decreased and frequency of bubble departure increased.

Gray et al.¹⁴⁴ obtained results for accelerations up to $a/g = 475$. Under these very high accelerations, cessation of nucleate boiling even occurred for some cases. Higher heat fluxes were required to sustain a given heat flux as acceleration increased presumably due to the reduced number of nucleation sites. Under these conditions single-phase heat transfer was a significant contributor and convective cells were visualized. The results of these experiments are somewhat plagued by the induced pressure system variable. Recently, Ulucakli and Merte¹⁴⁶ performed a similar, but much more controlled study investigating the combined effects of subcooling and acceleration on pool boiling. They found the same qualitative results of the above studies with increasing acceleration, that is reduced wall superheats at low heat fluxes and increased

wall superheats at high heat fluxes. Like previous investigators, they theorized that enhanced single-phase natural convection makes a significant contribution to the overall heat transfer at low heat fluxes. However, at higher heat fluxes they postulated that increased buoyancy increases the microlayer thickness, thus reducing the heat transfer from each nucleation site. Consequently, higher wall superheats were required to nucleate more sites to make up for the loss in heat transfer. As was intended by the investigators, the above results lend some understanding to the effect of acceleration on boiling heat transfer and CHF. However, these results cannot be directly extended to the present case.

Very little literature is available for flow boiling with geometries similar to the present situation. The closest semblance is that of boiling in uniformly heated tube coils and channels. These geometries have been studied in an interest to enhance heat transfer in various heat exchanger applications. Unlike the case for swirl flow boiling in straight tubes, secondary flows have been determined to be an important factor in CHF enhancement. This is not to say that secondary flow does not exist in the former, in deed it does. As a tube flow with a typical laminar or turbulent velocity profile enters a bend, the higher velocity fluid in the core attains a larger radial momentum. Two counter rotating recirculating vortices are established in the tube, (see Fig. 4.1). The core fluid moves to the radially outward wall and then migrates along the pipe wall to the radially inward area of the wall. Secondary flows are typically less vigorous for turbulent flow because of the flatter velocity profile. The flow was turbulent, ($1.7 \times 10^4 < Re < 1.5 \times 10^5$), for the entire range of conditions of this investigation. Figure 4.2 shows the secondary flow pattern for a square curved duct as obtained numerically by Hur et al.¹⁴⁷ The RHS of Figs. 4.2 (a) and (b) show the azimuthal velocity profile. Whether or not either of these flow patterns exists for the present case is unknown. For the current geometries, $4 < R/h < 8$, and the channels are rectangular with $0.12 < h/w < 0.24$. The much smaller h/w will cause the secondary flow pattern to be suppressed. It is interesting to note that Fig. 4.2 (b) shows a presumably adverse secondary flow pattern. The azimuthal flow pattern of Fig. 4.2 (b) shows that some advantage may be gained by moving the heated surface from the centerline towards one side of the channel.

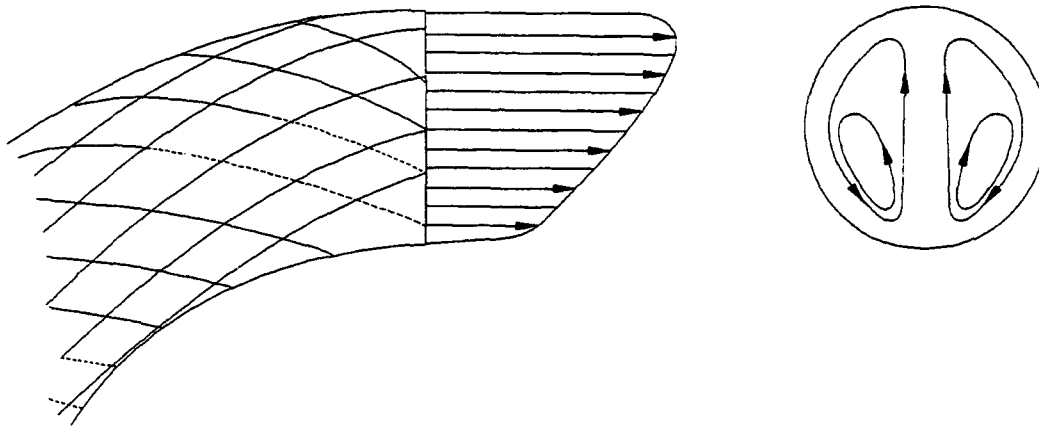
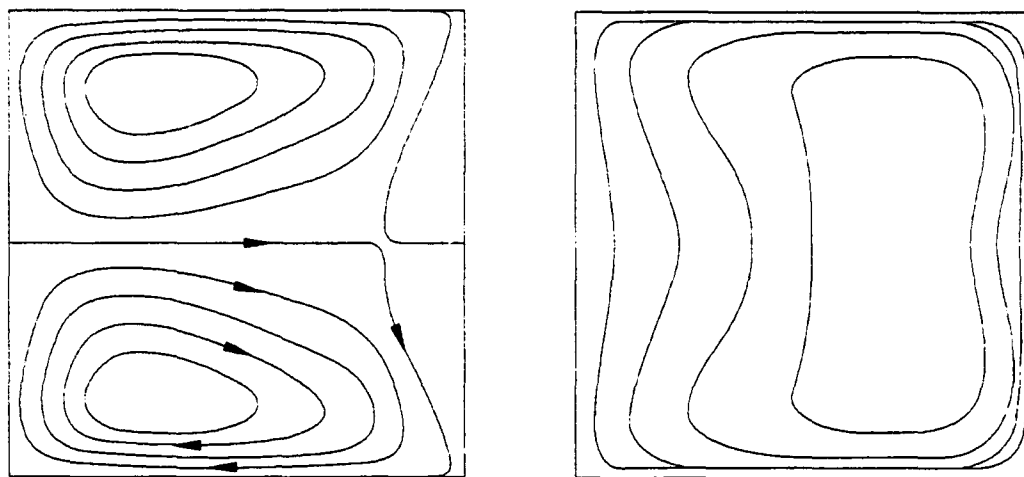
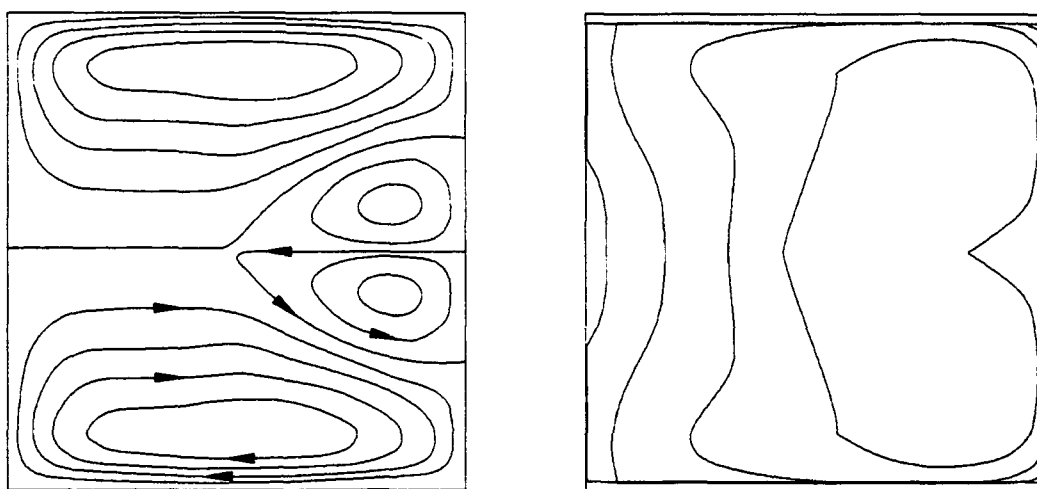


Figure 4.1 Secondary flow pattern in a curved pipe.



(a)



(b)

Figure 4.2 Secondary flow pattern and azimuthal velocity contours in a square duct.¹⁴⁷
 (a) $R/h = 125$, (b) $R/h = 15.63$. Center of curvature is to the left.

The study of Owhadi et al.¹⁴⁸ is representative of those for flow boiling in tube coils. CHF occurs at different circumferential locations as the flow progresses axially down the tube. In general, CHF first occurs on the tube quadrants which separate the radially inward and outward most quadrants. For a helix shaped tube coil with the helix oriented vertically, these locations would be the top and bottom of the tube. With nucleate boiling sustained on the radial inward and outward quadrants, the flow progresses down the tube until dryout (CHF) of the radially inward quadrant occurs. Finally, some distance from this point, complete dryout of the tube occurs. The fact that boiling can be simultaneously maintained on the radially inward and outward surfaces while the top and bottom surfaces experience film boiling is explained by secondary flow. The centrifugal acceleration of the liquid-vapor mixture causes the denser liquid to be deposited on the outer wall of the tube. What liquid that does not evaporate is carried by the same secondary flow to the inner most part of the tube bend. At this location, the bifurcation of the counter rotating vortices and a smaller axial flow velocity allow the liquid to pool on the surface. High velocity vapor shears liquid from the surface of the slow moving liquid pooled on the wall, and centrifugal acceleration of the drops causes them to be redeposited on the outer wall, thus repeating the cycle. Consequently, the inner and outer most surfaces remain wetted for a longer period of time. Although the majority of the liquid remains on the inner wall, the fast moving thin film on the outer wall allows higher heat fluxes to be achieved at that location. CHF has been increased by up to a factor of six over a comparable straight geometry.¹⁴⁹

Miropol'skiy and Pikus²³ obtained CHF data for water flowing in a heated 360° tube coil. They also found that with increasing heat input, CHF first occurred on the inner radius and then (at a much higher heat input), on the outer radius of the bend. For subcooled and low quality flow, CHF (averaged over the tube circumference), was less than that for a straight tube of equal diameter, however. At higher qualities, results similar to those of Owhadi et al.¹⁴⁸ were obtained. Jensen and Bergles¹⁵⁰ noted the same reverse in the relative difference of curved and straight tube CHF. For the low quality and subcooled conditions, they further found that the ratio of curved to straight tube CHF decreased with increasing subcooling and decreasing bend radius (increasing centrifugal

forces). They explained that contrary to the high quality mechanism explained above, the recirculating motion of predominantly liquid flow caused the vapor to be pushed to the walls. The vapor coalesced at the walls caused the wetting of the surface to be impeded and subsequently reduced the CHF. As subcooling is decreased, the net vapor increases and eventually becomes the dominant flow, thus reversing the trend.

Hughes¹⁵¹ has obtained results which are most directly applicable to the present experiments. Hughes' experiment consisted of a 90° bend of square cross section with a thin heater on each of the walls normal to the radial direction. Results were obtained for only one heater operating at a time. In these experiments the channel dimensions were 12.7 × 12.7 mm in cross section and 82.6 mm in radius. Hughes does not give the heater dimensions, but they are estimated to be 3 mm wide by 100 and 120 mm long for the inner and outer surfaces, respectively. By comparison, the heater dimension of the present experiments is 9.5 by 9.5 mm square. Most interestingly, Hughes' results imply that CHF becomes independent of a/g for accelerations ratios greater than 20. Furthermore, the ratio of outer wall CHF to straight channel CHF decreases from roughly 1.6 to 1.3 for subcoolings of 10 and 43°C, respectively. Although immaterial to the present study, Hughes found that the ratio of inner wall CHF to straight channel CHF varied from 0.8 to 0.7 for the same range of subcoolings. It may be concluded from the forgoing studies that curved channel boiling is most effective when there is significant vapor generation. Significant vapor generation only occurs with long heated lengths. Therefore, the CHF conclusions for the longer heaters of Hughes' study cannot be directly applied to the short heater length results of the present study, but are more applicable than the conclusions drawn from uniformly heated tube coils and tubes with twisted tape inserts.

CHF in rotating films has also been studied. Mudawar et al.¹⁵² studied a geometry simulating an idealized gas-turbine blade cooling passage. Water flowed radially outward in a rectangular channel which rotated about one end. A small heater provided enough energy to attain heat fluxes slightly over 1kW/cm² at 5.4 atm. and $a/g = 146$. Galloway and Mudawar¹⁵³ studied CHF for heat sources mounted on the circumference of a drum in which a pool of liquid was stirred to such a degree that a thin film of liquid

formed on the drum wall. Their efforts were directed at enhanced heat transfer for electronics cooling. However, their values of CHF for a supposed film velocity were lower than would be expected by comparison to results for the current straight channel geometry and similar velocity and subcooling. By virtue of the experimental apparatus, their investigation was more system oriented rather than basic in nature. They did find that CHF was independent of heater length for lengths of 12.7 to 50.8 mm. The results of the former study were found to be weakly dependent on velocity which is quite contrary to the present results. The data of the latter study depend on a number of system variables, such as fill volume and number of stirrer blades, and consequently cannot be directly applied to the present study.

The precursor to the present study was that reported by Gu et al.²⁴ They obtained results for a simulated electronic chip in a curved rectangular channel, specifically, channel #1 of Table 3.1. CHF was found to increase 8 and 44% over results for a straight channel at 20°C subcooling and velocities of 1 and 4 m/s respectively. Their results were somewhat higher than those of the present study due to an assumption of the system pressure. This error caused higher than reported subcoolings at higher velocities which consequently caused the CHF values to be higher than what they should have been for the reported subcooling. In an effort to determine the effects of centrifugal force, secondary flow, and buoyancy on CHF, the present results have been obtained for the three test sections with dimensions shown in Table 3.1.

4.1 Experimental Apparatus - Curved Channel Details

Although the experimental apparatus was described in detail in Chapter 2, Section 2.1, a few details pertinent only to the curved channel experiments will be discussed. Figure 2.2 shows the general design of the three test sections or flow channels. The flow was turbulent in all cases, ($1.7 \times 10^4 < Re < 1.5 \times 10^5$). The entrance length is greater than 20 hydraulic diameters in all cases to insure fully developed flow. The curved section heater was placed 135° from the bend entrance where the secondary flow is believed to be fully developed. Literature on turbulent flow in curved geometries is scarce and data for channels of square cross section is even more scarce. Squire¹⁵⁴ indicates that for

turbulent flow in a curved pipe of 8.9-cm diameter and 106.7-cm radius of curvature, the flow is fully developed after 120°. For an identical geometry and turbulent flow of air ($Re = 2.36 \times 10^5$), Rowe¹⁵⁵ finds that the flow is fully developed at 90°, (his measurements were taken at 45° intervals). Wattendorf's¹⁵⁶ data imply that fully developed secondary flow exists at 150°. His results were obtained for turbulent flow of air ($Re = 1.57 \times 10^5$) in a 5-cm by 90-cm rectangular channel with a mean radius of curvature of 22.5 cm. Finally, the detailed measurements of Eskinazi and Yeh¹⁵⁷ of turbulent flow ($Re = 7.42 \times 10^4$) in a 7.6-cm by 118.1-cm rectangular channel of 87.6-cm radius of curvature, show that the stream-wise velocity profile changes very little after 108° and that the flow is fully developed at 172°. Thus, the nature of secondary flow, (two counter rotating vortices in the plane perpendicular to the stream-wise direction), is established well before 90° and is well developed at 135°.

A flexible coupling at the intake of the channel allowed the channel to be rotated. This was done so that the heater surfaces could be maintained in a vertical orientation with the flow direction being upward. The author as well as Willingham and Mudawar¹³³ found that the orientation to gravity had little effect on the results for the straight section heater and velocities greater than 2 m/s, though. Considering the high radial acceleration forces, the effect of orientation on the curved section heater is certainly negligible, at least for velocities greater than 2 m/s.

The bulk temperature was measured at a point 40 to 50 mm upstream of the straight section heater. Temperature drop from the point of measurement to the test heater was negligible as confirmed by measurements taken at the test section exit with both heaters off. Static pressure measurements were made at the channel wall at a distance of 35 mm upstream of each straight section heater leading edge. This distance was 33 mm and 23 mm for the 56.4-mm and 28.6-mm radius curved sections, respectively. The saturation temperature at the heater surface is based on the static pressure measurement, thus a small error in saturation temperature is incurred because of the pressure drop from the point of measurement to the heater surface. This error is slightly greater for the curved section due to the developing secondary flow and induced acceleration.

The error induced by the pressure taps being upstream of the heater was estimated using the Blasius relationship,

$$f_{str} = 0.316 Re^{-1/4} \quad (4.1)$$

and that of Ito³⁰,

$$\frac{f_{cur}}{f_{str}} = \left[Re \left(\frac{D_h}{2R} \right)^2 \right]^{1/20} \quad (4.2)$$

for the friction factors of the straight and curved sections, respectively. The calculated pressure drop error ranges from 70 Pa at $U = 1$ m/s to 2.36 kPa at $U = 5$ m/s. This range was nearly the same for both the straight and curved sections of each channels because the pressure drop distance in the curved sections was shorter to compensate for the larger friction factor. For the channels where $h \geq 5.56$ mm, the error at $U = 5$ m/s was 1.21 kPa. Using the Clausius-Clapeyron equation, Eq. (2.3), the resulting error in saturation temperature reaches an average maximum of less than 0.5°C for both the straight and curved sections. Because the error is small and the correction factor would vary for each geometry, flow rate, and subcooling; and considering the uncertainty of applying Ito's³⁰ equation, no correction of T_{sat} for pressure drop was made. The uncertainty of the pressure measurement itself, was only 5 Pa.

4.2 Experimental Results

The boiling curves shown in Figures 4.3 to 4.5 for the curved channel do not vary in characteristic form from those shown in Figs. 3.5 to 3.7 for the straight channel. The notable difference is the extended nucleate boiling regime, (the NBR comprises the first three regions defined by Gaertner⁴⁹ see Fig. 3.1). Figures 4.6 to 4.8 directly compare the boiling curves of the curved and straight channels. The fact that the NBRs coincide is an indication that the surface properties of the straight and curved section heaters are nearly the same. Figures 4.6 to 4.8 also show that as velocity increases the relative difference

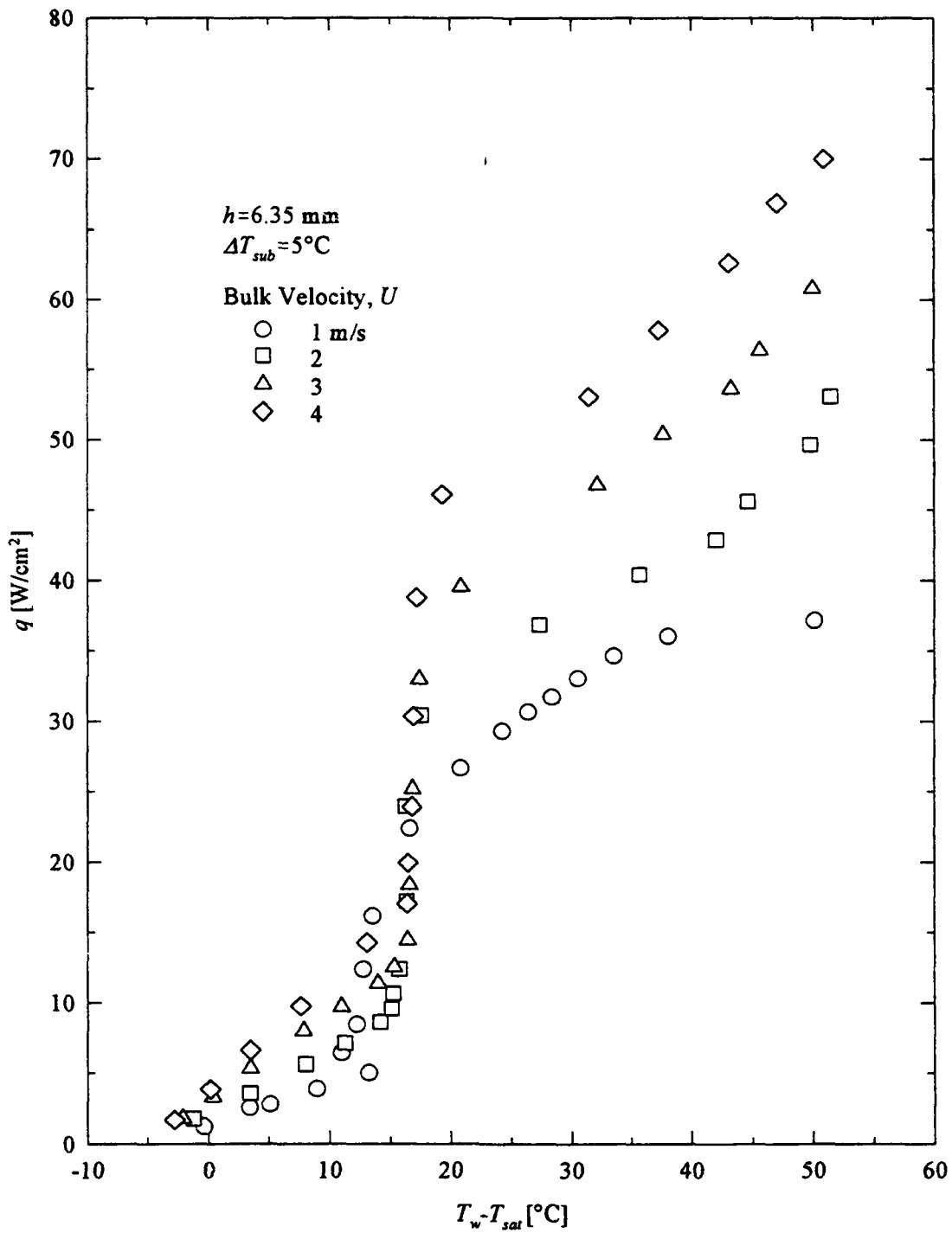


Figure 4.3 Heat flux versus wall superheat for curved channel and 5°C subcooling.

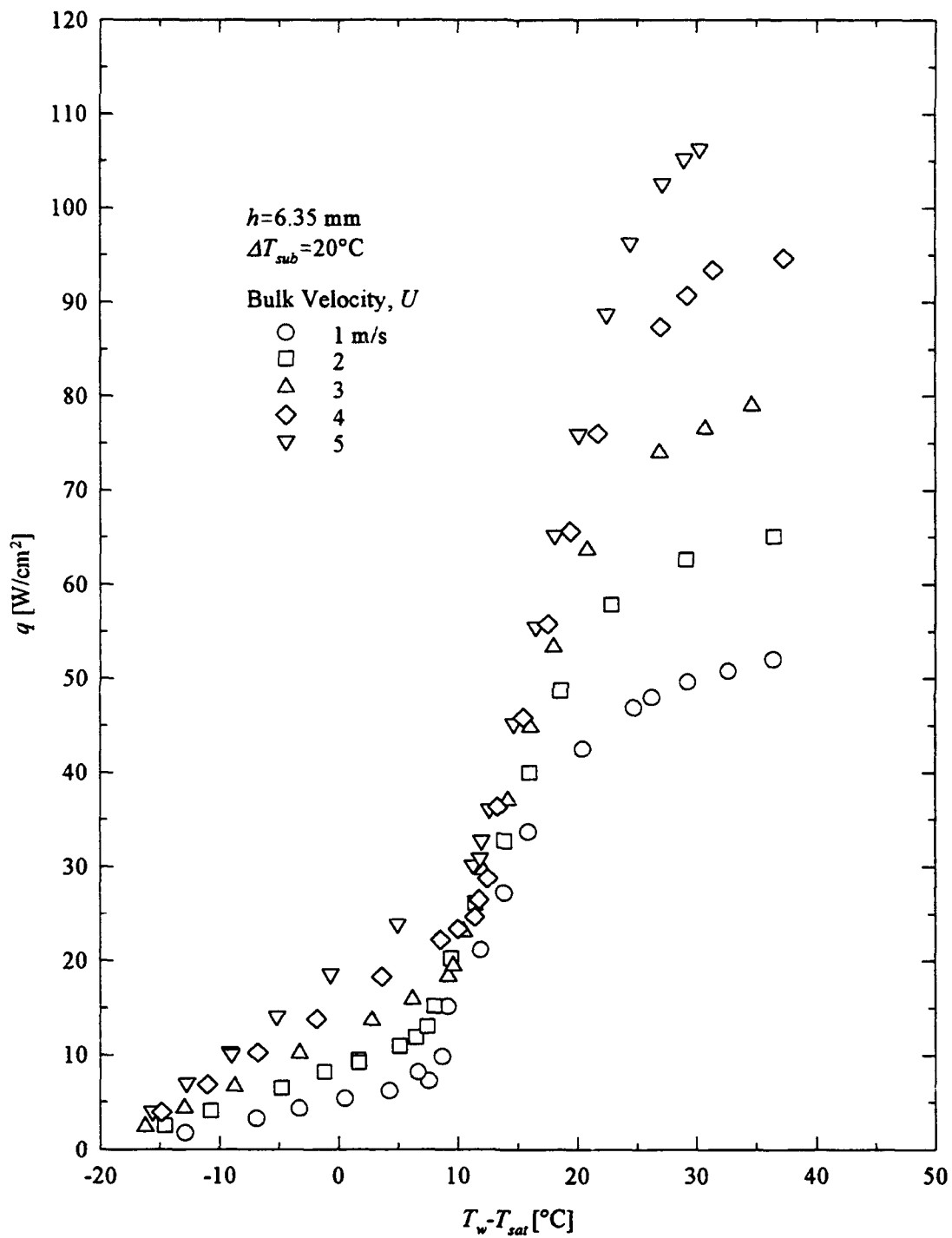


Figure 4.4 Heat flux versus wall superheat for curved channel and 20°C subcooling.

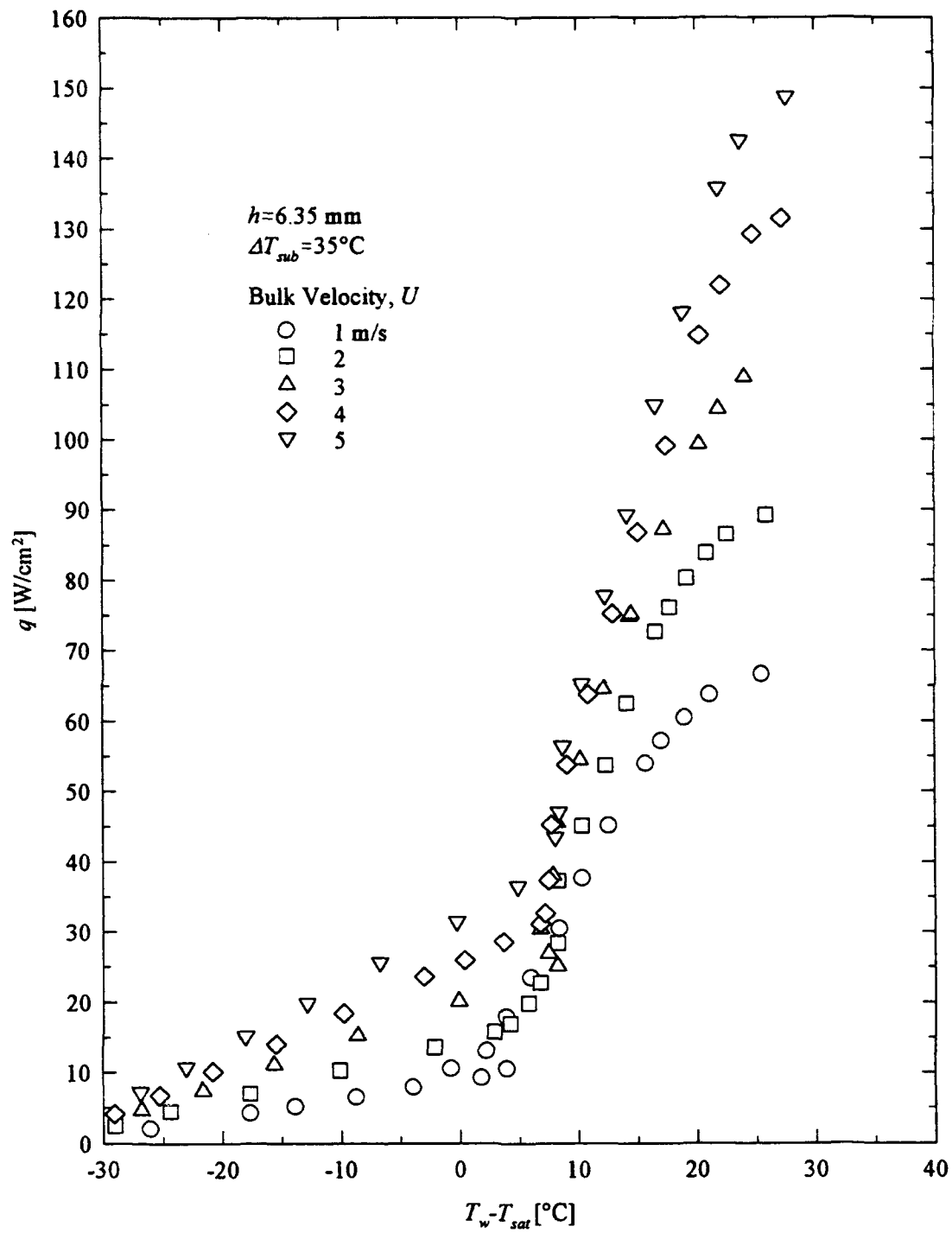


Figure 4.5 Heat flux versus wall superheat for curved channel and 35°C subcooling.

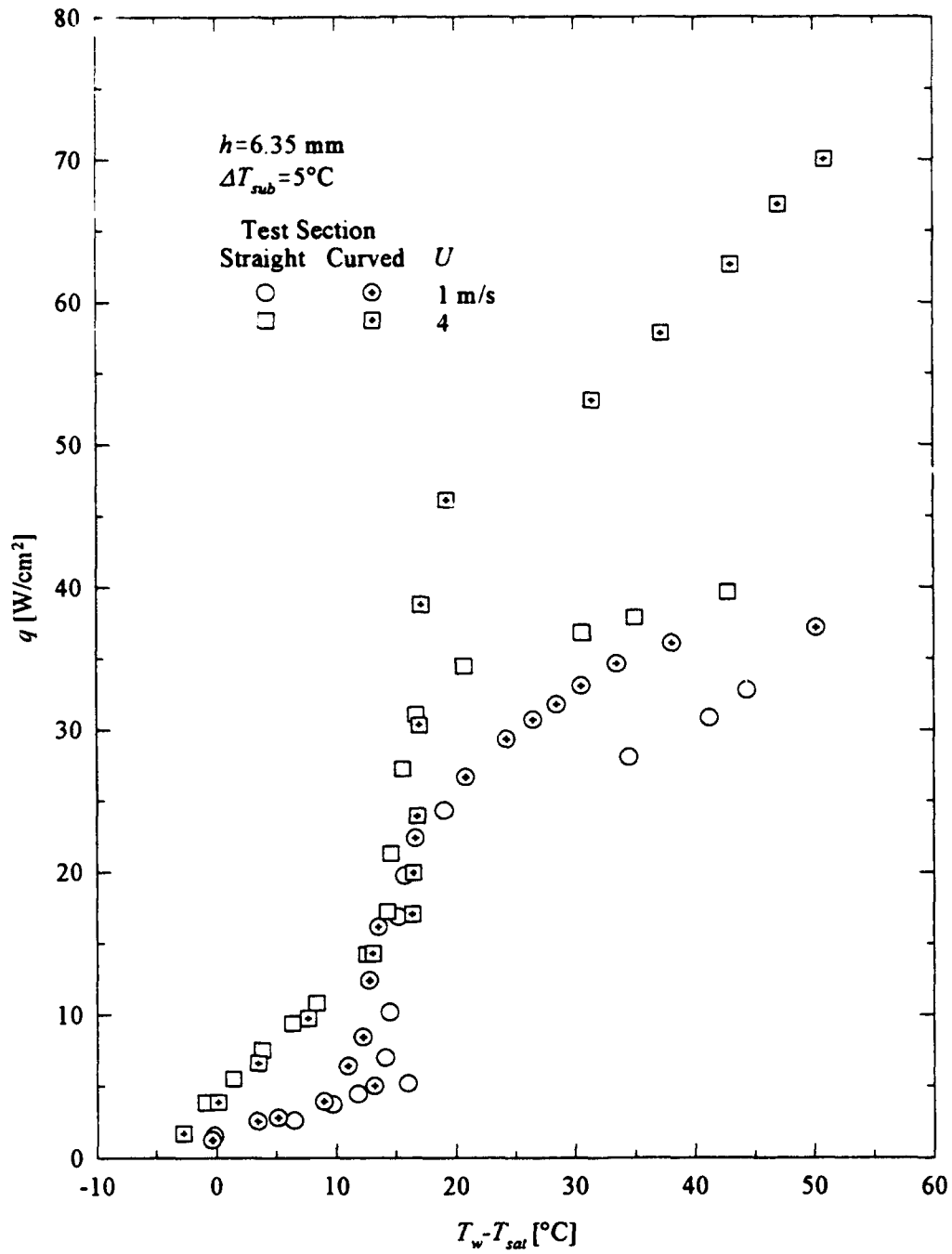


Figure 4.6 Comparison of straight and curved channel boiling curves for $\Delta T_{sub} = 5^\circ\text{C}$.

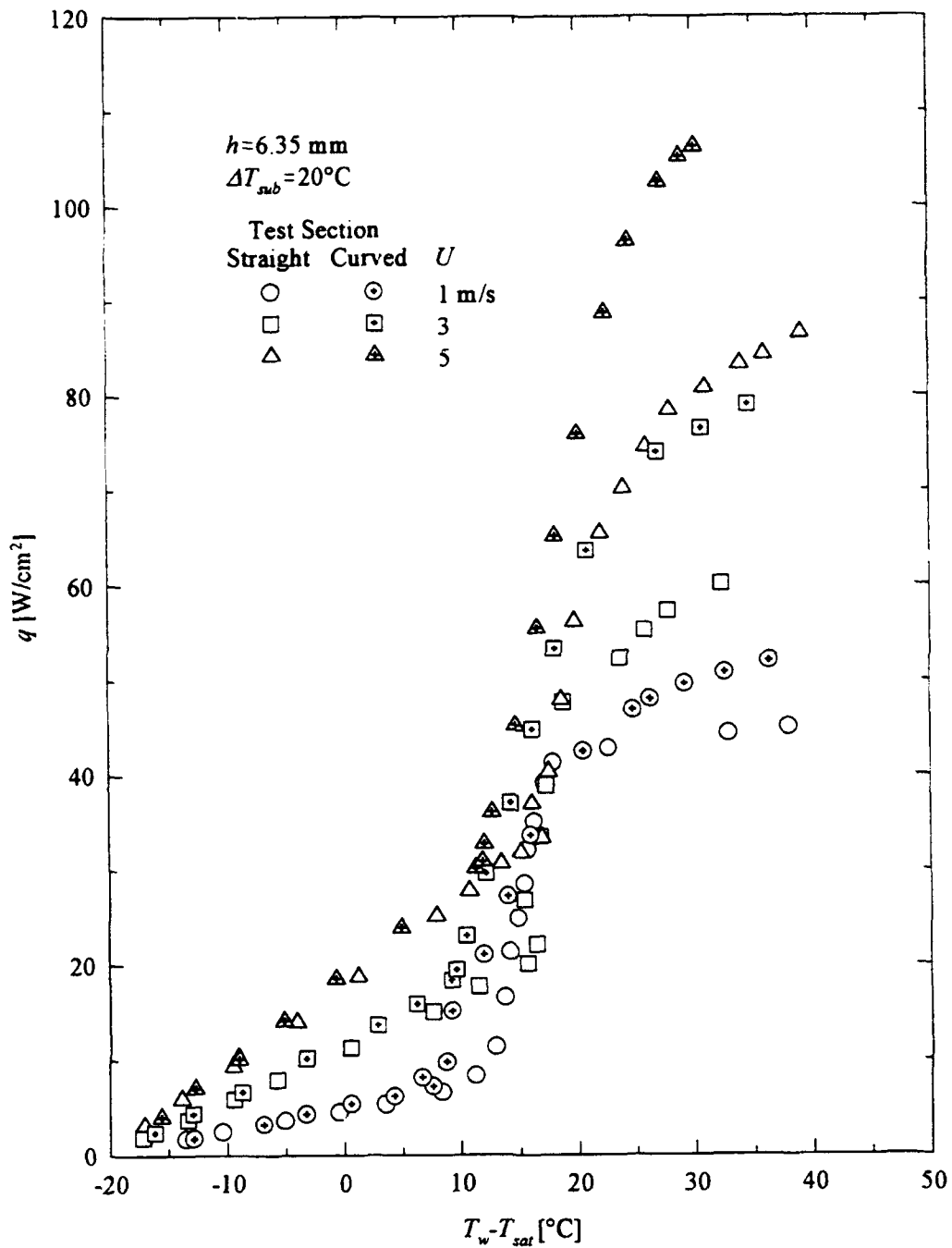


Figure 4.7 Comparison of straight and curved channel boiling curves for $\Delta T_{sub} = 20^\circ\text{C}$.

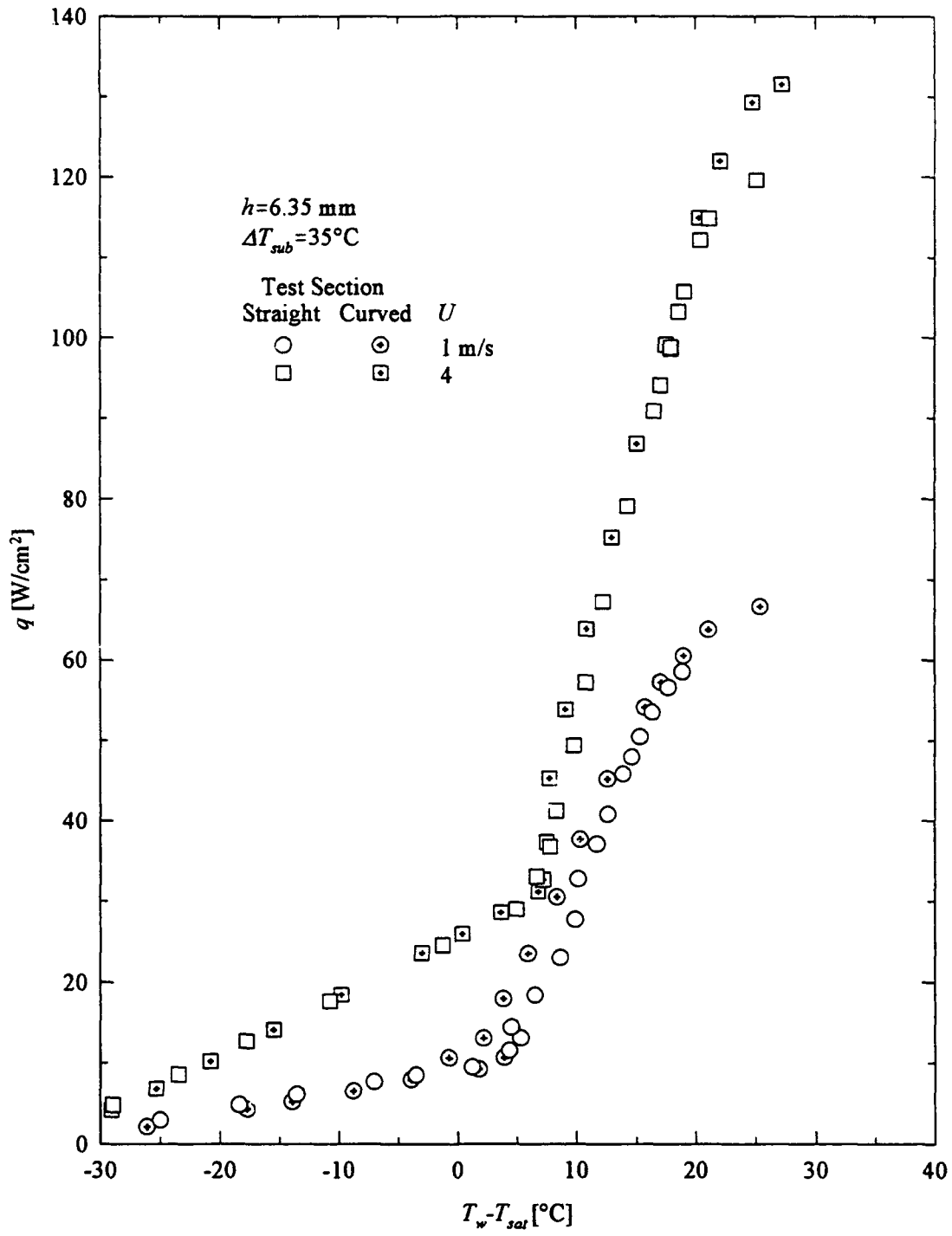


Figure 4.8 Comparison of straight and curved channel boiling curves for $\Delta T_{sub} = 35^\circ\text{C}$.

between straight and curved test section CHF's also increases. These figures also show that as subcooling increases, the relative difference in CHF decreases. Figure 4.9 shows more clearly how CHF varies with subcooling, flow velocity and channel geometry. Figure 4.10 shows the same data plotted against Eqs. (3.23) and (3.24). It may be seen that the curved channel data follow the same general trend with We as the straight channel data. For the purpose of clarity, the straight section data are the average of those values for $h = 3.18, 5.56$ and 6.35 mm and the curve section data are the average value for each velocity and subcooling. It should be noted that heat flux is based on the exposed heated surface rather than the cross-sectional area for the curved section heater. This correction is small however, because the ratio of the surface area to the cross-sectional area is only 1.004.

In all cases but one, channel curvature has a positive effect on CHF. Channel curvature has a detrimental effect for $R = 28.6$ mm, $h = 3.18$ mm, and $\Delta T_{sub} = 35^\circ\text{C}$. The results of Gu et al.²⁴ show that compared to the data of Fig. 4.9, much greater increases were obtained for velocities of 3 and 4 m/s. Their results may be in error, however, due to the investigators' assumption that the test section pressure was constant and equal to the ambient pressure plus the static head of the fluid. Although this assumption is acceptable for low flow rates, the absolute system pressure can increase by as much as 0.5 atm for a flow velocity of 5 m/s. This would lead to greater than 10°C under reporting of the subcooling. Nonetheless, this error would occur for both the straight and curved section heaters, thus lending some credibility to their results.

The effects of channel curvature on nucleate boiling manifest in three ways: 1) increased buoyant forces, 2) the establishment of secondary flow, and 3) increased wall shear stresses on the outer wall which yields a higher fluid velocity gradient near the wall. Increased buoyant forces can cause the vapor to escape from the heated surface more rapidly, thus improving the ability of liquid to wet the surface. This is the mechanism to which Gambill and Greene³ attributed their extremely high heat fluxes. Because CHF occurs as a result of liquid flow being impeded by the bubble layer, it was concluded that increased buoyant forces would cause the bubbles to leave the surface much more quickly thus increasing the CHF. For the present experiments, buoyancy is a

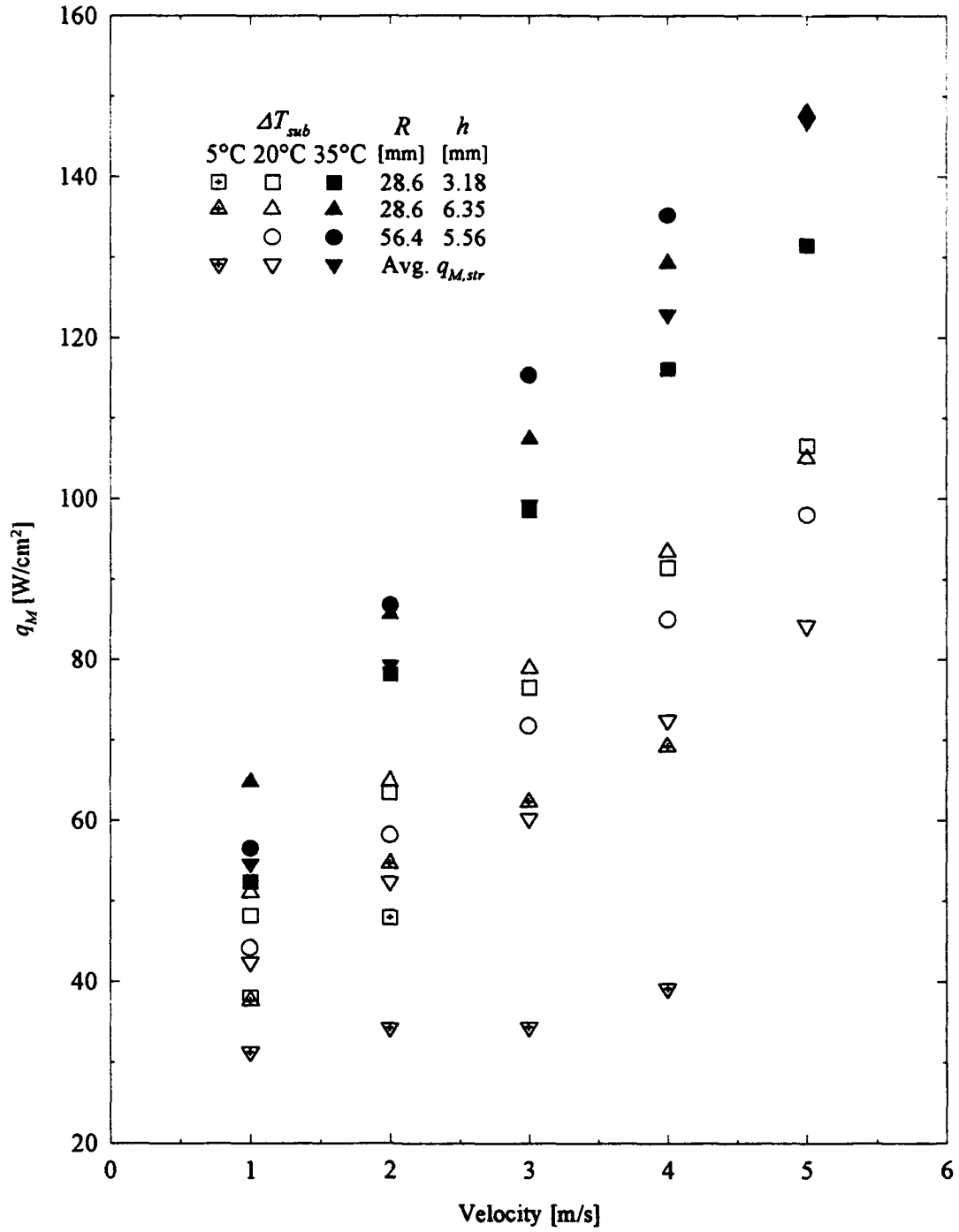


Figure 4.9 Comparison of CHF for straight and curved test sections.

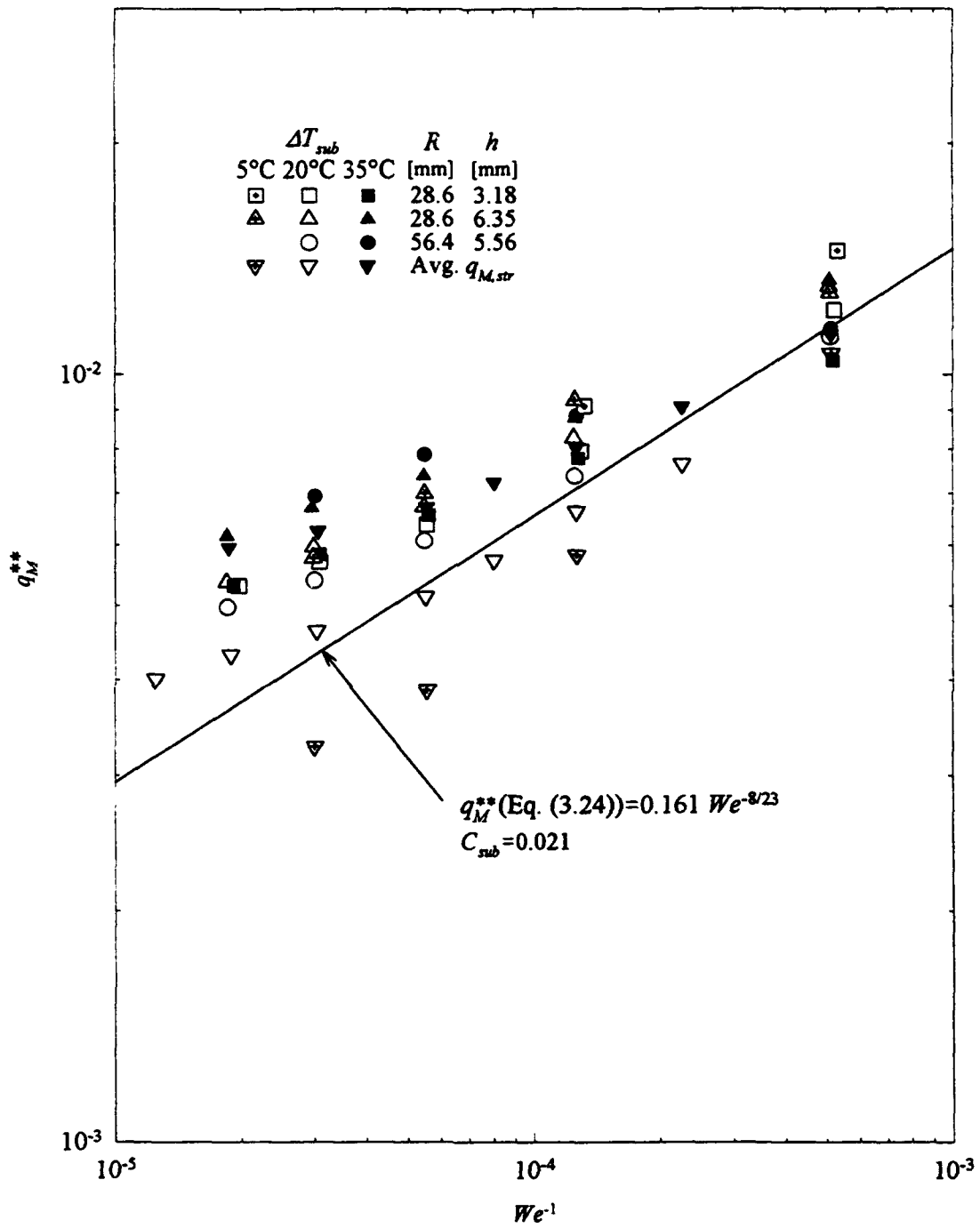


Figure 4.10 Comparison of straight and curved section data with Eq. (3.23).

function of U^2/R . Large buoyant forces may also have a detrimental effect on CHF. As a result of pool boiling experiments under high acceleration, Ulucakli and Merte¹⁴⁶ have postulated that increased buoyant forces cause attached bubbles to elongate and thus increase the microlayer thickness below the bubble. This theory was used to explain the increase of wall superheat at higher levels of heat flux for increasing gravity. A reduction of wall superheat with increasing gravity was found at low levels of heat flux. Although their investigation did not include the effects on CHF, an increased wall superheat could cause premature dry out of the sublayer.

Another manifestation of curved channel flow is secondary flow. When a fluid enters a curved duct, the sudden change in direction causes high velocity, large momentum fluid in the core to be driven radially outward toward the heated surface. This condition aids in driving liquid through the bubble layer to the wall, but may also tend to drive bubbles back towards the wall. Although it is a weak indicator of turbulent secondary flows, the Dean number,

$$K = Re \sqrt{\frac{D_h}{2R}} \quad (4.3)$$

is still sometimes used in turbulent single-phase heat transfer correlations. For a given velocity, K is 2.6 and 1.75 times greater for $R = 28.6$ mm and $h = 6.35$ mm than for $R = 28.6$ mm and $h = 3.18$ mm, and $R = 56.4$ mm and $h = 5.68$ mm, respectively. Finally, channel curvature causes higher velocity gradients at the outer wall. Thus, higher velocity fluid feeds the sublayer for the curved channel as compared to the straight channel for the same bulk velocity. Higher velocity fluid near the wall provides improved wetting of the surface and therefore, increases the CHF. This third consequence of curved channel flow can be accounted for by a modified version of the Mudawar and Maddox¹⁹ model. Equations (3.23) and (3.24) may be rederived considering the velocity profile for the curved channel.

Velocity data for curved channels of rectangular cross section are very scarce and a *law of the wall* does not exist for the curved channel. Marris¹⁵⁸ found that Reynolds

similarity of the stream-wise velocity profiles does exist for a square channel with a mean radius to width ratio (R/h) of 5.9 and $Re = 4.2 \times 10^4$ to 1.39×10^5 . But experiments for a smaller mean radius to width ratio of 2.1 showed that Reynolds similarity of the velocity profiles was lost. The mean radius to width ratios of the current experiments are 10.1, 9.0, and 4.5 for channels 1, 2, and 3, respectively and a similar range of Re . Ellis and Joubert¹⁵⁹ have also shown experimentally that velocity profiles for the curved channel do follow the *law of the wall* up to $y^* = 200$ for values of Ru_r/ν greater than 4×10^4 . Note that as $R \rightarrow \infty$, the straight flow velocity profile is obtained. For the current experiments, Ru_r/ν ranges from 5×10^3 to 2×10^4 which will cause the velocity profile to depart from the *law of the wall* at a y^* less than 200. Despite this, Table 4.1 shows that the wall coordinate equivalent to $y^* = 200$ extends well past the point where the velocity profile is considered important, (i.e., the macrolayer thickness), especially for velocities of 1 to 2 m/s, (the valid range of Eqs. (3.23) and (3.24)). Table 4.1 also shows that neglecting the laminar sublayer and buffer layer velocity distributions is a much better assumption for the present geometry than for that of Mudawar and Maddox.¹⁹

Table 4.1. Velocity layer thicknesses for channel #2.

Velocity [mm]	Laminar Sublayer [mm], $y^*=5$	Buffer Layer [mm], $y^*=30$	Limit of Turbulent Core [mm], $y^*=200$
1	0.02	0.12	0.798
2	0.011	0.064	0.428
3	0.007	0.045	0.297
4	0.006	0.034	0.229
5	0.005	0.028	0.187

Proceeding similar to the method described in Chapter 3, page 51, a derivation of a curved channel counterpart to Eqs. (3.23) and (3.24) is briefly described as follows.

First a sublayer dryout criteria is written as

$$q_M L = \rho_f (c_p \Delta T_{sub} + h_{fg}) \int_0^{\delta_M} u dy \quad (4.4)$$

where δ_M is the liquid sublayer thickness that is completely transformed to vapor. The velocity profile is obtained from the power-law form of the turbulent core velocity profile or

$$u^+ = 8.56 y^{+1/7} \quad (4.5)$$

where

$$u^+ = \frac{u}{u_\tau} = \sqrt{\frac{C_{f_{cur}}}{2}} \quad (4.6)$$

At this point, the effect of wall curvature is introduced through Ito's³⁰ relation for the curved pipe friction factor, Eq. (4.2). Using the Blasius solution, Eq. (4.1), and assuming $C_f = f/4$, Eq. (4.4) may be integrated to obtain

$$\frac{q_M}{U \rho_g h_{fg}} = 1.183 \left(\frac{\rho_f}{\rho_g} \right) \left(1 + \frac{c_p \Delta T_{sub}}{h_{fg}} \right) \left(\frac{L}{D_h} \right)^{1/7} \left(\frac{\delta_M}{L} \right)^{8/7} \left[Re \left(\frac{D_h}{2R} \right)^2 \right]^{1/35} \quad (4.7)$$

where the last bracketed term on the RHS is the only change from the straight channel derivation, Eq. (3.17). Note the similarity of the last bracketed term on the RHS to the Dean number, Eq. (4.3). The remaining unknown, δ_M , is obtained from Eq. (3.21) which is independent of the flow geometry*, or

$$\frac{\delta_M}{L} = \psi \left(\frac{\rho_f}{\rho_g} \right) \frac{\frac{\sigma}{\rho_f U^2 L}}{\left(\frac{q_M}{U \rho_g h_{fg}} \right)^2} \left(1 + C_{sub} \frac{\rho_f c_p \Delta T_{sub}}{\rho_g h_{fg}} \right)^2 \quad (4.8)$$

* The induced acceleration acts normal to the heater surface. Thus, the effect of acceleration on the Helmholtz type instability of the vertical vapor columns is neglected.

where again, ψ and C_{sub} are constants. Combining Eqs. (4.7) and (4.8) gives

$$q_M^{**} = 1.052 \psi^{8/23} We^{-8/23} \quad (4.9)$$

where

$$q_M^{**} = \frac{q_M}{U \rho_g h_{fg}} \quad (4.10)$$

$$\left(\frac{\rho_f}{\rho_g} \right)^{15} \left(\frac{L}{D_h} \right)^{1/23} \left[1 + \frac{c_p \Delta T_{sub}}{h_{fg}} \right]^{7/23} \left[1 + C_{sub} \frac{\rho_f c_p \Delta T_{sub}}{\rho_g h_{fg}} \right]^{16/23} \left[Re \left(\frac{D_h}{2R} \right)^2 \right]^{1/115}$$

Note that Eq. (4.9) is identical to Eq. (3.23) and that the addition of the last bracketed term in the denominator of Eq. (4.10) is the only difference from Eq. (3.24). Although any quantity to the power 1/115 would appear insignificant, Re is very large relative to the other terms in the denominator. To see the effect of the curvature term on q_M directly, the last bracketed term in Eq. (4.10) is evaluated and presented in Table 4.2 as $It^{1/115}$ **

It can be seen that not much difference can be expected over the range of geometries and velocities explored even though the aforementioned Dean number and buoyancy forces change dramatically, (cf. Table 4.2). The values of $It^{1/115}$ indicate an increase of q_M of only 5-8% over the range of velocities, subcoolings and geometries explored. Figure 4.11, (top plot), shows the data of Fig. 4.10 replotted using Eqs. (4.9) and (4.10) for the curved channel data. The data are only slightly closer to the correlation, thus illustrating the limited ability of Eq. (4.10) to account for channel curvature.

** The author does not wish to imply that there is an "Ito number." The definition

$$It = Re \left(\frac{D_h}{2R} \right)^2$$

is used merely for the sake of convenience and "It" seems appropriate for nomenclature.

The previously mentioned three effects of channel curvature on CHF are coupled and may work with or against each other in enhancing the CHF. Further complicating the understanding of the effects of channel curvature is the fact that a transition in the liquid supply mechanism occurs within the range of velocities studied. Nonetheless, in order to increase buoyant forces, secondary flow, or the velocity gradient near the outer wall, either D_h must be increased or R must be decreased. Neither alternative is attractive from a manufacturing point of view. Increasing D_h will yield a large flow channel, thus increasing pumping power, and reducing R may necessitate making a chip with a curved surface.

Figure 4.12 shows more clearly the effects of channel curvature and subcooling on the CHF. As subcooling decreases, the increase in $q_{M,cur}$ over $q_{M,str}$ increases. For $\Delta T_{sub} = 20^\circ\text{C}$, the percent increase of $q_{M,cur}$ over $q_{M,str}$ for the two 28.6-mm channels is roughly twice that of the 56.4-mm radius. If secondary flow is considered to enhance CHF, the results for channel #1 ($R = 56.4$ mm) should be greater than those for channel #2 and less than those for channel #3. The effects on CHF of secondary flow and wall shear stresses should not change appreciably with the level of subcooling. Buoyant forces do change with subcooling, however. As subcooling increases, bubble departure sizes decrease, thus causing buoyant forces to decrease. All of this implies that buoyant forces are the dominant contributor to increased CHF at lower subcoolings.

It may also be seen that in general, for a given subcooling and geometry the effect of buoyancy decreases with increasing velocity for $U > 3$ m/s. This may be due to

Table 4.2 Change of velocity profile, buoyancy, and secondary flow with velocity.

Parameter →	$It^{1/115}$			a [m/s ²]			$K \times 10^{-3}$		
Channel →	#1	#2	#3	#1	#2	#3	#1	#2	#3
$U = 1$ m/s	1.048	1.048	1.064	18	35	35	9.9	6.6	16.4
2	1.055	1.054	1.070	71	140	140	20.1	13.3	33.1
3	1.059	1.058	1.074	160	315	315	30.6	20.6	50.4
4	1.062	1.061	1.077	284	559	559	41.8	27.8	68.8
5	1.064	1.063	1.080	443	874	874	53.7	34.8	88.5

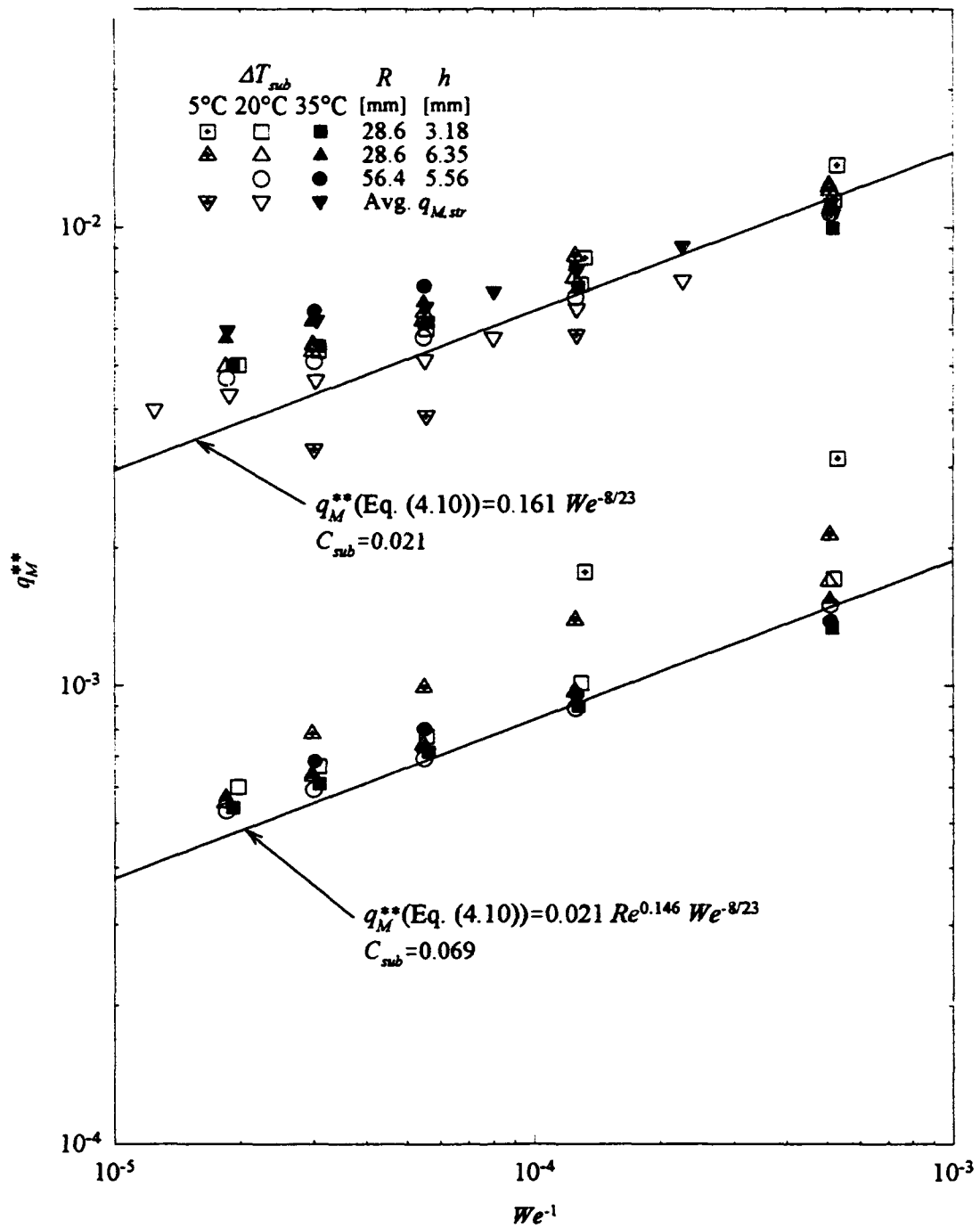


Figure 4.11 Comparison of data to Eqs. (4.9), (4.10) and Re modified Eq. (4.10).

thickening of the bubble microlayer, the effects of which were discussed above. Alternatively, increasing secondary flow may be forcing bubbles back towards the surface, thus impeding the liquid supply mechanism. Finally, the transition from increasing to decreasing percent enhancement occurs near the velocity for which there is a transition in the liquid supply mechanism. It is therefore difficult to draw any conclusions for this trend.

Figure 4.12 also shows that wall curvature has less of an effect at higher subcoolings. This is most likely due to the larger contribution of single-phase heat transfer. Unlike water, and to a lesser extent R-12, FC-72 has a low latent to sensible heat ratio, 3.8 and 2.2 for $\Delta T_{sub} = 20$ and 35°C , respectively. Thus, any enhancement in boiling heat transfer will have less of an effect as subcooling is increased. For $\Delta T_{sub} = 35^\circ\text{C}$, Fig. 4.12 shows that the relative degree of enhancement attributed to the various geometries is different from that for $\Delta T_{sub} = 20^\circ\text{C}$. For this subcooling, the large radius channel shows the largest degree of enhancement. The two geometries with larger channel heights, (i.e., larger secondary flows), show the greatest degree of enhancement. At a subcooling of 35°C , the bubble departure size is the smallest and buoyancy forces will consequently have the least effect. Therefore, the positive effects of secondary flow on the significant single-phase heat transfer may outweigh the negative effects of secondary flow on nucleate boiling heat transfer. There is no explanation for the seemingly anomalous behavior at $U = 1$ m/s and $\Delta T_{sub} = 35^\circ\text{C}$ for the channel with $R = 28.6$ mm and $h = 6.35$ mm.

In summary, the positive effects of channel curvature are most pronounced at lower subcoolings where buoyant forces are the greatest. The two channels with smaller radii of curvature show the greatest enhancement at lower subcoolings even though secondary flows and wall shear stresses would indicate otherwise. This further implies the importance of buoyant forces at lower subcoolings. At high subcooling, the positive effects of channel curvature on CHF diminish and channel curvature may even be detrimental. The positive effects of secondary flow on an increased single-phase heat transfer component appear to outweigh the negative effects of secondary flow on two-

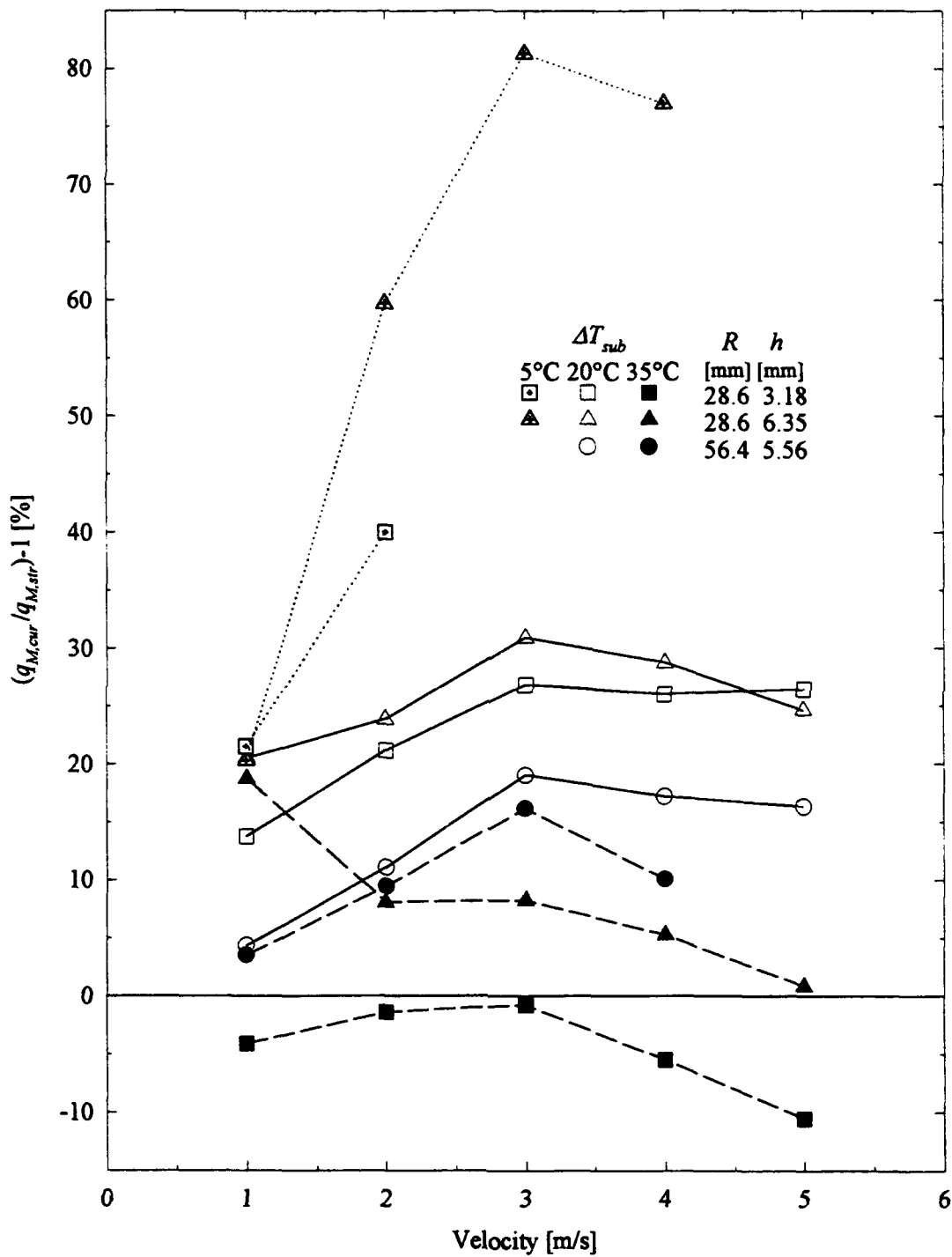


Figure 4.12 Relative difference of $q_{M,str}$ and $q_{M,cur}$

phase heat transfer at high subcooling. This implies that an optimal combination of radius of curvature and channel height exists at high subcooling.

4.3 An Improved Correlation for Curved Channels

In Chapter 3, the correlation given by Eqs. (3.23) and (3.24) was substantially improved by including the term $Re^{0.146}$ in the denominator of Eq. (3.24). Unfortunately, Table 4.3 and the bottom of Fig. 4.11 show that the same modification to the curved channel correlation, Eq. (4.10), yields less impressive results, particularly with the correlation of q_M'' to We^{-1} . The plot of the data in the bottom of Fig. 4.11 shows that almost all the data fall above the correlation line. Because the data fall predominantly above the prediction, but only slightly for larger subcoolings, a low i_{xy} and a low mean error are both achieved. Note that while the high subcooling data fit well, there is a glaring deficiency of the modified Eq. (4.10) to correlate the low subcooling data. This confirms that the effects of secondary flow are dominant at high subcooling while buoyancy is dominant at lower subcoolings. One cannot truly expect Eqs. (4.9) and (4.10) to fully account for the effects of curvature since there is no buoyancy term or secondary flow term in either. Thus an empirical correlation is sought.

Channel curvature introduces one new independent variable, R . Consequently, a correction to the straight channel correlation for channel curvature is sought in a form

Table 4.3 Correlation constants and accuracy parameters.

Correlation	$1.052 \psi^{8/23}$	C_{sub}	i_{xy}	$\overline{\text{Error}} [\%]$
Eqs. (3.23) & (3.24)	0.161	0.021	0.85	13.1
Eqs. (3.23) & (3.24)	0.120	0.049	0.88	10.7
Eqs. (3.23) & (3.24)/ $Re^{0.146}$	0.021	0.069	0.93	7.7
Eqs. (3.31) & (3.32)	N/A	N/A	0.96	5.7
Eqs. (4.9) & (4.10)	0.161	0.021	0.87	13.3
Eqs. (4.9) & (4.10)/ $Re^{0.146}$	0.021	0.069	0.75	11.4
Eqs. (3.31), (4.16), & (4.17)	N/A	N/A	0.99	4.5

similar to that for subcooling in Eq. (3.30) since the straight channel correlation must be obtained as $R \rightarrow \infty$. Once again employing the Pi theorem with the inclusion of R and $a(\rho_f - \rho_g)$ to account for buoyancy, and neglecting the independent variables not necessary for correcting for curvature yields

$$\varepsilon_{cur} = \left\{ 1 + C_{cur} \left(\frac{\rho_f U D_h}{\mu_f} \right)^{\alpha_1} \left(\frac{D_h}{2R} \right)^{\alpha_2} \left(\frac{a(\rho_f - \rho_g)L}{\rho_f U^2} \right)^{\alpha_3} \left(\frac{\rho_f}{\rho_g} \right)^{\alpha_4} \right. \\ \left. \times \left[1 + C_{buoy} \left(\frac{c_p \Delta T_{sub}}{h_{fg}} \right)^{\alpha_5} \right] \right\} \quad (4.11)$$

where ε_{cur} is the correction for channel curvature to be multiplied by the denominator of Eq. (3.32). Note that with the substitution of a for g in the third term on the RHS, the Richardson*** number, that this term becomes independent of velocity. A further modification of Eq. (4.11) must be made because the data of Fig. 4.12 show that curvature is inversely proportional to the subcooling which is represented by the last term on the RHS, the Jakob number. Therefore the exponent of the Jakob number, α_5 , will be negative and the equation will not make physical sense for zero subcooling. As mentioned earlier, the effect of increasing subcooling is to reduce the bubble departure diameter which results in reduced buoyancy forces. Furthermore, the bubble departure diameter would be more suitable than the heated length in the third term on the RHS of Eq. (4.11). Direct substitution would not be correct though, because the bubble departure diameter is not an independent variable. However, the bubble departure diameter is often given by correlations of the form¹⁶¹

*** The Richardson number is used in analyzing the stability of stratified flows and is sometimes called the stratification parameter.¹⁶⁰ The present situation where liquid flows over a vapor blanket is an extreme case of stratified flow.

$$d_d \propto C \left(\frac{c_p (T_w - T_{sat})}{h_{fg}} \right)^\alpha * \text{Other Terms} \quad (4.12)$$

As subcooling decreases, $T_w - T_{sat}$, the wall superheat, increases while the other terms in Eq. (4.12) change relatively little. Equation (4.12) thus indicates that d_d and ΔT_{sub} are inversely proportional as noted above. Because the wall superheat changes little with velocity, (cf. Figs. 4.3 to 4.4), the following approximation may be made

$$(T_w - T_{sat}) = -m \Delta T_{sub} + n \quad (4.13)$$

where m and n are positive constants. Substituting Eq. (4.13) into the wall superheat term of Eq. (4.12) gives

$$\frac{c_p (T_w - T_{sat})}{h_{fg}} = -m Ja + \frac{nc_p}{h_{fg}} \quad (4.14)$$

where the last term on the RHS may be assumed constant, for the present experiments. Equation (4.14) indicates the proper form for the subcooling term of Eq. (4.11). To simplify Eq. (4.11), Re and the hydraulic diameter to radius ratio were grouped to give the form It found in Ito's equation, (see Footnote ***). Incorporating the above changes, Eq. (4.11) becomes

$$\varepsilon_{cur} = 1 + C_{cur} It^{\alpha_1} Ri^{\alpha_2} \left(\frac{\rho_f}{\rho_g} \right)^{\alpha_3} [n^* - Ja]^{\alpha_4} \quad (4.15)$$

where $n^* = nc_p / m h_{fg}$ is assumed constant. Adding this correction to the denominator of Eq. (3.32) and fitting the constants to the curved channel yields a correlation coefficient of 0.99 and a mean absolute error of only 4.5%, (see Table 4.3). Thus, Eq. (3.32) may now be rewritten as

$$q_M^{**} = \frac{q_M / \rho_g h_{fg} U}{(\rho_f / \rho_g)^{0.167} (L/D_h)^{0.310} Re^{0.336} [1 + 4.561 Ja^{1.392}] \epsilon_{cur}} \quad (4.16)$$

where the correction for curvature is

$$\epsilon_{cur} = 1 + 0.086 It^{0.027} Ri^{1.013} (\rho_f / \rho_g)^{1.206} [0.746 - Ja]^{2.251} \quad (4.17)$$

As compared in Table 4.3, the above correlations fit the data with an overall mean absolute error of about 5%. The excellent fit provided by Eqs. (3.31), (4.16) and (4.17) is exemplified by the plot of Fig. (4.13). The first two terms on the RHS of Eq. (4.17) account for the combined effects of a changing velocity profile and the effects of secondary flow. The exponent of this term is about three times that of the same term in Eq. (4.10). This is to be expected, Ito's³⁰ correlation, Eq. (4.2), for the friction factor was found through application of the Darcy-Weisbach equation to a circular pipe over the length of a nearly 360° bend. Hence, his correlation averages the entrance effects with the fully developed flow and more importantly, also yields the average skin friction coefficient over the pipe circumference. Thus, the skin friction coefficient of the outer wall will be under predicted and the larger exponent found for the channel curvature term is warranted. Furthermore, the effects of secondary flow were not represented by the *It* factor of Eq. (4.10). It is also interesting to note that the constant, 0.746, of Eq. (4.17) is nearly equal to that estimated by use of Eq. (4.13) for one randomly chosen data set. Finally, Eq. (4.17) predicts that channel curvature will have a negative impact on CHF for sufficiently high subcooling, (approximately 55°C for near atmospheric conditions).

4.4 Conclusions

1. Curvature of the flow path appears to offer only a moderate advantage for the geometries studied and a subcooling of 20°C or more. Channel curvature where $R = 28.6$ mm yields a 50% increase of q_M for a subcooling of 5°C, however. Thus, channel curvature is advantageous only when it is desired to operate near the saturation temperature.

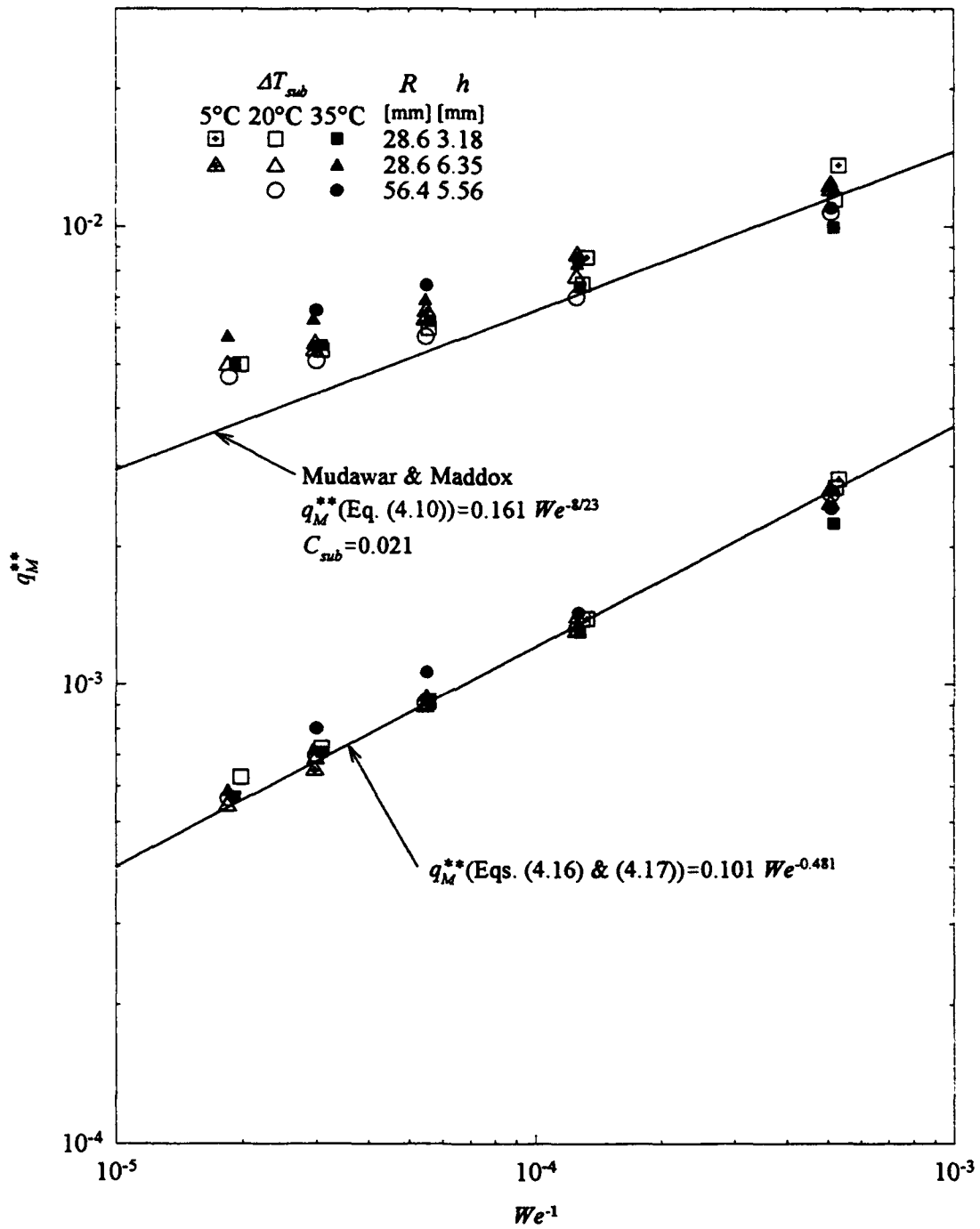


Figure 4.13 Comparison of data with Eqs. (3.31), (4.16), and (4.17).

2. Enhanced vapor removal due to increased buoyancy is the dominant mechanism responsible for increased CHF of the curved channels. The effect of buoyancy decreases with increased subcooling because of smaller bubble departure sizes at high subcoolings. A reduction in CHF may even occur for large subcooling. CHF enhancement caused by channel curvature also diminishes as subcooling increases because of the greater contribution of single-phase heat transfer for FC-72.

3. Secondary effects of an increased wall velocity gradient and secondary flows also aid in enhancing CHF. These effects begin to dominate only at very large subcoolings. An enhanced velocity profile provides higher velocity fluid near the wall for the curved channel as opposed to the straight channel. Thus, a better nucleation site liquid supply mechanism exists for the curved channel. This enhancement is nearly constant over the range of geometries and velocities investigated.

4. The effects of channel curvature may be partially described for subcoolings greater than 20°C by the additional inclusion of the term, $It^{1/15}$, to the denominator of Eq. (3.24), (cf. Eq. (4.10)). New values for the constants, ψ and C_{sub} , are provided in Table 4.3.

5. Equation (4.10) cannot account for the most dominant effect of channel curvature, enhanced vapor removal because of buoyancy. The Pi theorem was used to develop an empirical correlation for the curved channel results by first constructing a correlation for the straight channel results, Eqs. (3.31) and (3.32), (i.e., Eq. (4.16)) and then adding a correction for channel curvature, Eq. (4.17). The term in Eq. (4.17) that describes the subcooling dependence of buoyancy has rooting in the correlation of bubble departure diameter. Equations (3.31), (4.16) and (4.17) fit the sum total of the straight and curved channel data with a mean absolute error of about 5%.

Chapter 5

BOILING FROM A NONFLUSH SIMULATED ELECTRONIC CHIP

The thrust of the present chapter stems from the discovery of Gu et al.²⁴ that CHF decreases markedly if the heated surface is not maintained flush with the flow channel wall. This degradation occurred for heated surface* recess and protrusion heights of about 0.1 mm. As discussed in Chapter 1, much work has been done in the area of flow boiling heat transfer using fluorocarbons. Substantial studies by Samant and Simon²⁶, Mudawar and Maddox¹⁹, and Mudawwar et al.²⁵ have been concerned with heat transfer from simulated electronic chip heat sources that are flush with the flow channel wall. Mudawar and Maddox²⁷ have studied enhanced surfaces with various fin configurations that protrude into the flow path, however. Microgrooves, (stream-wise fins), microstuds, and pin fins were machined into the heater surface to enhance heat transfer. The fins and studs of the "micro" surfaces extended slightly more than 1 mm into the flow path and each had an exposed area that was 4.34 times that of a smooth flush surface. The pin fins extended 11.7 mm into the flow path and had a combined exposed area that was 6.32 times the area of a smooth surface. These geometries yielded impressive increases of the CHF, but relied on increased surface area to do so. The relative increase in CHF was generally much less than the relative increase in surface area. The simple protrusion of the chip in the present study yields a maximum increase of surface of only 27% while CHF is increased by about 60% for the best case.

There are some data for boiling from single fins¹⁶², but are not applicable to the present case where the aspect ratio of the protruding heater is much less than one. Concurrent with the present study, McGillis et al.²⁸ investigated the effect of heated surface protrusion height (0.8 to 2.4 mm), for velocities of 9.6 to 103.9 cm/s and subcoolings of 20 to 40°C. Heated surface refers to the top surface of the protruding block. They found a reduction in CHF for all combinations of velocity, subcooling and surface height.

* Heated surface refers to the top surface of the protruding block.

Because it is difficult to maintain flushness after repeated thermal cycling, even under closely controlled laboratory conditions, it is felt that the same problem may exist under application to electronic chip cooling. Thus, the present effort strives to quantify the effect of nonflush heated surfaces on heat transfer.

5.1 Experimental Apparatus – Nonflush Chip Details

The experimental apparatus is essentially the same as that described in Chapter 2 except for a different flow channel and heater test section. Figure 5.1 shows the flow loop system of Chapter 2, Fig. 2.1, with the different flow channel installed. The channel was constructed of optical grade plexiglas for flow visualization purposes. The design allowed both top and side views of the heated surface. As designed, the section of plexiglas containing the heater test section could slide up or down to vary the flow channel height. The flow channel, shown in Fig. 5.2, had a variable height that remained constant at 6.35 mm for these experiments. An entry length of 137 cm ensured fully developed flow for most configurable flow areas. Static pressure and fluid temperature were measured at a location 9 cm upstream of the test heater. Because the channel is vertically oriented, a small correction for hydrostatic pressure was made. Frictional pressure drop and heat loss over this length were assumed to be negligible for the same reasons presented in Section 2.3.

Similar to before, an oxygen free copper block was used to simulate an electronic device and is shown in Fig. 5.3. The copper block was enclosed in low thermal conductivity (0.3 W/m-K) Glastherm HT (General Electric Corp.) and heated from the back side by nichrome wire sandwiched between two plates of boron nitrate (65 W/m-K). Three 0.12-mm wire diameter type T thermocouples were imbedded in the block through 0.5-mm-diameter holes and a one-dimensional approximation of heat conduction was made to calculate heat flux. Heat loss, which occurred predominantly through the back of the enclosure was about 15% throughout the nucleate boiling regime (NBR) up to CHF. During the course of the experiments, the nichrome wire heater and boron nitride insulators were replaced with a thick film resistor (Emtron Corp.) as shown in Fig. 5.3. This design improvement allowed more intimate contact of the heater and copper block

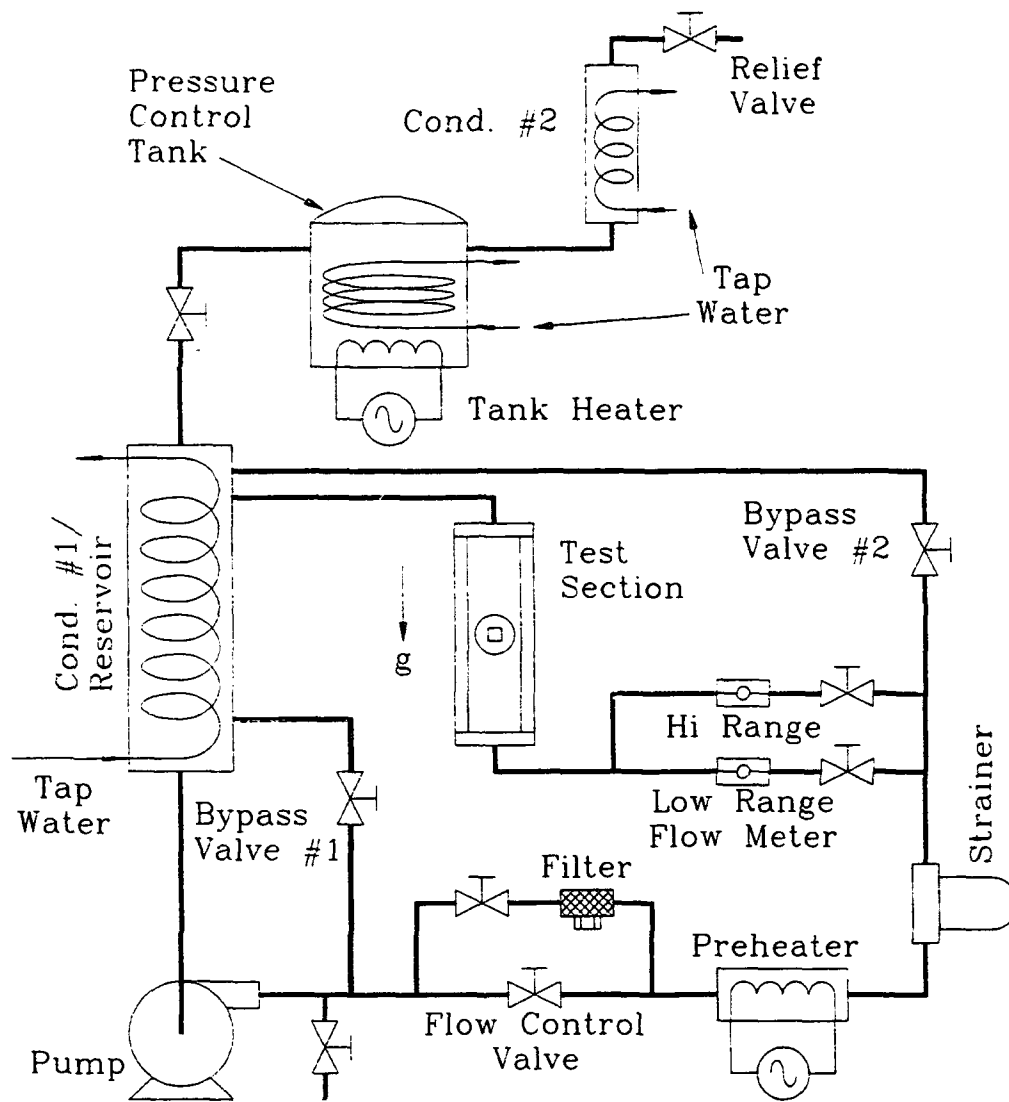


Figure 5.1 Flow loop schematic.

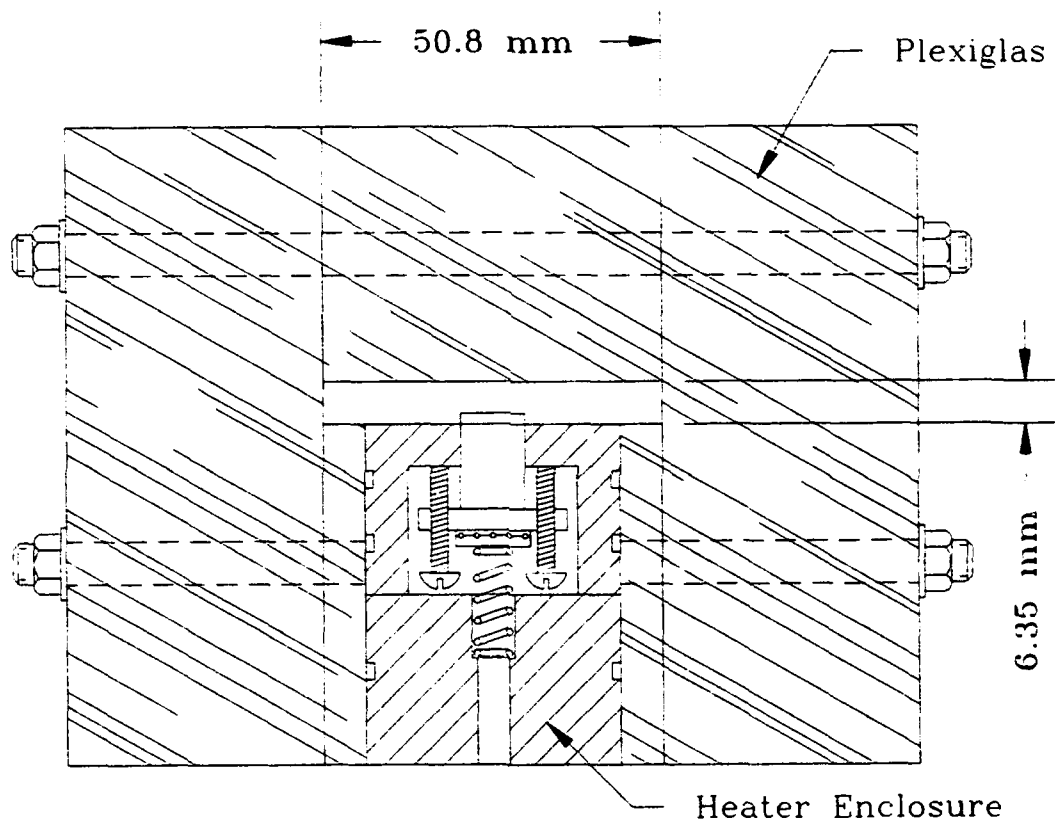


Figure 5.2 Flow channel cross section with test heater.

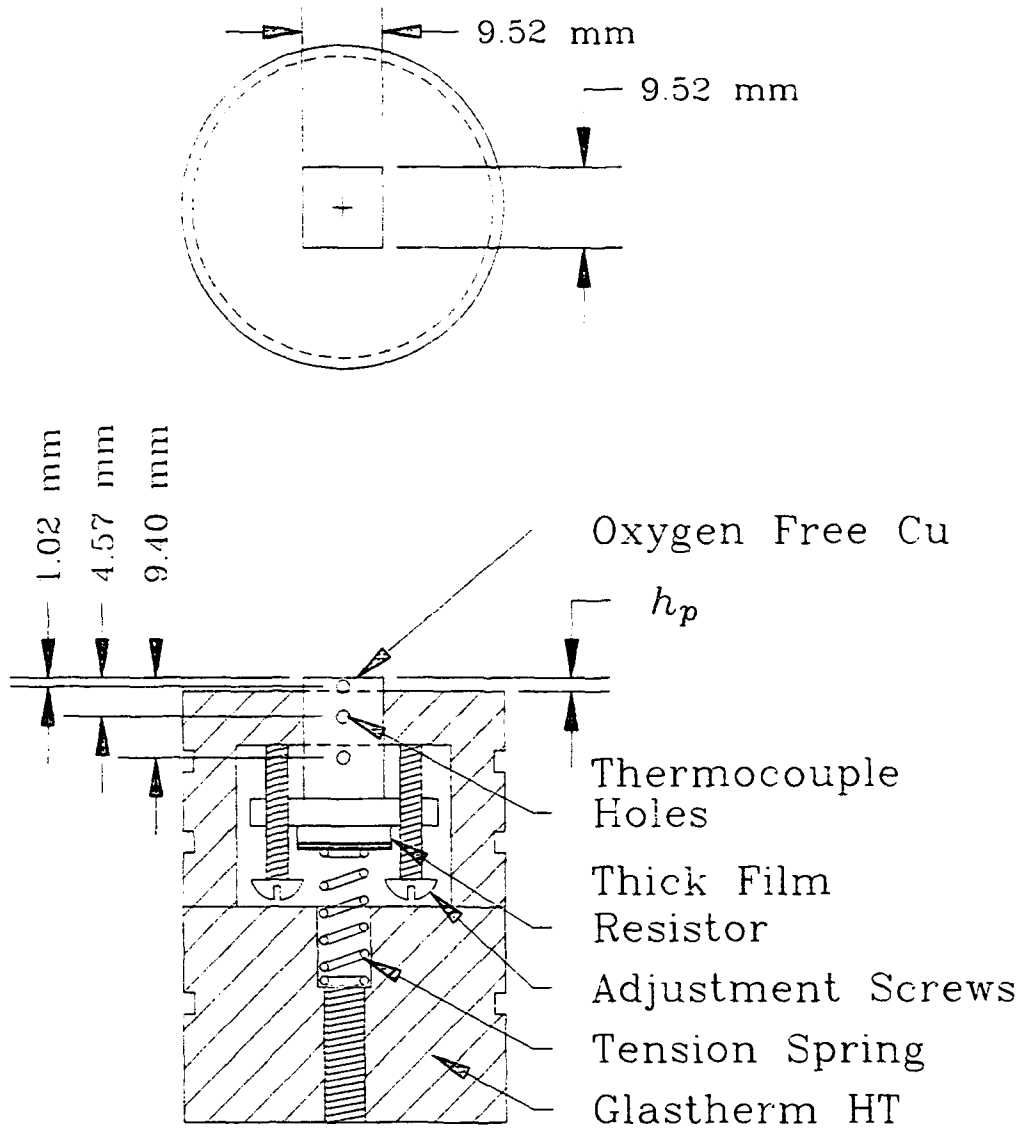


Figure 5.3 Simulated electronic chip and heater enclosure.

by virtue of one less contact resistance. This change resulted in a greater than 50% reduction in heat loss to yield an average heat loss of about 6%.

The protrusion height of the heater configuration was controlled by two screws (see Fig. 5.3). An adjustable spring kept the screws seated against the Glatherm enclosure. Great care was taken to ensure that the sides of the heater block sealed well against the Glatherm enclosure. High temperature silicone sealant was used for this purpose. The cylindrical design and triple o-ring seal of the heater enclosure allowed quick removal of the test section from the flow channel. A retaining mechanism permitted fine adjustment of the enclosure relative to the channel wall. The retainer also ensured that the leading edge remained perpendicular to the flow direction.

5.2 Uncertainty Analysis – Nonflush Chip Details

As described in Chapter 2 for the previous test sections, CHF was calculated from the one-dimensional heat conduction equation. For test section of Fig. 5.3, the individual temperatures given by two type T thermocouples, 4.57 and 9.40 mm from the top surface, were used for this calculation. These were well below the 0.635-mm maximum protrusion height and thus gradients produced by heat transfer from the sides of the block should have little effect on accuracy. T_w is extrapolated from the same two thermocouples and is thus an average value. A third thermocouple, 1.02 mm from the top surface, was generally within 2°C of the extrapolated value at this location. Thus, this thermocouple was not used in the calculation of T_w in order to maintain consistency with the results of the tests discussed in previous chapters which did not include a third thermocouple. It is realized that radial gradients do exist, especially for the protruded cases, but this method was considered best for obtaining a characteristic wall temperature. Previous results¹⁹ give a maximum upstream to downstream temperature difference of only 2.2°C for the flush mounted case. Because of this, and the added complexity, additional thermocouples to obtain the surface temperature distribution were not used.

Because of the high thermal diffusivity of copper and the distances of the thermocouples from the boiling surfaces, the measured temperatures and thus the

calculated heat flux and wall temperature fluctuated very little under all conditions but an instability condition discussed later. This unsteadiness translates into a heat flux variance of less than 0.5 W/cm^2 . In Chapter 2, it was shown that heat flux variations due to the cyclic nature of bubble ebullition were completely damped at a distance from the surface corresponding to the closest thermocouple. It was further explained that high bubble density, small maximum bubble diameters and the high thermal conductivity of copper are the reasons for a negligible temperature variation. Under these conditions, it was found that thermal gradients disappeared at a distance of about one bubble diameter, ($< 0.5 \text{ mm}$), below the surface.

A Helios I (John Fluke Mfg.) data acquisition system was used for all thermocouple and voltage measurements. This device has a resolution of 0.02°C and rated accuracies of 0.45 and 0.39°C for thermocouple types K and T respectively. The thermocouple pairs were compared to a precision thermistor (0.1°C accuracy) over the temperature range of the experiments. In both instances, the thermocouples of each pair agreed to within 0.3°C . All the thermocouples agreed with the precision thermistor to within 0.5°C . Thus, the thermocouple accuracies are considered to be well within 1°C for these experiments.

At the same time that the heater was redesigned, a Hewlett Packard 3852A data acquisition system was substituted to make all of the voltage and temperature measurements. This device has a resolution of 0.02°C and rated accuracies of 0.5 and 0.65°C for thermocouple types K and T respectively. The data acquisition unit and type T thermocouples were calibrated in unison against a precision digital RTD, (0.03°C rated accuracy), over the temperature range of interest. The system accuracy was found to be within 0.3°C . All type T thermocouples were found to agree with each other to within 0.1°C for the entire temperature range of interest.

As described in Chapter 2, the Kline and McClintock³¹ approach to random uncertainty calculation was taken. The uncertainties of the thermocouples, thermocouple locations, and thermal conductivity were considered. However, the contribution of thermocouple error is dominant for all cases. Because temperature difference is the only variable during testing, the uncertainty in CHF is a decaying

function of temperature difference or heat flux. For the Helios I data acquisition system, the uncertainty in CHF was calculated for a temperature difference uncertainty of 0.5. The calculated uncertainties in CHF are 13.4, 7.8, and 6.9% for heat fluxes of 34, 85, and 132 W/cm² respectively. For the HP 3852A data acquisition system, the system accuracy was 0.3°C and the thermocouples were found to agree to within 0.1°C of each other. Although the latter accuracy is more applicable to the heat flux calculation, the former accuracy is taken as a conservative value for the temperature difference uncertainty. Thus, for a temperature difference uncertainty of 0.3°C, the uncertainties in CHF are 10.2, 6.9, and 6.4% for heat fluxes of 34, 85, and 132 W/cm² respectively.

As before, the repeatability of CHF values was generally within 5% for heat fluxes greater than 50 W/cm². All data are subsequently presented as the average of all available points for a given test section and at a given velocity, subcooling and heater height. This was done to maintain clarity in the figures. Finally, the bias error was not estimated; however, the percentage of heat loss measured compares with that previously reported¹⁹ for a similar design. The uncertainty of the flow rate measurement was dominated by the uncertainty of the flow meter which was 0.5% of the reading. Flow velocity was based on channel cross-sectional area. The error in flow velocity due to the protruding surface was less than 2% for the worst case.

5.3 Experimental Results

Results were obtained for velocities of 1 to 4 m/s and subcoolings of 20 and 35°C. The vertical channel caused the pump to be much more prone to the cavitation problem discussed in Chapter 2. Consequently, data were not obtained for subcoolings less than 20°C. Data for five surface heights, as measured relative to the flow channel wall, were obtained. These were 0.127 mm recessed, 0.229, 0.457, and 0.635 mm protruded and flush with the flow channel wall. A reduction of CHF occurred at low velocities while an increase occurred at higher velocities for the protruded cases. A reduction of CHF occurred at all velocities for the recessed condition.

5.3.1 Flush Surface

A series of data was obtained for this case to establish a baseline for the nonflush cases and to validate the present test section by comparison with previously obtained data. The heat flux versus wall superheat characteristics are not much different from Figs. 3.5 - 3.7, but may be seen in Figs. 5.5 - 5.8. Figure 5.4 shows the data of this test section, (diamonds), and the previous straight channel data plotted against Eqs. (3.31) and (3.32). Close examination of the plot for Eqs. (3.31) and (3.32) shows that the data for the current test section are consistently overpredicted for $U > 1$ m/s. The only considerable change from the previous geometries is the channel width, w . As stated in Chapter 3, the exponents of the pi group, L/D_h , and the Reynolds number are approximately equal. Thus, the hydraulic diameter was not a governing independent variable, but was kept to provide consistency with the curved channel correction developed in Chapter 4. In Chapter 3, the CHF was found to be independent of channel height for $h \geq 3.18$ mm. However, the present results indicate that channel width plays a role, at least for the range considered here, $27.0 \text{ mm} < h < 50.8 \text{ mm}$. Bias errors are not considered to be any different than for the previous test sections because the construction is very similar and measured heat losses are similar. As discussed in Chapter 2, surface effects are also not considered to be the cause of the difference in measured heat flux.

New exponents were consequently determined for Eqs. (3.31) and (3.32). The resulting equations are

$$q_M^{**} = 0.330 We^{-0.344} \quad (5.1)$$

where

$$q_M^{**} = \frac{q_M / \rho_g h_{fg} U}{\left(\frac{\rho_f}{\rho_g} \right)^{0.302} \left(\frac{L}{D_h} \right)^{0.166} \left(\frac{\rho_f U D_h}{\mu_f} \right)^{0.067} \left[1 + 4.174 \left(\frac{c_p (T_{sat} - T_f)}{h_{fg}} \right)^{1.487} \right]} \quad (5.2)$$

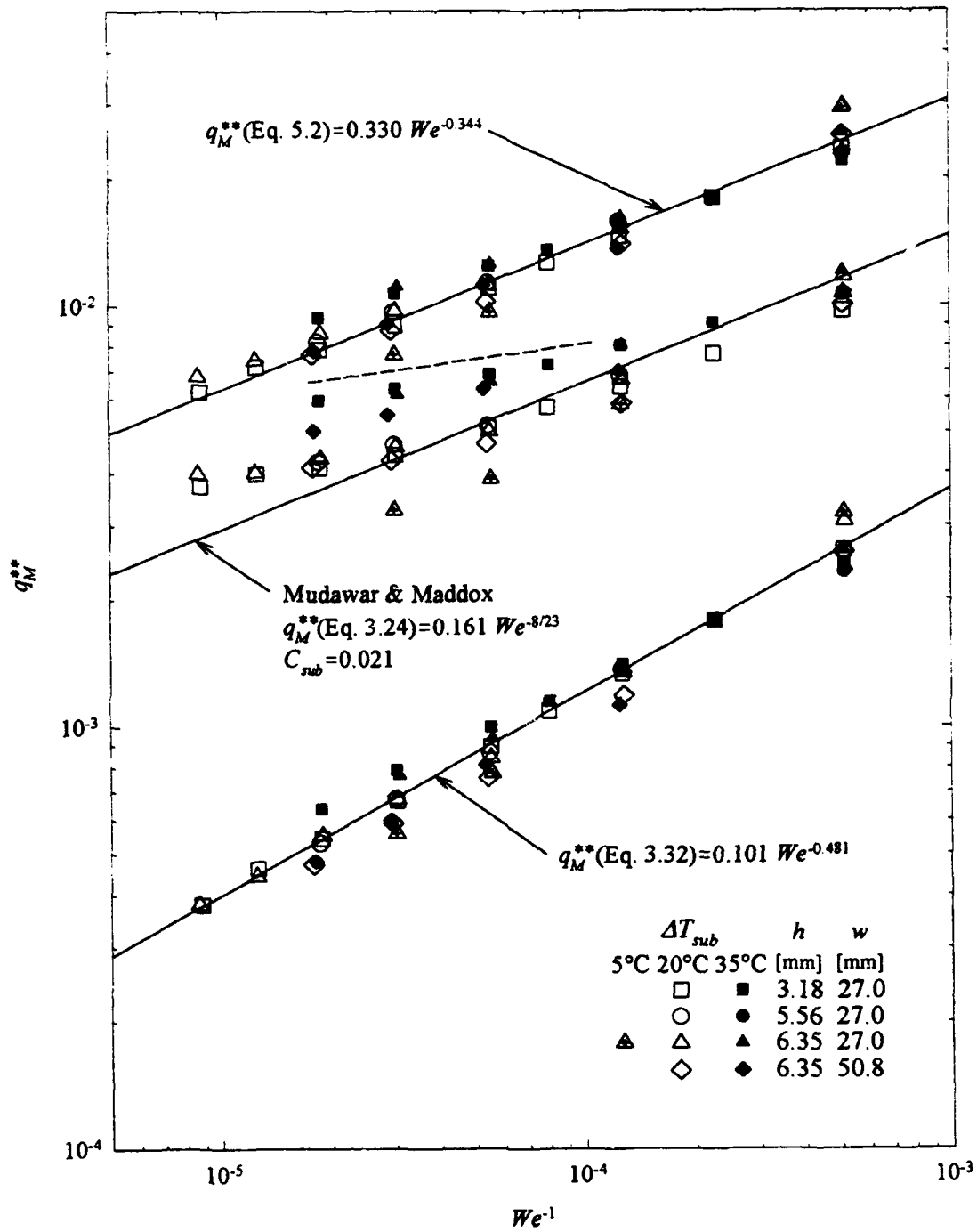


Figure 5.4 Comparison of new straight channel data with various correlations.

The most notable difference is that the exponent of the Reynolds number has changed from 0.310 to 0.067. The Reynolds number correlated the higher velocity data. With the addition of a large number of moderate to low velocity observations, Eqs. (5.1) and (5.2) are heavily weighted towards the lower velocity observations. Equations (5.1) and (5.2) fit the sum of the straight channel observations with a mean absolute error of 7.1 %.

The data are plotted against Eqs. (5.1) and (5.2) in Fig. 5.4. The data are also plotted against the theoretically obtained correlation of Mudawar and Maddox¹⁹, (Eqs. (3.23) and (3.24)) and are separated from Eqs. (5.1) and (5.2) by the dashed line. It is interesting to note that Eqs. (3.23) and (3.24) fit the data for the current geometry very well within the range of validity, (i.e., $10^{-4} < We^{-1} < 10^{-2}$). Furthermore, the current test section geometry is closer in dimension to that of Mudawar and Maddox where $h = 12.7$ mm and $w = 38.1$ mm. Eqs. (5.1) and (5.2) are valid for $U = 1-7$ m/s, $\Delta T_{sub} = 5-35$ °C, and $\rho_f/\rho_g = 77.7-123.3$.

5.3.2 Recessed Surface

By recessing the heated surface, a shallow cavity in the flow channel wall was created. Flow recirculation zones were consequently established on top of the heated surface at the leading and trailing edges during testing. The thermal boundary layer is thus thicker in these regions and nucleation should therefore occur first in or near these zones. This was true for a flow velocity of 4 m/s where incipience occurred at the leading edge followed by nucleation at the rear edge. For the other velocities, incipience occurred at preferred sites similar to the flush case. A boiling incipience temperature overshoot of 6°C occurred only once and at a velocity of 1 m/s and subcooling of 20°C.

The spread of nucleation sites first in the wake of a preferred site, and then upstream was similar to what occurred for the flush case. The 4 m/s condition was the exception. Following the leading and trailing edge nucleation described, preferred sites once again nucleated on the latter one-third of the heated surface. The bubble layer then grew similar to the lower velocity cases with the leading edge bubble layer growing at a much slower rate. The two fronts met in a sudden nucleation of the remaining sites.

Throughout this process, nucleate boiling occurred at higher wall superheats owing to the less effective vapor removal.

An average reduction in CHF of 9% over the flush condition was found for a flow velocity of 1 m/s. This reduction increased to 13 and 16% for flow velocities 2 and 3; and 4 m/s, respectively and 20°C subcooling. For a subcooling of 35°C, the reductions in CHF were greater than 20% for velocities of 1-3 m/s and almost 30% for a velocity of 4 m/s. Figures 5.5-5.8 compare the recessed cases with flush surface cases of the same velocity and subcooling. The single-phase heat transfer is not changed much by recession of the surface with the exception of the cases where $U = 1$ m/s. Figure 5.5 is somewhat deceptive, since early, but slight nucleation of the recessed surface for $U = 1$ m/s and $\Delta T_{sub} = 20^\circ\text{C}$ appears to be primarily enhanced single-phase convection for wall superheats up to about 6°C. Visual observation indicated that nucleation began at negative wall superheats owing to the surface hot spots created by recirculating zones.

The low velocity, low subcooling cases should have the lowest CHF reductions for the following reasons. For the flush surface, the ratio of single-phase heat flux to CHF is greatest at this velocity and subcooling. The data show that the single-phase heat transfer coefficient is generally unchanged by the change in surface height. Thus, a decrease in boiling heat transfer would have the least impact.

For a subcooling of 35°C, Figs. 5.7 and 5.8 show that CHF occurs abruptly with little increase in the wall superheat. The "second transition region" as described in Fig. 3.1 is essentially absent. This implies that CHF occurs immediately after the initial dry patch forms. It is not clear why this should occur at higher subcoolings. Figures 5.13 and 5.14 summarize the CHF results for the recessed surface.

5.3.3 Protruded Surface

The effect on boiling from a surface protruding into the flow stream was studied for surface heights, h_p , of 0.229, 0.457, and 0.635 mm. For the following results, heat flux is based on *exposed area* instead of cross-sectional area unless otherwise noted. The exposed area is the total area of the top and sides of the block while the cross-sectional

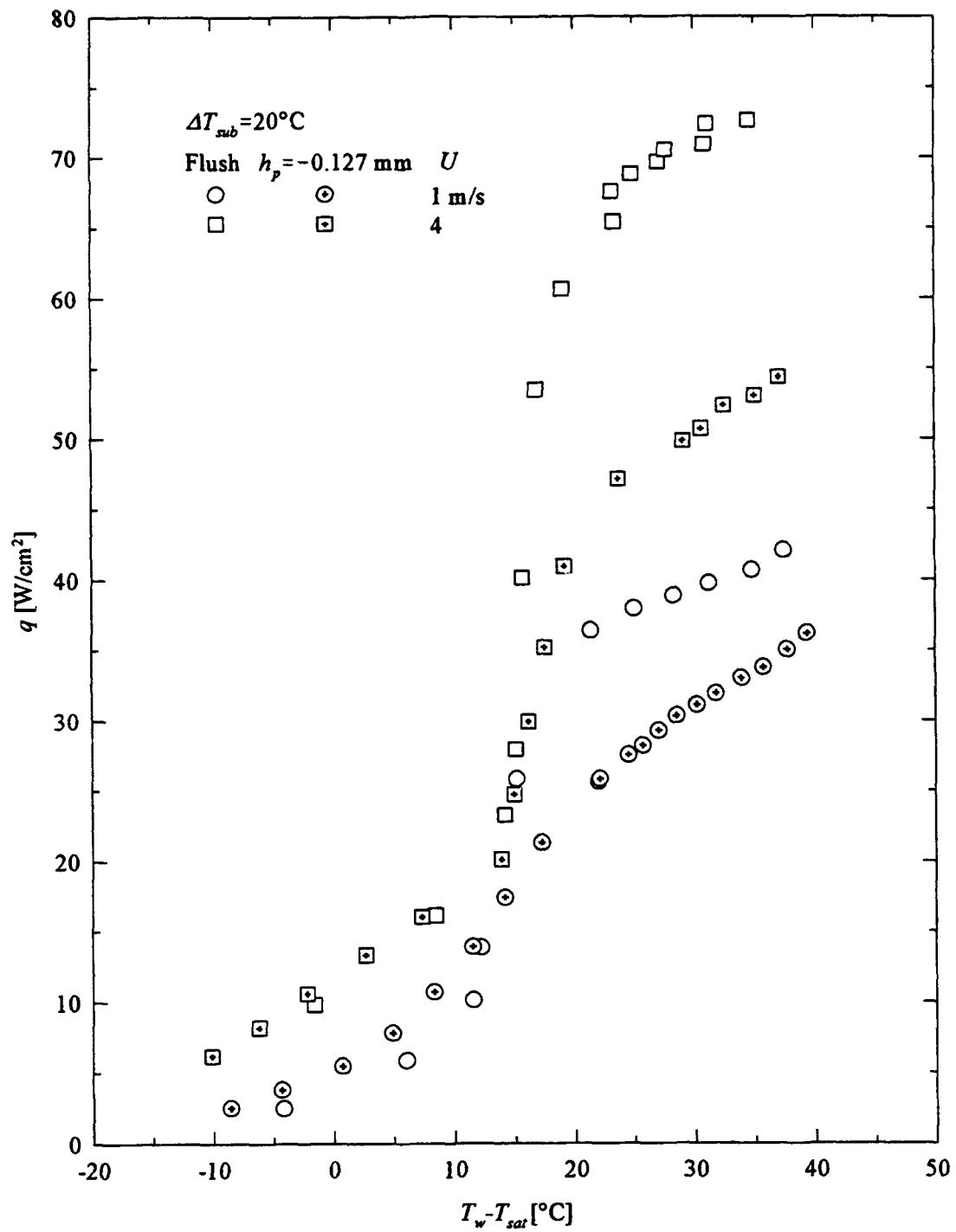


Figure 5.5 Comparison of retracted and flush cases for $\Delta T_{sub} = 20^\circ\text{C}$ and $U = 1$ and 4 m/s.

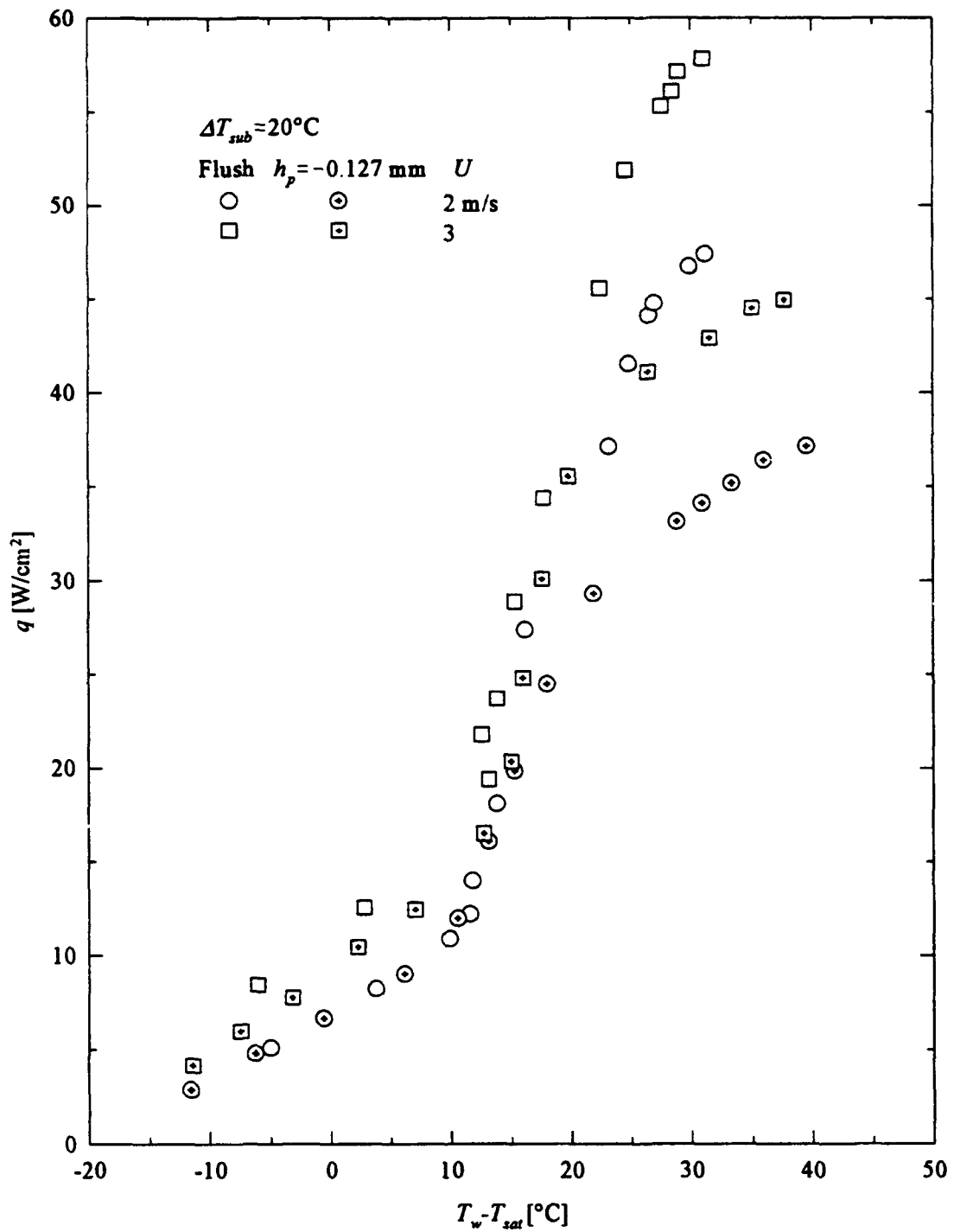


Figure 5.6 Comparison of recessed and flush cases for $\Delta T_{sub} = 20^\circ\text{C}$ and $U = 2$ and 3 m/s .

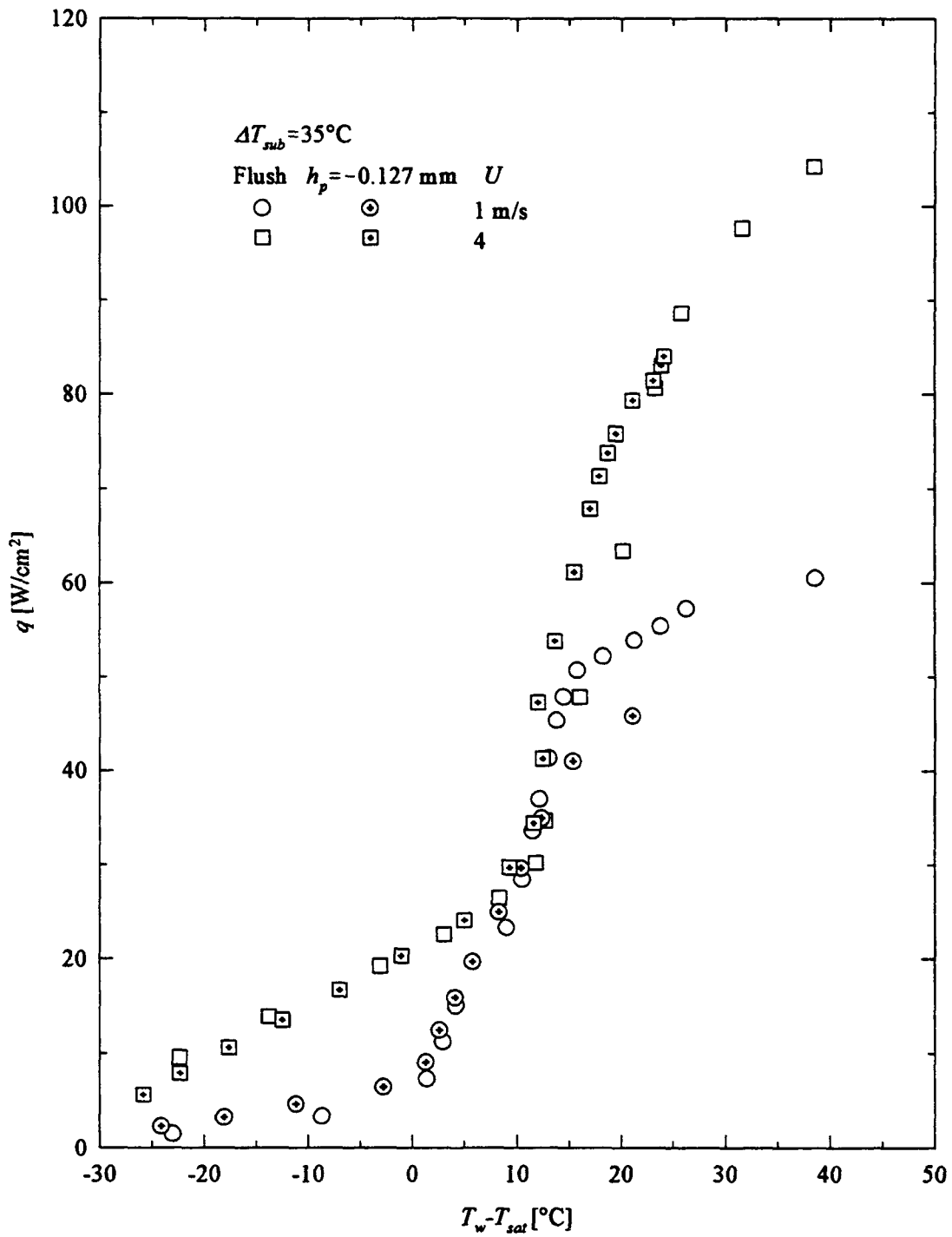


Figure 5.7 Comparison of recessed and flush cases for $\Delta T_{sub} = 35^\circ\text{C}$ and $U = 1$ and 4 m/s .

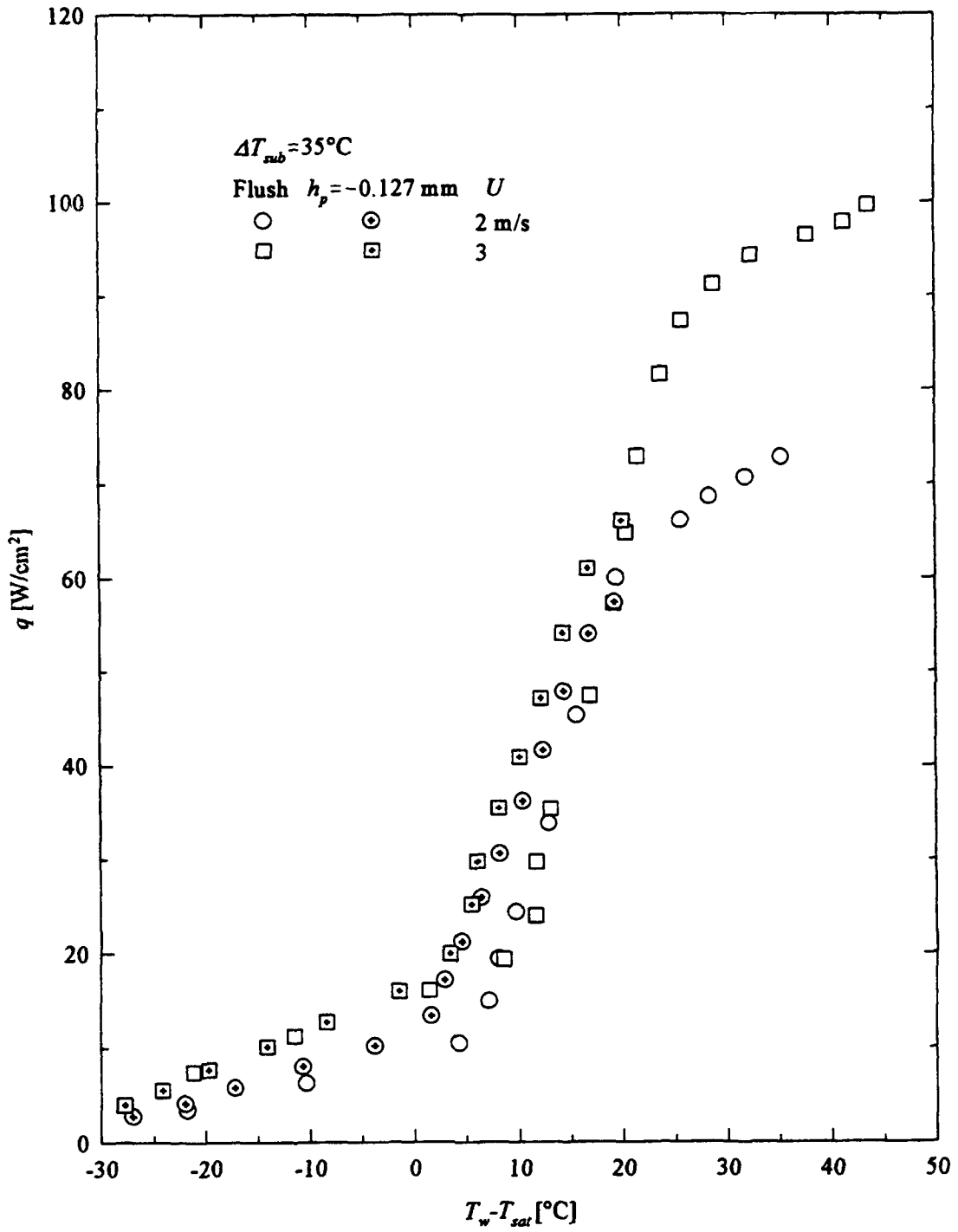


Figure 5.8 Comparison of recessed and flush cases for $\Delta T_{sub} = 35^\circ\text{C}$ and $U = 2$ and 3 m/s .

area is the area of the top only. Figures 5.9 - 5.12 show how the boiling curves progress with velocity and subcooling for $h_p = 0.635$ mm as compared to the flush cases under the same conditions. For the case of $U = 1$ m/s and $\Delta T_{sub} = 20^\circ\text{C}$, Fig. 5.10, an unusual shift in the boiling curve occurs at higher heat fluxes. This anomaly will be discussed later. Figures 5.13 and 5.14 summarize the CHF results of all the protruded and recessed surface cases.

For the protruding block, a stagnation point exists at the leading face and separation occurs at the trailing edge. The following describes nucleation as heat flux is increased. First, nucleation occurs on the trailing face while a very small vapor blanket forms quickly after that on the leading face. Nucleation then proceeds from a preferred site on the trailing one-third of the surface while a sheet of vapor breaking into bubbles grows from the leading edge (see Fig. 5.15). This sheet of vapor did not grow beyond the leading edge for shorter surface heights and low velocities, however. Specifically, the vapor blanket did not grow for $U < 3$ m/s and $h_p = 0.229$ mm and $U < 2$ m/s and $h_p = 0.457$ and 0.635 mm. Bubble generation from these shorter blankets did increase with increasing heat flux, although. Excluding the above circumstances, the sheet of vapor grew from the leading edge to cover a significant portion of the surface. But, this was true for 20°C subcooling only. At 35°C subcooling the vapor sheet grew to a length of only about 1 mm, ($L = 9.5$ mm). Nucleation from the sides parallel to the direction of flow was not visible for any case throughout the entire boiling regime.

An interesting instability phenomenon occurred at a flow velocity of 2 m/s and 20°C subcooling for surface heights of 0.457 and 0.635 mm. This instability was marked by the sudden appearance and disappearance of the aforementioned vapor sheet emanating from the leading edge. Remember that the vapor sheet did not exist at 2 m/s for $h_p = 0.229$ mm. Also, for 35°C subcooling, the vapor sheet never stretched beyond 1 mm, and therefore remained stable. The alternate pair of panels for 71% of CHF ($h_p = 0.635$ mm), in Fig. 5.15 illustrate this event. Near the point of instability, the vapor sheet covered roughly the upstream 50% of the heated surface before breaking into vapor bubbles. The vapor sheet grew steadily up to this point while oscillating with an amplitude of about 1 mm. Just before the instability, the vapor sheet receded to the

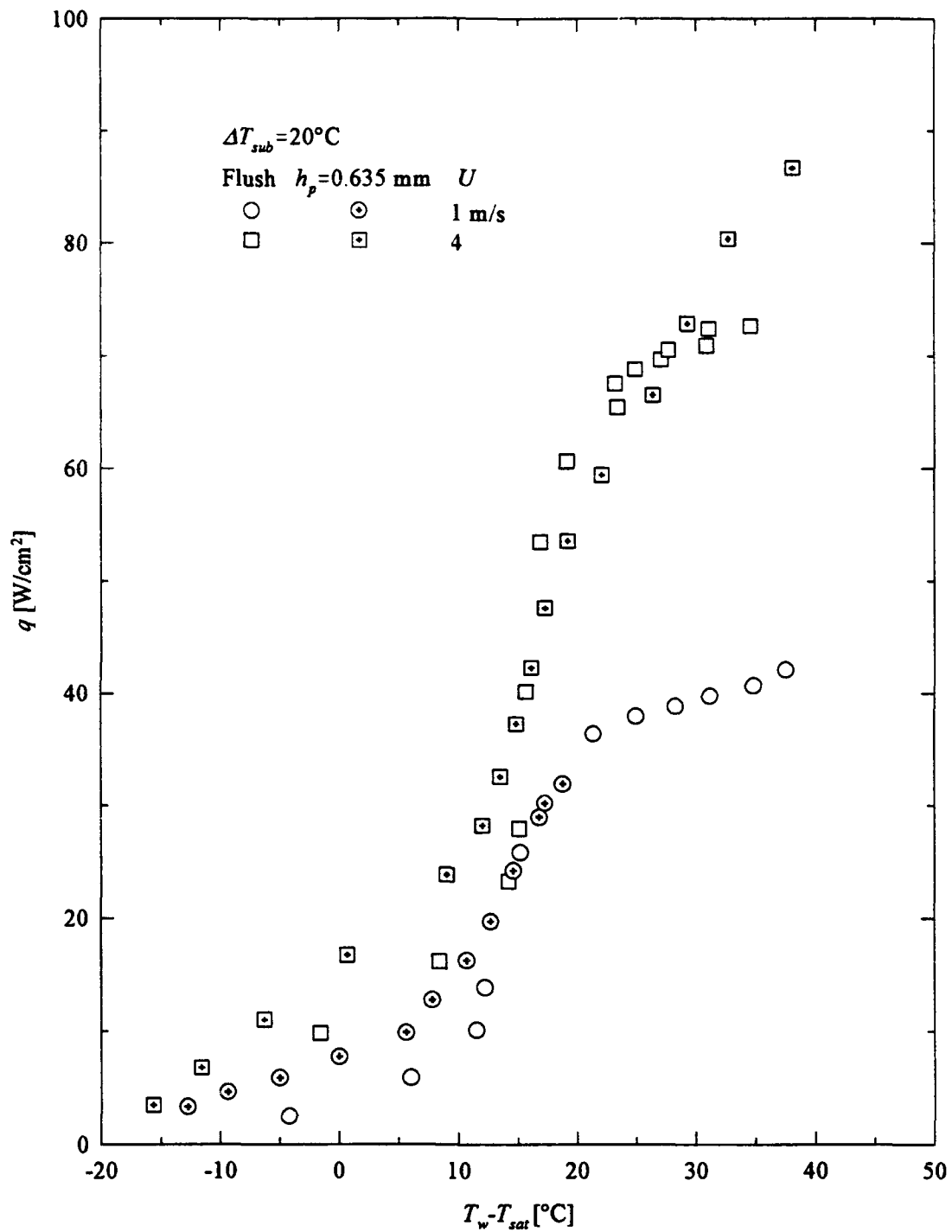


Figure 5.9 Comparison of protruded and flush cases for $\Delta T_{sub} = 20^\circ\text{C}$ and $U = 1$ and 4 m/s .

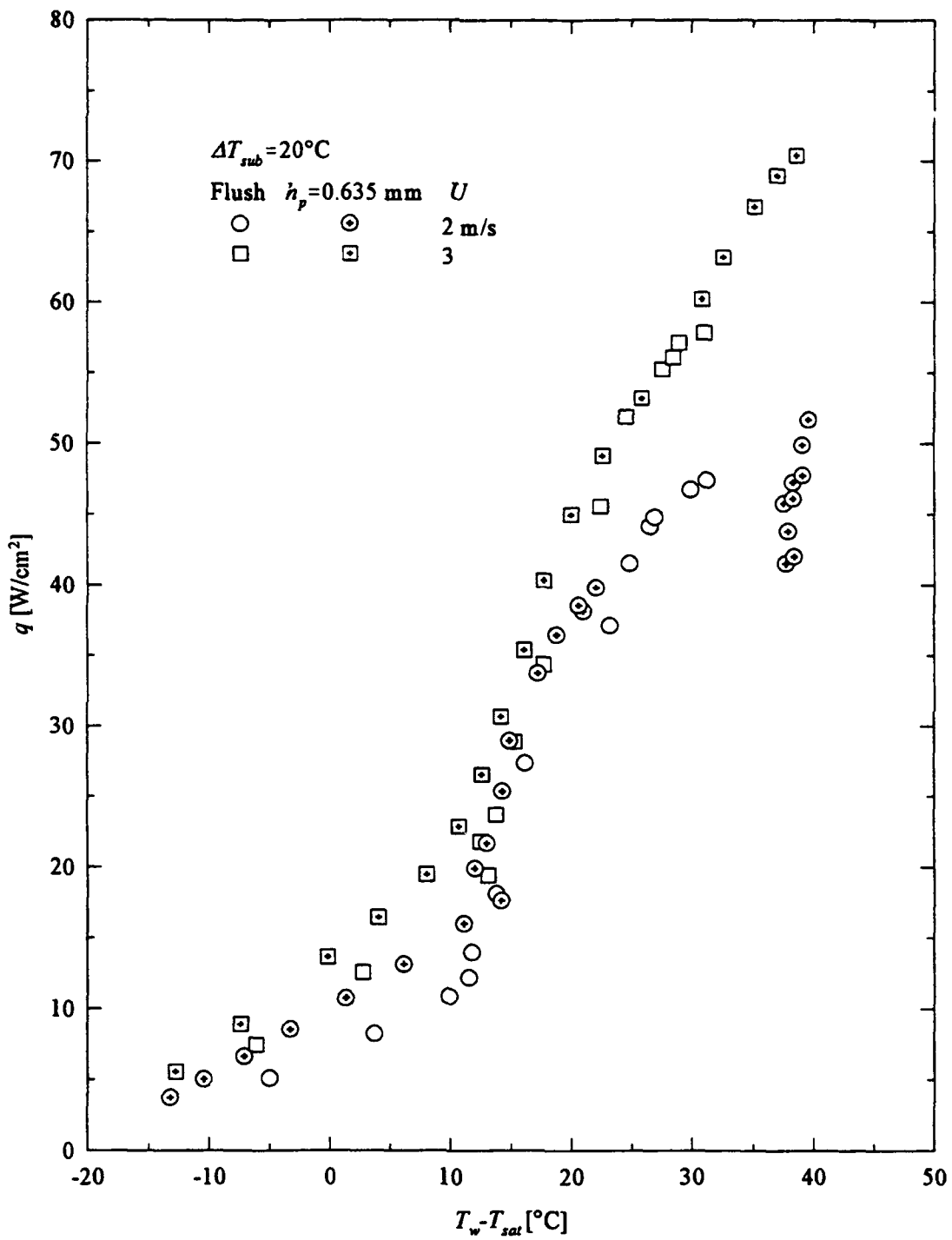


Figure 5.10 Comparison of protruded and flush cases for $\Delta T_{sub} = 20^\circ\text{C}$ and $U = 2$ and 3 m/s .

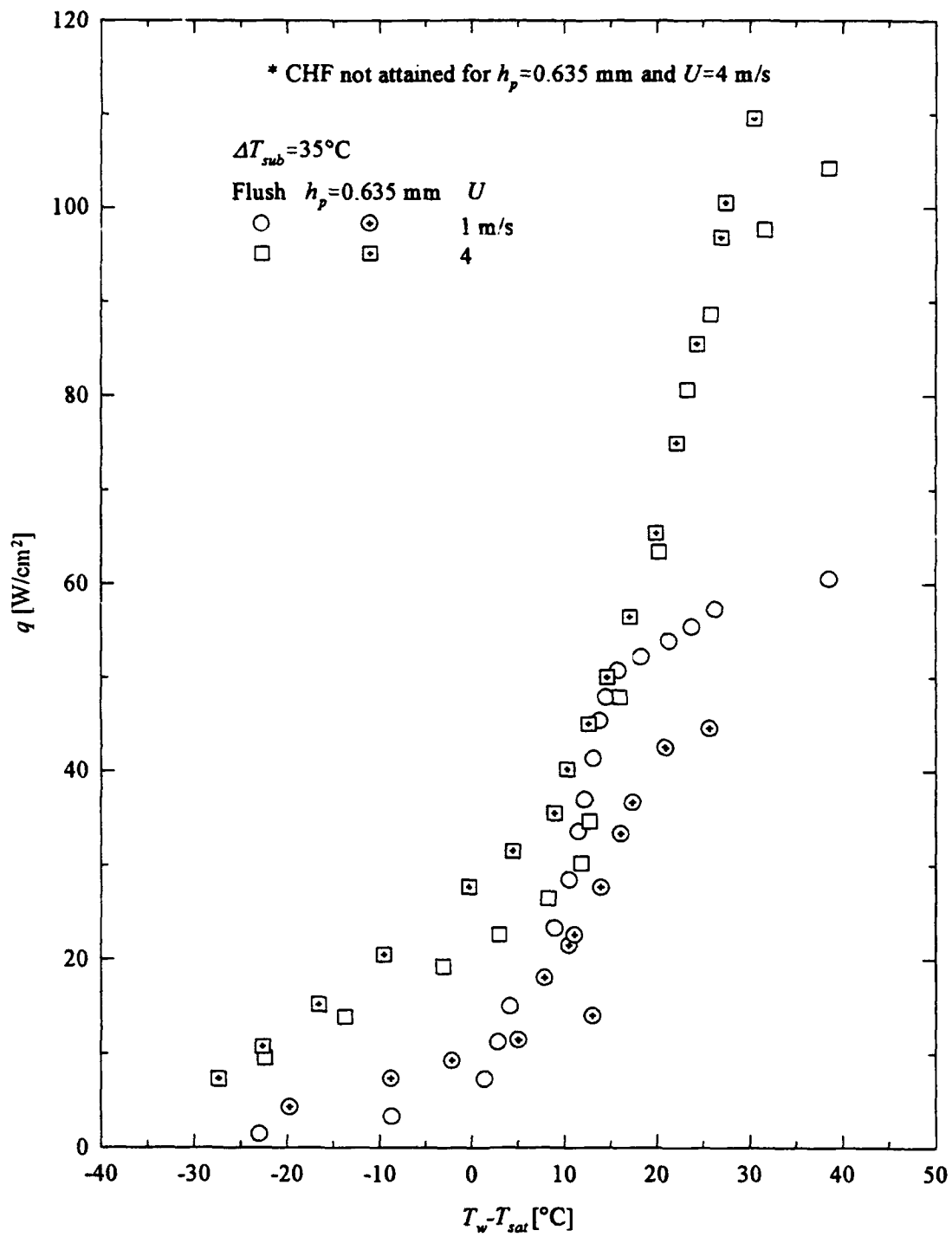


Figure 5.11 Comparison of protruded and flush cases for $\Delta T_{sub}=35^\circ\text{C}$ and $U=1$ and 4 m/s.

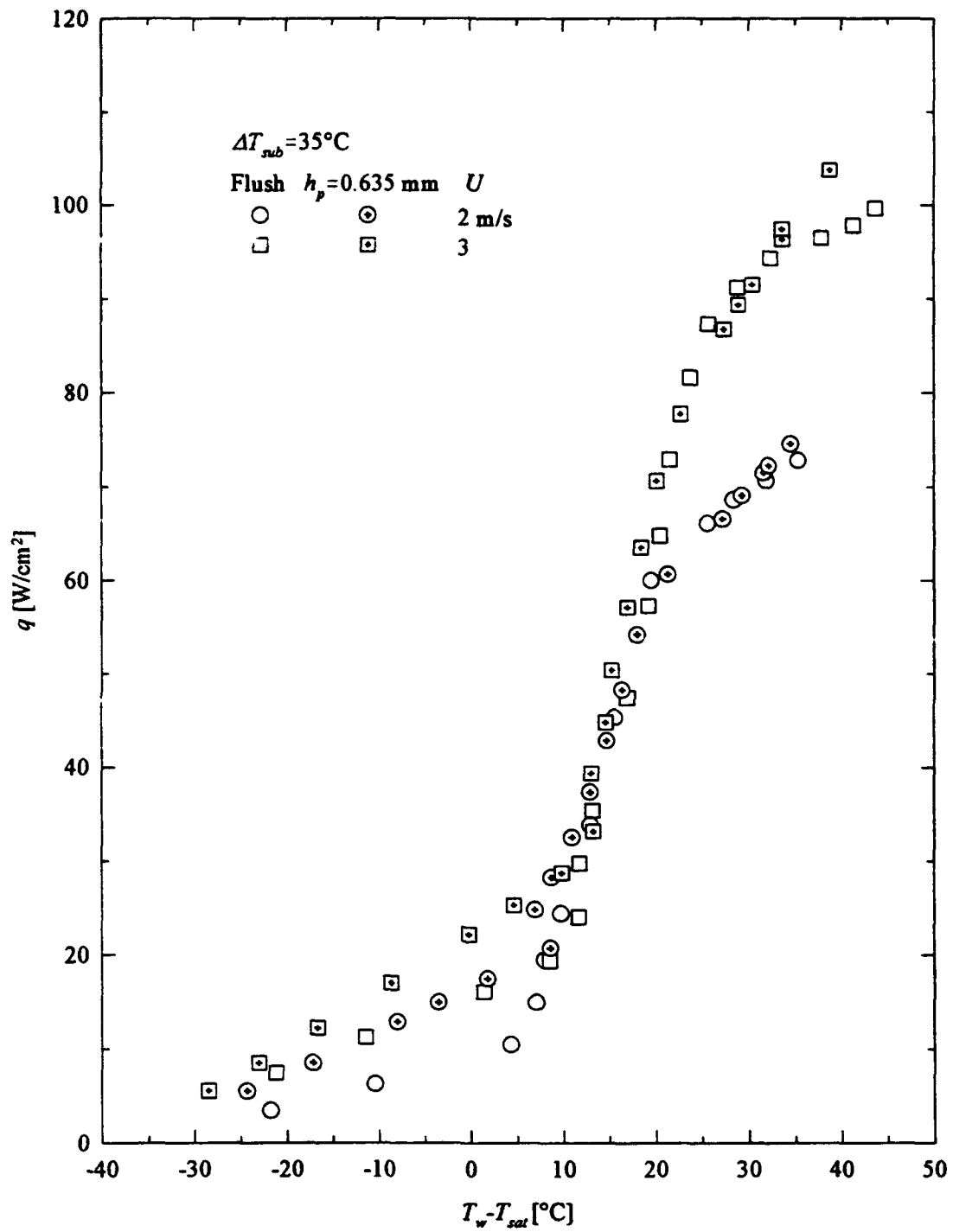


Figure 5.12 Comparison of protruded and flush cases for $\Delta T_{sub} = 35^\circ\text{C}$ and $U = 2$ and 3 m/s .

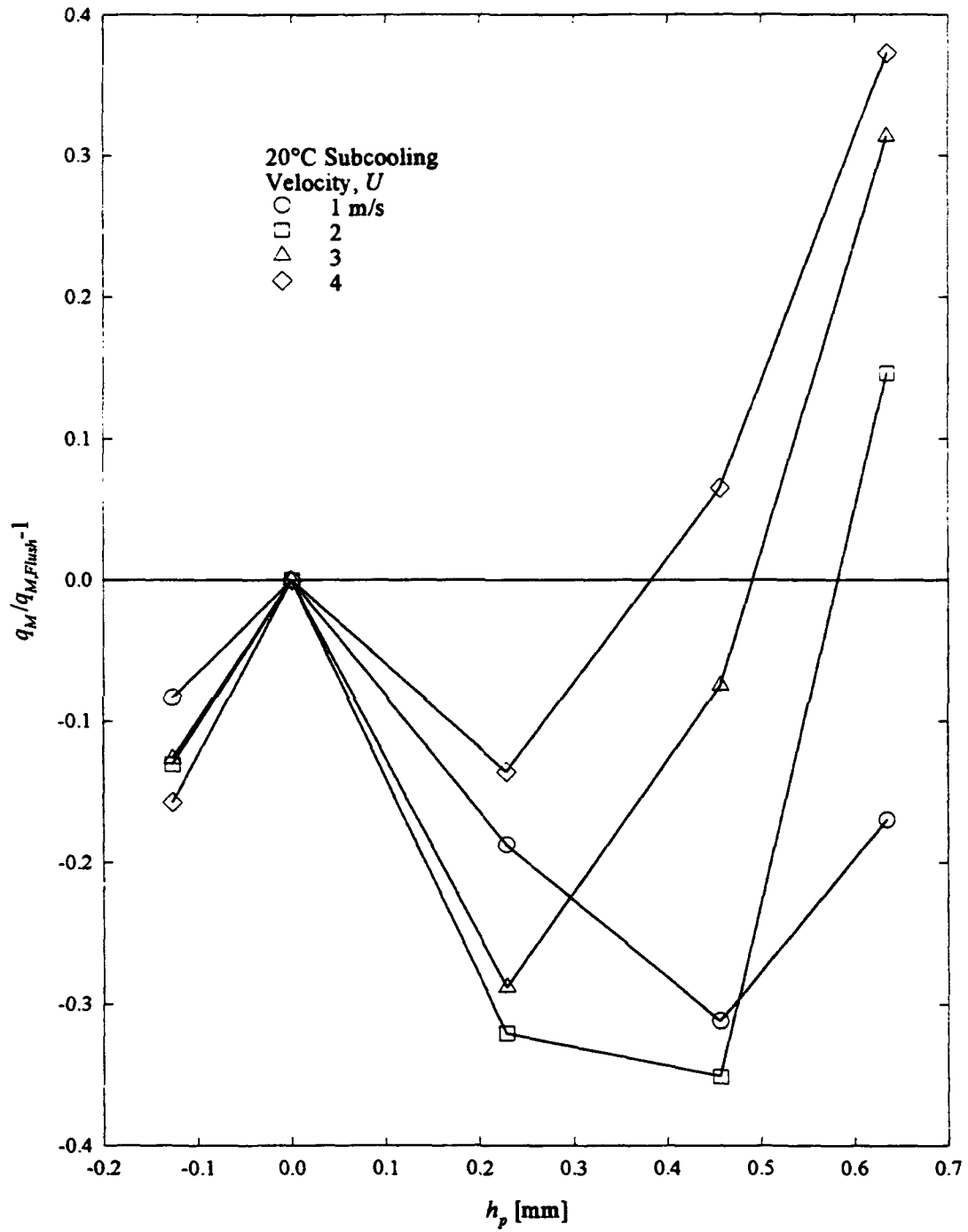


Figure 5.13 Variation of CHF with heater height and velocity for 20°C subcooling.

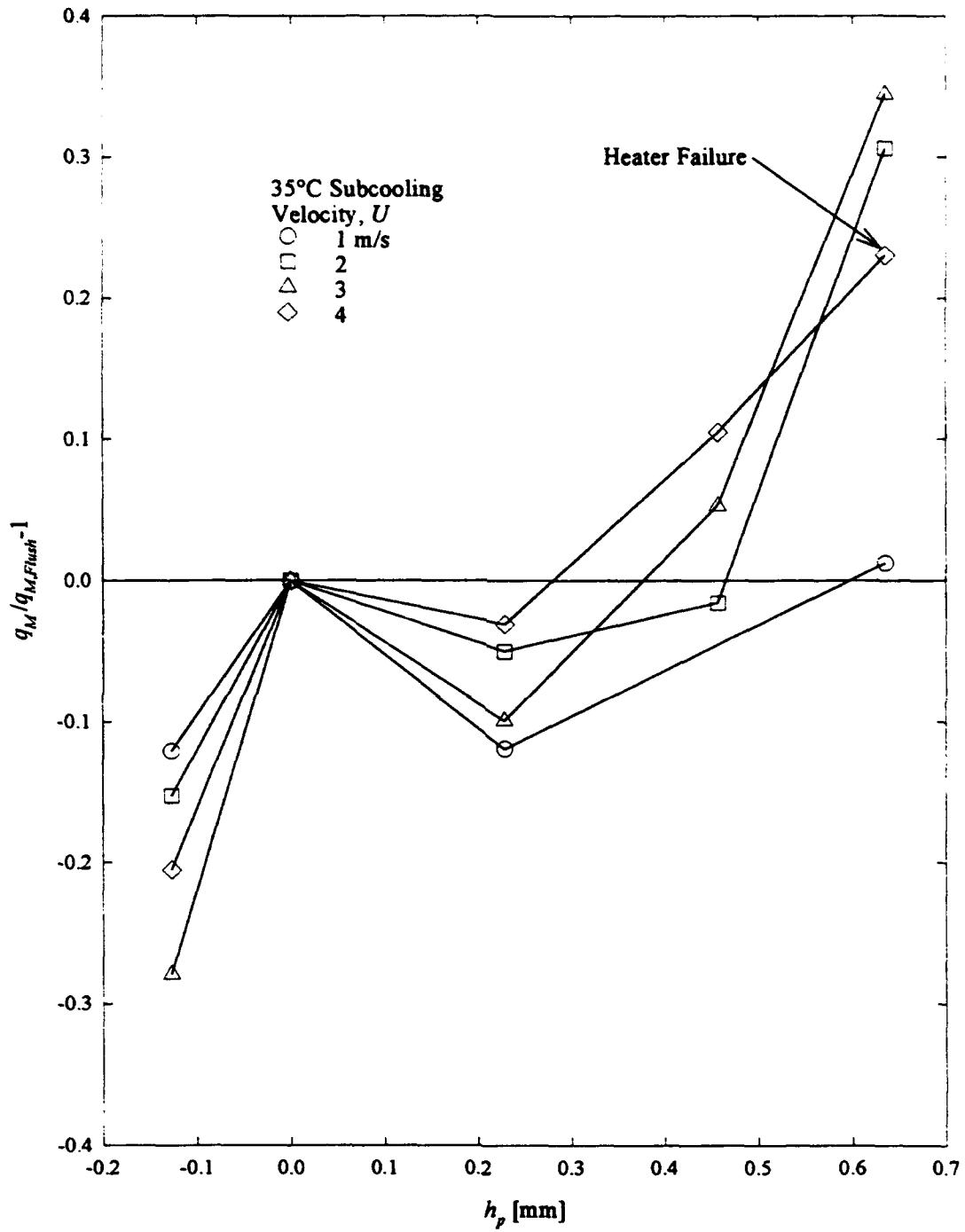


Figure 5.14 Variation of CHF with heater height and velocity for 35°C subcooling.

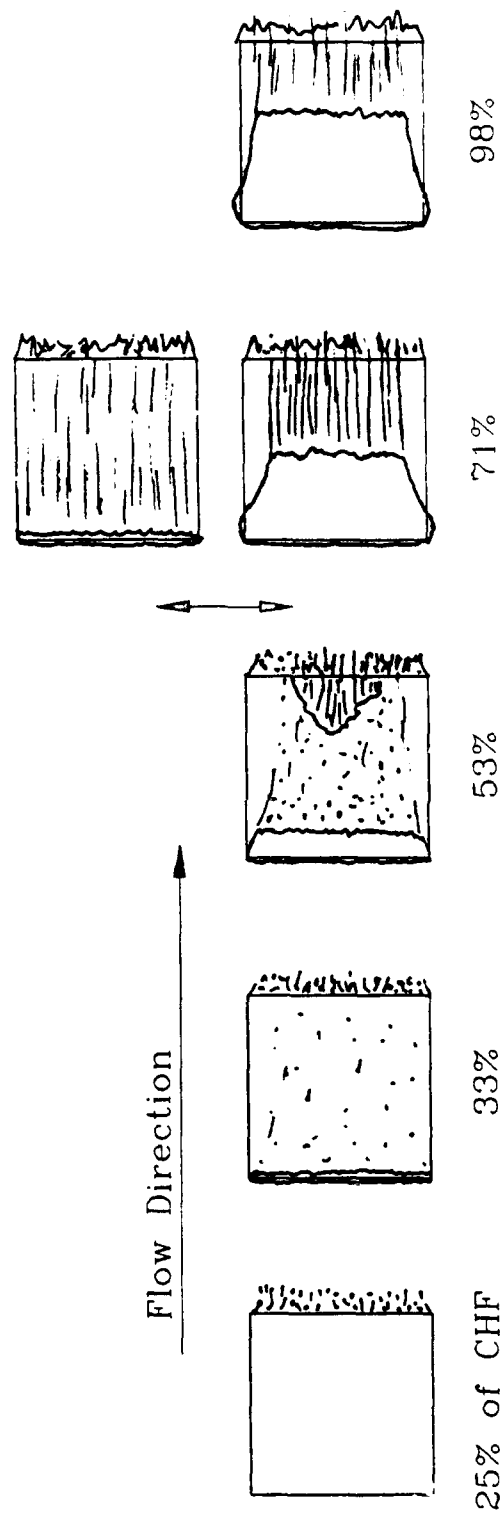


Figure 5.15 Progression of boiling and instability for $U = 2$ m/s, $h_p = 0.635$ mm, and $\Delta T_{sub} = 20^\circ\text{C}$.

leading edge and immediately returned to about $1/2 L$. The frequency of this occurrence was very unsteady, but was roughly 20 Hz. This large scale oscillation manifested as an oscillation of surface temperature, T_w , also

As power to the heater was further increased, a sudden increase in wall superheat preceded a second stable regime. This temperature excursion is depicted in Fig. 5.16 by representative data for each heater height case. After this temperature excursion, the vapor blanket covered about 60% of the heated surface (see Fig. 5.15). The vapor sheet length continued to oscillate with an amplitude of roughly 2 mm. As power to the heater was increased, the heat flux increased at almost constant wall temperature. This implies that additional nucleation sites were activated. The 2-mm amplitude oscillation also dies out with increasing power and surface temperature consequently becomes more steady.

CHF occurred more abruptly at lower velocities as compared to the low-subcooling-recessed and flush cases. For velocities of 3 and 4 m/s and 20°C subcooling, initial nucleation, bubble layer growth and vapor sheet growth occurred as described previously with the exception of any instability point. The vapor sheet grew to cover about 60% of the heated surface before CHF.

Results for 35°C subcooling are comparable with those for 20°C subcooling but, with the notable absence of any flow instabilities. Comparing Figs. 5.13 and 5.14, it can be seen that protrusion height has less of an effect at higher subcooling. This may be due in part to the larger contribution of single phase heat transfer. Unlike water, and to a lesser extent R-12, FC-72 has a low latent to sensible heat ratio, 3.8 and 2.2 for $\Delta T_{sub} = 20$ and 35°C respectively. As noted in Fig. 5.11, CHF for 4 m/s and 35°C subcooling was not attained due to failure of the nichrome heater wire. However, readings prior to failure indicated an increase of more than 20%.

The behavior of CHF with h_p is intriguing. Recall Figs. 5.13 and 5.14; for a given h_p , a reduction in CHF occurred for a low flow velocity. As velocity increased, the magnitude of this reduction decreased and an *increase* in CHF was realized in some instances. For $h_p = 0.635$ mm, a 20% increase was gained for a flow velocity of 3 m/s. This translated into 50% increase in power dissipation which is the real goal of electronics cooling. Power dissipation is simply the product of heat flux and area. If

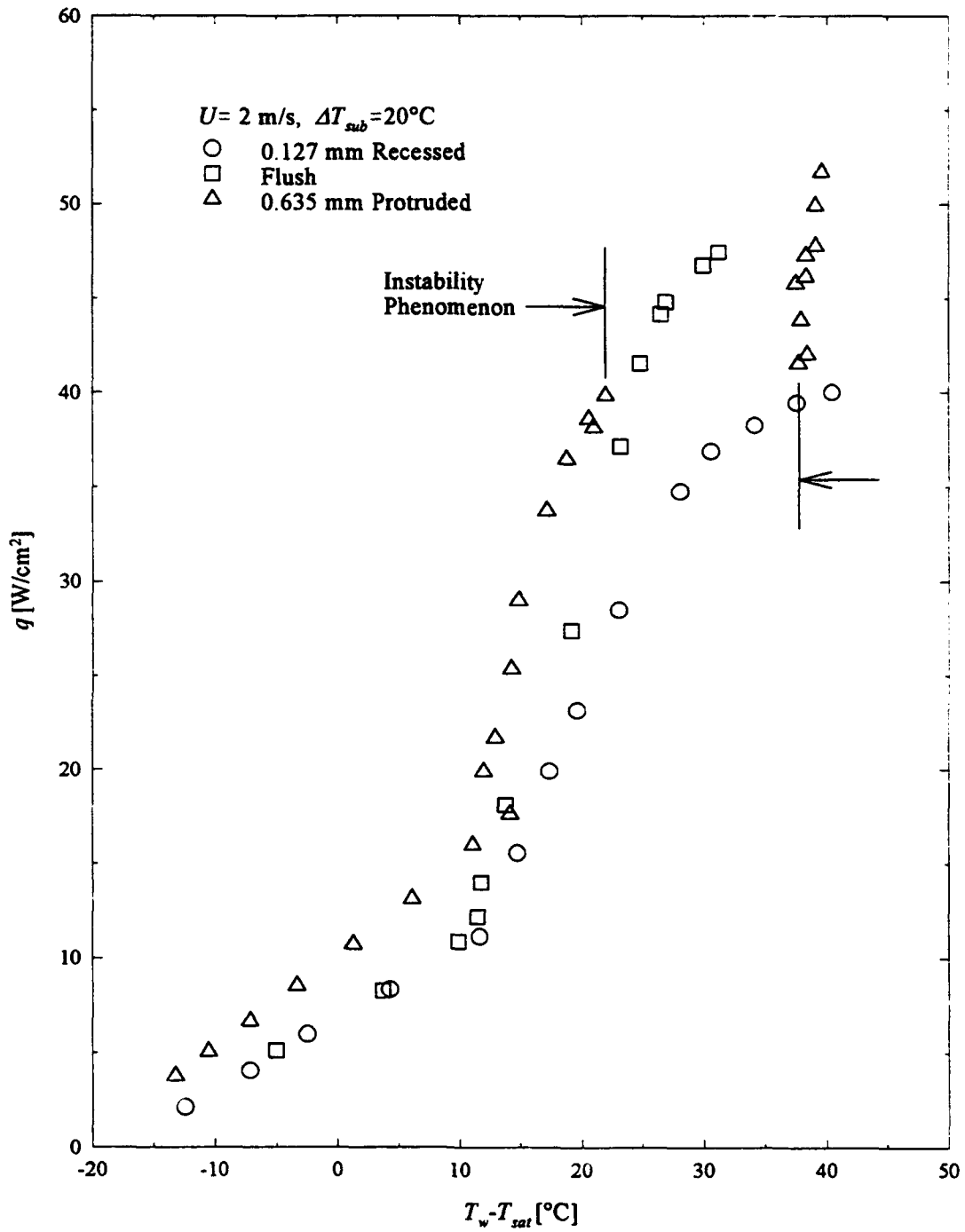


Figure 5.16 Behavior of boiling curve with heater height.

CHF increases with heater height, this product increases at a greater rate since exposed area also increases. For example, at 20°C subcooling and a flow velocity of 2 m/s, $q_M / q_{M, Flush} = 1$ for $h_p = 0.635$ mm. Considering the increase in surface area, power dissipation is improved by a factor of 1.27. Figures 5.17 and 5.18 illustrate how dramatically power dissipation increases with velocity for various h_p .

Figure 5.17 also shows that CHF becomes a strong function of U above a certain velocity, 3, 2, and 1 m/s for $h_p = 0.229$, 0.457 and 0.635 mm respectively. Figure 5.18 shows the same behavior exists for all velocities at 35°C subcooling. Because CHF is a stronger function of U for the protruded surface than for the flush surface, there is a point for each h_p where $q_M / q_{M, Flush} = 1$. Consequently, an enhancement of boiling heat transfer may be gained for sufficiently large h_p and/or U . A possible explanation of this increase is that protrusion of the surface creates a favorable flow pattern which has an effect only at higher velocities. The latter two panels of Fig. 5.15 also illustrate by the narrowing of the vapor blanket that liquid may be feeding from the sides at the downstream portion of the surface. The narrowing of the vapor blanket becomes more pronounced with velocity. Because CHF occurs first at the downstream portion of the top surface, liquid feeding from the sides at this location may be sustaining nucleate boiling.

The present results, nevertheless, agree with those of Gu et al.²⁴ and McGillis et al.²⁸ both of whom found only a reduction in CHF. Gu et al. obtained results for surface heights within ± 0.1 mm of flush and a flow velocity and subcooling of 2 m/s and 10°C, respectively. Figure 5.13 clearly suggests that a reduction is to be expected for these conditions. As mentioned previously, McGillis et al. obtained results for $h_p = 0.8$, 1.6, and 2.4 mm over a velocity and subcooling range of 0.10 to 1.04 m/s and 20 to 40°C respectively. Detailed results for $h_p = 0.8$ and 1.6 mm showed approximately equivalent values of CHF over the entire range of conditions mentioned. These results and those of Fig. 5.13 imply a decaying rate and possibly limiting value of CHF reduction for increasing h_p . If this is true, it can be inferred by extrapolation of the data in Figs. 5.13 and 5.14 that the present results also agree with those of McGillis et al.²⁸. Another indication of agreement is that a 25% reduction in CHF was reported for $h_p = 0.8$ mm and a velocity and subcooling of 1.04 m/s and 20°C respectively²⁸. By comparison with the

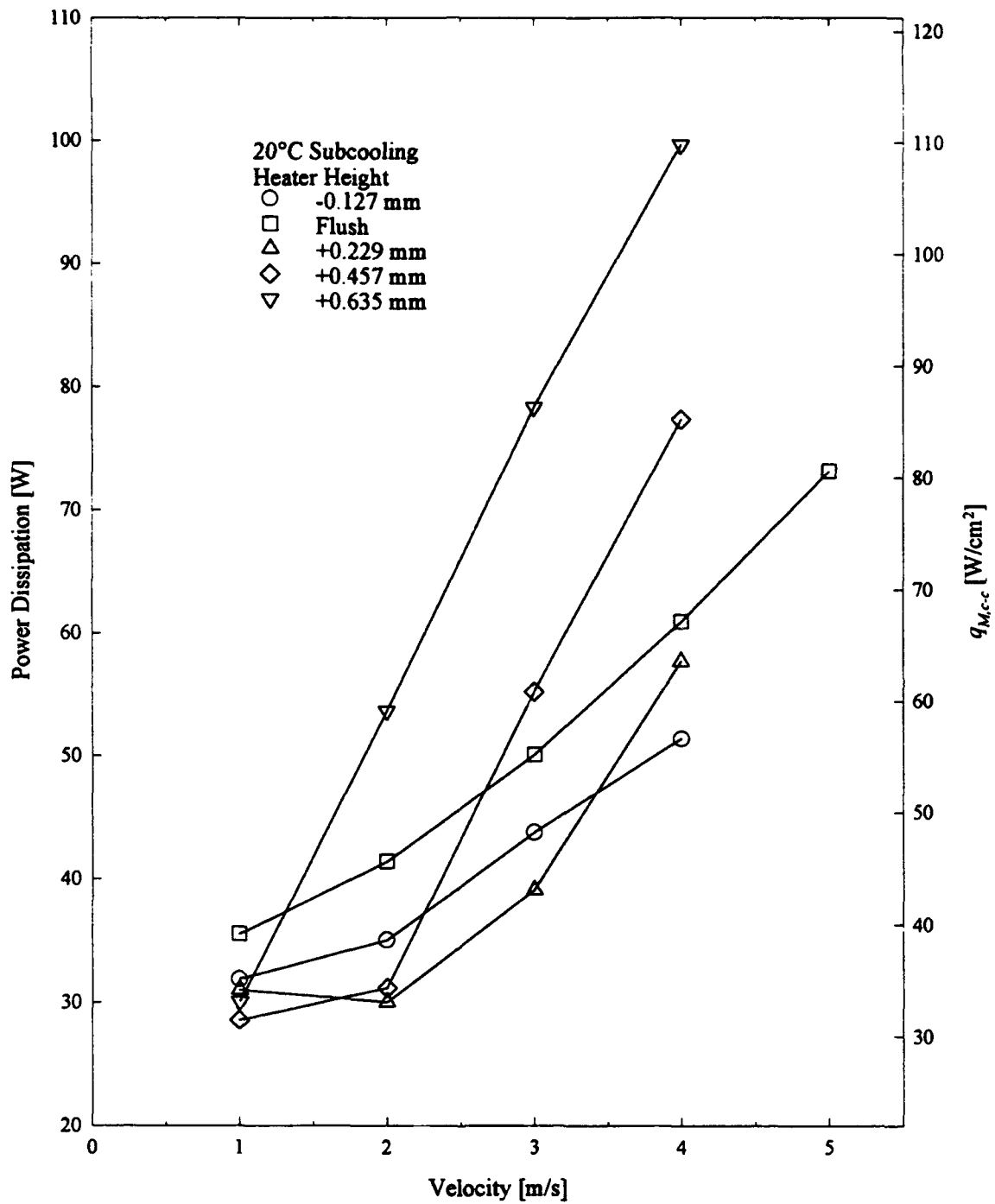


Figure 5.17 Variation of maximum power dissipation with h_p and U for $\Delta T_{sub}=20^\circ\text{C}$.

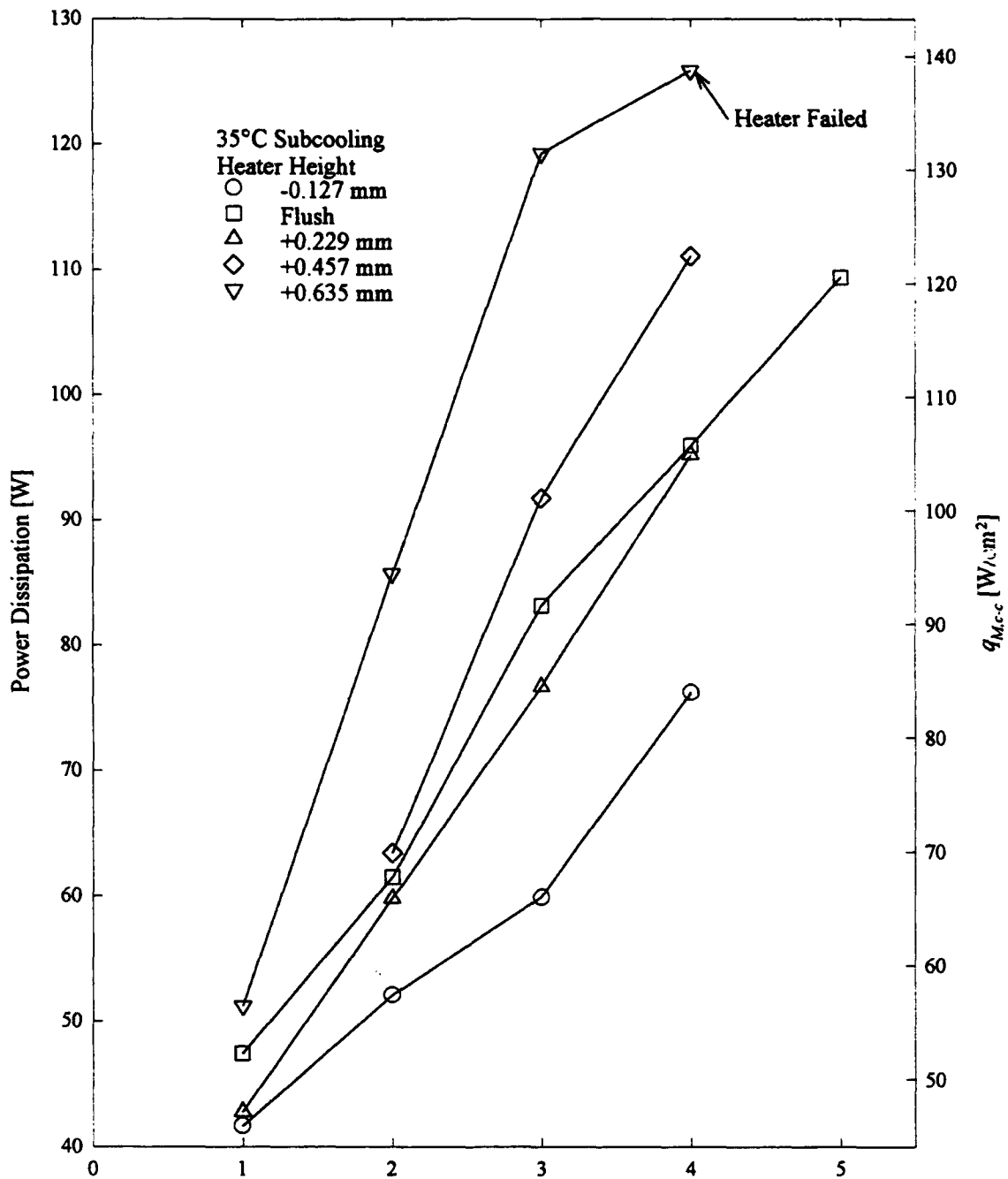


Figure 5.18 Variation of maximum power dissipation with h_p and U for $\Delta T_{sub}=35^\circ C$.

present results, a 27% reduction was found for $h_p = 0.635$ mm. and a velocity and subcooling of 1 m/s and 20°C respectively. The results of McGillis et al. and the present investigation suggest that CHF is less a function of h_p at lower velocities. McGillis et al. attribute this to a predominant pool boiling mechanism.

The most significant discovery is that for sufficiently large surface height and/or flow velocity, an increase in CHF is obtained. Not only is CHF increased, but power dissipation is increased even more because of increased surface area. This fact should be considered along with CHF by those designing cooling schemes for electronic components.

5.4 Correlation of Protruded Surface CHF Results

Correlation of the CHF results was attempted only for the protruded surface results since these are considered to be the only quantified results of interest to cooling system designers. Furthermore, the complex nature of CHF versus protrusion height makes correlation of these results difficult enough. Figure 5.19 shows how the data for $h_p \geq 0$ compare to Eqs. (5.1) and (5.2). As may be seen, a general trend with velocity or subcooling is absent.

Experimental data for the single-phase heat transfer coefficient of similar geometries have been correlated as a function of several variables. Roeller and Webb¹⁶³, use the flow channel dimensions, h and w , and the heated protrusion dimensions; protrusion width, w_p , protrusion length, l_p , and the protrusion height, h_p , for their correlation. Based on extensive experimental data, Roeller and Webb derived the following correlation

$$\overline{Nu} = 0.150 Re^{0.632} (A^*)^{-0.455} (h/l_p)^{-0.727} \quad (5.3)$$

where

$$A^* = 1 - (w_p/w)(h_p/h) \quad (5.4)$$

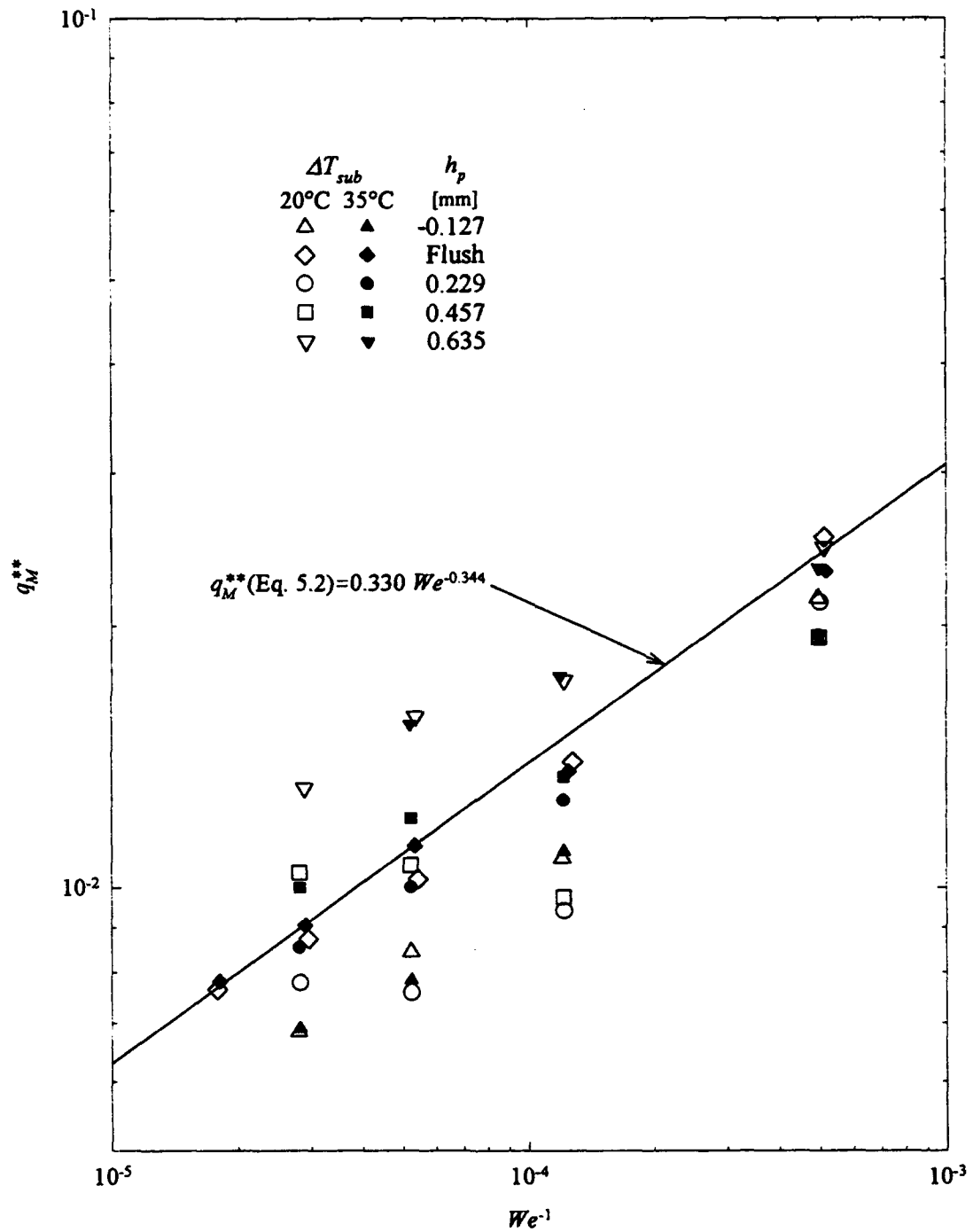


Figure 5.19 Comparison of protruded surface data with Eqs. (5.1) and (5.2).

For the present geometry, w_p and l_p are equivalent to the heated length, L . Because the channel height and width were held constant for the present experiments, a correction of the form

$$\varepsilon_p = [1 - (h_p / D_h)]^a \quad (5.5)$$

was multiplicatively combined with the denominator of Eq. (5.2). This form proved to be very unsuccessful in correlating the data. Through much trial and error, the following correction was found to correlate the data with reasonable success:

$$\varepsilon_p = (h_p / D_h)^{0.428} [(h_p / D_h)^{3.048} Re^{0.794} - 1.570] \quad (5.6)$$

This correction to Eqs. (5.1) and (5.2) fit the protruded surface data with a mean absolute error of 11.4%. The correlation coefficient, i_{xy} , was 0.88. Figure 5.20 shows the results of the above effort. While Figs. 5.13 and 5.14 indicate that the relative difference of flush and nonflush surface CHF is dependent on subcooling, any attempt to add subcooling to the above correction was met with failure. Figure 5.20 indicates that there is some slight dependence on subcooling however.

5.5 Conclusions

5.5.1 Flush

1. The data for the test section of this chapter indicate that channel width plays a minor role in determining the CHF of flush surfaces. The results are insufficient to make the same conclusion for nonflush heated surfaces. Equations (3.31) and (3.32) were modified to include the effect of channel width and are presented as Eqs. (5.1) and (5.2).

5.5.2 Recessed Surface

1. A reduction of CHF occurred for all combinations of velocity and subcooling. The percent reduction increased with either increased velocity, or increased subcooling.

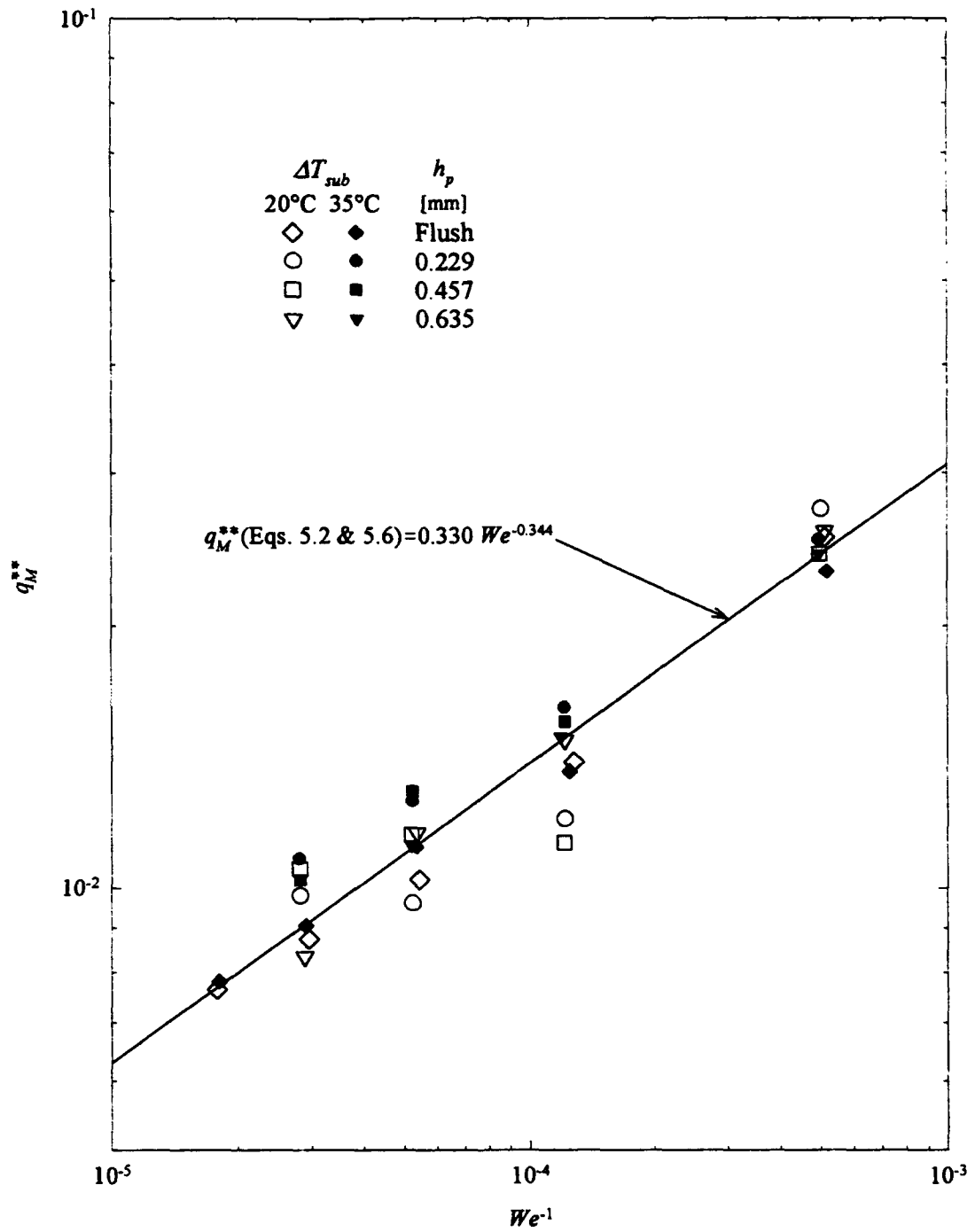


Figure 5.20 Comparison of protruded surface data with Eqs. (5.1), (5.2), and (5.6).

2. The recessed height of 0.127 mm creates what is considered a very shallow cavity. Further recession of the surface should yield even smaller values of CHF because the vapor removal mechanism is compromised even more.

5.5.3 Protruded Surface

1. For a given surface height, a decrease in $q_M / q_{M, Flush}$ is experienced at low velocities (< 2 m/s for most cases). As velocity increases beyond 2 m/s, $q_M / q_{M, Flush}$ increases to the point where $q_M / q_{M, Flush} = 1$. As heater height increases, the velocity for the condition $q_M / q_{M, Flush} = 1$ decreases.

2. The net increase in CHF at higher velocities may be due to enhanced liquid flow from the sides.

3. Both degradation and enhancement of heat transfer effectiveness are diminished with increased subcooling. This may be explained in part by the larger contribution of single phase heat transfer. The rate of enhancement also diminishes with increasing velocity for both subcoolings.

4. A flow instability phenomenon occurred for heater heights of 0.457 and 0.635 mm. In both cases, the instability occurred at a velocity and subcooling of 2 m/s and 20°C respectively.

5. A linear dependence of q_M on U is also suggested for protruded height cases by the data of Figs. 5.17 and 5.18. This dependence occurs at $U > 3$ m/s for a heater height of 0.229 mm and at lesser velocities for the larger heights.

6. A significant increase in total power dissipated is gained by increasing heater height (see Figs. 5.17 and 5.18). This is because of the combined contributions of increased q_M and greater exposed surface area. For a heater height of 0.635 mm and subcooling of 20°C, a 60% increase in power dissipated (i.e., $q_{M, c-c}$), occurred for velocities greater than 2 m/s.

7. If manufacturing complexity is considered, the enhancement of CHF for velocities of 3 and 4 m/s compares well to the enhancement obtained by Mudawar and Maddox²⁷ with the use of structured surfaces.

8. A correction for protrusion height was obtained for Eqs. (5.1) and (5.2). This correction, Eq. (5.6), fit the data with moderate success.

Chapter 6 OTHER EFFECTS OF PROTRUDING CHIP GEOMETRY ON BOILING AND CHF

In the preceding chapter, a copper block heated from below was used to simulate an electronic chip protruding into a rectangular flow channel. Boiling occurred predominantly on the front, top and rear faces of the block. For a given protrusion height, the critical heat flux (based on exposed area) was reduced at low velocities, was equal at some intermediate velocity and increased at higher velocities as compared to the case where the heated surface was flush. As protrusion height was increased, the break even velocity decreased and the increase in CHF was greater for a given velocity greater than the break even velocity. The net increase in CHF was unexpected and it was suspected to be due in part to the strong interaction between vapor emanating from the front face, (the upstream face normal to the direction of flow), and that from the top of the heated protrusion. Thus, the present effort was undertaken to determine the contributions of heat transfer from the sides and the top of the protruding block and how it relates to CHF.

6.1 Experimental Apparatus – Thin Foil Heater

The experimental apparatus is unchanged from that described in Chapter 5 with the exception of the heater. Two different heater assemblies were used, 1) a resistively heated thin foil and 2) and the copper block heated from below described in Chapter 5. The thin foil heater was designed such that boiling would occur only from the top of the protrusion. This heater was made of 0.025-mm-thick Monel 400 mounted on top of a low thermal conductivity (0.29 W/m-K) G-7 block as shown in Fig. 6.1. The Monel foil was soldered to thin copper strips which were slit lengthwise to provide voltage sensing taps at the heater. The resistance of the copper leads was negligible compared to the foil, however. Heat conduction through the leads was suppressed by bending the copper leads inward so that they would be insulated by additional pieces of G-7. The assembly was enclosed in the same Glastherm HT cylinder, Fig. 5.3.

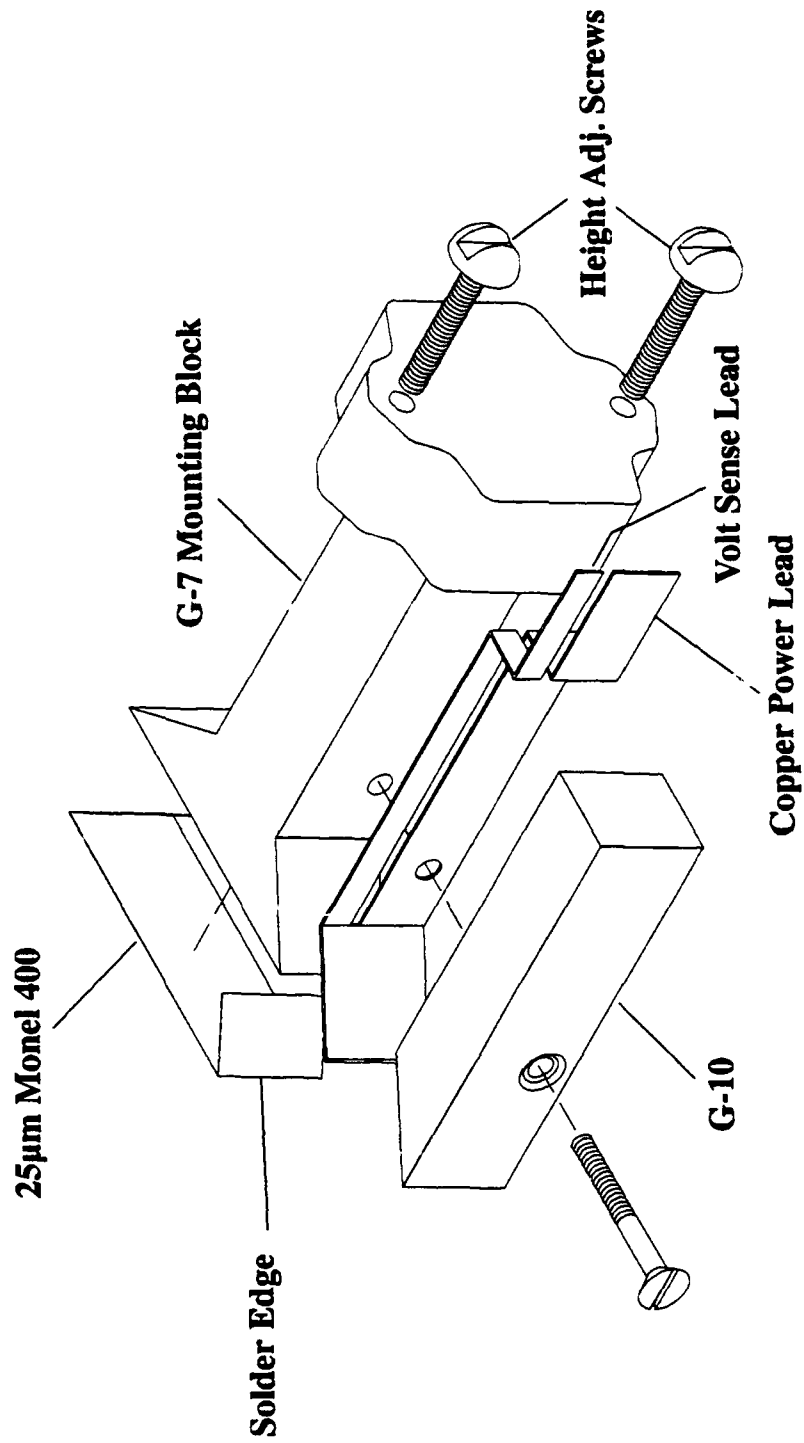


Figure 6.1 Thin foil heater assembly.

It was originally planned to obtain the average temperature of the foil heater by determining the electrical resistance from voltage and current measurements and knowing the resistance as a function of temperature. A detailed uncertainty analysis was performed to determine the best choices for the foil material and thickness. A minimum thickness of 0.025 mm was chosen to prevent foil damage during assembly. In retrospect, a minimum thickness of 0.01 would have sufficed also. The foil material properties governing the accuracy of the temperature measurement are the resistivity, ρ , and the temperature coefficient of resistance, α_ρ . The uncertainty analysis, presented in Appendix E, showed that a material with a high $\rho \cdot \alpha_\rho$ product would be the best choice. This interesting result is in contrast to that for RTDs and is a consequence of the foil acting as both heater and RTD. Because the foil is resistively heated, the electrical resistance must be obtained indirectly through voltage drop and current measurements, rather than directly as with the case for an RTD. Consequently, the foil resistivity comes into play. For RTDs, the temperature coefficient of resistance governs the accuracy of the device. Pure metals generally have a high α_ρ and low ρ , while alloys show the opposite trend. Platinum, nickel, tantalum, their alloys; and alloys of nichrome, stainless steel, and Monel were investigated. A particular alloy of Monel, Monel 400, had the highest reported product of $\rho \cdot \alpha_\rho$. Upon calibrating the foil heater, it was found that the temperature coefficient of resistance was much less than that reported by the manufacturer and a design incorporating thermocouples was resorted to.

Five 0.076-mm-diameter wire, type T thermocouples were subsequently used to monitor the temperature of the foil. Four of these are imbedded in grooves on the top of the G-7 block. Figure 6.2 shows that three of the four are used to measure the streamwise temperature variation, while two were used to measure the spanwise variation. The grooves were carefully contoured to ensure that the thermocouple beads were as close as possible to the backside of the foil. The foil was epoxied to the G-7 block using Omegabond 200 epoxy (Omega Engineering, Inc.) thus ensuring good thermal contact between the thermocouples and foil. A cure time of 8 hours at 120°C was found to be optimal. It is estimated that the thermocouple beads were separated by a thin layer of

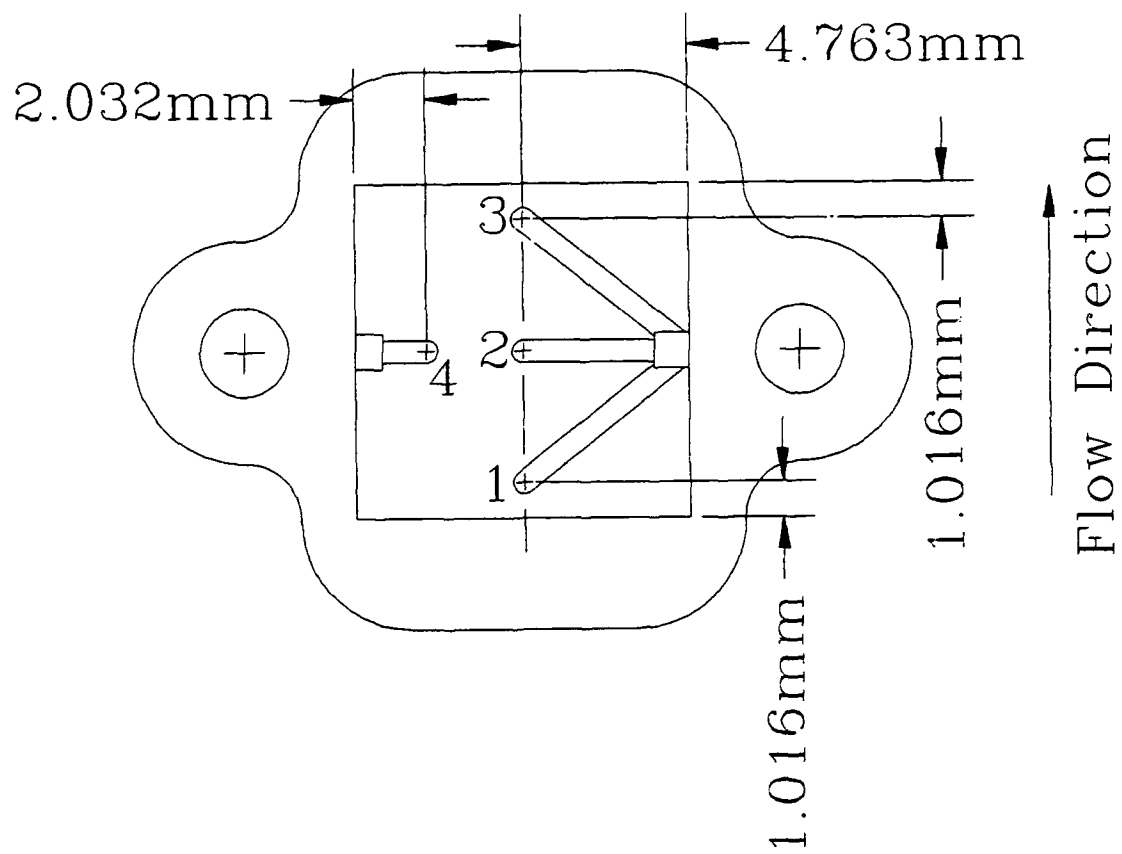


Figure 6.2 Foil heater thermocouple locations.

epoxy no more than 0.04 mm thick. The fifth thermocouple was located 0.25 mm below the center of the surface and was used to estimate the heat loss through the G-7.

The copper block test section is the same as described in Chapter 5 with the addition of a small block of insulating to the front face of the copper block. The insulating material covered either half or all of the front face of the block and eliminated boiling from the covered portion. Figure 6.3 shows the exact dimensions and location of these alternate pieces of insulation. The surface of the copper foil was prepared in the same way as described in Chapter 2 for the copper surface.

6.2 Uncertainty Analysis – Thin Foil Heater

The Hewlett Packard 3852A data acquisition system was used to make all voltage and temperature measurements. This device has a resolution of 0.02°C and rated accuracies of 0.5 and 0.65°C for thermocouple types K and T respectively. The data acquisition unit and type T thermocouples were compared to a precision digital RTD, (0.03°C rated accuracy), over the range of interest and the system accuracy was found to actually be within 0.3°C. The uncertainties for the tests with the copper block/thick film resistor test section were described in detail in Chapter 5, and are described in more detail in Appendix C. The uncertainty of the thin foil heater test section are described below.

For all tests with the foil heater, CHF was calculated from the electrical power measurement. The standard Kline and McClintock³¹ approach to random uncertainty calculation yields an uncertainty of 0.27%. A one-dimensional heat conduction assumption was made to estimate the heat loss from the back of the foil through the G-7 substrate. This method predicted less than one percent heat loss for heat fluxes greater than 15 W/cm². Because of assuming one-dimensional heat conduction, this method may underpredict the heat loss, but the error would still be small. Thus, no correction was made to the foil heater results.

The surface thermocouples fluctuated by as much as 1°C during testing depending on the location of the nucleation sites. The thermocouples would vary most when near the edge of the advancing nucleation sites, (see Fig. 5.15). Thermocouples

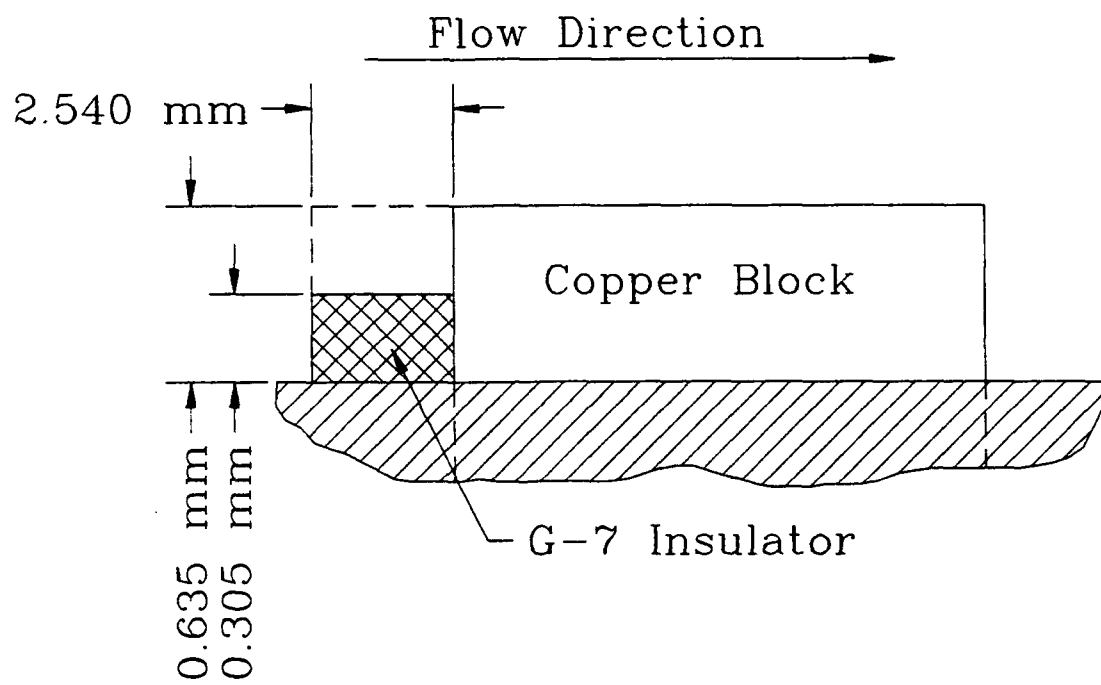


Figure 6.3 Front face insulator details.

well within the zone of nucleation were the most steady, fluctuating only 0.3°C. As mentioned previously, Kenning³² has shown that large errors may occur in the surface temperature measurement of thin foil heaters. These errors are caused by the large variation in heat flux below a single bubble at a nucleation site. The average heat flux at a given nucleation site also varies greatly from that between nucleation sites. Kenning³² measured a spatial temperature variation of 26°C for water boiling at 10 W/cm² on a stainless steel foil 0.13 mm thick.

Based on heat conduction from a cylinder of finite length, insulated on the radial boundary, and an annular step heat flux at one end, (see Appendix D), he was able to predict the temperature variation. This required fitting two constants, a and b , to the data. The constants a and b are the dimensionless inner and outer radius, respectively, of the annular step heat flux. These constants are made dimensionless with respect to S , the radius of the conduction domain of a nucleation site. The conduction domain radius is defined as:

$$S = (\pi N)^{-1/2} \quad (6.1)$$

where N is the nucleation site density. Characteristic values of $b^2 = 0.66$, $a^2 = 0$ and $b^2 = 0.36$, $a^2 = 0.30$ were given for the aforementioned water/stainless steel heater combination.

Kenning³² indicates that the product bS is approximately equal to the maximum bubble radius. For the current experiments, $bS \approx 0.15$ mm. Making two common assumptions, 1) that individual bubble centers are separated by twice the bubble

Table 6.1 Predicted temperature variation.

a^2	b^2	ΔT
0.00	0.66	4.8
0.55	0.36	4.8
0.25	1.00	6.0

departure radius and 2) that the nucleation sites are in a packed square grid, Eq. (5.1) gives $S = 0.16$. Thus, $b \approx 1.00$ and a conservative value of 0.5 is assigned to a . Results of this analysis are presented in Table 6.1. These values are over predicted because the conduction analysis and constants a and b were obtained for a foil heater supported in tension at both ends. The foil heater of the present study is in good thermal contact with a substrate. Although the substrate is of low thermal conductivity, it will still act in reducing site-to-site thermal gradients. Furthermore, these results are much lower than those reported³² because the high bubble density under high flux conditions creates a more uniform heat flux pattern on the surface. Also, maximum bubble sizes are much smaller under subcooled, force flow conditions thus, further damping thermal gradients.

6.3 Experimental Results

Results have been obtained for two heater configurations: 1) a thin foil heater and 2) a copper block heated from below. The effects of large scale (0.12-mm amplitude ripples) surface roughness and protrusion height were studied for the thin foil heater configuration. The effects of protrusion height and insulation of the front face were studied for the copper block heated from below. Data were obtained for velocities of 1 to 5 m/s and subcoolings of 20 to 35°C, respectively. However, foil heater data were not obtained for a subcooling 35°C.

6.3.1 Foil Heater Test Section

Because of the complexity of the thin foil heater configuration, many failures were experienced before an optimal assembly procedure was found. As a result, there are few quantitative results for the smooth foil and some of the results for the rippled foil were derived from single sample measurements. The qualitative results were significant, however, and are reported herein.

Incipient temperature overshoot was generally much higher for the thin foil configuration than previously noted in Chapter 3 for the copper block configuration. A maximum incipient overshoot of 20°C was measured for the smooth foil, 20°C

subcooling, and a velocity of 1 m/s. This could be explained by the different wettabilities of copper and Monel and a different cavity size distribution. Unlike the copper surfaces, the foil was sanded in one direction only. This was necessary to avoid damage. Furthermore, the very thin foil did not distribute the heat through itself nearly as well as the copper block test section. For the copper block, the surface temperature distribution varied by only 2.2°C. Thus, similar conditions existed over the surface and incipience occurred at the rear most edge of the heater where the thermal boundary layer was first sufficient for nucleation. For the foil heater, large thermal gradients were maintained and variations in the surface temperature could be significant, (see Fig. 6.4). Thus, incipience could occur more randomly over the surface at certain hot spots. Even if incipience occurred at a single point, substantial increases in heat could be necessary before more significant nucleation of the surface occurred. Incipient overshoot generally decreased with velocity which is in agreement with the trend noted in Chapter 3.

Figure 6.4 shows how the surface temperature progresses with heat flux for a typical case. The temperatures are plotted in reference to the upstream thermocouple, T_1 , (see Fig. 6.2 for key to thermocouple numbers). It may be seen that the downstream thermocouple, T_3 , is the hottest with the center thermocouple, T_2 , slightly cooler and the spanwise thermocouple, T_4 , the coolest. This trend is obviously expected with the possible exception of the spanwise temperature. As heat flux increases, nucleation occurs at the downstream thermocouple and a sharp drop in temperature ensues. With further increase in heat flux, nucleation occurs at the center and side locations. Throughout the NBR, 15 - 25 W/cm², the streamwise variation in temperature is very small, < 1°C. As the CHF is approached, the downstream location begins to rise dramatically with temperature. Also, the center location rises in temperature as CHF is approached, but less dramatically. This trend supports the dryout model proposed by Haramura and Katto⁹⁴ and adapted to the present geometry by Mudawar and Maddox.¹⁹

Figure 6.4 also shows that the side thermocouple remains about 2°C cooler throughout the single-phase and boiling regimes. Because the streamwise change in surface wetting yields less than a 1°C difference in temperature variation, the relatively larger spanwise variation indicates that there is significant flow of liquid from the sides

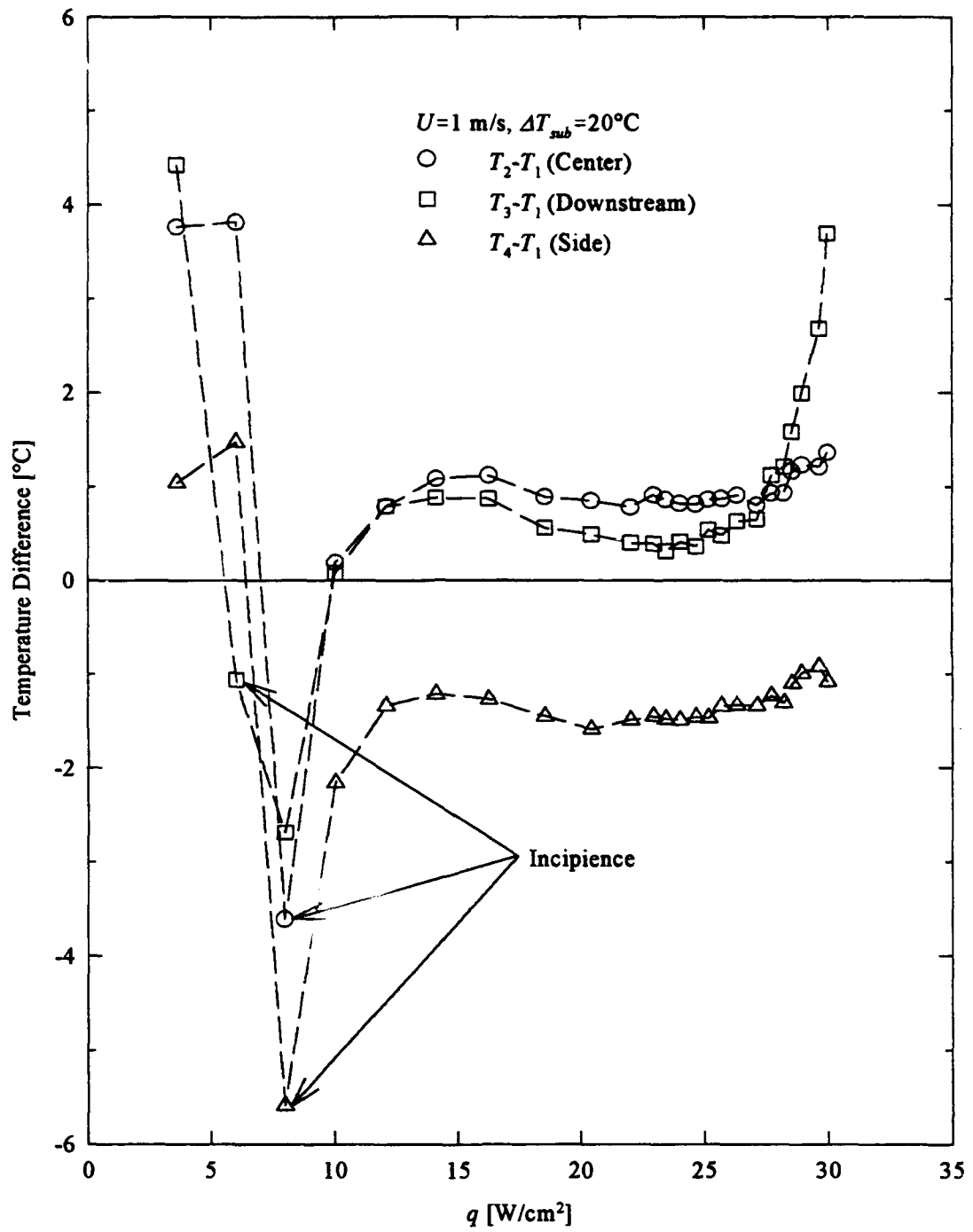


Figure 6.4 Variation of surface temperatures relative to T_1 with heat flux.

of the heated surface. The change in boiling mechanisms described by Mudawar and Maddox¹⁹, (see Fig. 3.4), is not supported by the same data since no significant change in the above trends was witnessed throughout the range of $1 \leq U \leq 4$ m/s.

CHF for the foil heater was generally 25% lower than that of the copper block heater for the same flow velocity and subcooling. This is to be expected. It has been known for some time that below a certain thickness, CHF begins to decrease with decreasing thickness. Bernath¹⁶⁴ surveyed a wealth of data and may have been the first to identify the systematic effect of wall thickness on pool boiling CHF. Carne¹⁶⁵ experimentally studied the effect of heater thickness on CHF for a number of organic liquids. He found that the same trend existed irregardless of the fluid used and that the results closely matched the curve suggested by Bernath.¹⁶⁴ Sharp¹⁶⁶ made an exhaustive study of pool boiling from various materials of small thickness and found that boiling heat transfer coefficient was dependent upon the material's thermal effusivity, $\sqrt{\rho ck}$. Sharp also suggested the trend of decreasing heat transfer coefficient with decreasing wall thickness. The thermal effusivity often arises in the solution of transient heat conduction problems. Dzakowic and Frost¹⁶⁷ obtained the same conclusions through a mathematical model of microlayer evaporation. Houchin and Lienhard¹⁶⁸ may have been the first to study the combined effects of heater material and heater wall thickness on pool boiling CHF. Based on theoretical models, they attempted to correlate their data to either $t \cdot k$ or $t \cdot \rho \cdot c$, and concluded that the latter grouping provided the best results. Houchin and Lienhard also found that CHF was independent of this term above a certain critical value. Later, Guglielmini and Nannei⁸⁰ showed that pool boiling CHF was indeed a function of both t and $\sqrt{\rho ck}$, but did not offer much additional information. Lin and Westwater¹⁶⁹ made the same conclusion with the additional discovery that the wall superheat at CHF increases with decreasing $\sqrt{\rho ck}$. Pan and Lin¹⁰⁷ successfully modeled the change of wall superheat with $\sqrt{\rho ck}$, but failed to accomplish the same for the variation of CHF.

Only recently has a comprehensive correlation of CHF to these effects been proposed. Carvalho and Bergles⁸¹ made an extensive experimental study and proposed the following correlation

$$\frac{q_M}{q_{asy}} = 1 - \frac{0.1712}{(t \sqrt{\rho ck})^{0.3334}} \quad (6.2)$$

where q_{asy} is the asymptotic value of q_M as $t\sqrt{\rho ck}$ approaches the critical value. The material properties are in SI units. Setting $q_M/q_{asy} = 0.9$, values of the critical thickness, t_{asy} , may be found. Table 6.2 gives representative values as found by Carvalho and Bergles. These values are substantially greater than those found experimentally by Guglielmini and Nannei.⁸⁰ At the same time that Carvalho and Bergles⁸¹ presented the results of their long study, Bar-Cohen and McNeil⁸³ presented the results of a comprehensive study of past results for CHF as a function of t and $\sqrt{\rho ck}$. They successfully correlated this wealth of data with the following correlation:

$$\frac{q_M}{q_{asy}} = \frac{t\sqrt{\rho ck}}{t\sqrt{\rho ck} + 0.8} \quad (6.3)$$

where the material properties are also in SI units. This equation predicts slightly higher values of t_{asy} than Eq. (6.2). Table 6.2 also shows characteristic values of t_{asy} as

Table 6.2 Predicted values of asymptotic thickness and q_M/q_{asy} for current experiments.

Heater Material	$\sqrt{\rho ck}$ [J/m ² Ks ^{-1/2}]	Equation (6.2)		Equation (6.3)	
		t_{asy} [mm]	$q_M/q_{asy} _{t=0.025}$	t_{asy} [mm]	$q_M/q_{asy} _{t=0.025}$
alumina, 96%	8,537.5	0.59	0.72	0.84	0.21
copper	35,545.0	0.14	0.82	0.2	0.53
Monel 400	9,067.7	0.55	0.72	0.79	0.22
nichrome	6,506.6	0.77	0.69	1.11	0.17
nickel	17,282.5	0.29	0.77	0.42	0.35
silicon	15,669.3	0.32	0.77	0.46	0.33
silicon carbide	20,394.5	0.25	0.79	0.35	0.39
stainless steel	7,763.9	0.64	0.71	0.93	0.20

predicted by Eq. (6.3) and the ratio of q_M/q_{asy} as predicted by both correlations for the current experiments, ($t = 0.025$ mm). Alumina, 96% pure, is one of the most common large scale chip substrates. Silicon carbide is more commonly used for high power applications. Table 6.2 indicates that silicon carbide is a better choice for chip substrate when boiling heat transfer is considered.

While Eqs. (6.2) and (6.3) predict similar values of t_{asy} , Eq. (6.3) predicts a much more severe effect of wall thickness for the current experiments. However, the applicability of either Eq. (6.2) or (6.3) to the present experiments is moot because these correlations were derived from pool boiling experimental results. Very little research has been performed with regard to the effects of $\sqrt{\rho ck}$ and wall thickness on forced convective CHF. Tippets¹⁷⁰ found that CHF was reduced by about 20% for the forced flow of high pressure water over 0.15-mm-thick stainless steel heater ribbons as compared to 0.25-mm-thick ribbons. Del Valle and Kenning¹⁷¹ found that CHF decreased about 40% for a 0.08 mm thick heater as compared to a 0.20 mm thick heater. Their experiments were also for the flow boiling of water of stainless steel ribbons. Del Valle and Kenning also suggested that the asymptotic thickness was equal to about 0.50 mm. This is comparable to the value shown for Eq. (6.2) in Table 6.2. There is some indication that the effect of heater thickness may be less significant in forced flow boiling. McAdams et al.⁵³ found that for the forced flow of water over a heated cylinder of 0.30 mm thickness, the CHF was not effected by the small wall thickness for velocities of 1.22 and 3.66 m/s. However, wall thickness reduced the CHF, as compared to that for thick wall cylinders, at a velocity of 0.30 m/s. One explanation may be the fact that bubble departure diameters are smaller and departure frequencies are higher for flow boiling as compare to pool boiling. Therefore, the dry spots may be smaller and shorter lived and the thermal capacity of the heater is not as important for mitigating the transient temperature rise. Finally, Akhanda and James⁸² found only a marginal effect of heater thickness on CHF for thicknesses of 0.54 and 1.60 mm. Their results were also obtained for the flow boiling of water over stainless steel ribbons. Because their heater thicknesses were relatively thick, the results are felt to be in agreement with those above.

The quantity $t\sqrt{\rho ck}$ is sometimes called the "heater thermal activity." What it really governs is the ability of the heater to mitigate a sudden hot spot. As the heater thermal activity decreases below the critical value, the heat below an intermittently created dry spot is not as effectively distributed to other parts of the surface where effective boiling heat transfer continues. As a result, the heater below the dry spot gets even hotter and eventually reaches the Leidenfrost temperature where wetting cannot occur. For the present experiments, CHF was found to be very sensitive to small imperfections in the foil surface. These imperfections created premature dry out and CHF could occur even at the leading edge of the heater. Dry out propagated so slowly that complete dryout of the surface took more than 5 seconds as opposed to the copper surface where complete dryout occurred in a fraction of a second. This implies that the nonuniform nature of heat generation within electronic chips could have a significant impact on CHF. This problem may not exist for power electronics where cooling is accomplished through a copper base typically 2.5 mm in thickness.

An example of more substantial surface imperfections is rippling of the foil caused during assembly. Results for the flush condition, rippled surface, are substantially lower than those obtained for a smooth surface. Reductions in CHF of 18 and 24% over the smooth foil were measured for flow velocities of 1 and 2 m/s, respectively. The ripples had an amplitude of no greater than 0.12 mm and a nonuniform distribution and frequency. Stating that the rippled surface is flush with the flow channel wall is, of course, questionable. However, most of the roughness elements were less than 0.02 mm in amplitude and thus were of the same order as the protrusion height measurement accuracy.

Results were also obtained for a protrusion height of 0.71 mm but, only for the rippled surface. These results are the most enlightening however. In Chapter 5, it was found that for a given protrusion height, CHF would be lower than that for the flush surface at low flow velocity. As flow velocity was increased, CHF would be equal to and then greater than the value of CHF for the flush surface. As h_p increased, the increase in CHF over the flush condition also increased. It is important to note that CHF was based on the exposed area of the protruding block. Thus, any increase was actually an

enhancement of the boiling mechanism and not merely an area augmentation. Figure 6.5 compares the current data, ($h_p = 0.71$ mm), to that of Fig 5.13.

The trend for the foil heater is somewhat different than that for the copper block. The reduction in CHF at low velocity for the foil heater is much less than the same reduction for the copper block. However, the gain in CHF at higher velocities for the foil heater is less than the gain for the copper block. This latter effect may be due to the rippled surface, however. Finally, in Chapter 5 a flow instability was reported for the protruded block, 20°C subcooling, and a flow velocity of 2 m/s. The disappearance and reappearance of a sheet of vapor emanating from the front face of the protruding block was evidence of this instability. The surface temperature of the block also fluctuated with the sheet of vapor and an amplitude of more than 1°C. The instability phenomenon was completely absent from the results of the protruded foil.

The above observations are explained by the lack of any boiling from the front face of the protruding block. A smooth, uniform bubble layer evolved on the top surface in a fashion similar to that described in Chapter 5 for the flush surface. The bubble layer is thinner than the flush surface bubble layer for a given velocity. This is because higher velocity fluid near the wall for the protruded case pushes the bubbles downstream a greater rate. The higher velocity is due to a redeveloping boundary layer. This higher velocity also acts towards improving the liquid supply mechanism for nucleate boiling and thus inhibits the onset of CHF. The previously mentioned vapor sheet probably acted in impeding the flow of the higher velocity fluid thus diminishing any gains in CHF. Figure 6.6 contrasts the shape of the vapor blanket for the foil and copper block test sections. The absence of any flow instability is also owed to the lack of any boiling from the front face.

6.3.2 Copper Block Test Section

For an actual computer chip, heat is generated from within and distributed somewhat evenly over its exposed faces. It was surmised that if boiling from the front edge could be eliminated, the full enhancement of a redeveloping velocity layer would be

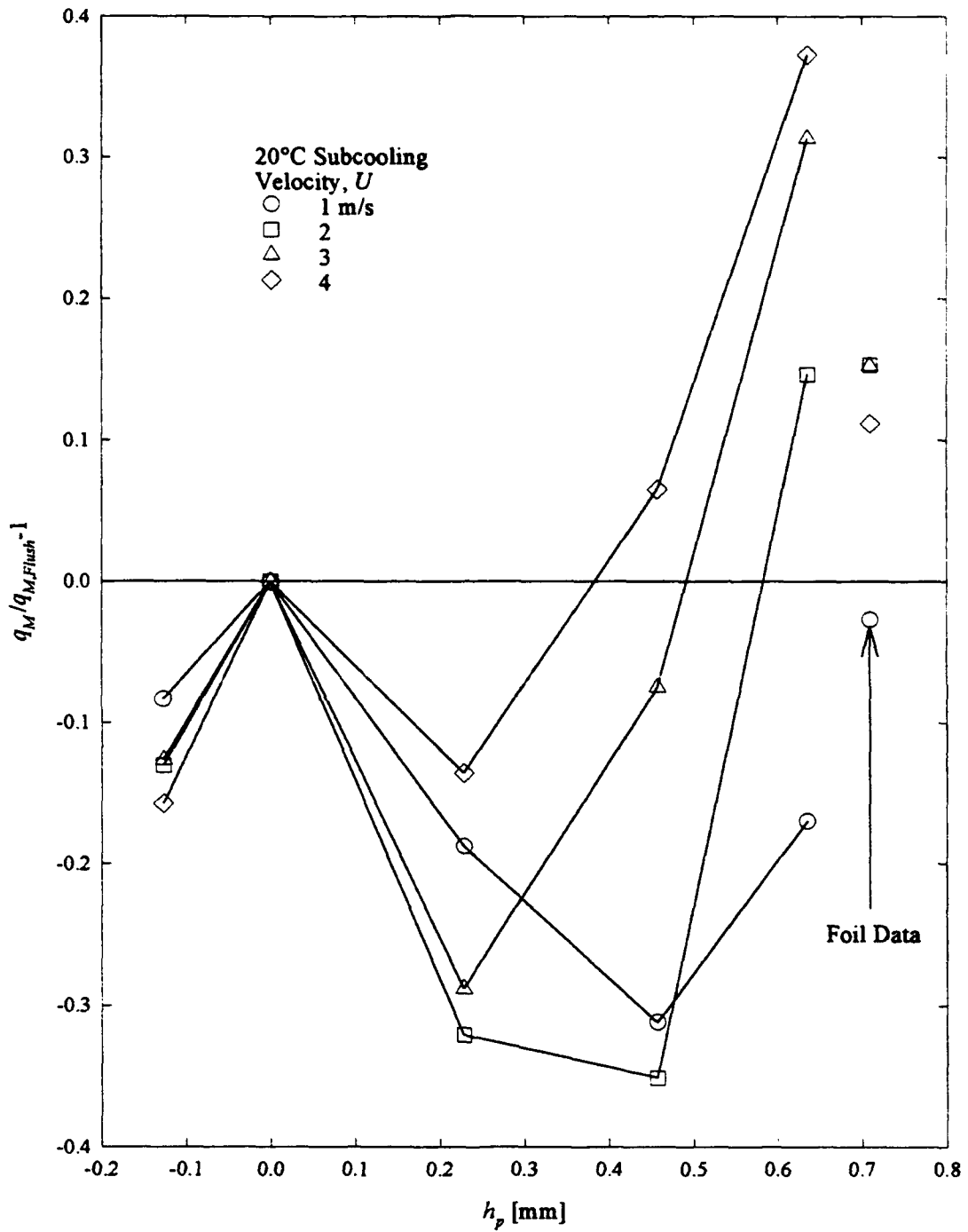


Figure 6.5 Comparison of CHF with heater height and velocity for thin and thick heaters.

Flow Direction

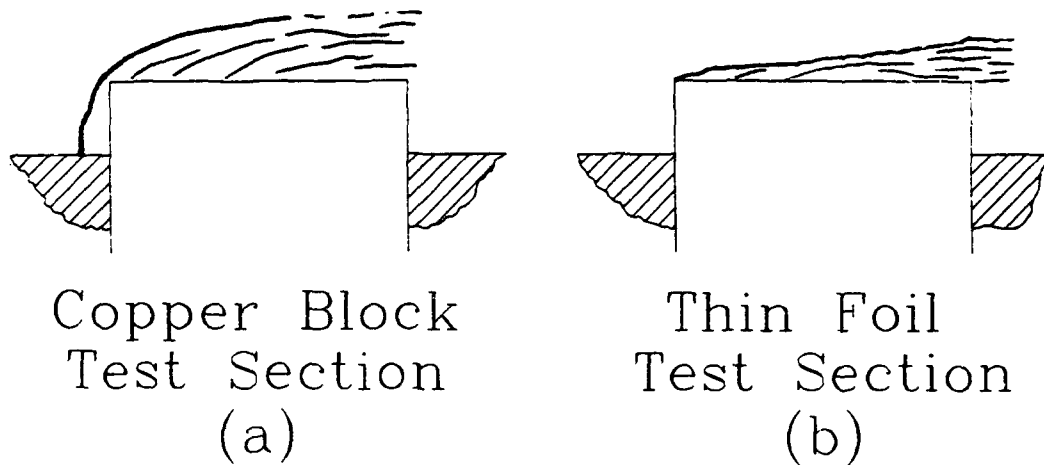


Figure 6.6 Schematic of boiling from thin and thick heater test sections.

realized. The loss of heat transfer area would amount to only 5% for the maximum protrusion height investigated. The area advantage of the remaining three sides would still be enjoyed.

Elimination of boiling from the front face was accomplished by the installation of a small block of G-7 laminated plastic, (see Fig. 6.3). The effects of the G-7 block were studied for a protrusion height of 0.635 mm. This included two cases, 100% and 48% coverage of the front face. Figure 6.7 shows that both sizes of the G-7 plastic insulator did indeed stabilize the boiling heat transfer at the 20°C subcooling, 2 m/s flow velocity condition. The aforementioned flow and heat transfer instability was completely absent. It was shown in Chapter 5 that the instability did not occur for protrusion heights up to 0.457 mm. Therefore, an even thinner piece of insulating material may suffice in stabilizing heat transfer for this condition.

Figure 6.8 shows the effect of the front face insulators on CHF. The reduction in CHF at 1 m/s was sharply reduced. Besides elimination of the instability condition, further heat transfer enhancement was not realized for velocities greater than 1 m/s. Full coverage of the front face yields essentially zero net heat flux gain over the flush condition for a subcooling of 20°C. It should be remembered that increased power dissipation is still realized. For 35°C subcooling, heat flux is actually decreased. For 48% coverage the flow instability remained absent and better heat transfer results were obtained.

The opposing effects of the insulators for $U = 1$ m/s and $U > 1$ m/s can be explained by the existence of two different liquid supply mechanisms. Mudawar and Maddox¹⁹ used flow visualization results to describe two liquid supply mechanisms for the flush condition, 1) a low speed (< 2 m/s) and, 2) a high speed (> 2 m/s) mechanism as shown in Fig. 3.4. For $U < 2$ m/s, the liquid is fed tangential to the surface from the upstream edge to the downstream edge. As a result, liquid supply to the most downstream sites is impeded and CHF is initiated at the most downstream portion of the heated surface. The vapor blanket increases in thickness with L for this case. For $U > 2$ m/s, the vapor blanket is uniform in thickness and liquid feeds from above. For this regime, CHF is much less sensitive to L as noted in Section 3.5.

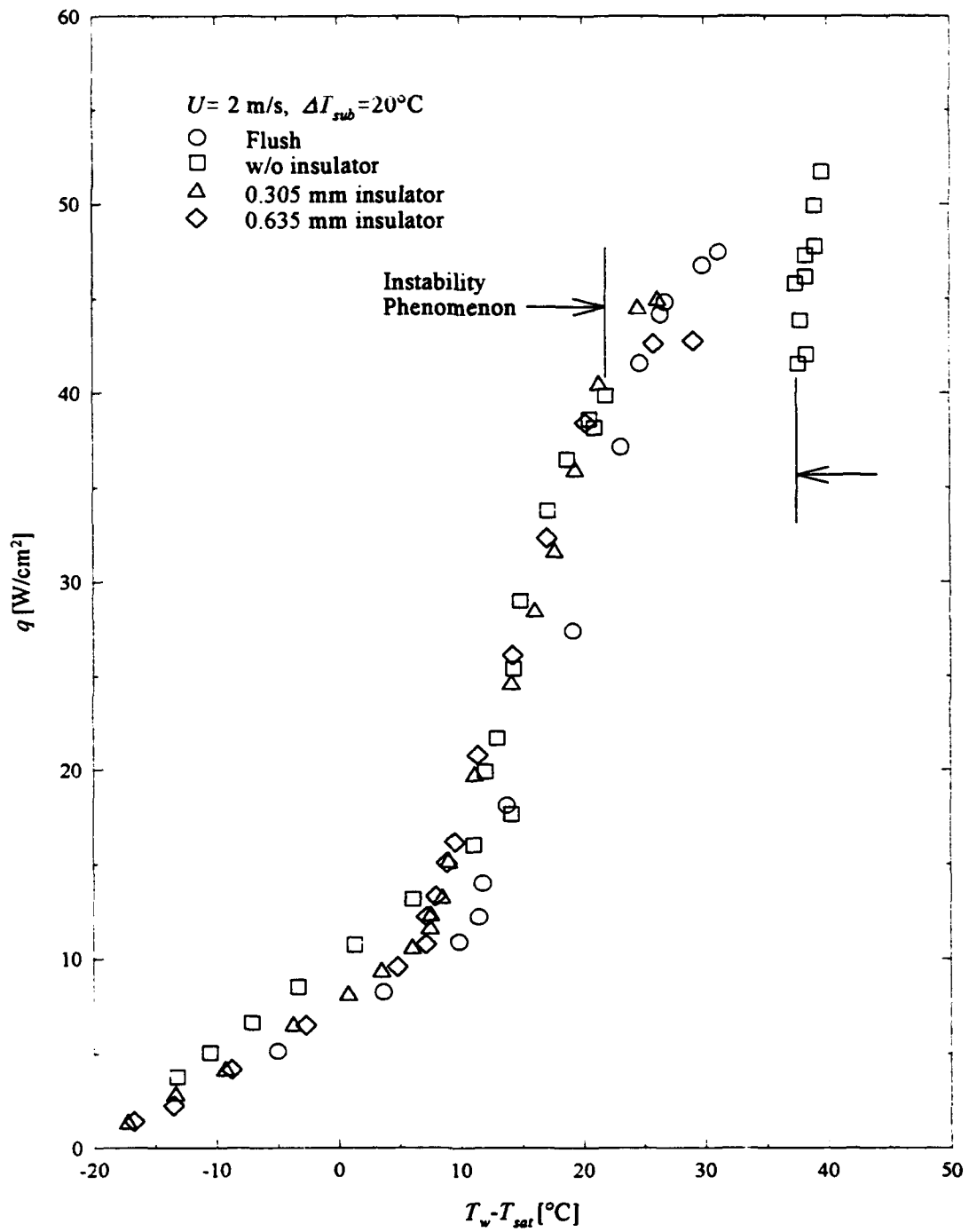


Figure 6.7 Behavior of boiling curve with and without insulators.

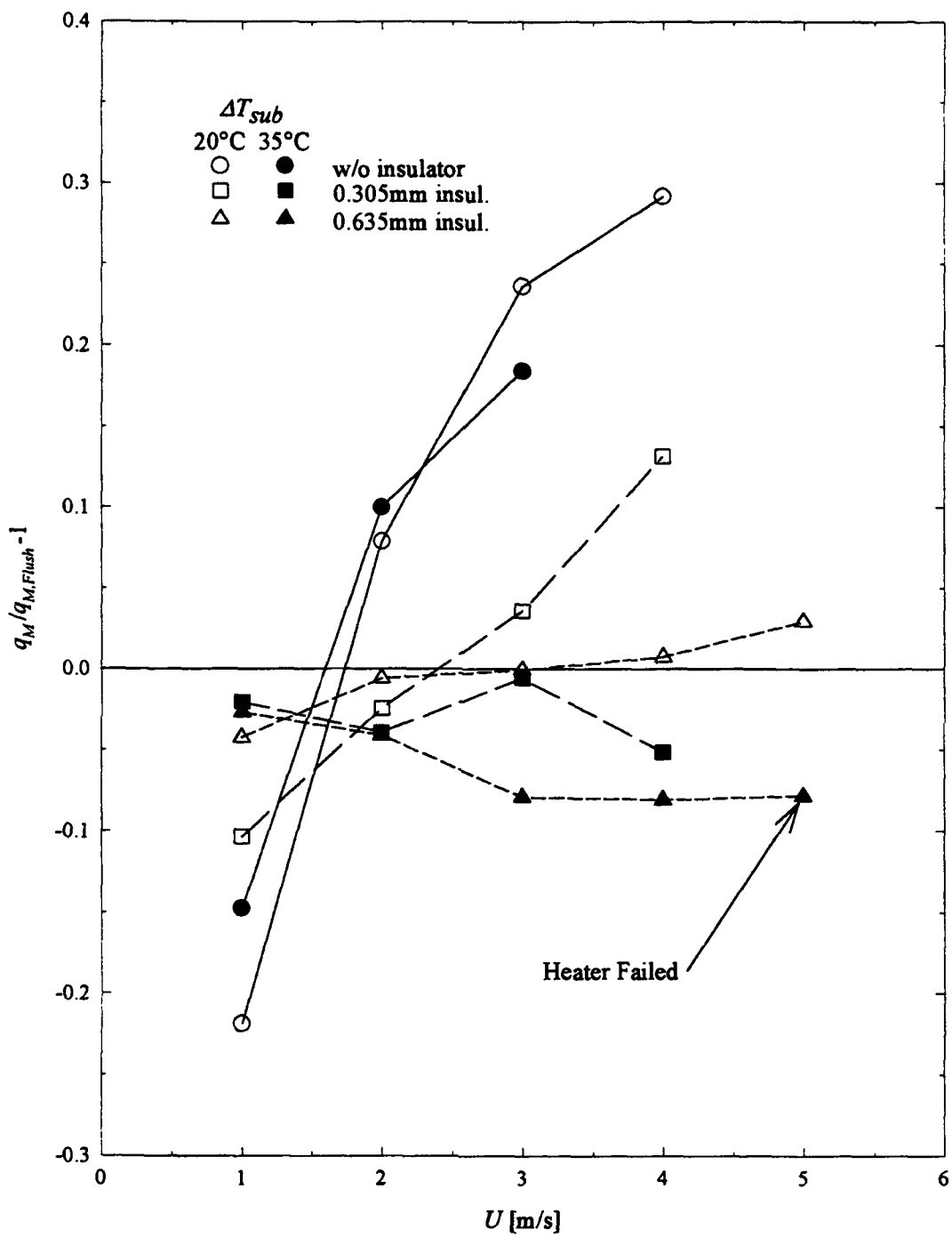


Figure 6.8 Insulated and non-insulated protruding heater CHF compared with flush heater CHF.

Because boiling from the front face creates a vapor blanket which obstructs the flow tangential to the top surface, it is easy to understand how CHF is enhanced by installation of the insulator. For $U > 2$ m/s, the flow mechanics created by the front face boiling must make a significant contribution to heat transfer as evidenced by the degradation of CHF with installation of the insulators. For example, a reduction of 26 W occurred by the total elimination of boiling from the front face for the case of $\Delta T_{\text{sub}} = 20^\circ\text{C}$ and $U = 4$ m/s. This translates to a heat flux of 430 W/cm^2 if heat transfer from the other surfaces is assumed to remain constant. Such a high heat flux is probably impossible. Therefore, the liquid supply mechanism for the other surfaces must be enhanced in some way by the vapor sheet emanating from the front face. One possibility may be that condensing bubbles above the surface draw cool liquid in from the sides to feed the nucleation sites. The blunt face of the protruding block causes the vapor generated on this face to be projected up. This vapor is outside of the thermal boundary layer and in the presence of cooler liquid where it is more likely to condense.

For 35°C subcooling, similar trends are noticed, but the results relative to the flush condition, (see Fig. 6.8), generally fall below the results for 20°C subcooling and $U > 2$ m/s. The reverse is true for $U < 2$ m/s. This can be explained by first noting that as velocity increases, the contribution of single-phase heat transfer becomes a smaller percentage of the total heat transfer near CHF. At 35°C subcooling the single-phase contribution is greater than at 20°C subcooling. Furthermore, unlike water, and to a lesser extent R-12, FC-72 has a low latent to sensible heat ratio, 3.8 and 2.2 for $\Delta T_{\text{sub}} = 20^\circ\text{C}$ and 35°C respectively. Thus, the results for 35°C subcooling are heavily biased towards single-phase heat transfer and augmentation or degradation of boiling heat transfer will have a lesser effect. For the case of no insulator this is easily seen. The effect of the insulator is to make the flow less turbulent. As a consequence, the single-phase and overall heat transfer is reduced, although the boiling heat transfer may be augmented.

For $U = 4$ m/s and $\Delta T_{\text{sub}} = 20^\circ\text{C}$, increases of 21, 39, and 64% over $Q_{M,\text{Flush}}$ were obtained for the 0.635-mm insulator, 0.305-mm insulator, and no insulator cases. These percentages are much higher than the heat flux based percentages. However, as

mentioned before, power dissipation is the real goal of electronics cooling. Power dissipation is simply the product of heat flux and area. If CHF increases with heater height, this product increases at a greater rate since exposed area also increases. Figure 6.9 illustrates how dramatically power dissipation increases with velocity.

6.4 Conclusions

1. CHF decreases with heater wall thickness. The exact value of the critical thickness and the percent reduction for various velocities were not determined. Factors such as nonuniform heat generation and the thermal effusivity of the chip substrate should be considered in a chip cooling design that employs boiling heat transfer.
2. Large scale roughness has an effect similar to small protrusion height and causes a marked reduction of CHF.
3. For the thin foil heater, CHF is improved at velocities greater than 1 m/s for $h_p = 0.71$ mm. A redeveloping velocity boundary layer yields higher velocity fluid tangential to the top surface and thus, more effective wetting of the surface.
4. Improved results for the foil heater, $h_p = 0.71$ mm, and $U = 1$ m/s indicate that front face boiling, for the copper block, impedes liquid supply and consequently reduces CHF.
5. Thin foil heater results display evidence that the instability condition at $\Delta T_{\text{sub}} = 20^\circ\text{C}$ and $U = 2$ m/s for the copper block is due to the interaction of vapor emanating from the front face and boiling on the top surface.
6. Full or partial elimination of boiling from the front face of the copper block prohibits the boiling instability at $\Delta T_{\text{sub}} = 20^\circ\text{C}$ and $U = 2$ m/s.
7. Full or partial elimination of boiling from the front face of the copper block increases CHF for $U = 1$ m/s but, reduces CHF for $U \geq 2$ m/s. The existence of two liquid supply mechanisms is used to explain this change in behavior.
8. Results for the 0.305-mm-thick insulator show that the negative effects of the 0.635-mm-thick insulator for $U \geq 2$ m/s may be reduced by making the insulator thinner while still preventing occurrence of the instability. Results for $h_p < 0.635$ -mm indicate

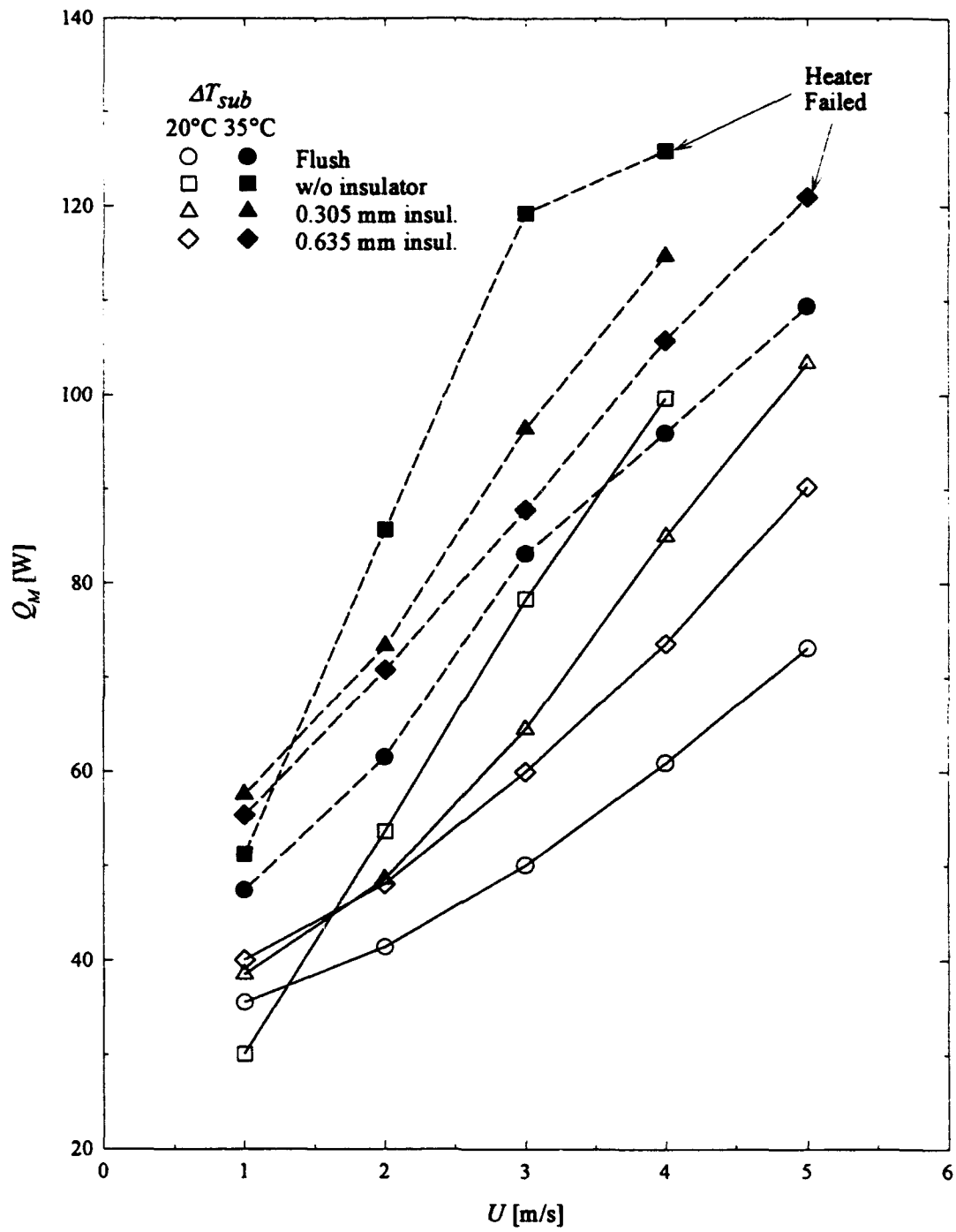


Figure 6.9 Power dissipation versus velocity for heaters with and without insulators.

that an insulator thickness less than 0.305 mm may be optimal. An optimal shape and spanwise coverage may also exist.

9. The interaction of vapor emanating from the front face and boiling from the top surface has a strong impact on increasing CHF for the case of no insulator and $U > 2$ m/s. Condensing vapor above the surface may induce flow from the sides to yield improved wetting of the downstream area of the top surface.

10. As compared to the flush condition and $U > 2$ m/s, the relative change in CHF is less for higher subcooling. This may be due to the higher contribution of single-phase heat transfer and consequent reduction in vapor interaction.

11. For all cases of the 0.635-mm protruded copper block, power dissipation is equal or improved over the flush condition. Thus, the concern for maintaining chips flush with the flow channel wall is unnecessary under certain conditions. The implications are simpler integration of direct immersion cooling with increased power dissipation. An insulator may be desired if the design specifies $U \leq 2$ m/s.

Chapter 7

CONCLUSIONS AND RECOMMENDATIONS

In summary, the preceding chapters discussed the effects of flow channel and chip geometries on CHF. The geometry effects were obtained in conjunction with the effects of flow velocity and subcooling so that a map of the CHF phenomenon could be obtained. Curvature of the flow channel was explored in an attempt to augment boiling heat transfer and increase the CHF. The flushness of the electronic chip with the flow channel wall was studied to obtain data which would show the criticality of manufacturing a very flush chip and flow channel configuration. In the former case, channel curvature was found to have less of an impact on boiling heat transfer than anticipated. In the latter case, the effect of chip protrusion height had a profound and unexpected impact on the CHF. Knowledge of the CHF is of paramount importance for the design of electronics cooling schemes that employ any type of boiling heat transfer. In all cases, correlations were offered so that the CHF could be predicted for a given geometry. Also of significance is the magnitude of the incipient temperature overshoot. This latter problem was found to be of little concern for the boiling geometries studied. A chapter-wise summary of the results follows.

In Chapter 2, the effects of various secondary variables on CHF were studied primarily to validate the experimental technique. Although these variables were not the main focus of this dissertation, some interesting results were obtained. The effects of surface roughness on nucleate boiling and CHF were in line with what is widely accepted. That is, rougher surfaces increase the distribution of cavity sizes which increases the probability of nucleation and consequently requires lower wall superheats for a given heat flux. Surface roughness does not affect the magnitude of the CHF until very smooth surface finishes are attained. The tenuous connection between cavity size distribution and the widely accepted parameter for surface roughness, R_a , was illustrated. Although this was first explained by Hsu and Graham³⁸ almost 20 years ago, many researchers still try to correlate data to R_a which for the case of boiling is a system variable rather than a universal variable. The equally easy to obtain roughness

parameter, S , which is the mean peak-to-peak spacing of surface roughness elements was suggested as a more appropriate parameter. Slightly more sophisticated equipment can also yield the distribution of S which would presumably be even better.

Contamination of the boiling surface has been shown to degrade boiling heat transfer in almost every way by previous investigators. Results for contamination which would be imperceptible by almost all methods of inspection, termed micro-contamination, was shown to also have a negative effect on boiling heat transfer and CHF. In particular, it was shown that silicone contamination of only of few molecular layers thick was sufficient to cause marked degradation. The silicone contamination was a consequence of the test section construction method which is very popular in the research field. It is often noted in the literature that frequent cleaning of the boiling surface by harsh mechanical means, (i.e., sanding or sand blasting), is necessary to obtain consistent results. It is felt that the same sort of contamination occurred under these studies. As a result of identifying the source of contamination, mild cleaners, (i.e., 20% potassium hydroxide and pure methanol), were successfully used to eliminate the effect of contamination. Furthermore, tests showed that the chemical procedure cleaned the surface much more thoroughly than mechanical means. This may be the reason that frequent cleaning of the surface was not necessary for the current study.

Oxidation of the copper surface was shown to improve the CHF, but primarily with a large increase in wall superheat. It was postulated that improved wetting of the surface was probably responsible because it is known that mildly oxidized copper has improved wettability. It was also shown in Chapter 2, that the effect of absorbed air on CHF and nucleate boiling was negligible. Insufficient data were obtained to prove this fact conclusively, but the literature supports the belief that absorbed air has an effect only at high subcooling or high pressure. This is true only for flow boiling, however. It has been shown that absorbed air has an effect even at low pressure and low subcooling for pool boiling. For flow boiling, it is reasoned that the air is driven out of the heated fluid before incipience occurs. Where as in pool boiling this would increase the single-phase convection because of the increase turbulence caused by the bubbles, the effect is negligible in forced flow convection where significant turbulence already exists.

Chapter 3 provided the background for the principal emphasis of this dissertation; the determination of the effects of flow channel and chip geometry on CHF. Chapter 3 discussed the pertinent literature leading to the evolution of the current model for the forced flow CHF of small heat sources. This development showed the numerous assumptions and competing theories leading up to the correlation given by Eqs. (3.23) and (3.24). Through examination of the assumptions leading to the development of Eqs. (3.23) and (3.24), it was shown that CHF is dependent on the Reynolds number. The efficacy of including the Reynolds number was shown by a simple modification to Eqs. (3.23) and (3.24). Based on data obtained for the straight flow channel, an improved correlation was derived which contained all of the dimensionless groupings found in Eqs. (3.23) and (3.24) and the Reynolds number. This correlation is valid over a much wider range of velocities with an improved fit to the data over that of Eqs. (3.23) and (3.24). This correlation was given by Eqs. (3.31) and (3.32), but was modified in Chapter 5 and presented as Eqs. (5.1) and (5.2) to include the presumed effect of channel width. The value of incipient temperature overshoot was less than 2°C for almost all cases. This is considered too small to be of concern.

Chapter 4 presents the effects flow path curvature on CHF. The literature indicates that a large increase in CHF may be expected for curved flow geometries. The enhancement of CHF found was much less than expected. The presumed discrepancy with the literature is explained by the difference in heated length and flow geometry of the present configuration with that of the literature. Results in the literature are for heated lengths which are relatively long compared to the simulated chip geometry of this study. CHF decreases with increasing heated length because the increase in net vapor generation begins to occlude the flow of liquid to the heated surface. Flow path curvature has the effect of driving the more dense liquid to the surface, thus mitigating the effect of long heated lengths. The effect of curvature is much less pronounced for the short heated lengths studied. However, a 50% increase in CHF was obtained at low subcooling.

The combination of subcooling and channel curvature was shown to be very important. As subcooling decreases, the volume of vapor generation increases for a

given heat flux. The mechanism of liquid wetting described above, consequently has a greater impact. On the other hand, increasing velocity had less of an impact on CHF in the curved geometry. In other words, the percentage increase in CHF remained roughly constant for velocities greater than 2 m/s. This result was in agreement with that of Hughes¹⁵¹ who studied boiling from long heated strips in a rectangular channel. Through modification of the theoretically derived correlation of Mudawar and Maddox¹⁹, it was shown that their model could not fully account for the effect of flow channel curvature. A correction to the correlation derived in Chapter 3 was derived. Dimensionless analysis predicted a reduced effect of velocity because velocity factored out of the buoyancy term, given by the Richardson number, as a consequence of the acceleration force being equal to U^2/R . The modification to the correlation developed in Chapter 3 proved to fit the curved channel data with equal accuracy as the fit of Eqs. (3.31) and (3.32) to the straight channel data.

Augmentation of CHF by curvature of the flow channel is advantageous only for situations where low subcooling is required. This situation could arise when the electronics operating temperature is close to the ambient temperature. The percentage increase in CHF decreases with increasing subcooling. In fact, a degradation occurs for sufficiently high subcoolings. Channel curvature would also be advantageous in the situation where long heated lengths are required. Although not specifically studied as a part of this research, the literature indicates that augmentation of CHF by channel curvature is most applicable to long heated lengths. Numerous heat sources inline in the flow channel could also be equated to long heated length. This configuration is highly probable given the current requirements for electronics cooling. Most designs incorporating power electronics typically require six or more high power chips.

The range of velocities and subcoolings covered adequately cover the range of operating conditions envisioned for electronics cooling. Further increases in CHF would have to be accomplished through other means. The radii of curvature studied are considered to already be as small as feasibly possible. Hence, the prospects for future developments in curved channel boiling for electronics cooling appear to be limited.

Chapter 5 presented results which are considered to be of great importance to electronics cooling system designers. Gu et al.²⁴ observed that small differences, 0.1 mm, in the height of the heat source surface with respect to the flow channel wall caused a severe reduction in CHF*. Even under the controlled conditions of a laboratory experiment, maintenance of a truly flush condition after repeated thermal cycling was difficult. It is believed that to do so in practice would be even more difficult. Heater heights of -0.127 to 0.635 mm were studied to quantify the effects and the results were intriguing. While a reduction in the CHF was observed for small protrusion heights and low velocities, a significant increase was observed for larger protrusion heights and higher velocities. When the increased surface area of a protruding chip is factored in, the power dissipation from a protruding chip is dramatically increased over that of a flush chip.

In contrast to channel curvature, the combined effect of velocity and protrusion height were more significant than the variation of CHF with protrusion height and subcooling. A lesser decrease and lesser enhancement of CHF was observed for the high subcooling case, however. As with the curved channel, this is explained by the relative difference of latent and sensible heat transfer at the low and high subcoolings. By changing the flow regime over and around the chip, protrusion of the chip effects the latent heat transfer much more than the sensible heat transfer. At low subcooling, the latent heat transfer is dominant, therefore any change in the latent heat effectiveness is more dramatic on the overall heat transfer. At higher subcooling, the sensible heat is more significant and a change in the latent heat transfer effectiveness has less of an impact on the overall heat transfer.

An interesting result of protruding the heater was discovered for the unique condition of $U = 2$ m/s and $\Delta T_{sub} = 20^\circ\text{C}$. For this condition, a flow and boiling instability occurred as heat flux increased towards the CHF. At a certain heat flux, which varied slightly from test to test, an oscillating pattern of the vapor blanket occurred. The

* Remember that CHF for the protruding heat sources is based on total exposed area rather than the cross sectional area.

vapor blanket would essentially disappear and reappear at a random frequency. This phenomenon was marked by large excursions of the surface temperature. Upon increasing the power to the heater further, the instability disappeared, but boiling ensued at a much higher superheat. Further increases in power resulted in increase heat flux with essentially no increase in wall superheat all the way up to CHF. Although this condition did not occur at 35°C subcooling, it could occur at some other combination of velocity and subcooling. The exact reason for this instability is unknown.

The trend of CHF with protrusion height, velocity, and subcooling is very complex. For the case of a recessed chip, CHF is sharply reduce for any combination of parameters. Therefore, the prediction of CHF for this case is not important because the recessed condition should be avoided in any design. By considering only the protruded surface data, a correction to the correlation derived in Chapter 3 and modified in Chapter 5, Eqs. (5.1) and (5.2), was obtained. This correction does not model all aspects of protrusion height as witnessed by Fig. 5.20, but reasonable accuracy was obtained.

The results of Chapter 5 indicate that the designer should not be concerned with maintaining absolute flushness of the chip with the flow channel wall. In fact, the design should plan on substantial protrusion of the chip into the flow channel. The designer must be cognizant of the instability condition and avoid operating the cooling system near this point.

Further attempts to understand the nature of CHF with chip protrusion were undertaken in Chapter 6. A thin foil heater design was exploited to eliminate the contribution of heat transfer from the sides of the protruding simulated chip of Chapter 5. Observation of boiling from this test section showed that a completely different flow pattern exists for the two heater designs. The flow pattern and bubble layer of the protruding foil heater was very much similar to the flush heater flow pattern for either heater design with the exception of the bubble layer being slightly thinner. The thinner bubble layer is a consequence of higher velocity fluid near the surface as a result of a redeveloping velocity boundary layer. This higher velocity fluid near the wall is responsible for the increase in CHF for the protruding case of the foil heater design.

The above observations brought to light the previous observations of the flow pattern and bubble layer for the protruding copper block heater. The vapor generated from the upstream face of the copper block is swept up and over the top surface of the copper block. This vapor serves to obstruct liquid flow to the surface at low velocities, but also serves to improve liquid flow at higher velocities. At high velocities, the upward motion of the vapor induces liquid flow from the sides of the protruding copper block, thus improving liquid supply to the downstream portion of the surface where dryout generally occurs first. Recognizing this mechanism, the effect of insulating the upstream face of the copper block to eliminate part or all of the vapor generation was investigated.

Two cases, 48% and 100% insulation of the upstream face were investigated. The profound effect of vapor emanating from the upstream face was demonstrated by insulating the same face. At a flow velocity of 1 m/s, the reduction in CHF for either 48% or 100% insulation of the surface was much less significant than for the case of no insulation. In contrast, for $U \geq 2$ m/s complete insulation of the upstream face produced no change in CHF 20°C subcooling while reducing CHF for 35° subcooling. The impact of 48% insulation of the surface was much less severe, but a reduction was still obtained for 35°C subcooling. If power dissipation is considered, these results are not so bad as a significant increase in power dissipation is realized under all conditions. Furthermore, the instability phenomenon observed for the uninsulated case was completely absent for the insulated cases. Finally, the detrimental effects of insulation could probably be reduced by decreasing the percentage of insulation.

During the course of the above effort, another effect of heater geometry on CHF was confirmed. Pool boiling results have shown that for very thin heaters, or heaters with a low thermal effusivity, $\sqrt{\rho ck}$, CHF is reduced. The reason is that the time constant for dispersion of sudden temperature excursions created by intermittent dry patches is greater. Remembering that the physical model of pool boiling CHF, identified by Haramura and Katto,⁹⁴ is based on the heated surface being rewetted within a specific period of time, it is easy to see that longer times produce larger dry spots which reduce the ability of the liquid to rewet the surface. Consequently, CHF is reduced. The same was found to be true for the case of flow boiling although the results of McAdams et al.⁵³

suggest that the effects of heater thickness and thermal effusivity are not as great for forced flow boiling. The results are insufficient to quantify this effect. The results do indicate that exceedingly thin packages of low thermal effusivity material should be avoided in the manufacture of electronic chips to be cooled by direct immersion boiling heat transfer. In particular, alumina, a very common chip substrate material, should be carefully considered under the above conditions.

Finally, detailed temperature measurements of the surface show that the downstream portion of the heater begins to sharply rise in temperature with every increase in heat flux as CHF is approached. This fact supports the dryout model proposed by Haramura and Katto⁹⁴ and adapted to the current geometry by Mudawar and Maddox.¹⁹ These measurements also show that the temperature variation in the spanwise direction is much greater than in the streamwise direction. This result is contrary to conventional thought and suggest that induced flow from the sides of the heater is important even for the flush case. This type of flow pattern does not support the liquid supply mechanism of Mudawar and Maddox's CHF model.

The work of this dissertation has answered many questions regarding the nature of boiling heat transfer and CHF for various channel and chip geometries. As with any study of this magnitude, more questions arise from the work than those that are answered. There are two complementary paths suggested as a follow on to this work. The first path should focus on a more detailed understanding of the CHF mechanism. Only with a detailed understanding can predictions of CHF be made without resorting to parametric experimentation. The assets and deficiencies of the dryout model of CHF have been well elaborated at this point. What remains to be known is how the macrolayer thickness varies with velocity and subcooling among other parameters. The liquid wetting mechanism in particular has been called into question by the preceding results. The distribution of jets within the macrolayer at high heat fluxes is also pertinent to the derivation of the dryout model of CHF. These unknowns can only be answered by direct visual observation. As discussed in Chapter 3, this is not a trivial prospect. The author has attempted high speed photography of forced flow boiling in the experimental

configuration of this dissertation. Although these attempts were less than successful, knowledge of how to tackle the problem in the future was acquired.

The primary problem of high speed photography of the very small boiling phenomena is that vast amounts of light are required. As characteristic dimensions decrease, (i.e., magnification requirements increase), and characteristic times decrease, (i.e., frame rate requirements increase), the amount of light necessary to expose a frame increases. For the dimension and time scales involved, only a strobed laser can provide the necessary amount of light. Another way to alleviate the problem, is to use light sensitive video as opposed to film. The sensitivity of video to light is many orders of magnitude greater than that for even the most highest speed film. Until recently, video was not capable of achieving the high frame rates necessary to satisfactorily capture the boiling phenomenon. The new video products which are capable are excessive in cost being about \$125,000 or greater in value.

Another problem involved with high speed photography of forced flow boiling is that the large amount of vapor produced tend to obscure visualization of the surface. Galloway and Mudawar^{124,125} recently attempted to solve this problem by observing boiling from a heat source within a very narrow channel. Under low velocity, low subcooling conditions, it is possible that the bubble size would be of the same order as the channel width. They obtained some very interesting results, but the qualitative nature of CHF for their configuration was not representative of what has been observed in the flow channel geometries similar to this study. Furthermore, the results of this study indicate that inflow from the sides of the heater play an important role in determining the CHF. Flow from the sides of the heater would be completely eliminated for the narrow geometry of Galloway and Mudawar's study. One means of solving this problem would be to employ laser sheet lighting. By dissecting the bubble layer with a very thin sheet of light, the same two-dimensional picture of boiling desired by Galloway and Mudawar could be obtained without the compromising effects of changing the channel geometry. Because the lighted volume of liquid would be very small, the aforementioned problem of insufficient light would be further exacerbated. By seeding the flow with fluorescing particles, this problem could also be alleviated.

By coupling a copper-vapor laser, (which is the only laser capable of providing the high strobe frequencies required), sheet-lighting, seeding of the liquid, and high-speed video, the observation of the macrolayer phenomena may finally be obtained. All of the technology required exists, but has never been combined for observation of boiling phenomena. To the author's knowledge, adding fluorescing particles to a boiling flow has not been done. This technique would have problems peculiar to boiling where in the particles may stick on the heated surface as a result of condensing out of the evaporating liquid. Flow visualization of boiling heat transfer could be a research topic unto itself, but should not be discouraged. True understanding of the boiling mechanism could yield insights that would lead to significant enhancement of boiling heat transfer.

Another question arising from the forgoing work is; how does the surface temperature vary with velocity, subcooling, and protrusion height? The experiments with the thin metal foil heater provided some interesting results, but the amount of experimentation was not sufficient to quantify the temperature variation under all situations. Such a study could yield insight as to whether the liquid supply mechanism or dryout mechanism changes with velocity as claimed by others. It could also confirm the position of the author, that a change in the liquid supply mechanism occurs when the chip is protruded into the flow channel.

The other path that this research could follow is one that strives to determine the systematic effects on boiling heat transfer. In the experiments of this dissertation, only single heat sources were studied. In practice, cooling of a number of chips would be required. For example, two high power switching chips are generally required for each phase of a motor. Some designs may even require four chips per phase. It is entirely likely that as many as 12 chips along with some associated electronics would have to be cooled. Placing these chips in-line in the flow channel could cause the CHF of the most downstream chip to be drastically reduced. This would limit the cooling potential of the entire system to the CHF of the weakest link, the most downstream chip. McGillis et al.²⁸ studied such a configuration and found only a small reduction in CHF for the most downstream chip as compared to the most upstream chip. Their results were obtained at velocities of less than 1 m/s where the liquid supply mechanism has been postulated to be

different from that at higher velocities. Most of the results of this dissertation indicate that the nature of CHF is different at velocities less than 2 m/s. Thus it is necessary to determine the magnitude of degradation at higher velocities.

The work in Chapter 5 explored a rather limited range of protrusion heights. While the maximum height of 0.635 mm is comparable to the height of surface mounted devices, it is not comparable to what would be anticipated for power electronics, 2.5 mm. The work of Chapter 6 indicated that nonuniform heat generation could also play a role in determining CHF. It would be highly desirable to determine how the CHF for an actual chip compares to that predicted by results for ideal test sections. Consequently, these are also areas for continued study. Designers will, of course, want to minimize the cooling system size and pump requirements. This would present the need for determining the combined effects of channel height, channel width, protrusion height, and number of chips. It may then be desirable to improve the liquid supply mechanism by employing flow deflectors and similar devices.

The future electronics requirements of the Air Force indicate that heat fluxes in excess of 500 W/cm^2 may someday be required of cooling technologies. Thus, the quest for even greater augmentation of boiling heat transfer should not be halted. It is easy to see that there are many more years worth of research to be done and the need for more research can be easily appreciated.

REFERENCES

1. Incropera, F. P., "Convection Heat Transfer in Electronic Equipment Cooling," *ASME Journal of Heat Transfer*, Vol. 110, No. 4, 1988, pp. 1097-1111.
2. Bar-Cohen, A., "Thermal Management of Air- and Liquid-Cooled Multichip Modules," *IEEE Transactions On Components, Hybrids, And Manufacturing Technology*, Vol. CHMT-10, No. 2, 1987, pp. 159-175.
3. Gambill, W. R. and Greene, N. D., "Boiling Burnout with Water in Vortex Flow," *AIChE Chemical Engineering Progress Symposium Series*, Vol. 54, No. 10, 1958, pp. 68-76.
4. Leslie, B., Neukermans, A., Simon, T., and Foster, J., "Enhanced Brightness X-ray Source," *Journal of Vacuum Science and Technology B*, Vol. 1, No. 4, 1983, pp. 1251-1256.
5. Chu, R.C., "Heat Transfer in Electronic Systems," *Proceedings of the Eighth International Heat Transfer Conference*, Vol. 1, August 1986, pp. 293-305.
6. Nakayama, W. and Bergles, A.E., "Cooling Electronic Equipment: Past, Present, and Future," *The International Symposium on Heat Transfer in Electronic and Microelectronic Equipment*, ICHMT, Dubrovnik, Yugoslavia, August 29-September 2, 1988, pp. 1-37.
7. Antonetti, V.W., Oktay, S., and Simons, R.E., "Heat Transfer in Electronic Packages," *Microelectronics Packaging Handbook*, Tummala, R.R. and Rymaszewski, E.J., Editors, Van Nostrand Reinhold, New York, 1989, p. 168.
8. Greene, A.O. and Wightman, J.C., "Cooling Electronic Equipment by Direct

Evaporation of Liquid Refrigerant," Air Material Command Report PB 136065, Wright-Patterson Air Force Base, OH, 1948.

9. Baker, E., "Liquid Immersion Cooling of Small Electronic Devices," *Microelectronics and Reliability*, Vol. 12, 1973, pp. 163-173.
10. Costlow, T., "Liquid Cooling Flows to Desktop PC's," *Electronic Engineering Times*, Issue 765, September 27, 1993.
11. Hoadley, A.W. and Porter, A.J., "Thermal Management of Closed Computer Modules Utilizing High Density Circuitry," AIAA Paper 90-1748, Presented at The AIAA/ASME Fifth Joint Thermophysics and Heat Transfer Conference, Seattle WA, June 18-20, 1990.
12. Drexel, W.H., "Fluorochemical Cooling for High Heat Dissipation," *Electronic Design*, Vol. 9, No. 11, May 24, 1961, pp. 40-43.
13. Mark, M., Stephenson, M., and Goltzos, C., "An Evaporative-Gravity Technique for Airborne Equipment Cooling," *IRE Transactions On Aeronautical And Navigational Electronics*, Vol. ANE-5, No. 1, March 1958, pp. 47-52.
14. Anderson, T.M. and Mudawwar, I., "Microelectronic Cooling by Exhanced (sic) Pool Boiling of a Dielectric Fluorocarbon Liquid," *Proceedings of the 1988 National Heat Transfer Conference*, ASME HTD-96, Vol. 1, 1988, pp. 551-560.
15. Marto, P.J. and Lepere, Lt. V.J., USN, "Pool Boiling Heat Transfer from Enhanced Surfaces to Dielectric Fluids," *ASME Journal of Heat Transfer*, Vol. 104, No. 2, 1982, pp. 292-299.
16. Yang, W., Takizawa, H., and Vrable, D.L., "Augmented Boiling on Copper-

Graphite Composite Surface," *International Journal of Heat and Mass Transfer*, Vol. 34, No. 11, pp. 2751-2758.

17. Lee, T. Y. and Simon, T. W., "Critical Heat Flux In Forced Convection Boiling From Small Regions," *Heat Transfer In High Energy/High Heat Flux Applications*, ASME HTD-Vol. 119, 1989, pp. 1-7.

18. Leland, J. E. and Chow, L. C., "Forced Convection Boiling from a Non-Flush Simulated Electronic Chip," *AIAA Journal of Thermophysics and Heat Transfer*, Vol. 7, No. 4, 1993, pp. 588-594.

19. Mudawwar, I. and Maddox, D. E., "Critical Heat Flux in Subcooled Flow Boiling of Fluorocarbon Liquid on a Simulated Electronic Chip in a Vertical Rectangular Channel," *International Journal of Heat and Mass Transfer*, Vol. 32, No. 2, pp. 379-394.

20. Ma, C. F. and Bergles, A. E., "Boiling Jet Impingement Cooling of Simulated Microelectronic Chips," *Heat Transfer in Electronic Equipment*, ASME HTD-Vol. 28, 1983, pp. 5-12.

21. Wadsworth, D. C. and Mudawar, I., "Cooling of a Multichip Electronic Module by Means of Confined Two-Dimensional Jets of Dielectric Liquid," *Heat Transfer in Electronics*, ASME HTD-Vol. 111, 1989, pp. 79-87.

22. Pais, M. R., Tilton, D., Chow, L. C., and Mahefkey, E. T., "High Heat Flux Low Superheat Evaporative Spray Cooling," AIAA Paper 89-0241, 1989.

23. Miropol'skiy, Z. L. and Pikus, V. Yu, "Critical Boiling Heat Fluxes in Curved Channels," *Heat Transfer-Soviet Research*, Vol. 1, No. 1, 1969, pp. 74-79.

24. Gu, C. B., Chow, L. C. and Beam, J. E., "Flow Boiling in a Curved Channel,"

Heat Transfer in High Energy/High Heat Flux Applications, ASME HTD-Vol. 119, 1989, pp. 25-32.

25. Mudawwar, I. A., Incropera, T. A., and Incropera, F. P., "Boiling Heat Transfer and Critical Heat Flux in Liquid Films Falling on Vertically-Mounted Heat Sources," *International Journal of Heat and Mass Transfer*, Vol. 30, No. 10, 1987, pp. 2083-2095.

26. Samant, K. R. and Simon, T. W., "Heat Transfer From a Small Heated Region to R-113 and FC-72," *ASME Journal of Heat Transfer*, Vol. 111, No. 4, 1989, pp. 1053-1059.

27. Mudawar, I. and Maddox, D. E., "Enhancement of Critical Heat Flux from High Power Microelectronic Heat Sources in a Flow Channel," *Heat Transfer in Electronics*, ASME HTD-Vol. 111, 1989, pp. 51-58.

28. McGillis, W. R., Carey, V. P., and Strom, B. D., "Geometry Effects on Critical Heat Flux for Subcooled Convective Boiling From an Array of Heated Elements," *ASME Journal of Heat Transfer*, Vol. 113, No. 2, 1991, pp. 463-471.

29. Gersey, C.O. and Mudawar, I., "Orientation Effects on Critical Heat Flux from Discrete, In-Line Heat Sources in a Flow Channel," *ASME Journal of Heat Transfer*, Vol. 115, No. 4, 1993, pp. 973-985.

30. Ito, H., "Friction Factors for Turbulent Flow in Curved Pipes," *ASME Journal of Basic Engineering*, Vol. 81, June, 1959, pp. 123-134.

31. Kline, S. J. and McClintock, F. A., "Describing Uncertainties in Single-Sample Experiments," *Mechanical Engineering*, ASME, January, 1953, pp. 3-8.

32. Kenning, D. B. R., "Wall Temperature Patterns in Nucleate Boiling,"

International Journal of Heat and Mass Transfer, Vol. 35, No. 1, 1992, pp. 73-85.

33. Jakob, M. and Fritz, W., *Forschung a. d. Gebiete. d. Ingenieurwes.*, Vol. 2, 1931, p. 435, as described in Jakob, M., *Heat Transfer*, Vol. 1, John Wiley & Sons, New York, 1949, p. 636.

34. Corty, C. and Foust, A.S., "Surface Variables in Nucleate Boiling," *AIChE Chemical Engineering Progress Symposium Series*, Vol. 51, No. 17, 1955, pp. 1-12.

35. Nishikawa, K., Fujita, Y., Ohta, H., and Hidaka, S., "Effect of the Surface Roughness on the Nucleate Boiling Heat Transfer over the Wide Range of Pressure," *Heat Transfer 1982*, PB-10, Hemisphere Publishing Corp., 1982, pp. 61-66.

36. Hsu, Y.Y., "On the Size Range of Active Nucleation Cavities on a Heating Surface," *ASME Journal of Heat Transfer*, Vol. 84, No. 3, 1962, pp. 207-216.

37. Cole, R., "Boiling Nucleation," *Advances in Heat Transfer*, Vol. 10, 1974, pp. 127-133.

38. Hsu, Y.Y. and Graham, R.W., *Transport Processes in Boiling and Two-Phase Systems*, Hemisphere Publishing Corp., Washington D.C., 1976, p. 36.

39. Hahne, E., Spindler, K., and Shen, N., "Incipience of Flow Boiling in Subcooled Well Wetting Fluids," *Proceedings of the Ninth International Heat Transfer Conference*, Jerusalem, Israel, Vol. 2, 1990, pp. 69-74.

40. Davis, E. J. and Anderson, G. H., "The Incipience of Nucleate Boiling in Forced Convection Flow," *AIChE Journal*, Vol. 12, No. 4, 1966, pp. 774-780.

41. Aladyev, I.T., Miropolsky (sic), Z.L., Doroshchuk, V.E., and Styrikovich, M.A.,

"Boiling Crisis in Tubes," *International Developments in Heat Transfer*, ASME, New York, 1962, pp. 237-243.

42. Bernath, L. and Begell, W., "Forced-Convection, Local-Boiling Heat Transfer in Narrow Annuli," *Chemical Engineering Progress Symposium Series*, Vol. 55, No. 29, 1959, pp. 59-65.

43. Bier, K., Gorenflo, D., Salem, M., and Tanes, Y., "Effect of Pressure and Surface Roughness on Pool Boiling of Refrigerants," *International Journal of Refrigeration*, Vol. 2, 1979, pp. 211-219.

44. Leung, A., Banerjee, S., and Groeneveld, D.C., "Investigation of the Effects of Heater Characteristics on CHF Performance of a Long Vertical Annulus in High Pressure Water," *Proceedings of the 7th International Heat Transfer Conference*, Vol. 4, 1982, pp. 303-308.

45. Berenson, P.J., "Experiments On Pool-Boiling Heat Transfer," *International Journal of Heat and Mass Transfer*, Vol. 5, No. 10, 1962, pp. 985-999.

46. Ramlison, J.M. and Lienhard, J.H., "Transition Boiling Heat Transfer and the Film Transition Regime," *ASME Journal of Heat Transfer*, Vol. 109, No. 3, 1987, pp. 746-752.

47. Roy Chowdhury, S.K. and Winterton, R.H.S., "Surface Effect in Pool Boiling," *International Journal of Heat and Mass Transfer*, Vol. 28, No. 10, 1985, pp. 1881-1889.

48. Weatherhead, R.J., "Nucleate Boiling Characteristics and the Critical Heat Flux Occurrence in Sub-Cooled Axial Flow Water Systems," Report ANL 6675, Argonne National Laboratory, 1963.

49. Gaertner, R.F., "Photographic Study of Nucleate Pool Boiling on a Horizontal Surface," *ASME Journal of Heat Transfer*, Vol. 87, No. 1, 1965, pp. 17-29.
50. Costello, C.P. and Heath, C.A., "The Interaction of Surface Effects and Acceleration in the Burnout Heat Flux Problem," *AIChE Journal*, Vol. 10, No. 2, 1964, p. 278 and pp. 285-288.
51. Farber, E.A. and Scoria, R.I., "Heat Transfer to Water Boiling Under Pressure," *Transactions of the ASME*, Vol. 70, May 1948, pp. 369-384.
52. Behar, M., Courtaud, M., Ricque, R., and Semeria, R., "Fundamental Aspects of Subcooled Boiling with and Without Dissolved Gasses," *Proceedings of the Third International Heat Transfer Conference*, Vol. 4, AIChE-ASME, 1966, pp. 1-11.
53. McAdams, W. H., Kennel, W. E., Minden, C. S. L., Carl, R., Picornell, P. M., and Dew, J.E., "Heat Transfer at High Rates to Water with Surface Boiling," *Industrial Engineering Chemistry*, Vol. 41, No. 9, 1949, pp. 1945-1953.
54. Murphy, R.W., and Bergles, A.E., "Subcooled Flow Boiling of Fluorocarbons-- Hysteresis and Dissolved Gas Effects on Heat Transfer," *Proceedings of Heat Transfer and Fluid Mechanics Institute*, Stanford Univ. Press, 1972, pp. 400-416.
55. Pike, F. P., Miller, P. D., and Beatty, K. O., Jr., "The Effect of Gas Evolution on Surface Boiling at Wire Coils," Heat Transfer St. Louis, *AIChE Chemical Engineering Progress Symposium Series*, Vol. 51, No. 17, 1955, pp. 13-19.
56. You, S. M., Simon, T. W., and Bar-Cohen, A., "Experiments on Nucleate Boiling Heat Transfer With a Highly-Wetting Dielectric Fluid: Effects of Pressure, Subcooling and Dissolved Gas Content," *Cryogenic and Immersion Cooling of Optics and Electronic Equipment*, ASME HTD-Vol. 131, 1990, pp. 45-52.

57. Kutateladze, S.S., "On the Transition to Film Boiling under Natural Convection," *Kotloturbostroenie, (Steam Turbine Construction)*, Vol. 3, 1948, p. 10.
58. Kutateladze, S.S., "Hydrodynamic Theory of Changes in the Boiling Process Under Free Convection," *Izv. Akademia Nauk SSSR, Otdelenie Tekh. Nauk*, Vol. 4 1951, pp. 529-536, translated as Report AEC-TR-1441.
59. Kutateladze, S.S., "Heat Transfer in Condensation and Boiling," *State Scientific and Technical Publishers of Literature on Machinery*, Moscow, 1952, translated as Report AEC-TR-3770.
60. Chang, Y.P., "A Theoretical Analysis of Heat Transfer in Natural Convection and in Boiling," *Transactions of the ASME, Series C*, Vol. 79, No. 7, 1957, pp. 1501-1513.
61. Jakob, M., *Heat Transfer*, Vol. 1, John Wiley & Sons, New York, 1949, pp. 634-635.
62. Gunther, F.C., "Photographic Study of Surface-Boiling Heat Transfer to Water with Forced Convection," *Transactions of the ASME*, Vol. 73, February 1951, pp. 115-123.
63. Rohsenow, W. and Clark, J., "A Study of the Mechanism of Boiling Heat Transfer," *Transactions of the ASME*, Vol. 73, 1951, pp. 609-620.
64. Zuber, N. and Tribus, M., "Further Remarks on the Stability of Boiling Heat Transfer," Report AECU-3631, 1958.
65. Zuber, N., "On The Stability of Boiling Heat Transfer," *Transactions of the ASME, Series C*, Vol. 80, April, 1958, pp. 711-720.

66. Zuber, N., "Hydrodynamic Aspects of Boiling Heat Transfer (thesis)," Report AECU-4439, June, 1959.
67. Zuber, N., Tribus, M., and Westwater, J.W., "The Hydrodynamic Crisis in Pool Boiling of Saturated and Subcooled Liquids," *International Developments in Heat Transfer*, ASME, New York, 1961, pp. 230-236.
68. Chang, Y.P. and Snyder, N.W., "Heat Transfer in Saturated Boiling," *AIChE Chemical Engineering Progress Symposium Series*, Vol. 56, No. 30, 1960, pp. 25-38.
69. Chang, Y.P., "Some Possible Critical Conditions in Nucleate Boiling," *ASME Journal of Heat Transfer*, Vol. 85, No.2, 1963, pp. 89-100.
70. Moissis, R. and Berenson, P.J., "On The Hydrodynamic Transitions in Nucleate Boiling," *ASME Journal of Heat Transfer*, Vol. 85, No. 3, August, 1963, pp. 221-229.
71. Cole, R., "A Photographic Study of Pool Boiling in the Region of the Critical Heat Flux," *AIChE Journal*, Vol. 6, No. 4, 1960, pp. 533-538.
72. Zuber, N., Tribus, M., and Westwater, J.W., "Discussion of Paper No. 27, (The Hydrodynamic Crisis in Pool Boiling of Saturated and Subcooled Liquids)," *International Developments in Heat Transfer*, ASME, New York, 1961, pp. D70-D98.
73. Westwater, J.W. and Santangelo, J.G., "Photographic Study of Boiling," *Industrial and Engineering Chemistry*, Vol. 47, No. 8, 1955, pp. 1605-1610.
74. Westwater, J.W., "Boiling Heat Transfer," *American Scientist*, Vol. 47, 1959, pp. 427-446.
75. Gaertner, R.F., "Distribution of Active Sites in the Nucleate Boiling of Liquids,"

AICHE Chemical Engineering Progress Symposium Series, Vol. 59, No. 41, 1963, pp. 52-61.

76. Gaertner, R.F. and Westwater, J.W., "Population of Active Sites in Nucleate Boiling Heat Transfer," *AICHE Chemical Engineering Progress Symposium Series*, Vol. 56, No. 30, 1960, pp. 39-48.

77. Kirby, D.B. and Westwater, J.W., "Bubble and Vapor Behavior on a Heated Horizontal Plate During Pool Boiling Near Burnout," *AICHE Chemical Engineering Progress Symposium Series*, Vol. 61, No. 57, 1965, pp. 238-248.

78. Kenning, D.B.R., "Wall Temperatures in Nucleate Boiling: Spatial and Temporal Variation," *Proceedings of the Ninth International Heat Transfer Conference*, Vol. 3, 1990, pp. 33-38.

79. Kenning, D.B.R., "Wall Temperature Variations and the Modeling of Bubble Nucleation Sites," *Pool and External Flow Boiling*, ASME, New York, 1992, pp. 105-110.

80. Guglielmini, G. and Nannei, E., "On the Effect of Heating Wall Thickness on Pool Boiling Burnout," *International Journal of Heat and Mass Transfer*, Vol. 19, No. 9, pp. 1073-1075.

81. Carvalho, R.D.M., and Bergles, A.E., "The Effects of the Heater Thermal Conductance/Capacitance on the Pool Boiling Critical Heat Flux," *Pool and External Flow Boiling*, ASME, New York, 1992, pp. 203-211.

82. Akhanda, M.A.R. and James, D.D., "An Experimental Investigation into the Influence of Heating Plate Thickness on the Heat Transfer Rate in Flow Boiling," *Fundamentals of Phase Change: Boiling and Condensation*, HTD-Vol. 136, 1990, pp.

35-39.

83. Bar-Cohen, A. and McNeil, A., "Parametric Effects on Pool Boiling Critical Heat Flux in Dielectric Liquids," *Pool and External Flow Boiling*, ASME, New York, 1992, pp. 171-175.

84. Bar-Cohen, A., "Thermal Management of Electronic Components with Dielectric Liquids," *Proceedings of the 1991 ASME/JSME Thermal Engineering Joint Conference*, Vol. 2, 1991, pp. xv-xxxiv.

85. Lienhard, J.H., and Wong, P.T.Y., "The Dominant Unstable Wavelength and Minimum Heat Flux During Film Boiling on a Horizontal Cylinder," *ASME Journal of Heat Transfer*, Vol. 86, No. 2, 1964, pp. 220-226.

86. Sun, K.H. and Lienhard, J.H., "The Peak Pool Boiling Heat Flux on Horizontal Cylinders," *International Journal of Heat and Mass Transfer*, Vol 13, No. 9, 1970, pp. 1425-1438.

87. Lienhard, J.H. and Dhir, V.K., "Hydrodynamic Prediction of Peak Pool-Boiling Heat Fluxes for Finite Bodies," *ASME Journal of Heat Transfer*, Vol. 95, No. 2, 1973, pp. 152-158.

88. Sernas, V., Lienhard, J.H., and Dhir, V.K., "The Taylor Wave Configuration During Boiling from a Flat Plate," *International Journal of Heat and Mass Transfer*, Vol. 16, No. 9, 1973, pp. 1820-1821.

89. Lienhard, J.H., Dhir, V.K., and Rihard, D.M., "Peak Pool Boiling Heat-Flux Measurements on Finite Horizontal Flat Plates," *ASME Journal of Heat Transfer*, Vol. 95, No. 4, 1973, pp. 477-482.

90. Lienhard, J.H. and Eichhorn, R., "On Predicting Boiling Burnout for Heaters Cooled by Liquid Jets," *International Journal of Heat and Mass Transfer*, Vol. 22, 1979, pp. 774-776.
91. Lienhard, J.H. and Eichhorn, R., "Peak Boiling Heat Flux on Cylinders in a Cross Flow," *International Journal of Heat Mass Transfer*, Vol. 19, 1976, pp. 1135-1141.
92. Lienhard, J.H. and Hasan M.M., "On Predicting Boiling Burnout with the Mechanical Energy Stability Criterion," *ASME Journal of Heat Transfer*, Vol. 101, No. 2, 1979, pp. 276-279.
93. Katto, Y. and Yokoya, S., "Principal Mechanism of Boiling Crisis in Pool Boiling," *International Journal of Heat Mass Transfer*, Vol. 11, 1968, pp. 993-1002.
94. Haramura, Y. and Katto, Y., "A New Hydrodynamic Model of Critical Heat Flux, Applicable Widely to Both Pool and Forced Convection Boiling on Submerged Bodies in Saturated Liquids," *International Journal of Heat Mass Transfer*, Vol. 26, No. 3, 1983, pp. 389-399.
95. Davidson, J.F. and Schuler, B.O.G., "Bubble Formation at an Orifice in a Viscous Liquid," *Transactions of the Institution of Chemical Engineers*, Vol. 38, No. 3, 1960, pp. 144-154.
96. Davidson, J.F. and Schuler, B.O.G., "Bubble Formation at an Orifice in an Inviscid Liquid," *Transactions of the Institution of Chemical Engineers*, Vol. 38, No. 6, 1960, pp. 335-342.
97. Walters, J.K. and Davidson, J.F., "The Initial Motion of a Gas Bubble Formed in an Inviscid Liquid," *Journal of Fluid Mechanics*, Vol. 17, Part 3, November 1963, pp. 321-336.

98. Pasamehmetoglu, K.O. and Nelson, R.A., "The Effect of Helmholtz Instability on the Macrolayer Thickness in Vapor Mushroom Region of Nucleate Pool Boiling," *International Communications in Heat and Mass Transfer*, Vol. 14, No. 6, 1987, pp. 709-720.
99. Yu, C.L. and Mesler, R.B., "A Study of Nucleate Boiling Near the Peak Heat Flux Through Measurement of Transient Surface Temperature," *International Journal of Heat and Mass Transfer*, Vol. 20, No. 8, 1977, pp. 827-840.
100. Bhat, A.M., Prakash, R., and Saini, J.S., "On the Mechanism of Macrolayer Formation in Nucleate Pool Boiling at High Heat Flux," *International Journal of Heat and Mass Transfer*, Vol. 26, No. 5, 1983, pp. 735-740.
101. Bhat, A.M., Prakash, R., and Saini, J.S., "Heat Transfer in Nucleate Pool Boiling at High Heat Flux," *International Journal of Heat and Mass Transfer*, Vol. 26, No. 6, 1983, pp. 833-840.
102. Bhat, A.M., Saini, J.S., and Prakash, R., "Role of Macrolayer Evaporation in Pool Boiling at High Heat Flux," *International Journal of Heat and Mass Transfer*, Vol. 29, No. 12, 1986, pp. 1953-1961.
103. Liaw, S.P. and Dhir, V.K., "Void Fraction Measurements During Saturated Pool Boiling of Water on Partially Wetted Vertical Surfaces," *ASME Journal of Heat Transfer*, Vol. 111, No. 3, 1989, pp. 731-738.
104. Dhir, V.K. and Liaw, S.P., "Framework for a Unified Model for Nucleate and Transition Pool Boiling," *ASME Journal of Heat Transfer*, Vol. 111, No.3, 1989, pp. 739-746.
105. Pan, C., Hwang, J.Y., and Lin, T.L., "The Mechanism of Heat Transfer in

Transition Boiling," *International Journal of Heat and Mass Transfer*, Vol. 32, No. 7, 1989, pp. 1337-1349.

106. Pan, C. and Lin, T.L., "A Model for Surface Wettability Effect on Transition Boiling Heat Transfer," *The Ninth International Heat Transfer Conference*, Vol. 2, 1990, pp. 147-152.

107. Pan C. and Lin, T.L., "Predictions of Parametric Effect on Transition Boiling Under Pool Boiling Conditions," *International Journal of Heat and Mass Transfer*, Vol. 34, No. 6, 1991, pp. 1355-1370.

108. Lamb, H., *Hydrodynamics*, Sixth Edition, Dover Publications, New York, 1932, pp. 455-462.

109. Katto Y. and Kurata C., "Critical Heat Flux of Saturated Convective Boiling on Uniformly Heated Plates in a Parallel Flow," *International Journal of Multiphase Flow*, Vol. 6, pp. 575-582.

110. Katto, Y. and Ishii, K., "Burnout in a High Heat Flux Boiling System with a Forced Supply of Liquid Through a Plane Jet," *Sixth International Heat Transfer Conference*, Vol. 1, 1978, pp. 435-440.

111. Sharan, A. and Lienhard, J.H., "On Predicting Burnout in the Jet-Disk Configuration," *ASME Journal of Heat Transfer*, Vol. 107, No. 2, 1985, pp. 398-401.

112. Sadasivan P. and Lienhard J.H., "Considerations in Predicting Burnout of Cylinders in Flow Boiling," *ASME Journal of Heat Transfer*, Vol. 114, No. 1, 1992, pp. 185-193.

113. Monde, M. and Katto, Y., "Burnout in a High Heat-Flux Boiling System with an

Impinging Jet," *International Journal of Heat and Mass Transfer*, Vol. 21, 1978, pp. 295-305.

114. Katto, Y. and Shimizu M., "Upper Limit of CHF in the Saturated Forced Convection Boiling on a Heated Disk with a Small Impinging Jet," *ASME Journal of Heat Transfer*, Vol. 101, No. 2, 1979, pp. 265-269.

115. Katto, Y., "General Features of CHF of Forced Convection Boiling in Uniformly Heated Rectangular Channels," *International Journal of Heat and Mass Transfer*, Vol. 24, No. 8, 1981, pp. 1413-1419.

116. Katto, Y. and Haramura, Y., "Critical Heat Flux on a Uniformly Heated Horizontal Cylinder in an Upward Cross Flow of Saturated Liquid," *International Journal of Heat and Mass Transfer*, Vol. 26, No. 8, 1983, pp. 1199-1205.

117. Katto, Y., Yokoya, S., Maibe S., and Taniguchi, M., "Critical Heat Flux on a Uniformly Heated Cylinder in a Cross Flow of Saturated Liquid Over a Very Wide Range of Vapor-to-Liquid Density Ratio," *International Journal of Heat and Mass Transfer*, Vol. 30, No. 9, 1987, pp. 1971-1977.

118. Katto, Y. and Yokoya, S., "Critical Heat Flux on a Disk Heater Cooled by a Circular Jet of Saturated Liquid Impinging at the Center," *International Journal of Heat and Mass Transfer*, Vol. 31, No. 2, 1988, pp. 219-227.

119. Monde, M., "Critical Heat Flux in Saturated Forced Convection Boiling on a Heated Disk with an Impinging Jet," *ASME Journal of Heat Transfer*, Vol. 109, No. 3, 1987, pp. 991-996.

120. Kandula, M., "Mechanisms and Predictions of Burnout in Flow Boiling over Heated Surfaces with an Impinging Jet," *International Journal of Heat and Mass*

Transfer, Vol. 33, No. 9, 1990, pp. 1795-1803.

121. Ueda, T., Inoue, M., and Nagatome, S., "Critical Heat Flux and Droplet Entrainment Rate in Boiling of Falling Liquid Films," *International Journal of Heat and Mass Transfer*, Vol. 24, No. 7, 1981, pp. 1257-1266.

122. Baines, R.P., El Masri, M.A., and Rohsenow, W.M., "Critical Heat Flux in Flowing Liquid Films," *International Journal of Heat and Mass Transfer*, Vol. 27, No. 9, 1984, pp. 1623-1629.

123. Lienhard, J.H., "Things We Don't Know About Boiling Heat Transfer: 1988," *International Communication in Heat and Mass Transfer*, Vol. 15, No. 4, 1988, pp. 401-428.

124. Galloway, J.E. and Mudawar, I., "CHF Mechanism in Flow Boiling From a Short Heated Wall - I. Examination of Near-Wall Conditions with the Aid of Photomicrography and High-Speed Video Imaging," *International Journal of Heat and Mass Transfer*, Vol. 36, No. 10, 1993, pp. 2511-2526.

125. Galloway, J.E. and Mudawar, I., "CHF Mechanism in Flow Boiling From a Short Heated Wall - II. Theoretical CHF Model," *International Journal of Heat and Mass Transfer*, Vol. 36, No. 10, 1993, pp. 2527-2540.

126. Tolubinskiy, V.I., Litoshenko, A.K., and Shevtsov, V.L., "Correlation of Experimental Data on Critical Heat Fluxes in Annular Channels," *Heat Transfer-Soviet Research*, Vol. 1, No. 1, 1969, pp. 80-87.

127. Tolubinskiy, V.I., Litoshenko, A.K., and Shevtsov, V.L., "Critical Heat Flux Densities in Internally-Heated Annuli," *Heat Transfer-Soviet Research*, Vol. 2, No. 6, 1970, pp. 183-186.

128. Hung, Y.H. and Yao, S.C., "Critical Heat Flux of Convective Freon-113 in Very Narrow Annuli," ASME Paper 83-HT-10, 1983.
129. Bergles, A.E., "Subcooled Burnout in Tubes of Small Diameter," ASME Paper 63-WA-182, 1963.
130. Glushchenko, L.F., "Correlation of Experimental Data on Critical Heat Fluxes in Subcooled Boiling," *Heat Transfer-Soviet Research*, Vol. 2, No.1, 1970, pp. 139-143.
131. Ornatskiy, A.P., "The Effect of Basic Regime Parameters and Channel Geometry on Critical Heat Fluxes in Forced Convection of Subcooled Water," *Heat Transfer-Soviet Research*, Vol. 1, No. 3, 1963, pp. 17-22.
132. Leland, J.E. and Chow, L.C., "Effect of Channel Height and Radius of Curvature on Forced Convection Boiling in a Rectangular Channel," AIAA Paper 92-0250, 1992.
133. Willingham, T.C. and Mudawar, I., "Channel Height Effects on Forced-Convection Boiling and Critical Heat Flux from a Linear Array of Discrete Heat Sources," *International Journal of Heat and Mass Transfer*, Vol. 35, No.8, 1992, pp. 1865-1880.
134. Glantz, S.A. and Slinker, B.K., *Primer of Applied Regression and Analysis of Variance*, McGraw-Hill, Inc., New York, 1990, pp. 68-69.
135. Borishanskii, V.M., "An Equation Generalizing Experimental Data on the Cessation of Bubble Boiling in a Large Volume of Liquid," *Zhurn. Tekh. Fiz.*, Vol. 26, 1956, p. 452, translated in *Soviet Physics-Technical Physics*, Vol.1, No. 2, 1956, pp. 438-442.
136. Bar-Cohen, A. and Simon, T.W., "Wall Superheat Excursion in the Boiling

Incipience of Dielectric Fluids," *Heat Transfer in Electronic Equipment*, HTD-Vol. 57, ASME, New York, 1986, pp. 83-94.

137. Lopina, R.F. and Bergles, A.E., "Subcooled Boiling of Water in Tape-Generated Swirl Flow," *ASME Journal of Heat Transfer*, Vol. 95, No. 2, 1973, pp. 281-283.

138. Viskanta, R., "Critical Heat Flux for Water in Swirling Flow," *Nuclear Science and Engineering*, Vol. 10, 1961, pp. 202-203.

139. Gambill, W.R., "Subcooled Swirl-Flow Boiling and Burnout with Electrically Heated Twisted Tapes and Zero Wall Flux," *ASME Journal of Heat Transfer*, Vol. 87, No. 3, 1965, pp. 342-348.

140. Winovich, W. and Carlson, W.C.A., "The 60-MW Shuttle Interaction Heating Facility," *Proceedings of the 25th International Instrumentation Symposium*, Vol. 25, *Advances in Test Measurement*, Vol. 16, Pt. 1, 1979, pp. 59-75.

141. Merte, H. Jr. and Clark, J.A., "Pool Boiling in an Accelerating System," *ASME Journal of Heat Transfer*, Vol. 83, No.3, 1961, pp. 233-242.

142. Costello, C.P. and Adams, J.M., "Burnout Heat Fluxes in Pool Boiling at High Acceleration," *International Developments in Heat Transfer*, ASME, New York, 1961, pp. 255-261.

143. Beckman, W.A. and Merte, H. Jr., "A Photographic Study of Boiling in an Accelerating System," *ASME Journal of Heat Transfer*, Vol. 87, No. 3, 1965, pp. 374-380.

144. Gray, V.H., Marto, P.J., and Joslyn, A.W., "Boiling Heat-Transfer Coefficients, Interface Behavior, and Vapor Quality in Rotating Boiler Operating to 475 G's,"

NASA Report TN D-4136, March, 1968.

145. Marto, P.J. and Gray, V.H., "Effects of High Accelerations and Heat Fluxes on Nucleate Boiling of Water in an Axisymmetric Rotating Boiler," NASA Report TN D-6307, May, 1971.

146. Ulucakli, M. E., and Merte, H., Jr., "Nucleate Boiling with High Gravity and Large Subcooling," *ASME Journal of Heat Transfer*, Vol. 112, No. 2, 1990, pp. 451-457.

147. Hur, N., Thangam, S., and Speziale, C.G., "Numerical Study of Turbulent Secondary Flows in Curved Ducts," *ASME Journal of Fluids Engineering*, Vol. 112, No. 2, 1990, pp. 205-211.

148. Owhadi, A., Bell, K.J., and Crain, B., "Forced Convection Boiling Inside Helically-Coiled Tubes," *International Journal of Heat and Mass Transfer*, Vol. 11, No. 12, 1968, pp. 1779-1793.

149. Cumo, M., Giovanni, E.F., and Ferrari, G., "The Influence of Curvature in Post Dry-Out Heat Transfer," *International Journal of Heat and Mass Transfer*, Vol. 15, No. 11, 1972, pp. 2045-2062.

150. Jensen, M.K. and Bergles, A.E., "Critical Heat Flux in Helically Coiled Tubes," *ASME Journal of Heat Transfer*, Vol. 103, No. 4, 1981, pp. 660-666.

151. Hughes, T.G., *Critical Heat Fluxes for Curved and Straight Surfaces During Subcooling Flow Boiling*, Thesis, Pennsylvania State University, TM-74-194, (AD-A-003036), November, 1974.

152. Mudawwar, I.A., El-Masri, M.A., Wu, C.S., and Ausman-Mudawwar, J.R., "Boiling Heat Transfer and Critical Heat Flux in High-Speed Rotating Liquid Films,"

International Journal of Heat and Mass Transfer, Vol. 28, No. 4, 1985 pp. 795-806.

153. Galloway, J.E. and Mudawar, I., "Critical Heat Flux Enhancement by Means of Liquid Subcooling and Centrifugal Force Induced by Flow Curvature," *International Journal of Heat and Mass Transfer*, Vol. 35, No. 5, 1992, pp. 1247-1260.

154. Squire, H. B., "Note on Secondary Flow in a Curved Circular Pipe," Aeronautical Research Council Report No. 16601, 1954.

155. Rowe, M., "Measurements and Computations of Flow in Pipe Bends," *Journal of Fluid Mechanics*, Vol. 43, No. 4, 1970, pp.771-783.

156. Wattendorf, F.L., "A Study of the Effect of Curvature on Fully Developed Turbulent Flow," *Proceedings of the Royal Society of London, Series A—Mathematical and Physical Sciences*, Vol. CXLVIII, February, 1935, pp. 565-598.

157. Eskinazi, S., and Yeh, H., "An Investigation on Fully Developed Turbulent Flows in a Curved Channel," *Journal of the Aeronautical Sciences*, Vol. 23, No. 1, 1956, pp. 23-34, and p. 75.

158. Marris, A. W., "Radial Distributions of Temporal-Mean Peripheral Velocity and Pressure for Fully Developed Turbulent Flow in Curved Channels," *ASME Journal of Basic Engineering*, Vol. 82, No. 3, 1960, pp. 528-538.

159. Ellis, L. B., and Joubert, P. N., "Turbulent Shear Flow in a Curved Duct," *Journal of Fluid Mechanics*, Vol. 62, Part 1, 1974, pp. 65-84.

160. Schlichting, H., *Boundary-Layer Theory*, Seventh Edition, McGraw Hill Book Co., New York, 1979, p. 512.

161. Carey, V.P., *Liquid-Vapor Phase-Change Phenomena*, Hemisphere Publishing Corp., Washington, 1992, p. 206.
162. Haley, K.W. and Westwater, J.W., "Boiling Heat Transfer from Single Fins," *Proceedings of the Third International Heat Transfer Conference*, Vol. 3, 1966, pp. 245-253.
163. Roeller, P.T. and Webb, B.W., "A Composite Correlation for Heat Transfer from Isolated Two- and Three-Dimensional Protrusions in Channels," *International Journal of Heat and Mass Transfer*, Vol. 35, No. 4, 1992, pp. 987-990.
164. Bernath, L., "A Theory of Local-Boiling Burnout and its Application to Existing Data," *AIChE Chemical Engineering Progress Symposium Series*, Vol. 56, No. 30, 1960, pp. 95-116.
165. Carne, M., "Some Effects of Test Section Geometry in Saturated Pool Boiling on the Critical Heat Flux for Some Organic Liquids and Liquid Mixtures," *AIChE Chemical Engineering Progress Symposium Series*, Vol. 61, No. 59, 1965, pp. 281-289.
166. Sharp, R.R., "The Nature of Liquid Film Evaporation During Nucleate Boiling," NASA Report TN D-1997, October, 1964.
167. Dzakowic, G.S. and Frost, W., "Vapor Bubble Growth in Saturated Pool Boiling by Microlayer Evaporation of Liquid at the Heated Surface," *Proceedings of the Fourth International Heat Transfer Conference*, Vol. 5, Paper B2.2, 1970, pp. 1-11.
168. Houchin, W.R. and Lienhard, J.H., "Boiling Burnout in Low Thermal Capacity Heaters," ASME Paper 66-WA/HT-40, 1966.
169. Lin, D.Y.T. and Westwater, J.W., "Effect of Metal Thermal Properties on Boiling

Curves Obtained by the Quenching Method," *Proceedings of the Seventh International Heat Transfer Conference*, Vol. 4, Paper PB24, 1982, pp. 155-160.

170. Tippets, F.E., "Critical Heat Fluxes and Flow Patterns in High Pressure Boiling Water Flows," ASME Paper 62-WA-162, 1962.

171. Del Valle M., V.H. and Kenning, D.B.R., "Subcooled Flow Boiling at High Heat Flux," *International Journal of Heat and Mass Transfer*, Vol. 28, No. 10, 1985, pp. 1907-1920.

Appendix A

DETAILS OF CURVED CHANNEL TEST SECTION GEOMETRY

Details of the flow channel and heater test section are shown in Figs. A-1 - A.8. The dimensions shown are for one of the three flow channels, but are indicative of the other flow channels. Figures A.1 - A.5 show the construction of the flow channel which was made of Zelux-W optical grade plastic. Zelux can withstand higher temperatures than plexiglas and is much more shatter resistant.

The curved section heater enclosure is shown in Fig. A.6 and the cover is shown in Fig. A.8. The straight section heater enclosure is not shown, but is very similar to the curved section heater enclosure. These parts were made of Glastherm HT, a high temperature resistant plastic made by General Electric Corp. Unlike more commonly used G-7 and G-10 laminated fiberglass plastics, Glastherm is made of randomly oriented fiberglass strands in a resin binder. Consequently, Glastherm is more isotropic which was important to the design of this test section. High temperatures within the heater enclosure caused earlier versions made of G-7 to separate.

The electronic chip was simulated by an oxygen free copper (OFC) block shown in Fig. A.7. Oxygen free copper is free of large quantities of air in the volume of the copper. OFC oxidizes in air the same as regular copper. The high thermal conductivity of the copper, (39.1 W/mK at 20°C), coupled with the very low thermal conductivity of the Glastherm enclosure, (0.57 W/mK at 20°C), caused the temperature profile of the block to be nearly uniform in the plane normal to the radius of curvature. This was verified through a numerical model of an axisymmetric approximation of the heater test section. This model was constructed and solved using a commercial finite element based solver, ANSYS, (Swanson Analysis Systems, Inc.). This model also showed the heat loss to be less than 10% for several characteristic cases.

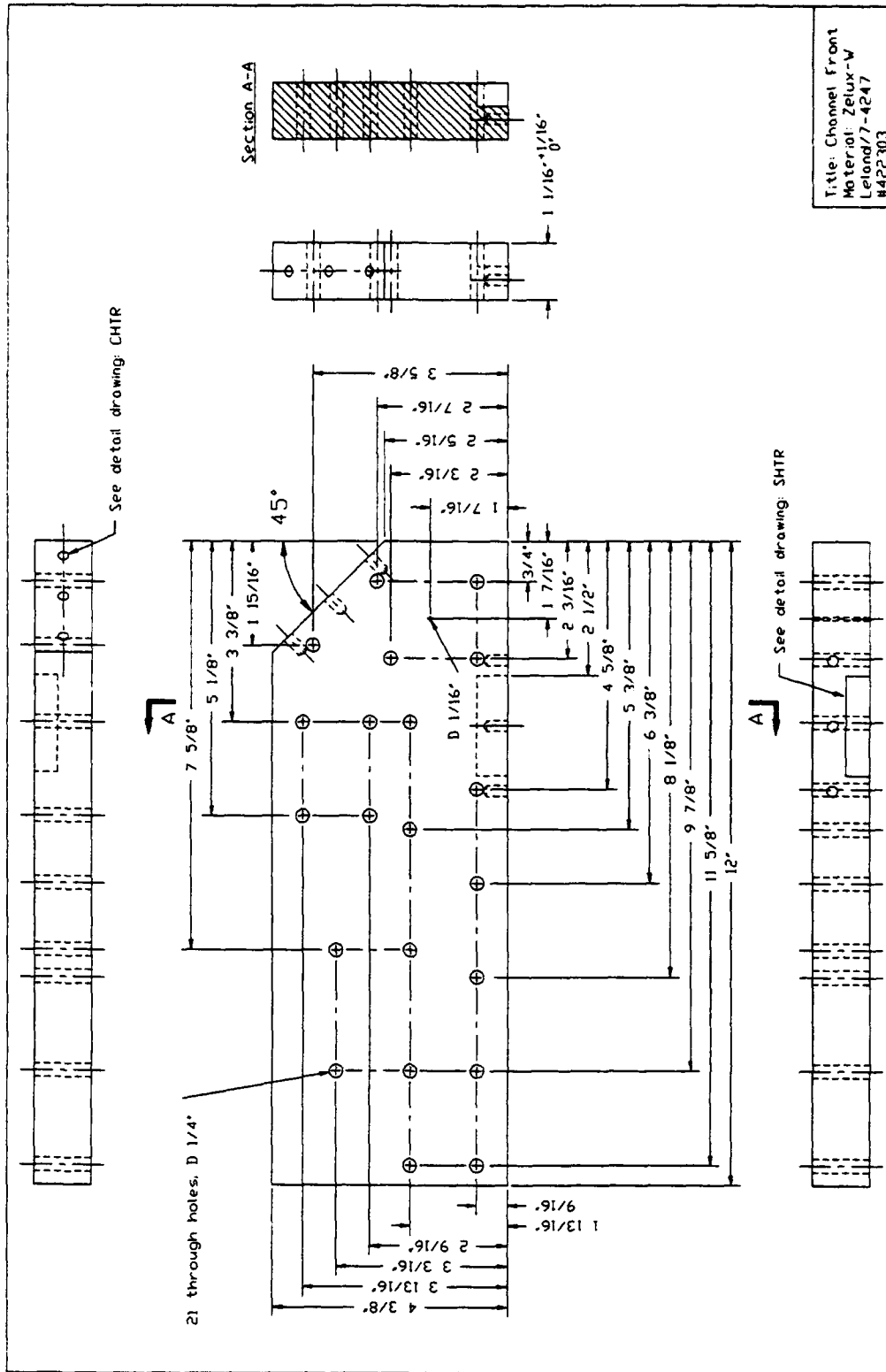


Figure A.1 Front lamina of channel test section.

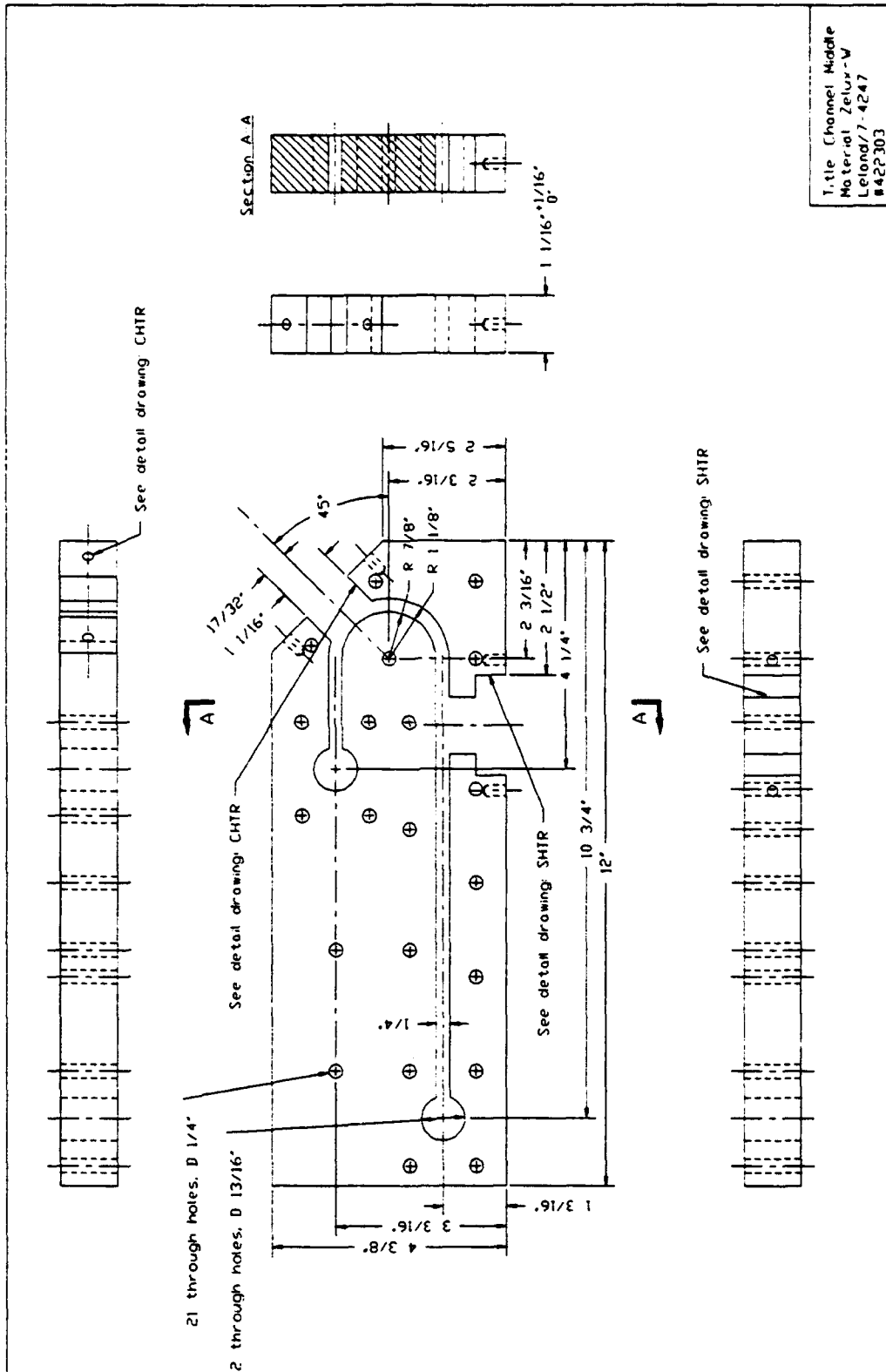


Figure A.2 Center lamina of channel test section.

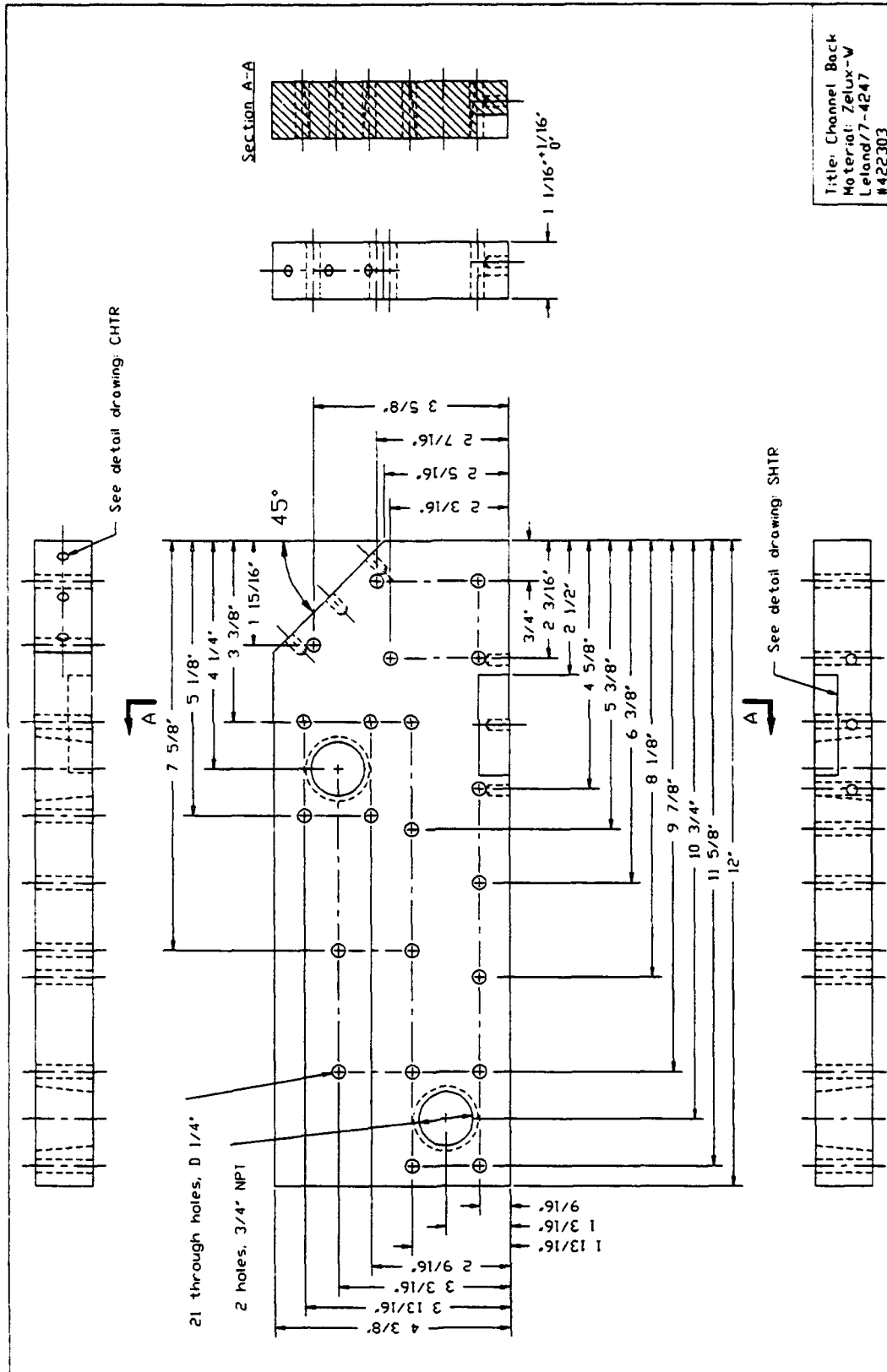


Figure A.3 Back lamina of channel test section.

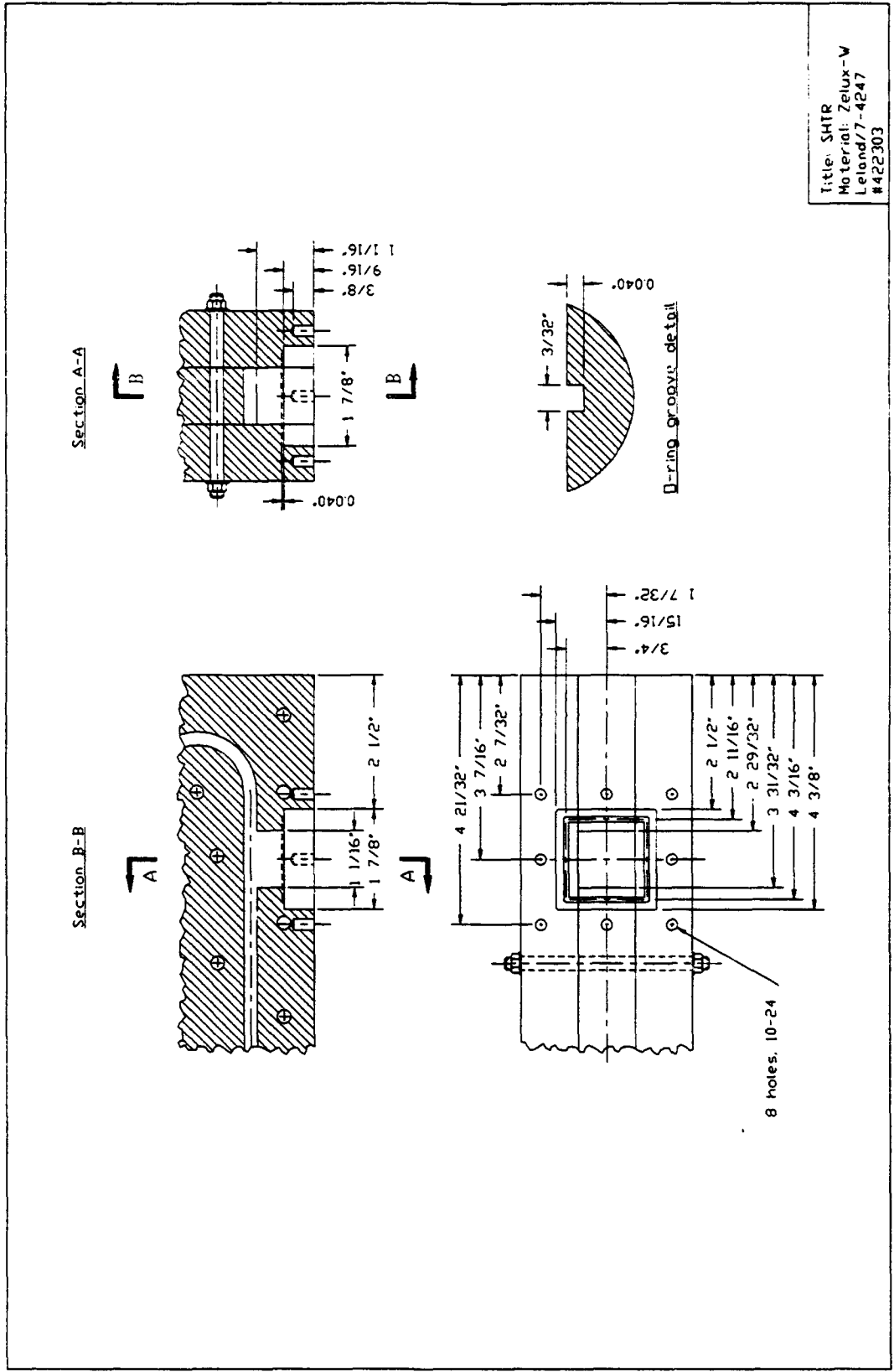


Figure A.5 Details of straight section heater insertion hole.

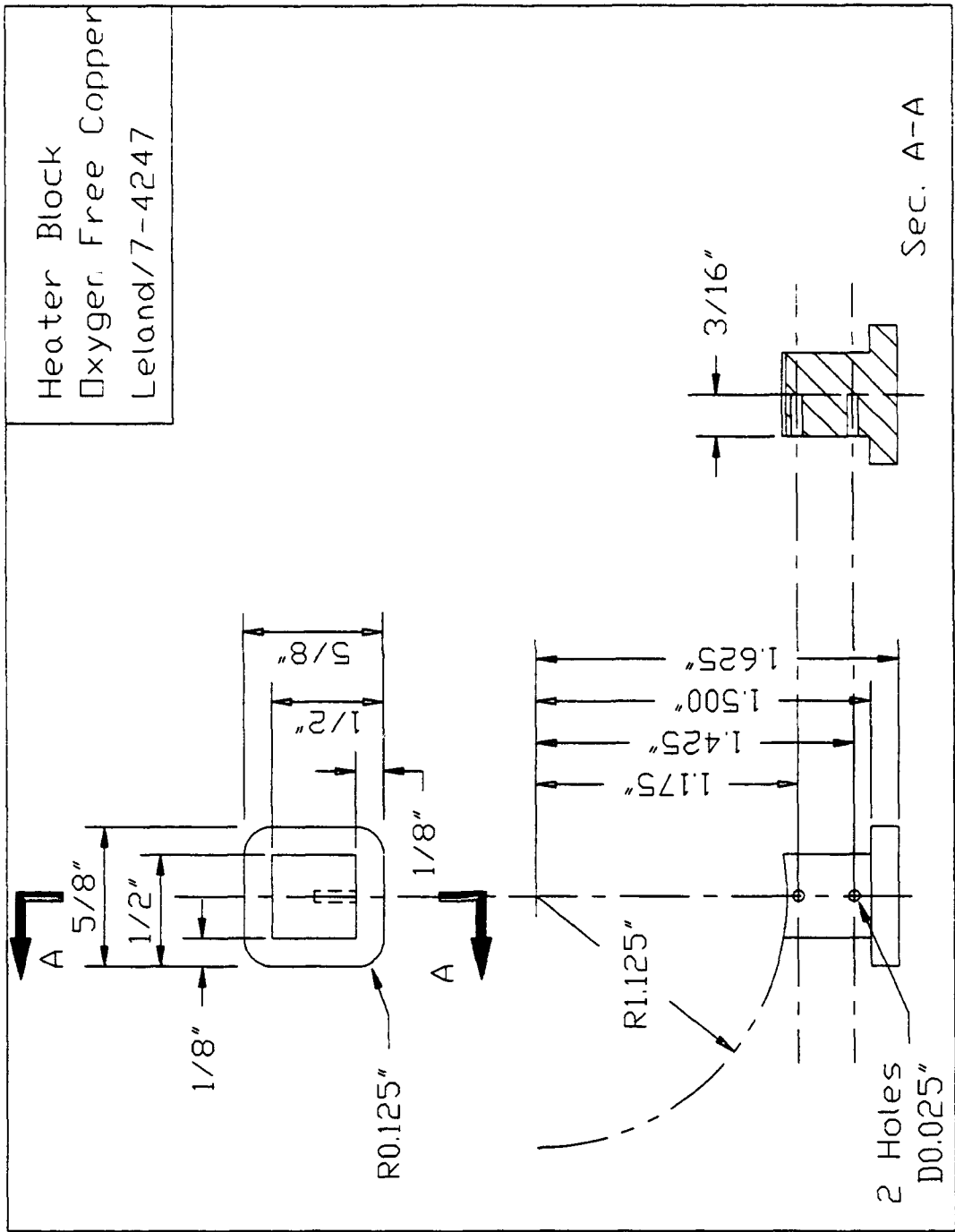
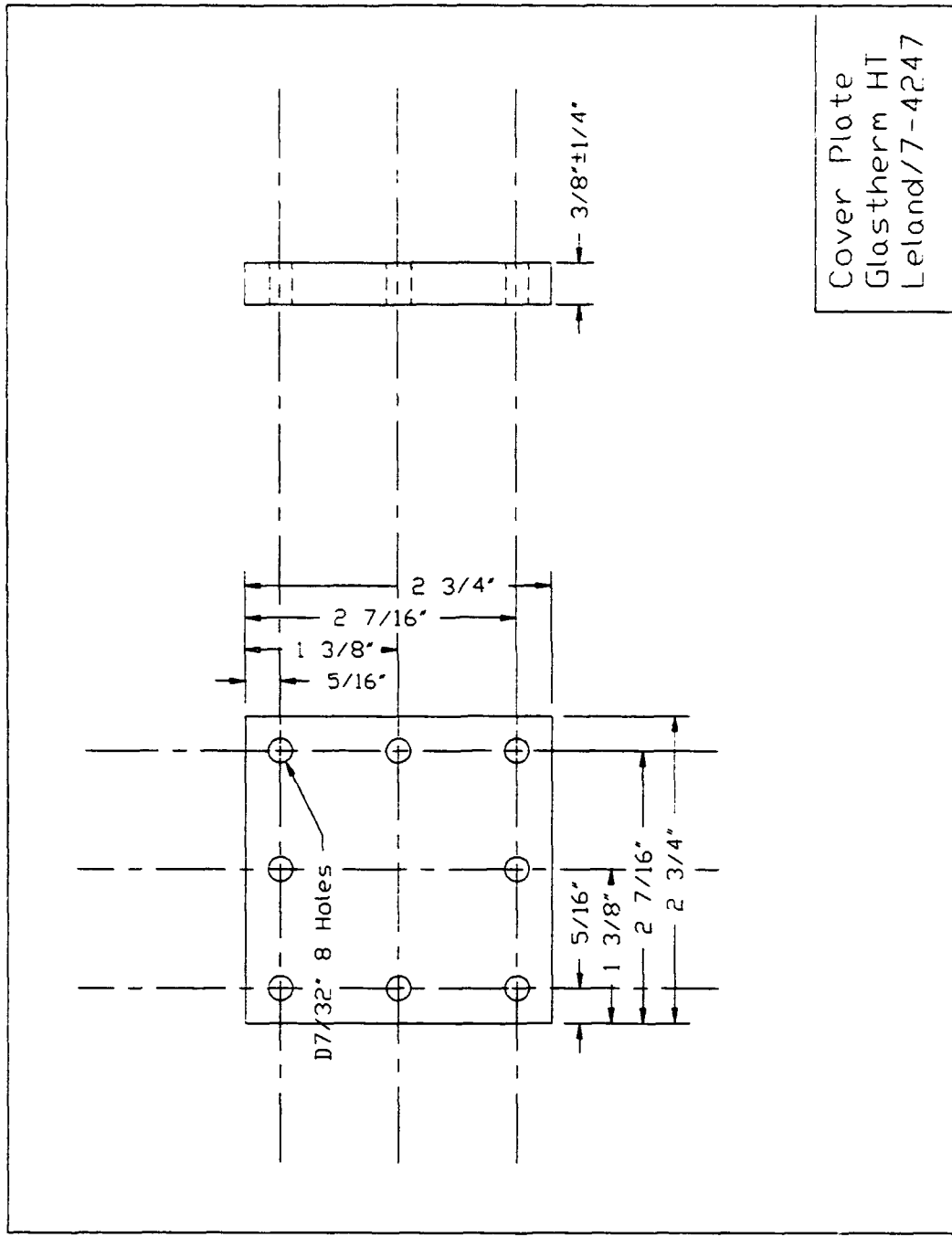


Figure A.7 Copper block heater/simulated electronic chip.



Cover Plote
 Glastherm HT
 Leland/7-4247

Figure A.8 Backside cover for heater enclosure.

Appendix B
DEFINITION OF ROUGHNESS PARAMETERS

Figure B.1 shows a typical roughness profile where $l_1 - l_5$ are consecutive and equal sampling lengths. The evaluation length, L , is defined as the length of the roughness profile used for the measurement of surface roughness parameters. L should not be confused with the same nomenclature used for heated length. For the experiments of this thesis, $l = 50 \mu\text{m}$ and $L = 250 \mu\text{m}$. The horizontal line dividing the peaks and valleys in Fig. B.1 is called the "mean line." Its location is defined such that the area of the peaks above the line is equal to the area of the valleys below the line. The mean line is a reference by which most roughness parameters are obtained.

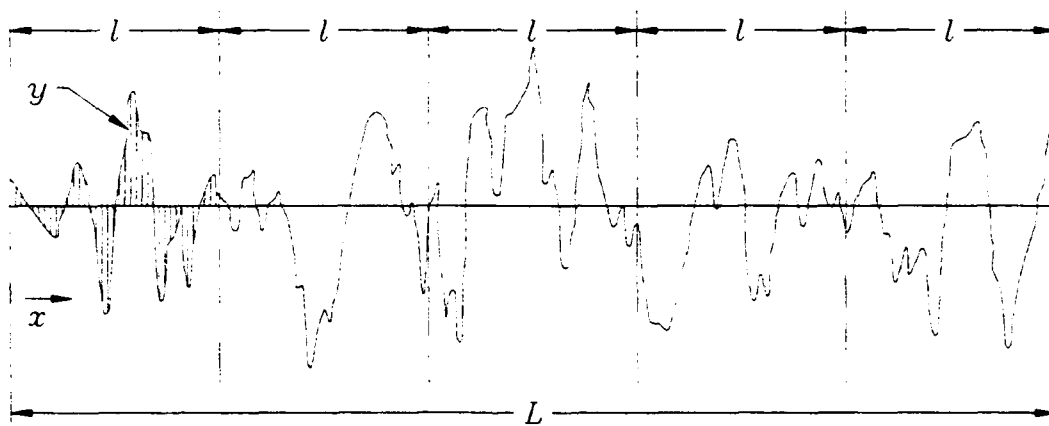


Figure B.1 Roughness profile with basic parameters for measuring surface roughness.

The most common parameter for roughness is R_a which the International Organization for Standardization defines in the standard ISO R468. R_a is simply defined as the mean of the departures of the roughness profile from the mean line, or

$$R_a = \frac{1}{L} \int_0^L |y(x)| dx$$

Another parameter for roughness is R_p , (defined in DIN 4762). R_p is simply the

maximum height of the profile above the mean line within the assessment length. Figure B.2 shows the individual R_p for the roughness profile example. For this case, $R_p = R_{p3}$. It is easy to see that this parameter is even less appropriate for indicating the size distribution of nucleation sites.

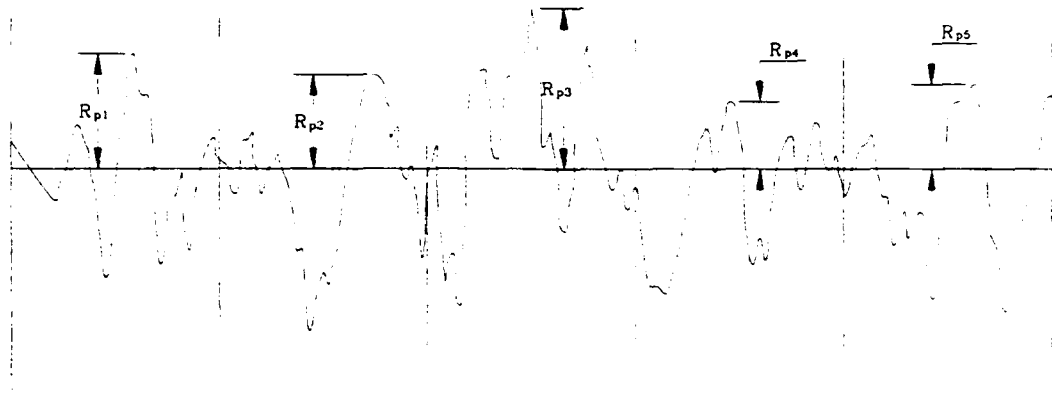


Figure B.2 Definition of R_p .

Finally, S , is the mean peak-to-peak spacing between roughness elements. Figure B.3 shows S defined for the same sample roughness profile. Note that S does not depend on the location of the mean line. Some instruments are capable of providing a distribution of S_n . Unfortunately, the instrument used for these tests, a Surtronic P3 profilometer (Rank Taylor Hobson Ltd.), could only provide the mean spacing.

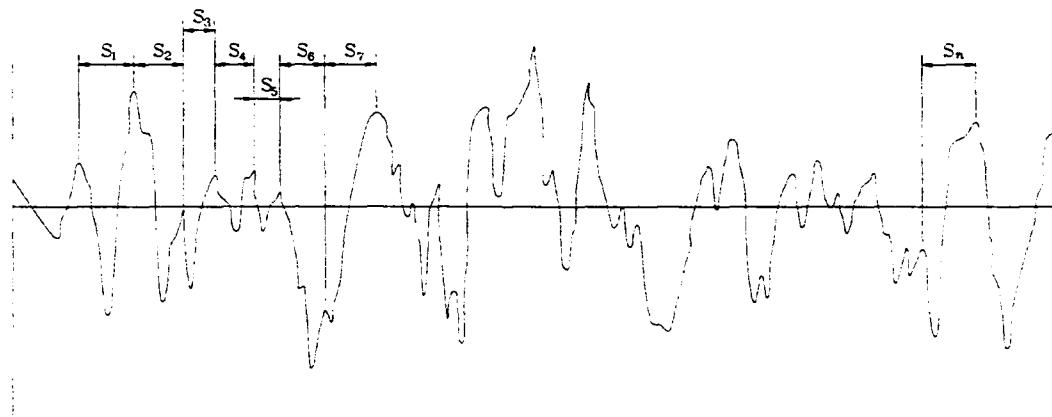


Figure B.3 Definition of S .

Appendix C
UNCERTAINTY ANALYSIS FOR EXPERIMENTAL APPARATUS
OF CHAPTERS 2-5

C.1 Heat Flux

The heat flux is based on a one-dimensional approximation to heat conduction. Figure C.1 shows the geometry of a representative curved test section geometry. For this configuration, the heat flux is approximated by,

$$q = -\frac{kA_{c-c}}{A_w} \cdot \frac{\Delta T_{12}}{\Delta X_{12}} \quad (C.1)$$

where

$$\frac{A_{c-c}}{A_w} = \frac{L^2}{2LR \sin^{-1}\left(\frac{L}{2R}\right)} \quad (C.2)$$

Combining Eqs. (C.1) and (C.2) yields

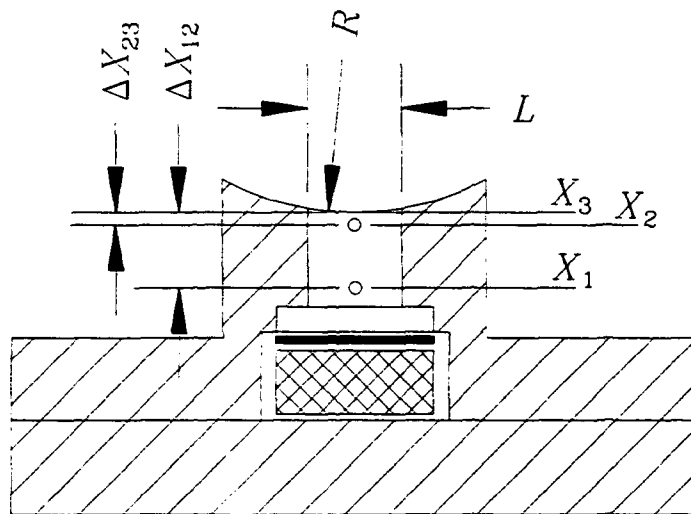


Figure C.1 Schematic of curved test section heater.

$$q = -\frac{kL\Delta T_{12}}{2R\sin^{-1}\left(\frac{L}{2R}\right)\Delta X_{12}} \quad (\text{C.3})$$

Following the standard Kline and McClinton³¹ approach to calculating random uncertainty, the uncertainty in the heat flux is given as

$$\delta_q = \sqrt{\left(\frac{\partial q}{\partial \Delta T_{12}} \delta \Delta T_{12}\right)^2 + \left(\frac{\partial q}{\partial k} \delta k\right)^2 + \left(\frac{\partial q}{\partial L} \delta L\right)^2 + \left(\frac{\partial q}{\partial R} \delta R\right)^2 + \left(\frac{\partial q}{\partial \Delta X_{12}} \delta \Delta X_{12}\right)^2} \quad (\text{C.4})$$

Evaluating the individual partial derivatives yields

$$\begin{aligned} \frac{\partial q}{\partial \Delta T_{12}} &= -\frac{kL}{2R\sin^{-1}\left(\frac{L}{2R}\right)\Delta X_{12}} \\ &= \frac{q}{\Delta T_{12}} \end{aligned} \quad (\text{C.5a})$$

$$\begin{aligned} \frac{\partial q}{\partial k} &= -\frac{L\Delta T_{12}}{2R\sin^{-1}\left(\frac{L}{2R}\right)\Delta X_{12}} \\ &= \frac{q}{k} \end{aligned} \quad (\text{C.5b})$$

$$\begin{aligned} \frac{\partial q}{\partial R} &= \frac{kL\Delta T_{12}}{2R^2\sin^{-1}\left(\frac{L}{2R}\right)\Delta X_{12}} \left\{ 1 - \frac{L}{2R\sin^{-1}\left(\frac{L}{2R}\right)\sqrt{1-\left(\frac{L}{2R}\right)^2}} \right\} \\ &= \frac{q}{R} \left\{ -1 + \frac{L}{2R\sin^{-1}\left(\frac{L}{2R}\right)\sqrt{1-\left(\frac{L}{2R}\right)^2}} \right\} \end{aligned} \quad (\text{C.5c})$$

$$\begin{aligned} \frac{\partial q}{\partial L} &= - \frac{k \Delta T_{12}}{2R \sin^{-1}\left(\frac{L}{2R}\right) \Delta X_{12}} \left\{ 1 - \frac{L}{2R \sin^{-1}\left(\frac{L}{2R}\right) \sqrt{1 - \left(\frac{L}{2R}\right)^2}} \right\} \\ &= \frac{q}{L} \left\{ 1 - \frac{L}{2R \sin^{-1}\left(\frac{L}{2R}\right) \sqrt{1 - \left(\frac{L}{2R}\right)^2}} \right\} \end{aligned} \quad (\text{C.5d})$$

where $L/2R < \pi/2$ for all cases.

$$\begin{aligned} \frac{\partial q}{\partial \Delta X_{12}} &= \frac{kL \Delta T_{12}}{2R \sin^{-1}\left(\frac{L}{2R}\right) \Delta X_{12}^2} \\ &= - \frac{q}{\Delta X_{12}} \end{aligned} \quad (\text{C.5e})$$

Substituting Eqs. (C.5a) - (C.5e) into Eq. (C.4) yields

$$\frac{\delta q}{q} = \sqrt{\left(\frac{\delta_{\Delta T_{12}}}{\Delta T_{12}}\right)^2 + \left(\frac{\delta_k}{k}\right)^2 + \left[\left(-\frac{1}{R} + \frac{L}{C_1 R}\right) \delta_R\right]^2 + \left[\left(\frac{1}{L} - \frac{1}{C_1}\right) \delta_L\right]^2 + \left(-\frac{\delta_{\Delta X_{12}}}{\Delta X_{12}}\right)^2} \quad (\text{C.6})$$

where

$$C_1 = 2R \sin^{-1}\left(\frac{L}{2R}\right) \sqrt{1 - \left(\frac{L}{2R}\right)^2}$$

and q is given by Eq. (C.3). Note that the percent uncertainty is

$$\frac{\delta q}{q} = \phi(k, R, L, \Delta X_{12}, \Delta T_{12})$$

where k , R , L and ΔX_{12} are constant for a given test section. Thus, for a given test section, the random uncertainty varies with ΔT_{12} , or in other words, q .

The uncertainties of the individual variables are

$$\delta_{\Delta T_{12}} = 0.5^{\circ}\text{C}, \text{ or } 0.3^{\circ}\text{C} \quad (\text{C.7a})$$

as verified by calibrating the thermocouples for the test sections of Chapters 3 and 4; and 5, respectively,

$$\delta_k = 10 \frac{\text{W}}{\text{mK}} \quad (\text{C.7b})$$

which is felt to be a conservative estimate based on reported values and the variation of k with temperature,

$$\delta_R = 0.13 \text{ mm} \quad (\text{C.7c})$$

and

$$\delta_L = 0.13 \text{ mm} \quad (\text{C.7d})$$

which are conservative estimates of the measurement accuracy.

The uncertainty of the distance between the thermocouples is a function of the uncertainty of the thermocouple locations. This includes the uncertainty in measuring the hole-center-to-hole-center distance and the uncertainty of the location of the bead within the hole. Assuming the worst case condition that the thermocouple bead touches either the top or the bottom of the conical ending of the drilled hole, (see Fig. C.2), the uncertainty of ΔX_{12} may be obtained as follows. Let

$$\Delta X_{12} = X_1 - X_2$$

Thus

$$\delta_{\Delta X_{12}} = \sqrt{\delta_{X_1}^2 + \delta_{X_2}^2}$$

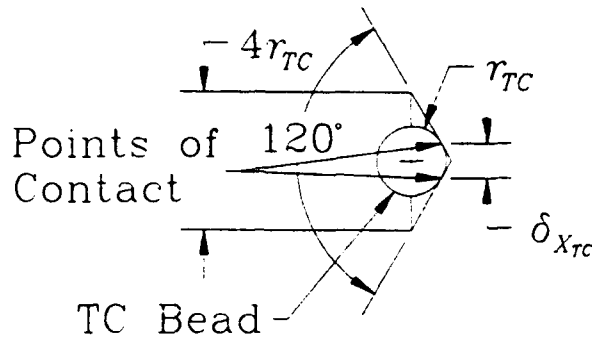


Figure C.2 Schematical representation of thermocouple bead in hole.

where

$$\delta_{x_1} = \delta_{x_2} = \delta_x$$

because the measurement accuracy is the same for each. Therefore,

$$\delta_{\Delta x_{12}} = \sqrt{2} \delta_x$$

where δ_x is a function of both the uncertainty of the hole location, $\delta_{x_{Meas}}$, and the uncertainty of the location of the thermocouple within the hole, $\delta_{x_{TC}}$. Thus

$$\delta_x = \sqrt{\delta_{x_{TC}}^2 + \delta_{x_{Meas}}^2}$$

For these experiments

$$\delta_{x_{Meas}} = 0.025 \text{ mm}$$

Referring to Fig. C.2, $\delta_{x_{TC}}$ is a function of the drill point angle, θ , and the thermocouple bead radius, r_{TC} , or

$$\delta_{x_{TC}} = r_{TC} \sin\left(\frac{\pi - \theta}{2}\right)$$

Thus, for a thermocouple bead radius of

$$r_{TC} = 0.13 \text{ mm}$$

and

$$\theta = 120^\circ$$

the uncertainty of the distance separating the thermocouples becomes

$$\delta_{\Delta X_{12}} = 0.10 \text{ mm} \quad (\text{C.7e})$$

The values of the remaining variables are

$$k = 391.1 \frac{\text{W}}{\text{mK}} \quad (\text{C.8a})$$

as reported by the manufacturer,

$$R = 28.6 \text{ mm, or } 56.4 \text{ mm} \quad (\text{C.8b})$$

for the flow channels tested,

$$L = 9.53 \text{ mm} \quad (\text{C.8c})$$

and

$$\Delta X_{12} = 5.1 \text{ mm} \quad (\text{C.8d})$$

The only remaining unknown in Eq. (C.6) is ΔT_{12} , which is a function of the power input. Solving Eq. (C.3) for ΔT_{12} and substituting into Eq. (C.6) gives the percent uncertainty, $\delta q/q$, as a function of q . The contributions of the uncertainties in L and R are found to be negligible. The conservatively chosen uncertainties for k and $\delta_{X_{12}}$ total about 3% which is the limiting value of the heat flux uncertainty as heat flux becomes very large. Fig. C.3 shows how rapidly the uncertainty in heat flux decreases with increasing heat flux and how important good thermocouple calibration is. Uncertainty for the straight test section heaters is similarly obtained.

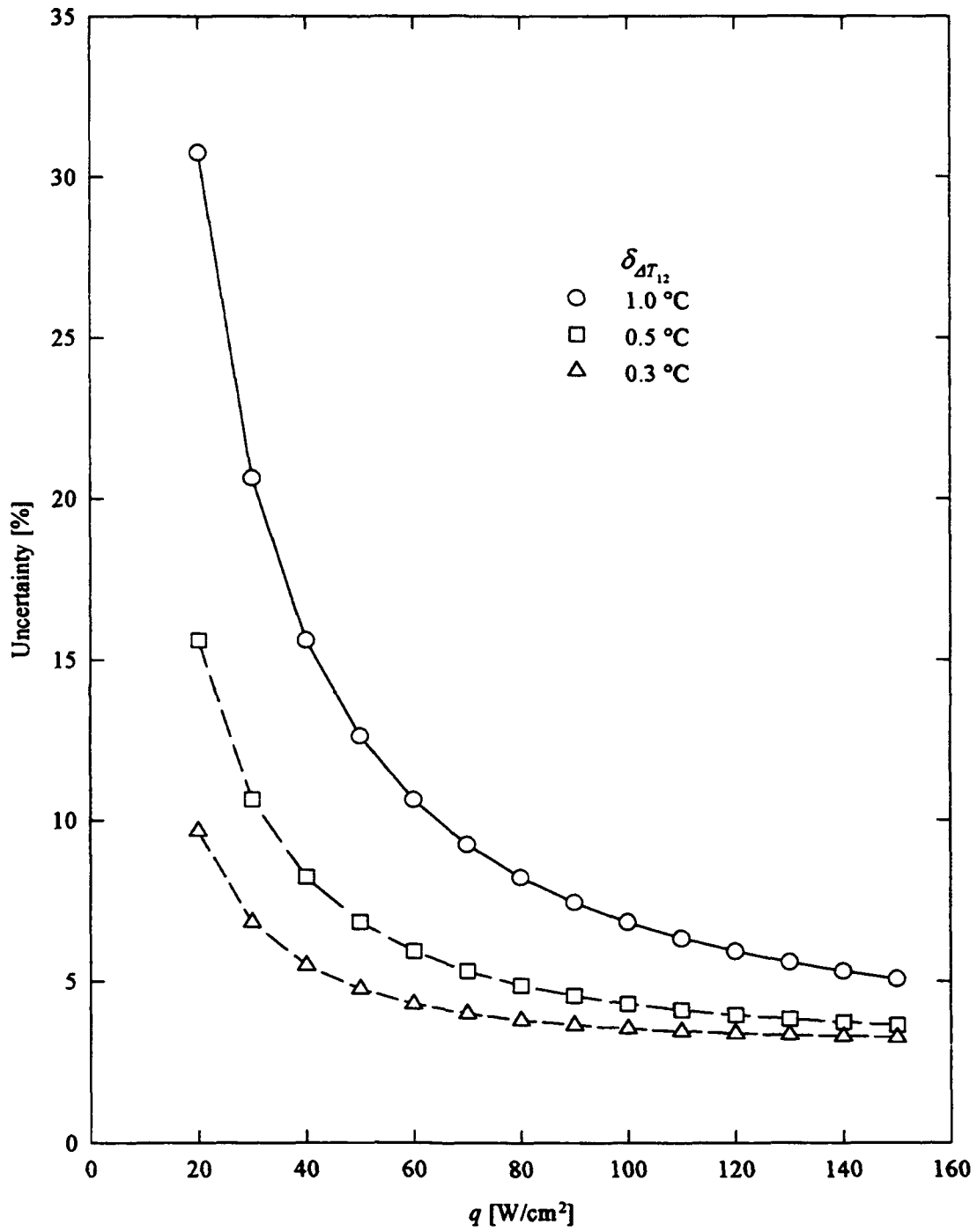


Figure C.3 Heat flux uncertainty versus heat flux.

C.2 Wall Temperature

The wall temperature is approximated by a linear extrapolation, Eq. (C.9), of the measured temperature difference.

$$T_w = T_2 + \frac{A_{c-c}}{A_w} \cdot \frac{\Delta X_{23}}{\Delta X_{12}} \Delta T_{12} \quad (\text{C.9})$$

The uncertainty is given by

$$\delta_{T_w} = C_2 \left[\left(\frac{\delta_{T_2}}{C_2} \right)^2 + \left(\frac{\delta_{\Delta X_{23}}}{\Delta X_{23}} \right)^2 + \left(\frac{\delta_{\Delta X_{12}}}{\Delta X_{12}} \right)^2 + \left(\frac{\delta_{\Delta T_{12}}}{\Delta T_{12}} \right)^2 + \left(\frac{1}{L} - \frac{1}{C_1} \right)^2 \delta_L^2 + \left(\frac{1}{R} - \frac{L}{RC_1} \right)^2 \delta_R^2 \right]^{\frac{1}{2}} \quad (\text{C.10})$$

where C_1 is as previously defined and

$$C_2 = \frac{A_{c-c}}{A_w} \cdot \frac{\Delta X_{23}}{\Delta X_{12}} \Delta T_{12}$$

Here, the uncertainty is dominated by the uncertainty in the single measurement of T_2 . The uncertainty in T_w is only slightly higher than that of T_2 alone throughout the temperature range. The additional parameters are

$$\delta_{T_2} = 0.5 \text{ } ^\circ\text{C}$$

$$\delta_{X_{23}} = \delta_{X_{12}} = 0.10 \text{ mm}$$

$$\Delta X_{23} = 1.27 \text{ mm}$$

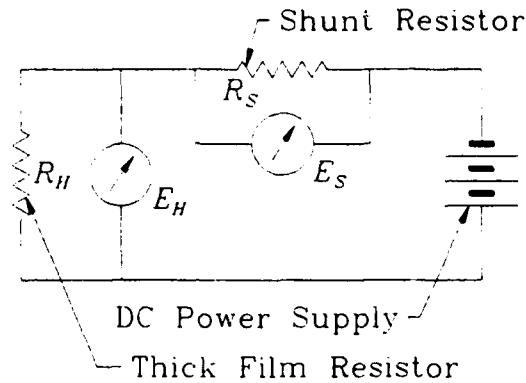


Figure C.4 Electrical schematic of heater power circuit.

C.3 Electrical Power

The electrical circuit used to measure the power input to the heater is shown in Fig. C.4. In this figure, E_H and R_H are the heater voltage drop and resistance, respectively. Because the resistance of the heater is unknown function of its temperature, a precision shunt resistor was used to measure the current through the heater. The voltage drop and resistance of the shunt are denoted by E_S and R_S , respectively. The equation for the power is thus

$$P = \frac{E_H E_S}{R_S} \quad (\text{C.11})$$

The uncertainty is then given by

$$\frac{\delta_P}{P} = \sqrt{\left(\frac{\delta_{E_H}}{E_H}\right)^2 + \left(\frac{\delta_{E_S}}{E_S}\right)^2 + \left(\frac{\delta_{R_S}}{R_S}\right)^2} \quad (\text{C.12})$$

The individual uncertainties are

$$\delta_{E_H} = 8 \times 10^{-5} E_H + 8 \times 10^{-6} \text{ V}$$

$$\delta_{E_s} = 8 \times 10^{-5} E_s + 6 \times 10^{-6} \text{ V}$$

and

$$\frac{\delta_{R_s}}{R_s} = 0.002$$

Worst case values for the other unknowns are

$$E_H = 1.0 \text{ V}$$

and

$$E_s = 0.007 \text{ V}$$

Substituting these values into Eq. (C.12) yields an uncertainty slightly greater than that of the shunt resistor alone, or 0.22%.

C.4 Flow Velocity

The flow velocity was calculated with knowledge of the flow rate, Q , and channel dimensions. The equation for flow rate is

$$U = \frac{Q}{wh} \tag{C.13}$$

where Q is the flow rate and the flow channel cross sectional width and height are w and h , respectively. The uncertainty is simply

$$\frac{\delta_U}{U} = \sqrt{\left(\frac{\delta_Q}{Q}\right)^2 + \left(\frac{\delta_w}{w}\right)^2 + \left(\frac{\delta_h}{h}\right)^2} \quad (\text{C.14})$$

where the uncertainty in the flow rate dominates in all cases. Thus, the uncertainty in the flow velocity may be taken as 0.5%.

Appendix D

DERIVATION OF MODEL FOR SURFACE TEMPERATURE VARIATION

Kenning^{32,78,79} has investigated the effect of nucleate boiling on the temperature distribution of the heater surface. For the pool boiling of water at atmospheric pressure and a heat flux of 5 W/cm^2 , he found that the heater surface temperature could vary by over 30°C . Such a variation would surely call into question any indirect measurement of the surface temperature. The large variation in surface temperature arises from the large variation in heat flux over the surface. Kenning based several assumptions on the microlayer evaporation model for a single nucleation site shown in Fig. D.1. The first assumption is that at the center of the nucleation site, the surface is dry so that heat transfer is assumed negligible. Second of the assumptions, is that evaporation of the microlayer provides very high rates of heat transfer just outside the dryout zone. The third assumption is that radially outward from the microlayer region, the heat transfer is once again negligible. This last assumption is based on observations of pool boiling and is probably not applicable to the present case of flow boiling. Significant heat transfer outside of the microlayer would serve to moderate the temperature variation.

Kenning derived an analytical model for predicting the temperature distribution on the heater surface. He considered the idealized situation of boiling from a cylinder of radius $R = 2R_b$ where R_b is the maximum bubble radius, (see Fig. D.2). The sphere of influence of bubble is often assume to be twice the bubble radius in analyses of boiling. The surface heat flux is considered to be the superposition of a steady uniform heat flux due

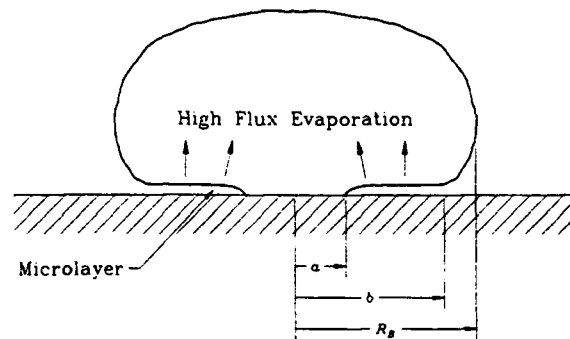


Figure D.1 Mechanisms of heat flux variation beneath a bubble.

to internal generation or heating from below, and a perturbation heat flux, $f(r)$, which makes no net contribution to the overall heat transfer. Thus

$$\frac{1}{\pi} \int_0^1 2\pi r f(r) dr = 0 \quad (\text{D.1})$$

Although the surface temperature also varies with time due to the ebullition cycle of a nucleation site, Kenning considered only the time averaged perturbation heat flux. For his experiments, the spatial variation was much larger than the temporal variation of surface temperature. For the model shown in Fig. D.2, the domain of the perturbation heat flux is

$$f(r) = q, \quad 0 \leq r \leq a, \quad b \leq r \leq R \quad (\text{D.2a})$$

$$f(r) = -q \left[\frac{1}{b^2 - a^2} - 1 \right], \quad a < r < b \quad (\text{D.2b})$$

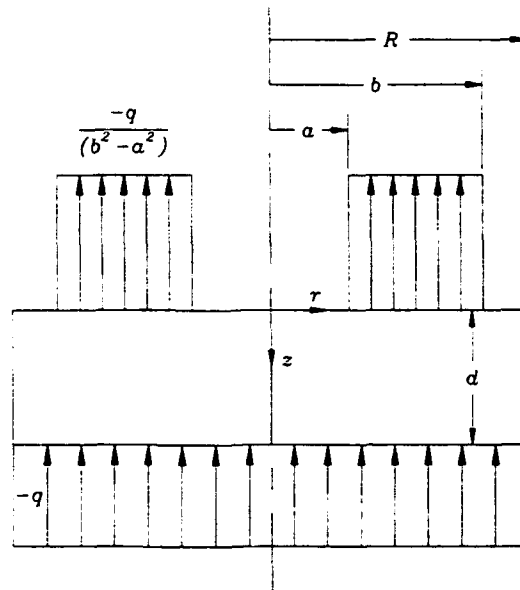


Figure D.2 Schematic of model to describe surface temperature variation.³²

Because the temperature variation due to the perturbation does not depend on the uniform heat flux applied, the problem is described by the conduction equation

$$\frac{\partial^2 \theta}{\partial r^2} + \frac{1}{r} \frac{\partial \theta}{\partial r} + \frac{\partial^2 \theta}{\partial z^2} = 0 \quad (\text{D.3})$$

where θ is the difference between the surface temperature and the mean temperature. Kenning's model was for a heater of finite thickness as shown in Fig. D.2. He reported that for a thick wall heater, such as that of the present study, the solution for a semi-infinite cylinder would be more applicable. Thus, for a semi-infinite cylinder, the boundary conditions are

$$\frac{\partial \theta(0, z)}{\partial r} = 0, \text{ or is finite} \quad (\text{D.4a})$$

$$\frac{\partial \theta(R, z)}{\partial r} = 0 \quad (\text{D.4b})$$

$$\frac{\partial \theta(r, z \rightarrow \infty)}{\partial z} = 0 \quad (\text{D.4c})$$

$$k \frac{\partial \theta(r, 0)}{\partial z} = -q \quad 0 \leq r \leq a, \quad b \leq r \leq R$$

$$k \frac{\partial \theta(r, 0)}{\partial z} = q \left[\frac{1}{(b^2 - a^2)} - 1 \right] \quad a < r < b \quad (\text{D.4d})$$

where the lengths have been made nondimensional with respect to R or,

$$a' = \frac{a}{R} \qquad b' = \frac{b}{R}$$

$$r' = \frac{r}{R} \qquad z' = \frac{z}{R} \qquad R' = 1$$

and the temperature difference has been nondimensionalized as

$$\theta' = \frac{\theta k}{qR}$$

Separating variables and dropping the (') notation,

$$\theta(r, z) = \psi(r)\phi(z)$$

The boundary conditions become

$$\frac{\partial \psi(r=0)}{\partial r} = 0 \quad \text{or is finite} \qquad \text{(D.5a)}$$

$$\frac{\partial \psi(r=1)}{\partial r} = 0 \qquad \text{(D.5b)}$$

$$\frac{\partial \phi(z \rightarrow \infty)}{\partial z} = 0 \qquad \text{(D.5c)}$$

$$\frac{\partial \theta(r, 0)}{\partial z} = -1 \quad 0 \leq r \leq a, \quad b \leq r \leq 1$$

$$\frac{\partial \theta(r, 0)}{\partial z} = \left[\frac{1}{(b^2 - a^2)} - 1 \right] \quad a < r < b \qquad \text{(D.5d)}$$

Considering the radial coordinate, the general solution is

$$\psi(r) = AJ_0(\lambda r) + BY_0(\lambda r) \quad (\text{D.6})$$

Applying the boundary conditions, Eqs. (D.5a) and (D.5b), yields $B = 0$, and

$$A \lambda_n J_0(\lambda_n) = 0 \quad (\text{D.7})$$

where λ_n are the eigenvalues. For the axial coordinate, the general solution is

$$\phi_n = C_n e^{-\lambda_n z} = D_n e^{\lambda_n z} \quad (\text{D.8})$$

Applying the boundary condition, Eq. (D.5c) yields $D_n = 0$. Combining the solutions for $\psi(r)$ and $\phi(z)$

$$\theta(r, z) = A_0 + \sum_{n=1}^{\infty} A_n e^{-\lambda_n z} J_0(\lambda_n r) \quad (\text{D.9})$$

Applying the final boundary condition, Eq. (D.5d),

$$\frac{\partial \theta(z=0)}{\partial z} = f(r) = \sum_{n=1}^{\infty} -\lambda_n A_n e^{-\lambda_n z} J_0(\lambda_n r) \quad (\text{D.10})$$

Employing orthogonality,

$$A_n = \frac{-\int_0^R r f(r) J_0(\lambda_n r) dr}{\lambda_n \int_0^R r J_0^2(\lambda_n r) dr} = \frac{-\int_0^R r f(r) J_0(\lambda_n r) dr}{\lambda_n \frac{R^2}{2} J_0^2(\lambda_n R)} \quad (\text{D.11})$$

Integrating the numerator

$$-\int_0^a r J_0(\lambda_n r) dr = \frac{-a}{\lambda_n} J_1(\lambda_n a) \quad (\text{D.12a})$$

$$\left[\frac{1}{b^2 - a^2} - 1 \right] \int_a^b r J_0(\lambda_n r) dr = \left[\frac{1}{b^2 - a^2} - 1 \right] \left[\frac{b}{\lambda_n} J_1(\lambda_n b) - \frac{a}{\lambda_n} J_1(\lambda_n a) \right] \quad (\text{D.12b})$$

$$-\int_b^1 r J_0(\lambda_n r) dr = -\left[\frac{1}{\lambda_n} J_1(\lambda_n) - \frac{b}{\lambda_n} J_1(\lambda_n b) \right] \quad (\text{D.12c})$$

Combining Eqs. (D.12a) - (D.12c) gives,

$$-\int_0^1 r f(r) J_0(\lambda_n r) dr = -\frac{1}{(b^2 - a^2)} \left(\frac{b}{\lambda_n} J_1(\lambda_n b) - \frac{a}{\lambda_n} J_1(\lambda_n a) \right) \quad (\text{D.13})$$

and

$$A_n = -\frac{2}{(b^2 - a^2)} \cdot \frac{b J_1(\lambda_n b) - a J_1(\lambda_n a)}{\lambda_n^2 J_0^2(\lambda_n)} \quad (\text{D.14})$$

finally,

$$A_0 = \lim_{\lambda_0 \rightarrow 0} \left\{ -\frac{2}{b^2 - a^2} \cdot \frac{b \left[\frac{1}{\lambda_0} J_1(\lambda_0 b) - b J_2(\lambda_0 b) \right] - a \left[\frac{1}{\lambda_0} J_1(\lambda_0 a) - a J_2(\lambda_0 a) \right]}{2 \lambda_0 J_0^2(\lambda_0)} \right\} \quad (\text{D.15})$$

= 0

$$\theta(r, z) = -\frac{2}{b^2 - a^2} \sum_{n=1}^{\infty} \frac{[b J_1(\lambda_n b) - a J_1(\lambda_n a)]}{\lambda_n^2 J_0^2(\lambda_n)} e^{-\lambda_n z} J_0(\lambda_n r) \quad (\text{D.16})$$

Remembering that

$$\theta'(r, z) = \frac{\theta(r, z) k}{q R}$$

and that the prime notation was dropped, the surface temperature is

$$\theta(r, z) = -\frac{q R}{k} \cdot \frac{2}{b^2 - a^2} \sum_{n=1}^{\infty} \frac{[b J_1(\lambda_n b) - a J_1(\lambda_n a)]}{\lambda_n^2 J_0^2(\lambda_n)} e^{-\lambda_n z} J_0(\lambda_n r) \quad (\text{D.17})$$

This equation is valid for thick boiling surfaces of high thermal conductivity, (i.e., the copper heater test section of the present experiments). The maximum temperature difference across the surface is obtained by taking the difference of the maximum and minimum θ over the range $0 \leq r \leq 1$. Similarly, the solution for a finite length cylinder is given by

$$\theta(r, z) = -\frac{qR}{k} \cdot \frac{2}{b^2 - a^2} \sum_{n=1}^{\infty} \frac{\cosh(\lambda_n d - \lambda_n z) [b J_1(\lambda_n b) - a J_1(\lambda_n a)]}{\lambda_n^2 \sinh(\lambda_n d) J_0^2(\lambda_n)} J_0(\lambda_n r) \quad (\text{D.18})$$

This equation is applicable to thin heaters, (i.e., the thin Monel foil heater test section of Chapter 6). The inner and outer radii, (a and b), of the annular heat flux are the only unknowns. Kenning chose values of a and b which fit his data, which was for the discrete bubble regime, (see Fig. 3.1). To experimentally obtain these values is probably impossible at this time. For any combination of a and b , the temperature distribution is uniform at a depth equal to one bubble radius.

It must be noted that Eqs. (D.17) and (D.18) over estimate the extremes of the temperature difference for the case of flow boiling. First, the higher single-phase heat transfer rate will tend to level the heat flux distribution on the surface. Second, the bubbles are more closely packed, ($R \approx R_B$). The temporal variations in temperature will also be smaller for the case of flow boiling because the frequency of the bubble growth and departure cycle is much larger.

Appendix E
UNCERTAINTY ANALYSIS FOR AVERAGE WALL TEMPERATURE OF
THIN FOIL HEATER

This appendix presents calculations for determining the uncertainty in average surface temperature if measured indirectly by knowing the heater resistance as a function of temperature. Knowing the heater resistance as a function of temperature, the current through the heater and the voltage drop across the heater may be measured to obtain the resistance and thus the average surface temperature. The same voltage and current information could also be used to calculate the power going into the heater. Figure E.1 shows the simple electrical circuit used to accomplish this. Because the majority of the nomenclature is specific to this appendix, it is presented here.

Nomenclature

E_H	voltage across heater
E_S	voltage across shunt
I	current through heater
L	heater length
R_H	resistance of heater
R_0	resistance of foil at reference temperature, T_0
R_S	shunt resistance
t	thickness of foil heater
T	foil temperature during calibration
T_0	reference temperature
\bar{T}_w	average foil wall temperature obtained from indirect measurements
W	heater width
α_R	temperature coefficient of resistance
ρ	resistivity of foil
ρ_0	resistivity of foil at reference temperature, T_0

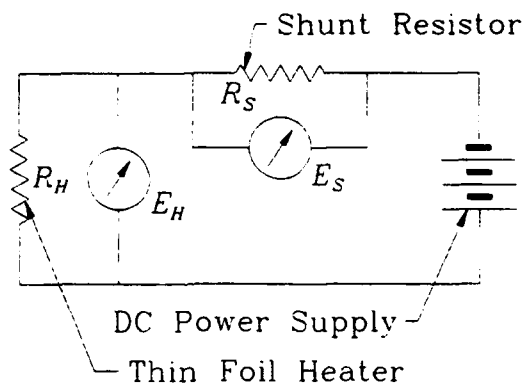


Figure E.1 Electrical circuit used for obtaining heater temperature and power.

The variation of resistance with temperature for a pure metal follows the law given by

$$\frac{dR}{R} = \alpha_{\Omega} dT \quad (\text{E.1})$$

This law holds for most alloys also. For the range of temperatures of interest, 20-120°C, the temperature coefficient of resistance, α_{Ω} , may be assumed constant. Over this same range, the change in resistance is also small. Thus, Eq. (E.1) may be integrated to obtain

$$\bar{T}_w = \frac{1}{\alpha_{\Omega}} \ln \left(\frac{R_H}{R_0} \right) + T_0 \quad (\text{E.2})$$

where

$$R_H = \frac{E_H}{I} \quad (\text{E.3})$$

and

$$I = \frac{E_S}{R_S} \quad (\text{E.4})$$

substituting Eqs. (E.3) and (E.4) into Eq. (E.2),

$$\bar{T}_w = \frac{1}{\alpha_o} \ln \left(\frac{E_H R_S}{R_o E_S} \right) + T_o \quad (\text{E.5})$$

and by the Kline and McKlintock³¹ method, the uncertainty of \bar{T}_w is given by

$$\delta \bar{T}_w = \left\{ \left[\frac{1}{\alpha_o^2} \ln \left(\frac{E_H R_S}{E_S} \right) \right]^2 \delta \alpha_o^2 + \left(\frac{1}{\alpha_o E_H} \right)^2 \delta E_H^2 + \left(\frac{1}{\alpha_o R_S} \right)^2 \delta R_S^2 + \left(\frac{1}{\alpha_o E_S} \right)^2 \delta E_S^2 + \left(\frac{1}{\alpha_o R_o} \right)^2 \delta R_o^2 + \delta T_o^2 \right\}^{1/2} \quad (\text{E.6})$$

In Eq. (E.6), all of the variables are a function of the test and test recording equipment except α_o which must be measured separately. A separate test was performed to determine $\alpha_o(T)$. Knowing that

$$\alpha_o = \ln \left(\frac{R_H}{R_o} \right) (T - T_o)^{-1} \quad (\text{E.7})$$

and assuming that $R_H = R_o$, the uncertainty of the temperature coefficient of resistance is given by

$$\frac{\delta \alpha_o}{\alpha_o} = \left\{ 2 \left[\frac{1}{R_H \ln(R_H/R_o)} \right]^2 \delta R_H^2 + 2 \left(\frac{1}{T - T_o} \right)^2 \delta T^2 \right\}^{1/2} \quad (\text{E.8})$$

Finally, if the substitution

$$R_o = \frac{\rho_o L}{W t} \quad (\text{E.9})$$

(where $W = L$ for the present experiments), is made into Eqs. (E.7) and (E.8); and Eqs.

(E.7) and (E.8) are substituted into Eq. (E.6), then $\delta\bar{T}_w$ can be solved as a function of the heater voltage, the shunt voltage, and other known parameters. The heater and shunt voltages may be obtained in terms of heat flux and known parameters as follows. An energy balance of the heater yields

$$q_M L^2 = E_H^2 R_o \quad (\text{E.10})$$

Solving for E_H gives

$$E_H = L \sqrt{q_M R_o} \quad (\text{E.11})$$

By combining Eqs. (E.3) and (E.4), E_H may be eliminated in Eq. (E.11) to yield

$$E_S = R_S L \sqrt{\frac{q_M}{R_H}} \quad (\text{E.12})$$

If Eqs. (E.11) and (E.12) are also substituted into Eq. (E.6), $\delta\bar{T}_w$ may be solved for in terms of known quantities, representative values of q_M and T and the material properties. Therefore, an optimal foil alloy may be chosen based on minimization of $\delta\bar{T}_w$ and other constraints such as peak amperage. As a result of this analysis, the material with the highest $\rho_o \cdot \alpha_o$ product was found to be the most desirable. This is somewhat contrary to the design strategy employed for resistance thermometry devices (RTDs) where only a high α_o is sought. This is a consequence of the foil also being used as a heater and the introduction of heat generation dependent variables such as E_H into the equation. Pure metals often have an α_o orders of magnitude greater than the α_o of alloys. This is one reason why RTDs are often made of platinum. On the other hand, alloys have a much greater value of ρ_o . Platinum, nickel, tantalum and alloys of nichrome and monel were considered.

Monel 400 was found to have the highest product of $\rho_o \cdot \alpha_o$. Monel also had excellent solderability, an important feature when working with very thin foils.

Furthermore, the resistance of the pure metals was too low to provide enough heat with the existing power supply. Unfortunately, the value of α_0 reported by the manufacturer was about 50 times greater than what was eventually measured. Consequently, the error became very large and this diagnostic technique was abandoned.

Appendix F
DATA

Geometries for channels 1-3 are listed in Table 3.1, (also see Fig. 2.2). Dimensions for channel #4 are given Fig. 5.2. Protrusion height cases for channel #4 are explained in Fig. 5.3 and cases with insulators are explained in Fig. 6.3. Where insufficient points were taken to obtain the incipient temperature overshoot, the lack of data is denoted by N/A. The grit sandpaper used to prepare the surfaces and other notes are listed in the last column.

Run Number	ΔT_{sub} [°C]	U [m/s]	$T_w - T_f$ @CHF [°C]	q_M [W/cm ²]	T_{sat} [°C]	Incipient Overshoot [°C]	Surface Preparation & Comments
Channel #1 - Straight Section							
V1S20STR	20.0	1.0	54.0	38.1	56.6	0	Polished
V2S20STR	20.0	2.0	56.1	50.1	56.6	0	Polished
V3S20STR	20.0	3.0	56.2	60.8	56.6	0	Polished
V4S20STR	20.0	4.0	59.1	73.3	56.6	0	Polished
B209301A	20.0	2.0	41.2	51.3	59.8	N/A	1000 grit sandpaper
B309301A	20.0	3.0	44.5	62.4	61.2	N/A	1000 grit
B409301C	20.0	4.0	42.4	74.3	63.0	N/A	1000 grit
B509301A	20.0	5.0	50.6	83.7	65.3	N/A	1000 grit
B212091A	20.0	2.0	61.2	55.9	59.5	0	1000 grit
B312161A	20.0	3.0	49.7	60.1	61.0	0	1000 grit
B412161A	20.0	4.0	45.8	73.1	62.7	5	1000 grit
C112161B	35.0	1.0	75.9	51.8	58.5	5	1000 grit
C212161B	35.0	2.0	75.1	78.7	59.5	5	1000 grit
Channel #1 - Curved Section							
B109291A	20.0	1.0	46.0	45.3	58.8	0	1000 grit
B209291A	20.0	2.0	40.4	57.0	59.8	1	1000 grit
B209291B	20.0	2.0	42.7	57.5	59.8	1	1000 grit
B309291A	20.0	3.0	42.0	72.1	61.2	0	1000 grit
B309291B	20.0	3.0	46.8	69.9	61.2	1	1000 grit
B409291A	20.0	4.0	42.9	84.1	62.9	N/A	1000 grit
B409291B	20.0	4.0	46.9	84.2	63.0	0	1000 grit

Run Number	ΔT_{sub} [°C]	U [m/s]	$T_w - T_f$ @CHF [°C]	q_M [W/cm ²]	T_{sat} [°C]	Incipient Overshoot [°C]	Surface Preparation & Comments
B509291A	20.0	5.0	47.6	97.8	65.3	N/A	1000 grit
B409301A	20.0	4.0	52.3	84.9	63.0	0	1000 grit
B409301B	20.0	4.0	52.6	85.3	63.0	0	1000 grit
B112151A	20.0	1.0	60.2	43.0	58.7	0	1000 grit
B212151A	20.0	2.0	59.8	60.0	59.6	0	1000 grit
B312151A	20.0	3.0	58.6	73.4	61.1	0	1000 grit
B412151A	20.0	4.0	66.1	86.4	62.8	0	1000 grit
B512151A	20.0	5.0	65.6	98.1	65.1	0	1000 grit
C112151A	35.0	1.0	78.6	56.7	58.7	0	1000 grit
C112161A	35.0	1.0	78.5	56.3	58.6	0	1000 grit
C212161A	35.0	2.0	78.0	86.8	59.5	0	1000 grit
C312161A	35.0	3.0	80.5	115.3	61.0	0	1000 grit
C412161A	35.0	4.0	79.2	135.2	62.8	0	1000 grit
Channel #2 - Straight Section							
B303131C	20.0	3.0	63.9	68.1	60.1	N/A	32% absorbed air
B303131D	20.0	3.0	63.3	65.7	60.1	N/A	250 grit, 31% abs. air
B303141A	20.0	3.0	66.6	66.7	60.1	0	250 grit, 15% abs. air
B303141B	20.0	3.0	67.4	64.3	60.1	N/A	250 grit, 24% abs. air
B303141C	20.0	3.0	65.4	63.9	60.1	N/A	250 grit, 30% abs. air
B210141A	20.0	2.0	39.4	51.1	59.3	0	1000 grit
B310141A	20.0	3.0	41.7	61.5	60.6	0	1000 grit
B410141A	20.0	4.0	42.7	73.2	62.2	0	1000 grit
B312141A	20.0	3.0	56.7	62.1	60.9	0	1000 grit
B212141A	20.0	2.0	58.7	52.4	59.6	4	1000 grit
B312211B	20.0	3.0	51.1	61.7	60.9	N/A	1000 grit
B412211A	20.0	4.0	46.5	71.4	62.5	N/A	1000 grit
B512211A	20.0	5.0	43.1	80.9	64.6	N/A	1000 grit
B112211B	20.0	1.0	53.0	38.9	58.6	N/A	1000 grit
B212211A	20.0	2.0	56.9	50.9	59.5	N/A	1000 grit
B412211B	20.0	4.0	49.7	70.9	62.5	N/A	1000 grit
B512211B	20.0	5.0	46.7	85.0	64.5	N/A	1000 grit
B612211A	20.0	6.0	45.3	96.1	66.8	N/A	1000 grit
B712211A	20.0	7.0	45.1	105.0	69.6	N/A	1000 grit

Run Number	ΔT_{sub} [°C]	U [m/s]	$T_w - T_f$ @CHF [°C]	q_M [W/cm ²]	T_{sat} [°C]	Incipient Overshoot [°C]	Surface Preparation & Comments
BC12211A	20.0	1.5	47.9	46.1	58.9	N/A	1000 grit
BD12211A	20.0	2.5	58.0	57.6	60.1	N/A	1000 grit
B412211C	20.0	4.0	56.3	69.1	62.4	N/A	1000 grit
C112211A	35.0	1.0	77.8	53.3	58.4	N/A	1000 grit
CC12211A	35.0	1.5	77.3	68.3	58.8	N/A	1000 grit
C212211A	35.0	2.0	77.8	80.5	59.3	N/A	1000 grit
CD12211A	35.0	2.5	78.4	90.4	60.0	N/A	1000 grit
C312211A	35.0	3.0	78.8	102.6	60.7	N/A	1000 grit
C412211A	35.0	4.0	79.5	126.1	62.5	N/A	1000 grit
C512211A	35.0	5.0	79.3	146.9	64.7	N/A	1000 grit
Channel #2 - Curved Section							
A102190A	5.0	1.0	40.0	39.9	56.0	N/A	As Machined
A102220A	5.0	1.0	45.7	36.0	56.0	N/A	As Machined
A202240A	5.0	2.0	47.7	47.9	56.0	N/A	As Machined
B103260A	20.0	1.0	61.5	46.4	57.4	0	Polished
B203260A	20.0	2.0	61.9	56.4	58.6	N/A	Polished
A203270A	5.0	2.0	37.0	35.5	58.0	N/A	Polished
B203270A	20.0	2.0	59.1	57.2	58.0	N/A	Polished
B206090A	20.0	2.0	64.3	62.1	57.6	0	600 grit
B206090B	20.0	2.0	64.5	64.0	57.6	1	600 grit
B206100A	20.0	2.0	63.2	63.4	57.7	0	600 grit
B206100B	20.0	2.0	63.8	64.4	57.7	0	600 grit
B306110A	20.0	3.0	64.4	83.6	58.5	0	600 grit
B306110B	20.0	3.0	63.2	83.8	58.5	0	600 grit
B306120A	20.0	3.0	64.1	82.6	58.4	0	600 grit
B306120B	20.0	3.0	64.2	85.4	58.4	0	600 grit
B306120C	20.0	3.0	64.2	83.1	58.4	0	600 grit
B106160A	20.0	1.0	62.8	52.1	57.4	1	600 grit
B106160B	20.0	1.0	63.0	49.8	57.4	0	600 grit
B106180A	20.0	1.0	60.9	47.3	57.0	0	600 grit
B106180B	20.0	1.0	62.2	46.8	57.0	0	600 grit
B108040A	20.0	1.0	54.9	47.1	57.6	0	250 grit
B108040B	20.0	1.0	56.4	45.8	57.6	N/A	250 grit

Run Number	ΔT_{sub} [°C]	U [m/s]	$T_w - T_f$ @CHF [°C]	q_M [W/cm ²]	T_{sat} [°C]	Incipient Overshoot [°C]	Surface Preparation & Comments
B108040C	20.0	1.0	54.5	48.0	57.6	N/A	250 grit
B308040A	20.0	3.0	53.0	74.6	63.6	N/A	250 grit
B308210A	20.0	3.0	55.1	74.2	59.7	0	250 grit
B408040A	20.0	4.0	57.1	91.4	61.2	N/A	250 grit
B508040A	20.0	5.0	56.6	106.5	61.2	0	250 grit
B312290A	20.0	3.0	58.3	73.4	59.5	0	250 grit
B301021A	20.0	3.0	71.8	79.1	59.8	0	250 grit
B301021B	20.0	3.0	72.1	85.9	59.8	N/A	44% absorbed air
B301031A	20.0	3.0	67.8	76.0	59.9	0	250 grit, 33% abs. air
B301031B	20.0	3.0	68.5	77.3	59.9	0	250 grit, 38% abs. air
B301031C	20.0	3.0	66.8	76.9	59.9	0	250 grit, 10% abs. air
B302201A	20.0	3.0	68.7	71.9	61.3	0	250 grit, 52% abs. air
B302201B	20.0	3.0	69.6	75.1	61.3	0	250 grit, 37% abs. air
B302201C	20.0	3.0	66.6	75.8	61.3	0	250 grit, 29% abs. air
B302211A	20.0	3.0	64.7	70.5	61.3	1	250 grit, 28% abs. air
B302221A	20.0	3.0	68.6	75.6	61.3	0	250 grit, 37% abs. air
B302221B	20.0	3.0	67.8	75.3	61.3	0	250 grit, 36% abs. air
B302221C	20.0	3.0	67.3	74.2	61.3	0	250 grit, 18% abs. air
B302281A	20.0	3.0	64.7	72.5	61.3	1	250 grit, 31% abs. air
B302281B	20.0	3.0	67.2	74.4	61.3	0	250 grit, 34% abs. air
B303091A	20.0	3.0	69.3	74.3	60.1	N/A	250 grit, 30% abs. air
B303091B	20.0	3.0	67.7	73.8	60.1	0	250 grit, 31% abs. air
B303091C	20.0	3.0	69.7	74.6	60.1	N/A	250 grit, 32% abs. air
B303131A	20.0	3.0	69.3	75.4	60.1	N/A	250 grit, 8% abs. air
B303131B	20.0	3.0	69.4	75.0	60.1	0	250 grit, 19% abs. air
B303231A	20.0	3.0	59.6	71.3	60.3	0	250 grit, 30% abs. air
B303231B	20.0	3.0	62.7	73.3	60.3	0	250 grit, 32% abs. air
B312141B	20.0	3.0	57.0	64.4	60.4	0	1000 grit
B412141A	20.0	4.0	81.4	76.8	61.8	0	1000 grit
B512141A	20.0	5.0	77.9	86.9	63.5	0	1000 grit
B312171A	20.0	3.0	46.6	67.0	60.0	0	1000 grit
B112221A	20.0	1.0	49.7	42.4	58.1	N/A	1000 grit
B212221A	20.0	2.0	56.9	55.0	58.8	N/A	1000 grit

Run Number	ΔT_{sub} [°C]	U [m/s]	$T_w - T_f$ @CHF [°C]	q_M [W/cm ²]	T_{sat} [°C]	Incipient Overshoot [°C]	Surface Preparation & Comments
B312221A	20.0	3.0	47.6	67.4	60.1	N/A	1000 grit
B312221B	20.0	3.0	55.0	68.0	59.7	N/A	1000 grit
B412221A	20.0	4.0	50.9	78.9	61.4	N/A	1000 grit
B512221A	20.0	5.0	54.7	91.4	63.2	N/A	1000 grit
B612221A	20.0	6.0	52.6	103.7	65.1	N/A	1000 grit
B712221A	20.0	7.0	55.2	115.1	67.4	N/A	1000 grit
C112221A	35.0	1.0	79.6	52.4	57.9	N/A	1000 grit
C212221A	35.0	2.0	81.1	78.2	58.5	N/A	1000 grit
C312221A	35.0	3.0	77.7	98.5	59.6	N/A	1000 grit
C412221A	35.0	4.0	72.6	116.1	61.1	N/A	1000 grit
C512221A	35.0	5.0	69.8	131.4	62.9	N/A	1000 grit
Channel #2 - Straight section with 2.00 mm shim.							
B211181A	20.0	2.0	47.8	56.5	58.8	N/A	1000 grit
B311181A	20.0	3.0	45.8	61.7	59.4	N/A	1000 grit
B411181A	20.0	4.0	47.2	66.5	60.1	N/A	1000 grit
B511181A	20.0	5.0	44.8	71.9	60.8	N/A	1000 grit
B111181A	20.0	1.0	53.0	50.3	58.3	N/A	1000 grit
B111181B	20.0	1.0	54.6	50.6	58.3	N/A	1000 grit
BC11181A	20.0	1.5	56.6	53.4	58.6	N/A	1000 grit
B211181B	20.0	2.0	57.8	56.7	58.8	N/A	1000 grit
BD11181A	20.0	2.5	59.6	58.3	59.1	N/A	1000 grit
B311181B	20.0	3.0	49.1	61.8	59.4	N/A	1000 grit
B411181B	20.0	4.0	50.5	65.8	60.1	N/A	1000 grit
B511181B	20.0	5.0	46.1	73.2	60.9	N/A	1000 grit
B611181A	20.0	6.0	43.5	78.9	61.6	N/A	1000 grit
B711181A	20.0	7.0	63.7	85.8	62.4	N/A	1000 grit
B111231A	20.0	1.0	55.6	56.2	58.3	N/A	1000 grit
BC11231A	20.0	1.5	57.4	59.0	58.5	N/A	1000 grit
B211231A	20.0	2.0	57.3	61.4	58.7	N/A	1000 grit
B311231A	20.0	3.0	49.9	67.0	59.3	N/A	1000 grit
B411231A	20.0	4.0	49.4	70.5	59.9	N/A	1000 grit
B111231B	20.0	1.0	58.3	53.9	58.2	N/A	1000 grit
B111241A	20.0	1.0	56.4	47.4	58.5	N/A	1000 grit

Run Number	ΔT_{sub} [°C]	U [m/s]	$T_w - T_f$ @CHF [°C]	q_M [W/cm ²]	T_{sat} [°C]	Incipient Overshoot [°C]	Surface Preparation & Comments
B411241A	20.0	4.0	49.7	62.3	60.7	N/A	1000 grit
B111261A	20.0	1.0	57.1	47.7	58.7	N/A	1000 grit
B411261A	20.0	4.0	54.0	61.0	60.8	N/A	1000 grit
B111261B	20.0	1.0	57.6	48.7	58.4	N/A	1000 grit
B411271A	20.0	4.0	49.8	63.5	60.8	N/A	1000 grit
B611271A	20.0	6.0	47.1	72.7	63.0	N/A	1000 grit
B711271A	20.0	7.0	41.3	77.4	64.5	N/A	1000 grit
C11271A	35.0	1.0	64.5	68.8	58.0	N/A	1000 grit
CC11271A	35.0	1.5	62.0	76.8	58.4	N/A	1000 grit
C211271A	35.0	2.0	61.0	83.6	58.7	N/A	1000 grit
CD11271A	35.0	2.5	60.4	89.4	59.2	N/A	1000 grit
C311271A	35.0	3.0	60.0	95.3	59.8	N/A	1000 grit
C411271A	35.0	4.0	61.2	107.0	60.7	N/A	1000 grit
C511271A	35.0	5.0	60.6	117.8	61.8	N/A	1000 grit
C611271A	35.0	6.0	60.5	124.6	63.1	N/A	1000 grit
C711271A	35.0	7.0	59.5	129.7	64.5	N/A	1000 grit
Channel #3 - Straight Section							
A110123A	5.0	1.0	49.4	32.8	58.2	3	1000 grit
A115123A	5.0	1.0	43.7	29.7	58.6	0	1000 grit
A210123A	5.0	2.0	51.9	36.3	58.8	1	1000 grit
A215123A	5.0	2.0	43.0	32.2	59.2	0	1000 grit
A310123A	5.0	3.0	50.9	36.4	60.2	0	1000 grit
A315123A	5.0	3.0	42.0	32.3	60.2	0	1000 grit
A410123A	5.0	4.0	47.8	39.7	63.4	0	1000 grit
A415123A	5.0	4.0	52.5	38.6	62.2	1	1000 grit
B110123A	20.0	1.0	59.7	46.4	58.1	8	1000 grit
B110123B	20.0	1.0	58.0	45.1	58.1	0	1000 grit
B125034A	20.0	1.0	46.3	45.3	58.3	0	1000 grit
B209221A	20.0	2.0	64.5	51.0	59.6	0	1000 grit
B210123A	20.0	2.0	39.6	53.5	58.8	2	1000 grit
B225034A	20.0	2.0	43.2	53.0	58.9	0	1000 grit
B225034B	20.0	2.0	56.0	48.0	59.2	1	1000 grit
B309211A	20.0	3.0	64.1	58.1	61.0	0	1000 grit

Run Number	ΔT_{sub} [°C]	U [m/s]	$T_w - T_f$ @CHF [°C]	q_M [W/cm ²]	T_{sat} [°C]	Incipient Overshoot [°C]	Surface Preparation & Comments
B313123A	20.0	3.0	52.3	60.1	60.6	1	1000 grit
B325034A	20.0	3.0	38.3	61.5	60.1	1	1000 grit
B325034B	20.0	3.0	53.9	59.2	60.0	9	1000 grit
B409211A	20.0	4.0	62.3	70.7	62.8	0	1000 grit
B413123A	20.0	4.0	61.2	74.5	62.0	1	1000 grit
B425034A	20.0	4.0	53.7	72.0	61.6	1	1000 grit
B509211A	20.0	5.0	62.3	83.7	64.8	0	1000 grit
B513123A	20.0	5.0	59.2	86.5	63.7	1	1000 grit
B525034A	20.0	5.0	52.5	84.8	63.4	2	1000 grit
B609221A	20.0	6.0	64.0	94.6	67.1	0	1000 grit
B709221A	20.0	7.0	68.3	109.7	70.4	0	1000 grit
C103123A	35.0	1.0	62.5	58.9	59.0	0	1000 grit
C114123A	35.0	1.0	53.9	58.5	58.2	1	1000 grit
C206123A	35.0	2.0	63.8	77.0	59.2	5	1000 grit
C214123A	35.0	2.0	56.5	80.5	58.8	0	1000 grit
C306123A	35.0	3.0	60.8	96.3	60.2	1	1000 grit
C314123A	35.0	3.0	55.3	95.6	59.9	2	1000 grit
C414123A	35.0	4.0	60.1	119.6	61.3	0	1000 grit
Channel #3 - Curved Section							
A102123A	5.0	1.0	55.2	37.2	59.0	3	1000 grit
A118113A	5.0	1.0	54.9	38.0	59.1	0	1000 grit
A202123A	5.0	2.0	56.5	53.1	59.8	0	1000 grit
A218113A	5.0	2.0	55.8	56.2	59.8	1	1000 grit
A302123A	5.0	3.0	55.0	60.8	61.2	0	1000 grit
A319113A	5.0	3.0	56.2	63.9	61.0	0	1000 grit
A402123A	5.0	4.0	56.0	70.0	63.4	0	1000 grit
A419113A	5.0	4.0	51.3	68.4	63.9	0	1000 grit
B101123A	20.0	1.0	56.4	52.0	59.2	2	1000 grit
B130113A	20.0	1.0	53.2	50.0	59.5	0	1000 grit
B201123A	20.0	2.0	56.5	65.1	60.0	0	1000 grit
B230113A	20.0	2.0	56.5	64.7	60.2	0	1000 grit
B301123A	20.0	3.0	54.6	79.0	61.4	0	1000 grit
B330113A	20.0	3.0	54.5	78.9	61.6	0	1000 grit

Run Number	ΔT_{sub} [°C]	U [m/s]	$T_w - T_f$ @CHF [°C]	q_M [W/cm ²]	T_{sat} [°C]	Incipient Overshoot [°C]	Surface Preparation & Comments
B401123A	20.0	4.0	57.3	94.7	63.2	0	1000 grit
B430113A	20.0	4.0	55.0	92.1	63.4	0	1000 grit
B501123A	20.0	5.0	50.3	106.3	65.5	1	1000 grit
B530113A	20.0	5.0	49.8	103.7	65.7	0	1000 grit
C117113A	35.0	1.0	58.9	65.4	59.0	6	1000 grit
C117113B	35.0	1.0	69.2	62.5	58.8	13	1000 grit
C130113A	35.0	1.0	60.4	66.6	59.6	5	1000 grit
C217113A	35.0	2.0	61.2	83.8	59.5	1	1000 grit
C218113A	35.0	2.0	69.2	84.0	60.1	1	1000 grit
C230113A	35.0	2.0	60.8	89.2	60.5	0	1000 grit
C317113A	35.0	3.0	67.1	106.2	61.0	3	1000 grit
C318113A	35.0	3.0	71.8	107.2	61.5	0	1000 grit
C330113A	35.0	3.0	59.0	108.9	61.7	2	1000 grit
C417113A	35.0	4.0	68.8	128.1	65.2	2	1000 grit
C418113A	35.0	4.0	68.8	128.2	63.3	0	1000 grit
C430113A	35.0	4.0	62.2	131.5	63.4	0	1000 grit
C517113A	35.0	5.0	65.8	146.8	65.1	2	1000 grit
C518113A	35.0	5.0	65.4	148.8	65.7	0	1000 grit
C530113A	35.0	5.0	62.6	148.8	65.7	0	1000 grit
Channel #4 - Flush Heat Source							
B104251A	20.0	1.0	41.4	36.4	61.2	N/A	1000grit
B104251B	20.0	1.0	57.8	29.9	61.5	0	1000grit
B204291B	20.0	2.0	51.2	47.4	62.0	0	1000grit
B304291A	20.0	3.0	49.3	55.9	64.2	0	1000grit
B304291B	20.0	3.0	51.0	57.8	64.2	N/A	1000grit
B404291A	20.0	4.0	44.3	67.9	66.5	0	1000grit
B404291B	20.0	4.0	54.6	72.6	66.5	N/A	1000grit
B504291A	20.0	5.0	52.8	85.3	69.6	0	1000grit
B104291A	20.0	1.0	57.5	42.1	61.0	N/A	1000grit
C104301A	35.0	1.0	73.6	60.5	61.2	N/A	1000grit
C304301A	35.0	3.0	78.7	99.6	64.4	N/A	1000grit
C205011A	35.0	2.0	70.3	72.8	62.5	N/A	1000grit
C305011A	35.0	3.0	76.4	92.3	64.4	0	1000grit

Run Number	ΔT_{sub} [°C]	U [m/s]	$T_w - T_f$ @CHF [°C]	q_M [W/cm ²]	T_{sat} [°C]	Incipient Overhoot [°C]	Surface Preparation & Comments
C405011A	35.0	4.0	73.5	104.2	66.8	0	Heater failed, no CHF.
C405011B	35.0	4.0	77.3	109.0	66.8	N/A	1000grit
C505011A	35.0	5.0	68.4	106.1	69.8	2	Heater failed, no CHF.
B103063A	20.0	1.0	57.0	41.6	56.5	0	1000grit
B103223B	20.0	1.0	55.3	38.6	56.6	1	1000grit
B203253A	20.0	2.0	56.5	44.0	58.5	1	1000grit
B303253A	20.0	3.0	55.6	53.5	60.7	1	1000grit
B403253A	20.0	4.0	56.7	64.5	63.4	0	1000grit
B103273A	20.0	1.0	50.1	39.3	56.6	0	1000grit
B203273A	20.0	2.0	49.8	43.9	58.1	2	1000grit
B303273A	20.0	3.0	49.2	52.0	60.5	1	1000grit
B403273A	20.0	4.0	56.6	63.8	63.5	1	1000grit
B503273B	20.0	5.0	55.3	76.5	66.8	N/A	1000grit
B503293A	20.0	5.0	44.7	79.9	66.6	1	1000grit
B403293A	20.0	4.0	40.1	66.8	60.3	1	1000grit
B303293A	20.0	3.0	40.4	56.6	60.3	0	1000grit
B203293A	20.0	2.0	44.9	47.1	56.5	2	1000grit
B103293A	20.0	1.0	55.8	40.5	56.4	1	1000grit
C103303A	35.0	1.0	64.3	48.0	56.5	2	1000grit
C503303A	35.0	5.0	60.6	120.5	66.9	0	1000grit
C403303A	35.0	4.0	66.3	102.4	63.4	1	1000grit
C303303A	35.0	3.0	55.0	82.9	60.4	1	1000grit
C203303A	35.0	2.0	56.8	62.7	58.0	2	1000grit
C103303B	35.0	1.0	60.1	48.3	56.3	3	1000grit
Channel #4 - Heat source recessed 0.127 mm.							
B105121A	20.0	1.0	56.5	35.2	60.8	0	1000 grit
B305121A	20.0	3.0	53.1	48.2	64.5	0	1000 grit
B305121B	20.0	3.0	53.7	51.3	64.6	0	1000 grit
B205131A	20.0	2.0	60.5	40.0	62.4	0	1000 grit
B105131A	20.0	1.0	59.4	36.2	60.9	0	1000 grit
B405131A	20.0	4.0	62.5	58.7	67.5	0	1000 grit
B106051A	20.0	1.0	57.0	34.0	61.0	6	1000 grit
B206051A	20.0	2.0	59.6	37.2	63.4	0	1000 grit

Run Number	ΔT_{sub} [°C]	U [m/s]	$T_w - T_f$ @CHF [°C]	q_M [W/cm ²]	T_{sat} [°C]	Incipient Overshoot [°C]	Surface Preparation & Comments
B306051A	20.0	3.0	57.7	45.0	64.5	0	1000 grit
B406051A	20.0	4.0	57.1	54.4	67.4	0	1000 grit
C106101A	35.0	1.0	56.1	45.9	60.5	0	1000 grit
C206101A	35.0	2.0	54.3	57.4	62.2	0	1000 grit
C306101A	35.0	3.0	55.0	66.0	64.3	0	1000 grit
C406101A	35.0	4.0	59.1	84.0	67.0	0	1000 grit
Channel #4 - Heat source protruded 0.229 mm.							
B106151A	20.0	1.0	50.3	38.6	60.0	0	1000 grit
B106151B	20.0	1.0	42.4	29.2	60.4	0	1000 grit
B206151A	20.0	2.0	44.8	31.9	61.8	0	1000 grit
B306151A	20.0	3.0	61.6	44.9	63.9	4	1000 grit
B406151A	20.0	4.0	56.9	64.3	66.5	0	1000 grit
B106181A	20.0	1.0	61.4	34.6	60.0	0	1000 grit
B206181A	20.0	2.0	58.1	34.2	62.3	0	1000 grit
B306181A	20.0	3.0	60.8	42.1	64.6	0	1000 grit
B406181A	20.0	4.0	55.0	62.8	67.3	0	1000 grit
B306181A	20.0	3.0	60.8	42.1	64.3	0	1000 grit
C106251A	35.0	1.0	75.7	47.1	60.9	6	1000 grit
C206251A	35.0	2.0	77.3	65.9	62.3	N/A	1000 grit
C306251A	35.0	3.0	78.6	84.5	64.5	0	1000 grit
C406251A	35.0	4.0	78.4	104.9	67.3	0	1000 grit
Channel #4 - Heat source protruded 0.457 mm.							
B107201A	20.0	1.0	51.0	30.8	60.4	7	1000 grit
B207201A	20.0	2.0	63.7	31.9	62.4	0	1000 grit
B307201A	20.0	3.0	61.3	60.8	64.6	0	1000 grit
B407201A	20.0	4.0	61.5	85.2	67.2	0	1000 grit
B107201B	20.0	1.0	49.5	32.1	60.9	15	1000 grit
B207201B	20.0	2.0	68.5	35.6	62.3	13	1000 grit
C207231A	35.0	2.0	76.4	69.9	62.2	4	1000 grit
C307231B	35.0	3.0	78.0	101.1	64.4	10	1000 grit
C407231A	35.0	4.0	76.6	122.4	67.1	0	1000 grit
B207241A	20.0	2.0	72.4	35.5	62.2	N/A	1000 grit

Run Number	ΔT_{sub} [°C]	U [m/s]	$T_w - T_f$ @CHF [°C]	q_M [W/cm ²]	T_{sat} [°C]	Incipient Overshoot [°C]	Surface Preparation & Comments
Channel #4 - Heat source protruded 0.635 mm.							
B105051A	20.0	1.0	44.9	36.4	60.7	3	1000 grit
B305051A	20.0	3.0	57.7	86.9	64.4	0	1000 grit
B105061A	20.0	1.0	51.6	34.3	61.0	3	1000 grit
B205061A	20.0	2.0	61.9	61.7	63.4	N/A	1000 grit
B305061A	20.0	3.0	58.7	82.8	64.6	N/A	1000 grit
B205071A	20.0	2.0	52.8	56.5	63.6	3	1000 grit
B305081A	20.0	3.0	58.6	89.2	64.8	0	1000 grit
B105081A	20.0	1.0	38.8	31.9		0	1000 grit
B405081A	20.0	4.0	58.1	109.8	67.8	0	1000 grit
C105081A	35.0	1.0	60.7	56.4	61.0	8	1000 grit
C205081A	35.0	2.0	69.5	94.4	63.6	5	1000 grit
C305081A	35.0	3.0	73.7	131.4	64.8	3	1000 grit
C405081A	35.0	4.0	65.4	138.7	67.5	0	Heater failed, no CHF.
B104053A	20.0	1.0	39.0	42.9	56.6	1	1000 grit
B104083A	20.0	1.0	40.2	41.9	56.3	1	1000 grit
B304083A	20.0	3.0	55.2	86.7	60.0	1	1000 grit
B104093A	20.0	1.0	42.6	40.2	55.8	0	1000 grit
B204123A	20.0	2.0	58.2	63.8	59.4	0	1000 grit
B304123A	20.0	3.0	54.1	86.2	59.8	4	1000 grit
B404123A	20.0	4.0	46.9	95.8	62.9	5	1000 grit
Channel #4 - Heat source protruded 0.635 mm with 0.305 mm insulator.							
B104233A	20.0	1.0	48.3	44.3	55.8	1	1000 grit
B204233A	20.0	2.0	46.3	55.4	57.4	1	1000 grit
B304273A	20.0	3.0	47.6	69.8	63.6	0	1000 grit
B404273A	20.0	4.0	55.9	93.1	63.5	1	1000 grit
C104303A	35.0	1.0	60.7	63.2	56.6	3	1000 grit
C204303A	35.0	2.0	60.1	80.4	58.1	2	1000 grit
C305033A	35.0	3.0	64.8	107.5	63.6	0	1000 grit
C405033A	35.0	4.0	67.2	123.8	63.5	1	1000 grit
B105033A	20.0	1.0	47.7	40.6	56.6	0	1000 grit
B205033A	20.0	2.0	44.5	51.6	58.1	1	1000 grit
B305033A	20.0	3.0	58.5	71.2	60.7	1	1000 grit

Run Number	ΔT_{sub} [°C]	U [m/s]	$T_w - T_f$ @CHF [°C]	q_M [W/cm ²]	T_{sat} [°C]	Incipient Overshoot [°C]	Surface Preparation & Comments
B405033A	20.0	4.0	56.2	94.3	63.5	0	1000 grit
B505033A	20.0	5.0	58.6	111.4	66.7	0	1000 grit
C105273A	35.0	1.0	60.3	63.7	58.6	2	1000 grit
C205273A	35.0	2.0	59.5	81.1	61.3	0	1000 grit
C305273A	35.0	3.0	64.3	104.8	61.2	1	1000 grit
C405283A	35.0	4.0	67.7	128.9	64.8	1	1000 grit
B305283A	20.0	3.0	59.4	72.4	61.7	0	1000 grit
B505283B	20.0	5.0	60.6	116.4	69.5	2	1000 grit
Channel #4 - Heat source protruded 0.635 mm with 0.635 mm insulator.							
B104153A	20.0	1.0	50.5	45.0	57.0	1	1000 grit
B204153A	20.0	2.0	41.1	53.0	57.2	1	1000 grit
B304153A	20.0	3.0	44.1	67.4	59.7	0	1000 grit
B404153A	20.0	4.0	48.5	82.1	62.6	1	1000 grit
B204153B	20.0	2.0	45.3	54.6	56.9	1	1000 grit
B504153A	20.0	5.0	55.3	99.5	65.7	0	1000 grit
C104203A	35.0	1.0	61.2	61.4	54.1	1	1000 grit
C204203A	35.0	2.0	61.5	78.2	56.2	1	1000 grit
C304203A	35.0	3.0	65.8	94.7	60.3	1	1000 grit
C404203A	35.0	4.0	64.3	116.5	62.8	1	1000 grit
C504203A	35.0	5.0	62.3	133.3	66.2	0	Heater failed, no CHF.
C104203B	35.0	1.0	60.6	60.6	55.4	0	1000 grit
C204203B	35.0	2.0	61.4	77.8	57.1	1	1000 grit
C304213A	35.0	3.0	61.4	98.9	60.0	1	1000 grit
C404213A	35.0	4.0	62.8	116.7	63.3	0	1000 grit
B104213A	20.0	1.0	50.8	43.1	55.8	0	1000 grit
B204213A	20.0	2.0	49.2	51.3	57.4	1	1000 grit
B304213A	20.0	3.0	54.3	64.9	60.1	1	1000 grit
B404213A	20.0	4.0	53.7	80.2	62.9	1	1000 grit
Channel #4 - Flush thin foil heater.							
B110142A	20.0	1.0	45.5	22.4	65.4	1	Very rough surface.
B110142B	20.0	1.0	45.6	21.5	65.9	3	Very rough surface.
B210142A	20.0	2.0	55.2	31.0	57.7	2	Very rough surface.
B110152A	20.0	1.0	42.0	26.1	55.1	12	Very rough surface.

Run Number	ΔT_{sub} [°C]	U [m/s]	$T_w - T_f$ @CHF [°C]	q_M [W/cm ²]	T_{sat} [°C]	Incipient Overshoot [°C]	Surface Preparation & Comments
B310152A	20.0	3.0	39.6	31.8	60.2	2	Very rough surface.
B110162A	20.0	1.0	41.0	25.7	55.0	12	Very rough surface.
B210162A	20.0	2.0	39.1	29.4	57.6	7	Very rough surface.
B310162A	20.0	3.0	38.6	34.1	60.0	2	Very rough surface.
B410162A	20.0	4.0	38.2	38.5	62.9	4	Very rough surface.
B510162A	20.0	5.0	38.2	44.2	66.2	5	Very rough surface.
B110162B	20.0	1.0	37.8	23.7	56.2	7	Very rough surface.
B210162B	20.0	2.0	38.1	29.2	57.7	7	Very rough surface.
B310162B	20.0	3.0	37.2	33.2	60.2	7	Very rough surface.
B410162B	20.0	4.0	37.0	37.8	63.1	7	Very rough surface.
B510162B	20.0	5.0	36.5	44.5	66.3	4	Very rough surface.
B111032A	20.0	1.0	40.5	30.0	55.2	1	1000 grit, smooth
B111042C	20.0	1.0	40.5	31.4	55.2	20	1000 grit, smooth
B211042A	20.0	2.0	38.6	38.8	57.7	8	1000 grit, smooth
Channel #4 - Thin foil heater protruded 0.711 mm.							
B110182A	20.0	1.0	41.2	25.0	55.9	8	Very rough surface.
B210182A	20.0	2.0	40.1	33.9	57.4	1	Very rough surface.
B310182A	20.0	3.0	37.5	39.3	59.9	1	Very rough surface.
B410182A	20.0	4.0	36.1	42.8	63.2	1	Very rough surface.
B410192A	20.0	4.0	37.9	42.8	63.2	0	Very rough surface.
B510192A	20.0	5.0	36.5	47.0	66.5	1	Very rough surface.

BIBLIOGRAPHY

Electronics Cooling

Aung, W., Editor, *Cooling Technology for Electronic Equipment*, Hemisphere Publishing Corp., New York, 1988.

Baker, E., "Liquid Cooling of Microelectronic Devices By Free And Forced Convection," *Microelectronics and Reliability*, Vol. 11, 1972, pp. 213-222.

Bergles, A.E., "High Flux Boiling Applied to Microelectronics Thermal Control," *International Communications in Heat and Mass Transfer*, Vol. 15, No. 4, 1988, pp. 509-531.

Drexel, W.H., "Fluorochemical Cooling for High Heat Dissipation," *Electronic Design*, Vol. 9, No. 11, 1961, pp. 40-43.

Krane, R.J., Parsons, J.R., and Bar-Cohen, A., "Design of a Candidate Thermal Control System for a Cryogenically Cooled Computer," *IEEE Transactions on Components, Hybrids, and Manufacturing Technology*, Vol. 11, No. 4, 1988, pp. 545-556.

Kraus, A.D., and Bar-Cohen, A., *Thermal Analysis and Control of Electronic Equipment*, Hemisphere, New York, 1983.

Saylor, J.R., Bar-Cohen, A., Lee, T., Simon, T.W., and Wu, P., "Fluid Selection and Property Effects in Single- and Two-Phase Immersion Cooling," *IEEE Transactions on Components, Hybrids, and Manufacturing Technology*, Vol. 11, No. 4, 1988, pp. 557-565.

Mark, M., Stephenson, M., and Goltsos, C., "An Evaporative-Gravity Technique for Airborne Equipment Cooling," *IRE Transactions On Aeronautical And Navigational*

Electronics, Vol. ANE-5, No. 1, 1958, pp. 47-52.

Pool Boiling with Acceleration Forces

Beckman, W.A., and Merte, H., "A Photographic Study of Boiling in an Accelerating System," *ASME Journal of Heat Transfer*, Vol. 87, No. 3, 1965, pp. 374-380.

Clark, J.A., and Merte, H., "Boiling Heat Transfer to a Cryogenic Fluid in Both Low and High Gravity Fields," *Advances in Cryogenic Engineering*, Vol. 7, Plenum Press, New York, 1961, pp. 347-355.

Costello, C.P., Adams, J.M., and Clinton, W.W., "Improvement of Burnout Heat Flux by Orientation of Semicircular Heaters," *AIChE Journal*, Vol. 8, No. 4, September, 1962, pp. 569-570.

Costello, C.P., and Adams, J.M., "The Interrelation of Geometry, Orientation, and Acceleration in the Peak Heat Flux Problem," *AIChE Journal*, Vol. 9, No. 5, September, 1963, pp. 663-671.

Costello, C.P., and Tuthill, W.E., "Effects of Acceleration on Nucleate Pool Boiling," *AIChE Chemical Engineering Progress Symposium Series*, Vol. 57, No. 32, 1961, pp. 189-196.

Ivey, H.J., "Acceleration and the Critical Heat Flux in Pool Boiling Heat Transfer," *Proceedings of The Institution of Mechanical Engineers, Thermodynamics and Fluid Mechanics Group*, Vol. 177, No. 1, 1963, pp. 15-42.

Lienhard, J.H., and Sun, K., "Effects of Gravity and Size Upon Film Boiling from Horizontal Cylinders," *ASME Journal of Heat Transfer*, Vol. 92, No. 2, 1970, pp. 292-298.

Lienhard, J.H., "Interacting Effects of Geometry and Gravity Upon the Extreme Boiling Heat Fluxes," *ASME Journal of Heat Transfer*, Vol. 90, No. 1, 1968, pp. 180-182.

Merte, H., and Clark, J.A., "Boiling Heat Transfer with Cryogenic Fluids at Standard, Fractional, and Near-Zero Gravity," *ASME Journal of Heat Transfer*, Vol. 86, No.3, 1964, pp. 351-359.

Merte, H., and Clark, J.A., "Boiling Heat-Transfer Data for Liquid Nitrogen at Standard and Near-Zero Gravity," *Advances in Cryogenic Engineering*, Vol. 7, 1962, pp. 546-550.

Pomerantz, M.L., "Film Boiling on a Horizontal Tube in Increased Gravity Fields," *ASME Journal of Heat Transfer*, Vol. 86, No.2, 1964, pp. 213-219.

Siegel, R., "Effects of Reduced Gravity on Heat Transfer," *Advances in Heat Transfer*, Vol. 4, Academic Press, New York, 1967, pp. 143-228.

Usiskin, C.M., and Siegel, R., "An Experimental Study of Boiling in Reduced and Zero Gravity Fields," *ASME Journal of Heat Transfer*, Vol. 83, No. 3, 1961, pp. 243-253.

Heat Transfer in Curved Tubes and Ducts

Cheng, K.C., and Akiyama, M., "Laminar Forced Convection Heat Transfer in Curved Rectangular Channels," *International Journal of Heat and Mass Transfer*, Vol. 13, 1970, pp. 471-489.

Emery, A.F., Neighbors, P.K., and Gessner, F.B., "The Numerical Prediction of Developing Turbulent Flow and Heat Transfer in a Square Duct," *ASME Journal of Heat Transfer*, Vol. 102, No. 1, 1980, pp. 51-57.

Mayle, R.E., Blair, M.F., and Kopper, F.C., "Turbulent Boundary Layer Heat Transfer on Curved Surfaces," *ASME Journal of Heat Transfer*, Vol. 101, No. 3, August, 1979, pp.

521-525.

Mori, Y., Uchida, Y., and Ukon, T., "Forced Convective Heat Transfer in a Curved Channel with a Square Cross Section," *International Journal of Heat and Mass Transfer*, Vol. 14, 1971, pp. 1787-1804.

Rogers, C.F.C., and Mayhew, Y.R., "Heat Transfer and Pressure Loss in Helically Coiled Tubes with Turbulent Flow," *International Journal of Heat and Mass Transfer*, Vol. 7, 1964, pp. 1207-1216.

Seban, R.A., and McLaughlin, E.F., "Heat Transfer in Tube Coils with Laminar and Turbulent Flow," *International Journal of Heat and Mass Transfer*, Vol. 6, 1963, pp. 387-395.

Thomann, H., "Effect of Streamwise Wall Curvature on Heat Transfer in a Turbulent Boundary Layer," *Journal of Fluid Mechanics*, Vol. 33, part 2, 1968, pp. 283-292.

Yee, G., Chilukuri, R., Humphrey, J.A.C., "Developing Flow and Heat Transfer in Strongly Curved Ducts of Rectangular Cross Section," *ASME Journal of Heat Transfer*, Vol. 102, No. 3, 1980, pp. 285-291.

Flow Boiling with Acceleration Forces

Dhir, V.K., and Scott, J.H., "On the Superposition of Injection Induced Swirl during Enhancement of Subcooled Critical Heat Flux," *International Journal of Heat and Mass Transfer*, Vol. 30, No. 10, 1987, pp. 2013-2022.

Gambill, W.R., and Bundy, R.D., "High-Flux Heat Transfer Characteristics of Pure Ethylene Glycol in Axial and Swirl Flow," *AIChE Journal*, Vol. 9, No. 1, 1963, pp. 55-59.

Gambill, W.R., Bundy, R.D., and Wansbrough, R.W., "Heat Transfer, Burnout, and Pressure Drop for Water in Swirl Flow Through Tubes with Internal Twisted Tapes," *AIChE Chemical Engineering Progress Symposium Series*, Vol. 57, No. 32, 1961, pp. 127-137.

Miropolskiy, Z.L., Picus, V.J., and Shitsman, M.E., "Regimes of Deteriorated Heat Transfer at Forced Flow of Fluids in Curvilinear Channels," *Proceedings of the Third International Heat Transfer Conference*, Chicago, Illinois, Vol. 2, 1966, pp. 95-101.

Miropolskiy, Z.L., Picus, V.J., and Shitsman, M.E., "Discussion of: Regimes of Deteriorated Heat Transfer at Forced Flow of Fluids in Curvilinear Channels," *Proceedings of the Third International Heat Transfer Conference*, Chicago, Illinois, Vol. 6, 1966, pp. 136-139.

Mudawwar, and El-Masri, M.A., "Boiling Incipience in Plane Rotating Water Films," *ASME Journal of Heat Transfer*, Vol. 110, No. 2, 1988, pp. 532-535.

Papell, S.S., Simoneau, R.J., and Brown, D.D., "Buoyancy Effects on Critical Heat Flux of Forced Convective Boiling in Vertical Flow," NASA Report TN D-3672, October, 1966.

Secondary Flow

Bradshaw, P., "Effects of Streamline Curvature on Turbulent Flow," *NATO Advisory Group for Aerospace Research and Development*, AGARDograph No. 169, August, 1973.

Cheng, K.C., Lin, R., Ou, J., "Fully Developed Laminar Flow in Curved Rectangular Channels," *ASME Journal of Fluids Engineering*, Vol. 98, No. 1, 1976, pp. 41-48.

Crawford, R.A., "Influence of Bulk Turbulence and Entrance Boundary Layer Thickness

on the Curved Duct Flow Field," NASA Contractor Report 4188, November, 1988.

Dean, W.R., "The Stream-Line Motion of Fluid in a Curved Pipe," *The London, Edinburgh & Dublin Philosophical Magazine and Journal of Science*, Vol. 5, 1928, pp. 673-695.

De Vriend, H.J., "Velocity Redistribution in Curved Rectangular Channels," *Journal of Fluid Mechanics*, Vol. 107, 1931, pp. 423-439.

Detra, R.W., "The Secondary Flow in Curved Pipes," *Mitteilungen Aus Dem Institut Für Aerodynamik*, No. 20., Verlag Leemann Zürich, Switzerland, 1953, (in English).

Hille, P., Vehrenkamp, R., and Schulz-Dubois, E.O., "The Development and Structure of Primary and Secondary Flow in a Curved Square Duct," *Journal of Fluid Mechanics*, Vol. 151, February, pp. 219-241.

Humphrey, J.A.C., Whitelaw, J.H., and Yee, G., "Turbulent Flow in a Square Duct with Strong Curvature," *Journal of Fluid Mechanics*, Vol. 103, February, pp. 443-463.

Hur, N., Thangam, S., Speziale, C.G., "Numerical Study of Turbulent Secondary Flows in Curved Ducts," *ASME Journal of Fluids Engineering*, Vol. 112, No. 2, 1990, pp. 205-211.

Ito, H., "Pressure Losses in Smooth Pipe Bends," *ASME Journal of Basic Engineering*, Vol. 82, March, 1960, pp. 131-143.

Melling, A., and Whitelaw, J.H., "Turbulent Flow in a Rectangular Duct," *Journal of Fluid Mechanics*, Vol. 78, part 2, 1976, pp. 289-315.

Taylor, A.M.K.P., Whitelaw, J.H., and Yianneskis, M., "Curved Ducts with Strong

Secondary Motion: Velocity Measurements of Developing Laminar and Turbulent Flow,"
ASME Journal of Fluids Engineering, Vol. 104, No. 3, 1982, pp. 350-359.

You, S.M., Simon, T.W., and Kim, J., "Free-Stream Turbulence Effects on Convex-
Curved Turbulent Boundary Layers," *ASME Journal of Heat Transfer*, Vol. 111, No. 1,
1989, pp. 66-72.

VITA

John Ernest Leland was born October 10, 1961 in Akron Ohio. He graduated from the University of Akron with a BSME in 1986. He received his MSME from the University of Dayton, Dayton Ohio, in 1989. He has worked for the United States Air Force since 1986 at the Wright Laboratory on Wright-Patterson Air Force Base. During this time he has worked in the areas of spacecraft thermal management, thermionic energy conversion, and most recently aircraft thermal management. He is a member of the American Society of Mechanical Engineers and an active member of the American Institute of Aeronautics and Astronautics. He was president of the University of Kentucky student chapter of the AIAA during the 1990 school year. He is currently a member of the AIAA Thermophysics Technical Committee. To date, Mr. Leland holds the following patents and has published or helped publish the following papers.

PATENTS:

Ferrofluid Piston Pump for Use With Heat Pipes or the Like, patent # 5,005,639.

Thermionic Fuel Element Pressure Vessel, patent # 5,039,475.

PUBLICATIONS:

Chow, L.C., Leland, J.E., Beam, J.E. and Mahefkey, E.T., "Movement of Air Bubbles In An Artery," *Proceedings of the 6th International Heat Pipe Conference*, Grenoble, France, June 1987.

Wen, C., Sheffield, J.W., O'Dell, P.O. and Leland, J.E., "An Analytical and Experimental Investigation of Melting Heat Transfer," AIAA-88-0357, presented at the 26th Aerospace Sciences Meeting, Reno, Nevada, January 1988.

Leland, J.E., Chow, L.C. and Iden, S.M., "A Long Life Pump for Spacecraft Applications," AIAA-88-2687, presented at the 23rd AIAA Thermophysics Conference,

June 1988.

Scaringe, R.P., Buckman, J.A., Grzyll, L.R., Mahefkey, E.T., and Leland, J.E.,
"Alternative Heat Pump Configurations," IECEC-889390, August 1988.

Grzyll, L.R., Mahefkey, E.T. and Leland, J.E., "Identification of New Working Fluids
For Use In High-Temperature Rankine Cycles," IECEC-889189, August 1988.

Sheffield, J.W., Wen, C., and Leland, J.E., "Melting Heat Transfer Inside a Cylinder,"
*Proceedings of 5th International Symposium on Multiphase Transport and Particulate
Phenomena*, Miami Beach, Florida, December 1988.

Scaringe, R.P., Buckman, J.A., Grzyll, L.R., Mahefkey, E.T., and Leland, J.E.,
"Investigation of Advanced Heat Pump Augmented Spacecraft Heat Rejection Systems,"
AIAA-89-0072, presented at the 27th Aerospace Sciences Meeting, Reno, Nevada,
January 9-12 1989.

Chang, W.S., and Leland, J.E., "Finite Difference Simulation of Transient Heat Pipe
Operation," AIAA-89-0320, presented at the 27th Aerospace Sciences Meeting, Reno,
Nevada, January 9-12 1989.

Leland, J.E. and Mahefkey, E.T., "Status and Potential of Heat Pump Augmented
Spacecraft Radiators," *Proceedings of the 6th Symposium on Space Nuclear Power
Systems*, Albuquerque, NM, January 1989.

Chow, L.C., Leland, J.E., Beam, J.E., and Mahefkey, E.T., "The Drag Coefficient of a
Sphere in a Square Channel," *ASME Journal of Fluids Engineering*, Vol. 111, pp. 229-
230, 1989.

Wen, C., Sheffield, J.W., O'Dell, M.P., Leland, J.E., "An Analytical and Experimental

Investigation of Melting Heat Transfer," *AIAA Journal of Thermophysics and Heat Transfer*, July 1989.

Scaringe, R.P., Buckman, J.A., Grzyll, L.R., Mahefkey, E.T., and Leland, J.E., "Heat-Pump-Augmented Spacecraft Heat-Rejection Systems," *Journal of Spacecraft and Rockets*, Vol. 27, pp. 318-323, 1990.

Brown, J.R., Chang, W.S. and Leland, J.E., "Transient Operating Characteristics of an Oxygen Heat Pipe," ASME # 91-HT-22, presented at National Heat Transfer Conference in Minneapolis, MN, July 28-31, 1990.

Leland, J.E. and Chow, L.C. "High Heat Flux Cooling for Spacecraft Electronics," *Proceedings of the Eighth Symposium on Space Nuclear Power Systems*, Albuquerque, NM, 7-10 January 1991.

Leland, J.E. and Chow, L.C., "Effect of Radius of Curvature on Boiling in a Curved Channel," AIAA-92-250, presented at the 30th Aerospace Sciences Meeting, Reno, NV, January 6-9, 1992.

Leland, J.E. and Chow, L.C., "Forced Convection Boiling from a Non-Flush Simulated Electronic Chip," AIAA-92-251, presented at the 30th Aerospace Sciences Meeting, Reno, NV, January 6-9, 1992.

Ponnappan, R., Leland, J.E., Chang, W.S., and Beam, J.E., "Results of a Single Phase Venturi Flow Cooling Experiment," *Proceedings of The Sixth International Symposium on Transport Phenomena (ISTP-6) in Thermal Engineering*, Seoul, Korea, May 9-13, 1993.

Leland, J.E. and Chow, L.C., "Boiling From the Top and Sides of a Protruding Simulated Electronic Chip," AIAA-93-2834, presented at the 28th AIAA Thermophysics

Conference, Orlando, FL, July 6-9, 1993.

Pais, M.R., Leland, J.E., Chang, W.S., and Chow, L.C., "Jet Impingement Cooling Using A Jet Fuel," *Proceedings 1993 National Heat Transfer Conference*, Atlanta, Georgia, August 8-11, 1993.

Leland, J.E. and Chow, L.C., "Forced Convection Boiling From a Non-Flush Simulated Electronic Chip," *AIAA Journal of Thermophysics and Heat Transfer*, Vol. 7, No. 4, pp. 588-594, 1993.

Ponnappan, R. and Leland, J.E., "Forced-Convection Heat Transfer In A Venturi-Type Annular Flow," *Proceedings of the First ISHMT-ASME Heat and Mass Transfer Conference*, BARC-Bombay, India, January 5-7, 1994.

Ponnappan, R. and Leland, J.E., "Rotating Heat Pipe for Cooling of Rotors In Advanced Generators," AIAA Paper 94-2033, to be presented at the AIAA/ASME 6th Joint Thermophysics and Heat Transfer Conference, Colorado Springs, CO, June 20-23, 1994.

Pais, M.R., Leland, J.E., Chang, W.S., and Chow, L.C., "Single-Phase Heat Transfer Characteristics of Submerged Jet Impingement Cooling Using JP-5," IThERM Symposium Paper #94018, InterSociety Conference on Thermal Phenomena, Washington D.C., May 4-7, 1994.

Pais, M.R., Leland, J.E., and Chang, W.S., "Single-Phase Spray Impingement Cooling of Submerged Surfaces Using JP-5," to be presented at the 1994 ASME Winter Annual meeting, Chicago, IL, 1994.

Leland, J.E. and Chow, L.C., "Effect of Radius of Curvature on Boiling in a Curved Channel," under final revision for *AIAA Journal of Thermophysics and Heat Transfer*.